TU Delft

Delft University of Technology

Micromechanics-guided development of strain-hardening alkali-activated composites Towards a low-carbon built environment

Zhang, S.

DOI
10.4233/uuid:cdea2e9d-e069-4683-a8ca-c436b43fa64c

Publication date
2022

Document Version
Final published version

Citation (APA)
Zhang, S. (2022). *Micromechanics-guided development of strain-hardening alkali-activated composites: Towards a low-carbon built environment*. [Dissertation (TU Delft), Delft University of Technology]. https://doi.org/10.4233/uuid:cdea2e9d-e069-4683-a8ca-c436b43fa64c

Important note
To cite this publication, please use the final published version (if applicable).
Please check the document version above.

Copyright
Other than for strictly personal use, it is not permitted to download, forward or distribute the text or part of it, without the consent of the author(s) and/or copyright holder(s), unless the work is under an open content license such as Creative Commons.

Takedown policy
Please contact us and provide details if you believe this document breaches copyrights.
We will remove access to the work immediately and investigate your claim.

This work is downloaded from Delft University of Technology.
For technical reasons the number of authors shown on this cover page is limited to a maximum of 10.

Micromechanics-guided development of strain-hardening alkali-activated composites

Towards a low-carbon built environment

Proefschrift

ter verkrijging van de graad van doctor
aan de Technische Universiteit Delft,
op gezag van de Rector Magnificus Prof. dr. ir. T.H.J.J. van der Hagen,
voorzitter van het College voor Promoties,
in het openbaar te verdedigen op donderdag 1 december 2022 om 10:00 uur

door

Shizhe ZHANG

Ingenieur in Technische Materiaalwetenschappen
Technische Universiteit Delft, Nederland
geboren te Dongying, P. R. China.

Dit proefschrift is goedgekeurd door de promotoren:

Prof. dr. ir. K. van Breugel
Dr. G. Ye

Samenstelling promotiecommissie:

Rector magnificus	Voorzitter
Prof.dr.ir. K. van Breugel	Technische Universiteit Delft, promotor
Dr. G. Ye	Technische Universiteit Delft, promotor

Onafhankelijke leden:

Prof.dr. P. Krivenko	Kyiv National University of Construction & Architecture, Ukraine
Dr. J.S. Dolado	Materials Physics Center, Spain
Prof.dr.-ing. V. Mechtcherine	Dresden University of Technology, Germany
Prof.dr.ir. M.A.N. Hendriks	Technische Universiteit Delft
Prof.dr.ir. H.E.J.G. Schlangen	Technische Universiteit Delft

This research was carried out in Microlab, Delft University of Technology and supported by the Netherlands Organization for Scientific Research (NWO), Grant No.729.001.013, and the National Natural Science Foundation of China (NSFC), Grant No. 5151101050.

Keywords: strain-hardening, alkali-activated materials, slag, fly ash, polyvinyl alcohol (PVA), fiber, micromechanics, fracture properties, interface bonding properties, adhesion, molecular dynamics, life-cycle assessment (LCA)

Printed by: Ipskamp Printing, the Netherlands

Cover design: Yu Chen and Shizhe Zhang

ISBN: 978-94-6421-961-6

Copyright © 2022 by Shizhe Zhang

All rights reserved. No part of the material protected by this copyright notice may be reproduced or utilized in any form or by any means, electronic or mechanical, including photocopying, recording, or by any information storage and retrieval system, without written permission from the author.

An electronic copy of this dissertation is available at: https://repository.tudelft.nl

To my parents

谨以此书献给我的父母

Table of Contents

Table of Contents ····· I
List of Symbols ····· V
List of Abbreviations ····· VII
Chapter 1
General introduction
1.1 Research background ····· 1
1.2 Research aim and objectives ····· 2
1.3 Research scope ····· 3
1.4 Research strategy ····· 3
1.5 Research outline ····· 4
Chapter 2
Literature survey on the development of strain-hardening geopolymer composite (SHGC)
2.1 Introduction ····· 7
2.2 Introduction of strain-hardening cementitious composite (SHCC) and engineered cementitious composite (ECC) ····· 7
2.2.1 Fiber-reinforced cementitious composite ····· 7
2.2.2 SHCC and ECC ····· 8
2.2.3 Mechanical properties of SHCC/ECC ····· 10
2.2.4 Engineering applications of SHCC/ECC ····· 11
2.2.5 Sustainability of SHCC/ECC ····· 12
2.3 The micromechanical design basis for SHCC and ECC ····· 13
2.3.1 Criteria for strain-hardening and multiple-cracking ····· 13
2.3.2 Micromechanics-based model ····· 15
2.3.3 Application of the strain-hardening criteria and the micromechanics-based model 18
2.4 General introduction to alkali-activated materials (AAMs) and geopolymer ····· 19
2.5 Development of strain-hardening geopolymer composite (SHGC) ····· 21
2.5.1 Heat-cured fly ash-based SHGC ····· 21
2.5.2 Ambient temperature cured slag-based and slag/fly ash-based SHGC ····· 21
2.5.3 The use of the micromechanics-based model in the development of SHGC ····· 22
2.6 Influencing factors on the strain-hardening behavior of SHGC ····· 22
2.6.1 Type and properties of fiber ····· 23
2.6.2 Fracture properties of the matrix ····· 24
2.6.3 Interface bonding properties ····· 25

2.7 Environmental impact of SHGC ····· 27
2.8 Challenges in the development of SHGC ····· 29

Chapter 3

Fracture properties and microstructure formation of hardened alkali-activated slag/fly ash matrix

3.1 Introduction ····· 31
3.2 Materials and methods ····· 32
3.2.1 Materials ····· 32
3.2.2 Mixture design and sample preparation ····· 33
3.2.3 Testing procedures ····· 34
3.3 Results and discussions ····· 36
3.3.1 Compressive strength and elastic modulus ····· 36
3.3.2 Fracture properties ····· 38
3.3.3 Microstructural characterization ····· 40
3.3.4 General discussion ····· 49
3.4 Observations and conclusions ····· 53

Chapter 4

Experimental characterization of polyvinyl alcohol (PVA) fiber/matrix interface properties

4.1 Introduction ····· 55
4.2 Materials and methods ····· 56
4.2.1 Materials ····· 56
4.2.2 Mixture design ····· 56
4.2.3 Determination of interface bonding properties ····· 57
4.2.4 Microstructural characterizations ····· 58
4.3 Results and discussions ····· 59
4.3.1 PVA fiber/matrix interface bonding properties characterization ····· 59
4.3.2 Microstructural characterization of ITZ ····· 63
4.3.3 General discussions ····· 70
4.4 Conclusions ····· 74

Chapter 5

Molecular dynamics simulation on the adhesion mechanism of polyvinyl alcohol (PVA) fiber to alkali-activated slag/fly ash matrix

5.1 Introduction ····· 77
5.2 MD simulation details ····· 78
5.2.1 Construction of the PVA molecule ····· 78
5.2.2 Chemical composition of the C-(N-)A-S-H structures ····· 79
5.2.3 Construction of the PVA/C-(N-)A-S-H composites ····· 79
5.2.4 Interaction between PVA molecule and C-(N-)A-S-H ····· 81

5.2.5 In situ polymerization ····· 83
5.2.6 Adhesion strength between PVA molecule and C-(N-)A-S-H ····· 83
5.3 Results and discussions ····· 84
5.3.1 The chemical composition of the simulated C-(N-)A-S-H structure and C-(N-)A-S-H gel in AASF ····· 84
5.3.2 Interactions between PVA molecule and C-(N-)A-S-H ····· 85
5.3.3 Hydrogen bonds between PVA molecule and C-(N-)A-S-H surface. ····· 87
5.3.4 Adhesion mechanism of PVA in C-(N-)A-S-H ····· 90
5.3.5 Experimental evidence of adhesion properties and mechanism ····· 91
5.4 Conclusions ····· 95

Chapter 6

Micromechanics-guided development of a slag/fly ash-based strain-hardening geopolymer composite (SHGC)

6.1 Introduction ····· 97
6.2 Micromechanics-based design approach ····· 98
6.2.1 The starting matrix designs ····· 98
6.2.2 Micromechanics criteria for composite strain-hardening ····· 99
6.2.3 Experimental determination of micromechanical parameter values for the micromechanical modeling ····· 100
6.2.4 Micromechanical modeling to guide the mixture design of SHGC ····· 102
6.2.5 Validation of the strain-hardening behavior of designed SHGC ····· 104
6.3 Results and discussions ····· 105
6.3.1 Choosing suitable fiber volume and fiber length ····· 105
6.3.2 Evaluation of strain-hardening potential using micromechanical modeling ····· 108
6.3.3 Uniaxial tensile properties of the designed SHGC mixtures ····· 110
6.4 Discussion on using the micromechanics-based approach ····· 117
6.5 Conclusions ····· 119

Chapter 7

Cradle-to-gate life cycle assessment (LCA) of the slag/fly ash-based strain-hardening geopolymer composite

7.1 Introduction ····· 121
7.2 The LCA Methodology ····· 122
7.2.1 Goal and scope of this study ····· 122
7.2.2 Life-Cycle Inventory ····· 124
7.2.3 Life-Cycle Impact Assessment (LCIA) ····· 127
7.3 Results and discussion ····· 130
7.3.1 Environmental impact of SHGC ····· 130
7.3.2 Contribution analysis ····· 133

7.3.3 Discussion on the use of alkaline activator and PVA fiber ····· 137
7.3.4 Discussion on the cradle-to-gate LCA of SHGC ····· 139
7.4 Conclusions ····· 140
Chapter 8
Conclusions, contributions, and future research
8.1 Conclusions ····· 141
8.2 Contribution of this study ····· 142
8.3 Recommendations for future research ····· 143
Appendix A
Micromechanics-based constitutive model
A.1 Numerical model for fiber debonding and pullout stages: the relationship between pullout load P and displacement u ····· 145
A.1.1 Fiber debonding stage ····· 145
A.1.2 Fiber pullout stage ····· 149
A.2 Scale linking model linking P(u) to σ(δ) ····· 150
A.2.1 $P(\delta, L_e)$ ····· 151
A.2.2 g(φ) ····· 153
A.2.3 p(φ) and p(z) ····· 153
A.3 Other considerations ····· 154
A.3.1 Strength reduction factor f' ····· 154
A.3.2 Matrix micro-spalling ····· 154
A.3.3 Cook-Gordon effect ····· 156
Appendix B
Chemical composition of the reaction product in the PVA fiber/matrix interfacial transition zone (ITZ)
B.1 Reaction product in the ITZ ····· 157
B.2 Density plots of phases based on EDX phases mapping ····· 159
Appendix C
Chemical composition determination of C-(N-)A-S-H gel for the construction of C-(N-)A-S-H structures in the molecular dynamics (MD) simulation
C.1 Introduction ····· 161
C.2 Procedures ····· 161
References ····· 165
Summary ····· 183
Samenvatting ····· 185
Acknowledgments ····· 187
Curriculum vitae ····· 191
List of publications ····· 193

List of Symbols

a	Full crack length	[m]
A_f	Cross-sectional area of the fiber	[m^2]
A_{lig}	Ligament area	[m^2]
b	bearing width of wood strip in splitting tensile strength test	[m]
B	Width of the specimen	[m]
D	Diameter of the specimen	[m]
d_f	Diameter of the fiber	[m]
E_f	Elastic modulus of the fiber	[GPa]
E_m	Elastic modulus of the matrix	[GPa]
f	Snubbing coefficient	[-]
f'	Strength reduction factor	[-]
f_c	Compressive strength	[MPa]
f_{st}	Splitting tensile strength	[MPa]
g	Gravity constant	[m/s^2]
G_d	Chemical bonding energy	[J/m^2]
G_F	Fracture energy	[J/m^2]
J_b'	Complementary energy	[J/m^2]
J_{tip}	Crack tip toughness	[J/m^2]
K_{Ic}	Fracture toughness	[$MPa \cdot m^{1/2}$]
L	Length of the specimen	[m]
L_d	Debonded length of the fiber	[m]
L_e	Fiber embedment length	[m]
L_f	Fiber length	[m]
M_s	Silicate modulus of the alkaline activator solution	[-]
N_A	Number of atom A	[-]
P_a	Pullout load when the fiber starts to debond	[N]
P_b	Pullout load when the fiber starts to slip	[N]
P_{max}	Maximum load	[N]
PSH_e	Pseudo strain-hardening energy index	[-]
PSH_s	Pseudo strain-hardening strength index	[-]
r	Defect size	[m]
R_{fs}	Fracture surface roughness	[-]
r_i	The position vector of particle i	[-]
S	Pullout displacement	[m]
T	Number of frames taken from the trajectory of MD simulation	[-]

V_f	Fiber volume	[%]
V_f^{crit}	Critical fiber volume	[%]
W	Depth of the specimen	[m]
W_{avg}	Average crack width of loaded specimens	[m]
z	Distance between the fiber centroid and the crack plane	[m]
α	Notch depth ratio	[-]
β	Slip-hardening coefficient	[-]
δ	Crack opening width	[m]
ΔH_{ads}	Adsorption enthalpy of PVA molecule in C-(N-)A-S-H gel	[J/m^2]
$\Delta H_{C\text{-}(N\text{-})A\text{-}S\text{-}H}$	Enthalpy of C-(N-)A-S-H gel without PVA	[J/m^2]
ΔH_{PVA}	Enthalpy of the PVA molecule	[J/m^2]
$\Delta H_{PVA/C\text{-}(N\text{-})A\text{-}S\text{-}H}$	Enthalpy of the PVA/C-(N-)A-S-H composite	[J/m^2]
δ_{mid}	Mid-point deflection	[m]
δ_{ss}	Steady-state crack opening width	[m]
ε	Tensile strain capacity	[%]
ε_{cc}	Tensile strain at the first crack of the composite	[%]
ε_{pc}	The maximum tensile strain of the composite	[%]
μ	Friction coefficient	[-]
σ	Fiber bridging stress	[MPa]
σ_0	Maximum fiber bridging stress	[MPa]
σ_{cc}	Tensile stress and strain at the first crack of the composite	[MPa]
σ_{fc}	First crack strength of the composite	[MPa]
σ_{pc}	Maximum tensile stress and strain of the composite	[MPa]
σ_{ss}	Steady-state external stress	[MPa]
σ_{ult}	Ultimate tensile strength	[MPa]
τ_0	Initial frictional bond	[MPa]
φ	The inclination angle of fiber to the perpendicular direction of the crack plane	[°]
$\measuredangle(x, y)$	The angle between two vectors x and y	[°]

List of Abbreviations

AAC	Alkali-activated concrete
AAM	Alkali-activated material
AAS	Alkali-activated slag
AASF	Alkali-activated slag/fly ash
ADF	Angle distribution function
ADPE	Abiotic depletion potential-elements
ADPF	Abiotic depletion potential-fossil fuels
AP	Acidification of soil and water potential
BSE	Backscattered electron
C-(N-)A-S-H	Alkali (sodium) calcium aluminosilicate hydrate
C-A-S-H	Calcium aluminosilicate hydrate
CDF	Combined distribution functions
CH	Portlandite
CHARMM	Chemistry at Harvard Macromolecular Mechanics
CMOD	Crack mouth opening displacement
CN	Coordination number
C-S-H	Calcium silicate hydrate
DTG	Differential thermogravimetry
ECC	Engineered cementitious composite
ECI	Environmental cost indicator
EDGC	Eco-friendly ductile geopolymer composite
EDX	Energy-dispersive X-ray
EE	Embodied energy
EGC	Engineered geopolymer composite
EP	Eutrophication potential
EPD	Environmental product declaration
ESEM	Environmental scanning electron microscopy
EU	European Union
FAETP	Freshwater ecotoxicity potential
FRCC	Fiber-reinforced cementitious composites
FTIR	Fourier-transform infrared spectroscopy
GWP	Global warming potential
HMPE	High modulus polyethylene
HPFRCC	high-performance fiber-reinforced cementitious composite
HPMC	Hydroxypropyl methylcellulose
HTP	Human toxicity potential
HTPP	High-tenacity polypropylene
HVFA	High-volume fly ash
ITZ	Interfacial transition zone
LAMMPS	Large-scale Atomic/Molecular Massively Parallel Simulator
LCA	Life-cycle assessment

LCI	Life-cycle inventory
LCIA	Life-Cycle Impact assessment
LDH	Layered double hydroxide
LEFM	Linear elastic fracture mechanics
LVDT	Linear variable differential transformer
MAETP	Marine water ecotoxicity potential
MCL	Mean chain length
MD	Molecular dynamics
MIP	Mercury intrusion porosimetry
MSWI	Municipal solid waste incineration
N-A-S-H	Sodium aluminosilicate hydrate
NBO	Non-bridging oxygen
NPT	Isobaric-isothermal ensemble
NVT	Canonical ensemble
ODP	Ozone layer depletion potential
OPC	Ordinary Portland cement
PBC	Periodic boundary condition
PCA	Principal component analysis
PDF	Probability distribution function
PE	Polyethylene
PET	Polyethylene terephthalate
POCP	Photochemical oxidants creation potential
PSD	Particle size distribution
PSH	Pseudo strain-hardening
PVA	polyvinyl alcohol
PVAc	Polyvinyl acetate
RDF	Radial distribution function
ROI	Area of interest
RTP	Recycled tire polymer
SBK	Dutch Stichting Bouwkwaliteit
SCM	Supplementary cementitious material
SE	Secondary electron
SHCC	Strain-hardening cementitious composite
SHGC	Strain-hardening geopolymer composite
SI	Spectral imaging
STD	Standard deviation
TETP	Ecotoxicity. Terrestrial potential
UHPC	Ultra-high performance concrete
VMA	viscosity modifying admixtures
w/b	Water to binder
XRD	X-ray diffraction
ZAF	Atomic number, absorption, and fluorescence
3PB	Three-point bending

Chapter 1

General introduction

1.1 Research background

The fast-increasing world population and its related industrialization have generated an explosive rise in the demand for raw materials, which is already causing increasing environmental and societal consequences in many countries. In the Netherlands, 68% of the raw materials have to be imported from abroad in 2011 [1]. Such high dependency on third countries will impact the stability of the raw material supplies and their related economy [2]. Regarding the construction sector, for example, the resource shortage of limestone in the Netherlands has already largely limited the local cement production. These potential problems and challenges necessitate more efficient use of raw materials and at the same time promotes the utilization of industrial by-products and waste.

Towards a more sustainable society, many industrial sectors start investing in the optimization of waste disposal management systems. The originally non-recyclable wastes are promoted to be recycled and re-used as primary or secondary raw materials in other industrial processes, ultimately lowering their negative environmental impacts, preserving natural resources, and generating high economical profit. Focus has been put on the construction sector. The primary reason is that the construction sector involves enormous consumption of raw materials, especially the use of ordinary Portland cement (OPC) based concrete as an essential material for infrastructures and buildings [3]. The European Union (EU) has already executed a Construction Products Regulation (CPR 305/2011/EU), which attempts to obtain more knowledge to create a generic and level playing field between EU member states regarding the re-use application of waste and secondary materials [4]. Up till now, some of the wastes and secondary materials are already used in concrete as supplementary cementitious materials (SCMs) to partially replace OPC. However, due to the requirements of composition and reactivity, not all wastes and industrial by-products can be adopted as SCMs in OPC concrete [5]. Therefore, a growing need still exists for a technology that can easily and cheaply handle large quantities of waste materials and by-products and use them in the construction industry.

One smart technology that enables the transformation of industrial by-products and wastes into valuable resources is alkaline activation [6, 7]. Using this technology, alkali-activated materials (AAMs), including those classified as geopolymers, are derived by the reaction between a solid precursor (alumina- and silica-containing solids) and an alkaline solution [8, 9]. Compared with OPC binders, these materials maintain comparable performance to traditional cementitious binders but provide added advantage in greenhouse gas emission reduction [10] and sustainable utilization of industrial by-products and residuals [11, 12]. Geopolymer concrete is thus considered an environment-friendly construction material with a great potential for the next generation concrete and was considered by the CUR

recommendation as one of the 7 high potential actions towards the Dutch initiatives on concrete sustainability [13].

In the last decades, many studies have been conducted on the development and characterization of AAMs/geopolymer-based binder and concrete [14]. However, like OPC concrete, geopolymer concrete is also inherently brittle [15, 16]. The low ductility of geopolymer concrete makes it prone to cracking and corresponding performance degradation, which is detrimental to its durability [17]. A promising solution is the development of fiber-reinforced composites that have high tensile ductility and multiple microcracking characteristics [18]. Strain-hardening geopolymer composite (SHGC) [1], like conventional strain-hardening cementitious composite (SHCC), or engineered cementitious composite (ECC) [19], belongs to one type of ultra-ductile high-performance composite material that exhibits unique strain-hardening behavior under direct tension [20]. Reinforced with only small volume fractions of randomly distributed short fibers, SHGC shows extraordinary tensile strain capacity up to several hundred times larger than OPC concrete (3 to 5%) and multiple-cracking potentials with controlled crack width [21, 22]. Furthermore, SHGC is also a promising option to demonstrate that industrial by-products and waste could be transformed into high-tech and high-value composite materials. Compared with convention SHCC, SHGC also has a significantly lower environmental footprint, particularly concerning CO_2 emission and embodied energy [21, 23].

While much effort has been taken to develop conventional SHCC, scientific and technical knowledge of SHGC is still in its infancy. Up till now, few studies were conducted regarding the development of SHGC [21, 23-25]. The fracture properties and fiber/matrix interface properties that are essential for the development of SHGC are not systematically studied as well. While the traditional trial-and-error method is time and cost-intensive, there is currently no systematic design methodology for SHGC. Besides, the environmental benefits of SHGC are also not yet well studied.

1.2 Research aim and objectives

This PhD project aims to develop a cement-free strain-hardening geopolymer composite (SHGC) as high-value construction materials using industrial wastes and by-products through alkaline activation technology. Based on this, the environmental impact of SHGC is explored. To reach this research aim, the following objectives are defined:

- to investigate the mechanical and fracture properties and the possible fracture mechanism
- to quantify the fiber/matrix bonding properties and to evaluate the effects of reaction products chemistry on the bonding properties

[1] By definition, the term geopolymer strictly relates to a synthetic alkali aluminosilicate material, which is characterized by its three-dimensional aluminosilicate network. However, the term geopolymer is more frequently used by civil engineers for AAMs, especially in the studies concerning the development of strain-hardening composite. In this thesis, the term SHGC is always used to be consistent with existing literatures.

- to clarify the fundamental adhesion mechanism of PVA fiber to geopolymer matrix at an atomic level
- to develop SHGC with a systematic design approach to achieve high tensile ductility and multiple-cracking, which is comparable to conventional SHCC.
- to evaluate the environmental impact the SHGC developed in this work using a comparative life-cycle assessment.

It should be emphasized here that the ultimate goal of this study is not to develop an SHGC material with ultra-high tensile performance. Rather, it focuses on a more efficient way to design SHGC and provides modification strategies by selecting and tailoring the matrix and fiber-matrix interface properties. By understanding the underlying mechanisms of material properties governing the performance of SHGC, this study aims to provide insights into the behavior of SHGC and frees the developer from the traditional time-consuming trial-and-error approach.

1.3 Research scope

In this research two types of industrial by-products, namely ground granulated blast furnace slag (in short: slag) and class F fly ash (in short: fly ash), and one type of commercially available short-cut PVA fiber are used to develop SHGC. No other type of industrial by-products is considered. The slag and fly ash are activated using sodium hydroxide combined with sodium-based silicate solutions. In this study, the development and performance of SHGC and related matrix and interface properties are studied with the following restrictions:

- Only slag/fly ash-based geopolymer and related SHGC are studied;
- A sodium silicate-based alkaline activators will be used;
- Curing in sealed conditions at ambient temperature (20 °C);
- No admixture is used;
- Only commercial PVA shortcut fiber is used;
- All mechanical properties, fracture properties, interface bonding properties, and uniaxial tensile properties of SHGC are tested at an age of 28 days.

1.4 Research strategy

The research covers studies on different scales from nano-, micro-, meso-, and macroscale, as schematically shown in Figure 1.1.

As the starting point of the research project, the chemical composition, the physical properties, and the reactivity of slag and fly ash were characterized. This provides a basis for further geopolymer matrix design.

The fracture properties and other mechanical properties were experimentally tested at the mesoscale. The microstructure and chemistry of the reaction products of the geopolymer matrix were also investigated to understand their effect on the fracture mechanism and to

provide further insights on matrix modification strategies by changing the content of alkali activator and solid precursors.

The fiber/matrix properties were also experimentally determined. The reaction product chemistry and microstructure were characterized at the microscale with a focus on the fiber/matrix interfacial transition zone (ITZ). The influence of reaction product chemistry on the interface bonding properties was also investigated.

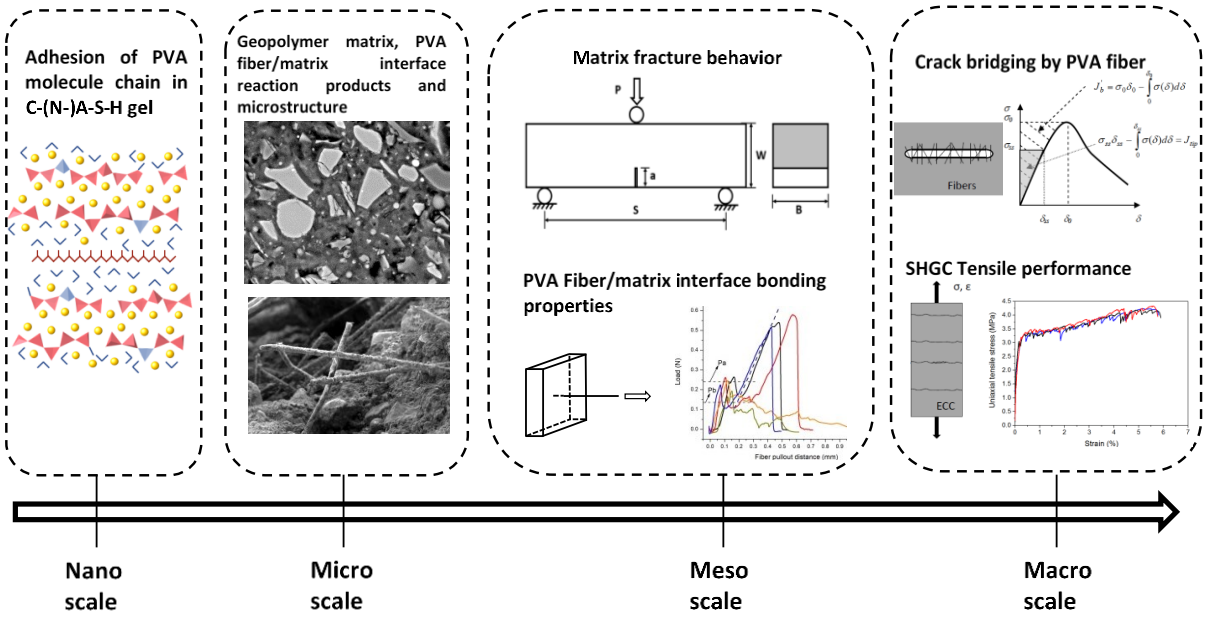

Figure 1.1 Research scope of different scales

Furthermore, the adhesion mechanism of the PVA molecule chain in reaction products was studied using molecular dynamic (MD) simulation to understand how the interface properties could be engineered.

The SHGC is then systematically developed, following a micromechanics-based design approach. The experimentally attained matrix and interface properties were used as input and also served as valuable input for the computational micromechanics model for simulating crack bridging at the macroscale. Through micromechanical modeling, the optimal fiber length and volume could be determined and the performance of mixtures with different fiber/matrix combinations could be predicted. Then, these predictions are experimentally verified to examine the validity and reliability of the proposed method. Finally, the environmental impact of the developed SHGC with the most promising performance was evaluated in comparison with that of the conventional SHCC materials.

1.5 Research outline

This thesis is subdivided into four parts as shown in Figure 1.2. **Part I** covers the research background and motivation of this PhD project. Following the introduction part, **Part II** focuses on the development and quantitative characterization of geopolymer matrix and fiber/matrix

interface properties as a design basis for the development of SHGC. **Part III** deals with the micromechanics-guided development of SHGC. Finally, **Part IV** presents the environmental impact evaluation and conclusions from this research. The content of each chapter is summarized as follows.

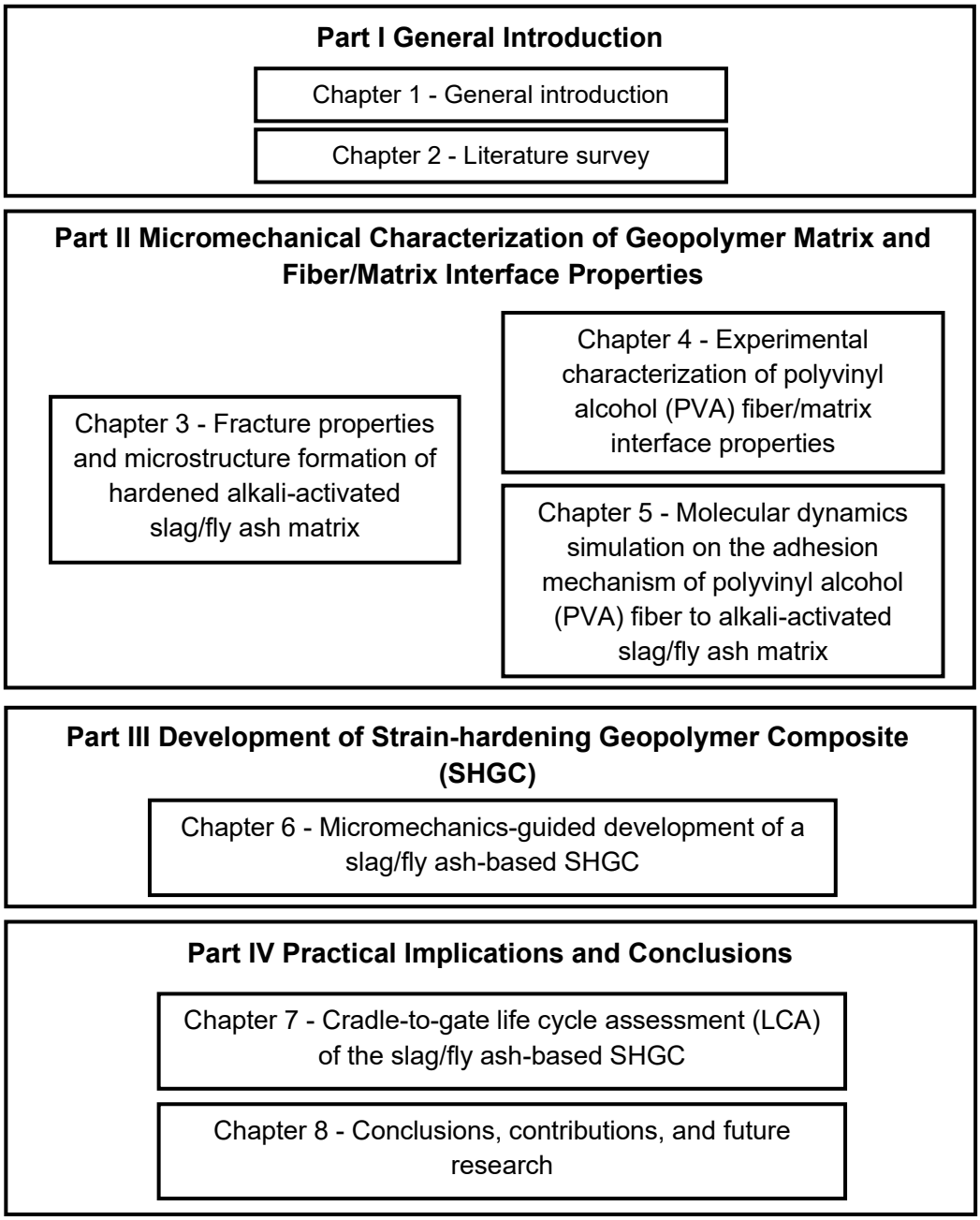

Figure 1.2 Research outline of this thesis

Chapter 2 gives a literature survey of previous research and development of conventional SHCC and SHGC, the micromechanics-guided design approach for strain-hardening and multiple-cracking behavior, matrix and interfacial properties of SHGC, and the environmental impact of conventional SHCC and SHGC.

Chapter 3 investigates the mechanical properties and fracture behavior of the slag/fly ash-based geopolymer matrix. The compressive strength, elastic modulus, fracture toughness, and fracture energy are tested experimentally. These properties are further correlated with results of microstructural characterization of the reaction products, which includes their chemical composition by ESEM/EDX and FTIR, amount of main reaction products by TGA, as well as the pore structure by N_2 adsorption. The effects of alkaline activator on the abovementioned mechanical and microstructural properties are also presented.

Chapter 4 quantifies the PVA fiber/matrix interface bonding properties using single fiber pullout tests. The chemical bonding energy, the interfacial frictional force, and the slip-hardening behavior are obtained. The influence of reaction product chemistry on the bonding properties is also studied.

Chapter 5 explores the PVA fiber/matrix adhesion mechanism using molecular dynamics simulation. The role of Ca and Na and the chemical composition of C-(N-)A-S-H gel in PVA/gel adhesion are simulated at the nanoscale. The adhesion energy between PVA molecules and C-(N-)A-S-H gel is also determined using adsorption enthalpies.

Chapter 6 proposes and applies a micromechanical-based design approach for the development of SHGC. As a result, SHGC with tensile performance comparable to conventional SHCC is successfully developed.

Chapter 7 presents a comparative LCA study of SHGC. The environmental impacts of SHGC developed in this project are evaluated and compared to conventional SHCC materials.

Chapter 8 summarizes the main conclusions and scientific contributions regarding matrix and interface bonding properties modification strategy, systematic development of SHGC as well as the environmental impact of SHGC. Based on experimental evidence and micromechanics modeling, a more efficient micromechanics-guided method for the development of SHGC is recommended and future research perspectives are also provided.

Chapter 2

Literature survey on the development of strain-hardening geopolymer composite (SHGC)

2.1 Introduction

This chapter provides a brief literature survey on the development of strain-hardening geopolymer composite (SHGC). The strain-hardening cementitious composite (SHCC), or engineered cementitious composite (ECC), i.e., the original version of this high-performance composite, is introduced first. The two criteria for strain-hardening behavior are then introduced. The micromechanics-based model and its application for describing strain-hardening behavior are also discussed. Afterwards, a general introduction about alkali-activated materials and geopolymer is given. The current status of the development of SHGC is summarized. The factors influencing the tensile performance of SHGC are also reviewed and discussed. Finally, sustainability aspects of previously developed SHGC are reviewed.

Based on the literature survey, the knowledge gaps and challenges to the development of SHGC are determined and outlined.

2.2 Introduction of strain-hardening cementitious composite (SHCC) and engineered cementitious composite (ECC)

2.2.1 Fiber-reinforced cementitious composite

Fiber-reinforced cementitious composites (FRCC) with short-cut fibers can be classified according to their performance in tension. They can be either strain-softening or strain-hardening composites [26]. The two kinds of fiber-reinforced cementitious composites are characterized by their typical stress-strain curves under uniaxial tensile loading as shown in Figure 2.1. With increasing elongation, the strain-softening FRCC shows crack localization immediately after the occurrence of the first crack. After the peak stress, the stress-strain curve has only a softening branch (point B to point C) shown in Figure 2.1 (a). In contrast, the strain-hardening FRCC, also known as high-performance fiber-reinforced cementitious composite (HPFRCC), shows typical strain-hardening behavior after the first crack. As shown in Figure 2.1 (b), the strain-hardening process is accompanied by the multiple-cracking of the composites. It starts from point A and ends when the maximum tensile stress and strain are reached at point B.

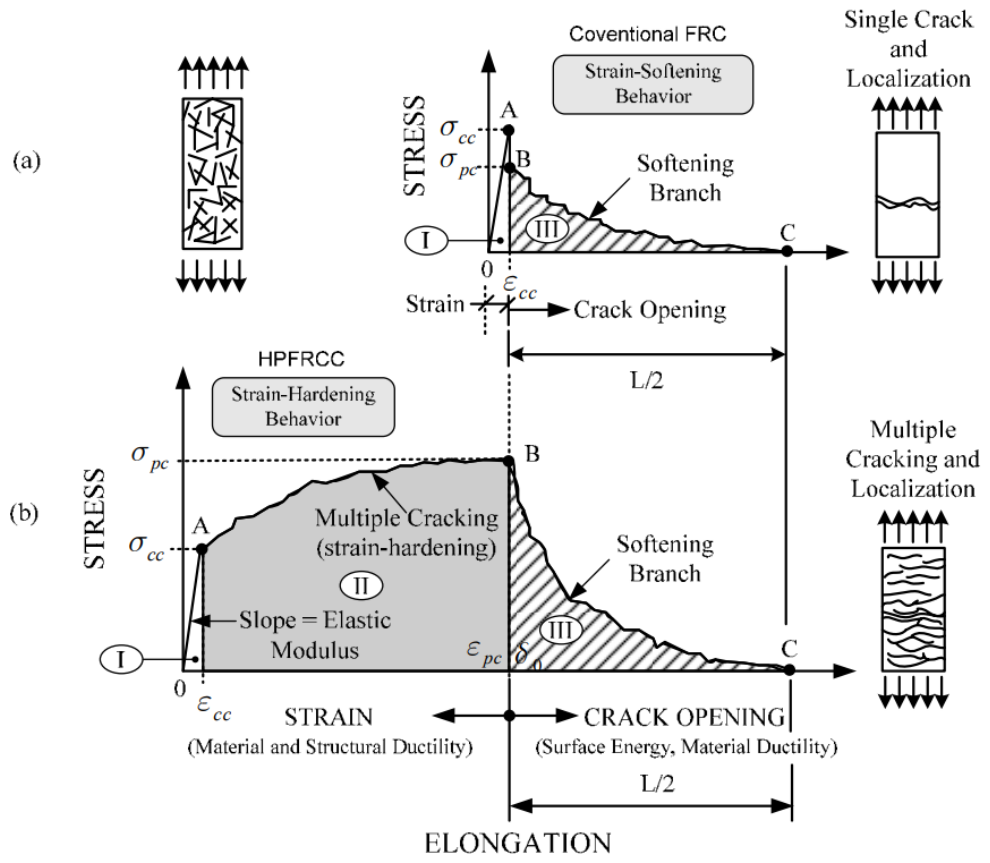

Figure 2.1 Typical stress-strain or elongation curve in tension up to complete failure: (a) Conventional strain-softening FRC composite; (b) strain-hardening FRC composite or high-performance fiber-reinforced cementitious composite (HPFRCC). (Adopted from [27]). The σ_{cc} and ε_{cc} correspond to the tensile stress and strain at the first crack of the composite, respectively. The σ_{pc} and ε_{pc} correspond to the maximum tensile stress and strain of the composite, respectively.

Since the term HPFRCC was first adopted by Naaman et al. [28], various classes of HPFRCCs have been developed by many researchers. At the beginning of its development, most HPFRCCs were prepared with very high fiber content (from 5% to 12%) to reach the tensile strain capacity of up to 1% [29]. A special class of HPFRCC was developed by Victor Li and co-workers and got the name engineered cementitious composites (ECC) [30-32]. ECC utilizes only a small amount of short-cut microfibers (typically 2% by volume) to achieve a very high tensile strain capacity of 3% to 6% with multiple-cracking behavior [33, 34]. For this reason, ECC is also known as strain-hardening cementitious composites (SHCC), a name that emphasizes the shape of its almost bi-linear stress-strain response in tension as shown in Figure 2.1 (b) [35]. The name ECC is still used by many researchers to show the micromechanics-based design nature of this material [36].

2.2.2 SHCC and ECC

Engineered cementitious composite (ECC) [19], or strain-hardening cementitious composite (SHCC), is a kind of high-performance fiber-reinforced cementitious composite (HPFRCC) with a micromechanics design basis [20]. Reinforced with only a small volume fraction of randomly

distributed short-cut fibers, these materials show extraordinary strain-hardening behavior in tension. Their strain capacity in tension normally falls in the range of 3-5% [30], which is several hundred times larger than conventional concrete [37]. After the first crack in the matrix, SHCC/ECC undergoes strain-hardening as illustrated in Figure 2.2. With increasing tensile deformation, it continues to bear increasing tensile load. The increasing stress in tension does not lead to crack localization at the first crack, but rather a multiple-cracking behavior. This advanced tensile performance of SHCC/ECC resolves the bottleneck of mechanical properties of convention concrete and FRC, i.e., the rapid exhaustion of tensile strain capacity after initiation of the first crack. The high tensile ductility of SHCC/ECC further translates into advantages under shear loading or flexural loading, which is beneficial to maintaining structural integrity.

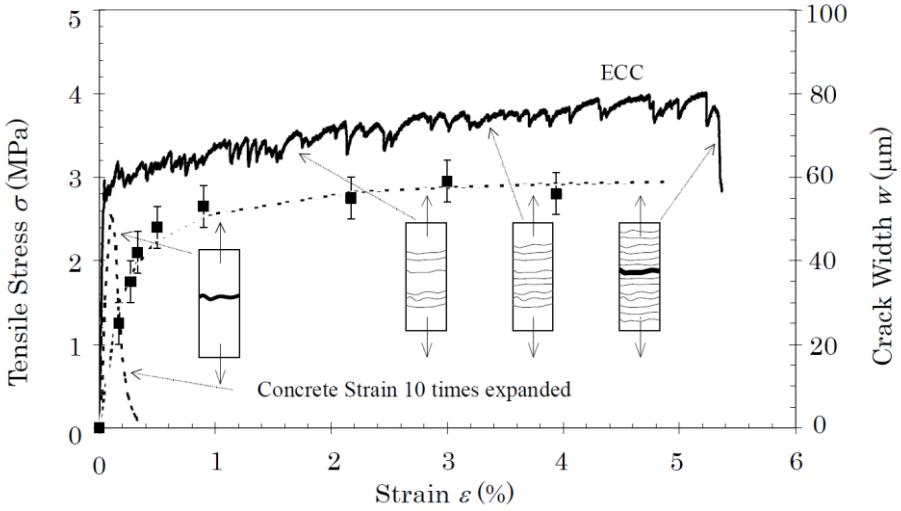

Figure 2.2 Typical tensile stress-strain curve and crack width development of SHCC [38]

During the multiple-cracking, the crack width in SHCC/ECC is also controlled to typically less than 100 μm before their final failure [38]. This width is small enough to prevent the ingress of harmful substances into the cracks. Furthermore, the small cracks formed in ECC also have autogenous self-healing potential [39, 40]. Therefore, the application of ECCs can improve the durability of new and repaired structures [41].

The constituent materials of SHCC/ECC are similar to that of cement mortar. They are in general prepared using cement, SCMs, water, fine aggregate, and short-cut microfibers. To guarantee homogeneous fiber distribution within the composite, the rheology control of the fresh SHCC/ECC is achieved by using a suitable combination of chemical admixtures, such as superplasticizer combined with viscosity modifying admixtures (VMA) [42]. In most cases, no coarse aggregate with a particle size above 0.2 mm is used in SHCC/ECC [43]. In this way, the matrix fracture toughness is limited to a certain extent so that multiple-cracking can occur before the maximum fiber bridging stress is reached. Due to the absence of coarse aggregate in the mixture design, ECC has high cement content (kg/m^3), typically two to three times higher than conventional concrete [44].

Various types of fibers have been applied to produce SHCC/ECC mixtures. The polyvinyl alcohol (PVA) fiber is the most commonly used in SHCC/ECC systems [45-47]. High modulus

polyethylene (HMPE) fiber [48, 49] is also frequently used. Other synthetic fibers such as polyethylene (PE) fiber [50], plasma surface-treated PE fiber [51], high tenacity polypropylene (HTPP) fiber [52], etc, have also been used to produce SHCC/ECC. Additionally, the feasibility of using natural fibers such as sisal, curaua, and jute fibers, has also been investigated [53-55]. However, according to those studies, the developed composite materials generally exhibit deflection-hardening rather than strain-hardening behavior.

2.2.3 Mechanical properties of SHCC/ECC

Since the invention of the first version of SHCC/ECC in the 1990s, various types of these materials have been developed successfully. According to their mechanical properties and intended applications, they can be classified into four broad categories as shown in Table 2.1.

Table 2.1 Four different classes of SHCC/ECC and their corresponding mechanical and physical properties (Adopted from [56]).

	FR-ECC [57, 58]	LW-ECC [59, 60]	Normal-ECC [45-47]	HS-ECC [48, 61, 62]
Density (kg/m^3)	550	930-1800	1800-2100	2300-2400
Compressive strength (MPa)	2.5-3.5	20-40	30-80	120-210
Elastic modulus (GPa)	4-6	8-12	15-23	41-48
First crack strength (MPa)	0.8-1	2-4	3-5	8-10
Ultimate tensile strength (MPa)	1-1.5	2-5	4-8	14-17
Tensile strain capacity (%)	2-3	3-4	2-8	3-8

The mechanical properties and density of the different classes of SHCC/ECC vary widely. The fire-resistant ECC (FR-ECC), developed for fire-proofing of steel structures and non-structural repair, have a very low density and a low compressive strength of several MPa. Lightweight ECC (LW-ECC) and normal-ECC, designed for most structural applications, have a compressive strength from 20 to 80 MPa and an elastic modulus of about 18 to 20 GPa. High-strength ECC (HS-ECC), including ultra-high-strength ECC, has also been successfully designed for the application in impact and blast-resistant structures. They have a very high compressive strength of 120 MPa and above and a very high elastic modulus of about 50 GPa. Up till now, the highest compressive strength of the existing SHCC/ECC reaches about 210 MPa. Still, these mixtures have over 3% tensile strain capacity [48, 61].

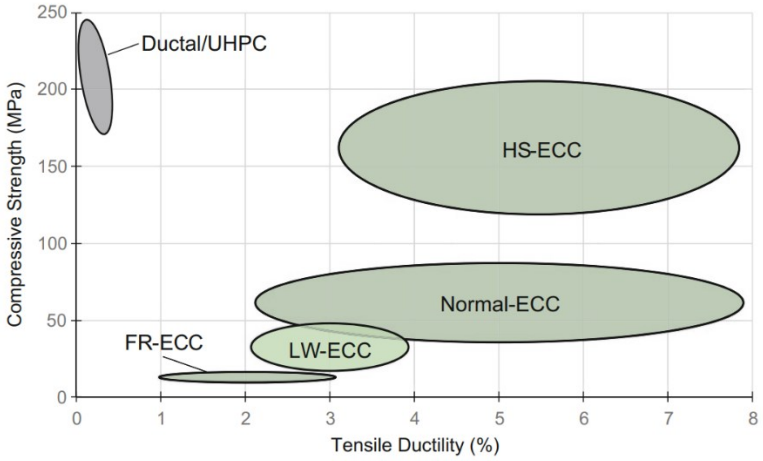

Figure 2.3 Compressive strength and tensile ductility of different types of SHCC/ECC (Adopted from [36]).

The range of compressive strength versus tensile strain capacity of these four broad classes of SHCC/ECC is further illustrated in Figure 2.3. An ultra-high performance concrete (UHPC) material is included in this plot. Despite the very high compressive strength, UHPC is featured by its low strain-hardening property with a tensile strain capacity of about 0.5% [63, 64]. In comparison, the tensile strain capacity of the majority of SHCC/ECC generally exceeds 3%, while the compressive strength ranges from 3 MPa to over 210 MPa. Even higher strain capacities of SHCC/ECC have been achieved by some researchers. With the use of HMPE fiber, SHCC/ECC mixtures with tensile strain capacity of from 8% to 12% have been developed [49].

2.2.4 Engineering applications of SHCC/ECC

The combination of unique tensile properties of SHCC/ECC, including tensile ductility, durability, and intrinsically self-controlled small crack width, makes SHCC/ECC a promising alternative in many different engineering applications. It has been applied in several full-scale field engineering practices in the domains of buildings, roads and bridges, and water infrastructures [65], in which the commercial viability and economic advantages of SHCC/ECC have been demonstrated. Some typical applications are shown in Figure 2.4. SHCC/ECC is commonly applied for structural/surface repair and retrofit [66, 67], structural elements which require large deformability [68] and fatigue resistance [69], and structural elements which need high flexibility and energy adsorption (seismic and impact resistance) [70].

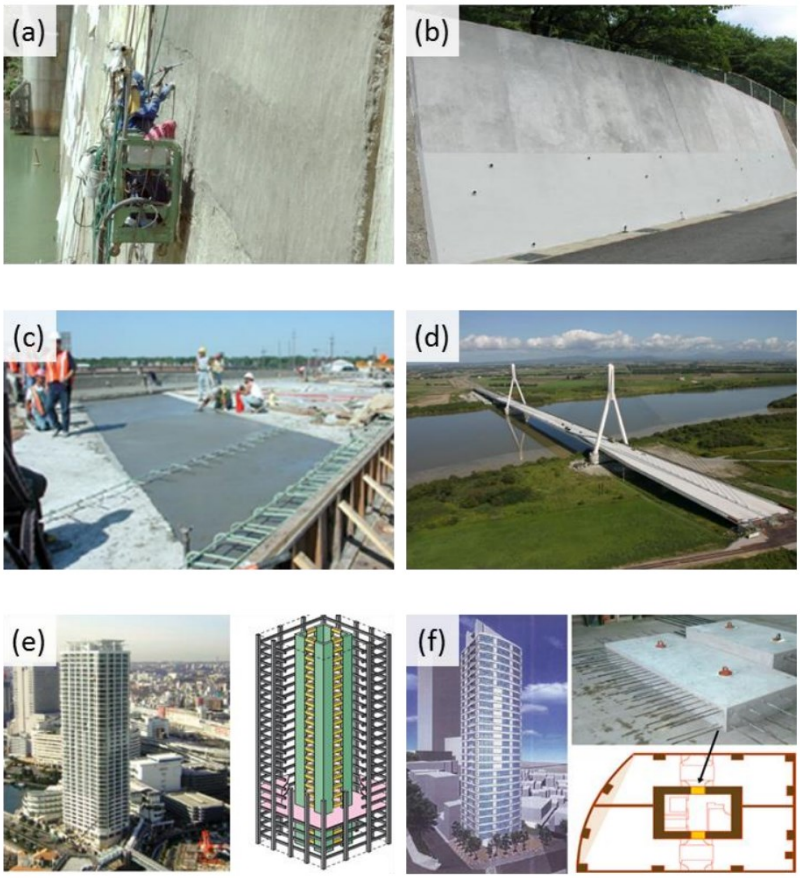

Figure 2.4 Different SHCC/ECC applications (after Ohno et al. [65]): (a) structural repair of concrete dam [66], (b) surface repair of retaining wall [67], (c) bridge-deck link slab [68], (d) bridge-deck overlay [69], (e) and (f) structural dampers for high-rise buildings [70].

2.2.5 Sustainability of SHCC/ECC

A typical SHCC mix design has a significantly higher cement content, which is typically 2 to 3 times higher compared to that of conventional OPC concrete. Although less volume of SHCC than conventional concrete is needed for certain applications, the high amount of cement in SHCC still makes it an energy-intensive product with high CO_2 emissions, which negatively impacts its sustainability [43]. Therefore, researchers have focused on developing a greener SHCC with comparable tensile ductility and lower environmental impact.

To improve the greenness of SHCC, one of the most adopted solutions is to replace cement in SHCC mixtures with supplementary cementitious materials (SCMs) [43, 46, 47]. The commonly used SCMs include fly ash [43, 46, 71], blast furnace slag [72-74], limestone powder [47], etc. These greener mixtures in general also exhibit comparable tensile strain capacity and multiple-cracking behavior. An even more effective approach to minimize the environmental impact is to replace the cement in SHCC completely with alkali-activated materials (AAMs), or geopolymer. A general introduction to AAMs and geopolymers is given in Section 2.4.

2.3 The micromechanical design basis for SHCC and ECC

The performance of SHCC/ECC is determined by the micromechanical interactions between fiber, matrix, and interfaces of the composite. Only suitable combinations of these properties can lead to strain-hardening and multiple-cracking of the composite in tension. Hence, the micromechanics of the composite form the design basis of SHCC/ECC. In previous studies, the use of a micromechanics design model has effectively assisted in the mixture design of SHCC/ECC [20]. In this section, the criteria for strain-hardening of the composite, the scale-linking micromechanical model, and finally their applications are reviewed.

2.3.1 Criteria for strain-hardening and multiple-cracking

The strain-hardening and multiple-cracking behavior of SHCC/ECC is a result of sequential initiation and steady-state propagation of micro-cracks in the composite under tension. Figure 2.5 illustrates a random crack initiation in a fiber-reinforced composite, such as SHCC/ECC. Here, the tendency of the crack opening under tension is resisted by the so-called fiber bridging stress[2] σ [75].

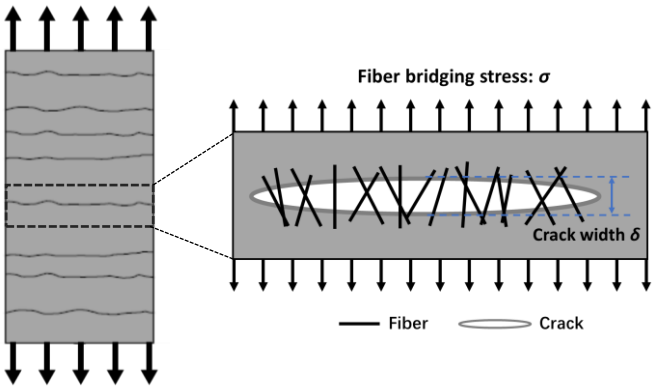

Figure 2.5 The representative σ-δ relationship for fiber bridging a single crack.

Marshall and Cox [76] derived an energy-based criterion for steady-state crack propagation in fiber-reinforced brittle matrix composites. Building on their derivation, Li and Leung [30] presented two necessary conditions for achieving steady-state multiple-cracking in randomly-distributed short fiber-reinforced composites, which can be expressed as follows:

For the steady-state multiple-cracking behavior to happen, the bridging fibers must be able to bear the applied tensile load after a crack passes completely through the matrix. In other words, the maximum fiber bridging stress σ_0 must exceed the first crack strength σ_{fc} of the matrix. This is generally known as the strength-based pseudo strain-hardening (PSH) criterion for crack initiation. It is formulated as Equation (2.1):

[2] Following the fictitious crack model by Hillerborg et al. [75], it is assumed that after the crack initiation, the tensile stresses may be transmitted across the crack through the bridging fibers.

$$\sigma_{fc} \leq \sigma_0 \tag{2.1}$$

The violation of the strength criterion leads to the failure of the composite from this crack plane. In this case, no more cracks can be formed and the composite does not have multiple-cracking behaviors.

The other fundamental condition for strain-hardening and multiple-cracking is the steady-state crack propagation under tension. During the crack propagation, apart from a small region near the crack tip, the crack is essentially flat with crack opening width δ_{ss} remaining constant under a constant external stress σ_{ss}. This is indicated in Figure 2.6 (a). Otherwise, if the mid-crack opening δ_m increases indefinitely with the increasing crack length, the fiber bridging capacity will be exhausted because the fibers away from the crack tip will either be pulled-out or ruptured as indicated in Figure 2.6 (b). This crack propagation mode, also known as "Griffith-type" crack propagation, leads to the tension-softening behavior of conventional concrete and FRCC [112].

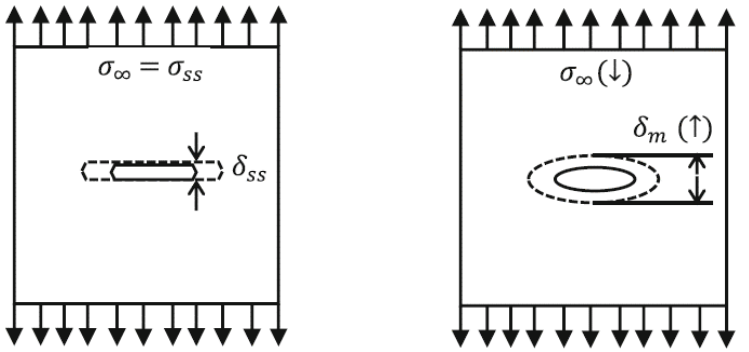

(a) a steady-state flat crack (b) a Griffith type crack crack

Figure 2.6 (a) A steady-state flat crack propagation limits the crack width δ_{ss} in tension and (b) a Griffith-type crack leading to an indefinite increase of crack width [77].

Based on the energy balance during a steady-state crack propagation with a constant crack opening width δ_{ss} under a constant external stress σ_{ss}, the condition is schematically illustrated in Figure 2.7 and formulated as Equation (2.2):

$$\sigma_{ss}\delta_{ss} - \int_0^{\sigma_{ss}} \sigma(\delta)d\delta = J_{tip} \approx \frac{{K_{Ic}}^2}{E_m} \tag{2.2}$$

where J_{tip} is crack tip toughness, K_{Ic} is the fracture toughness of the matrix, and E_m is the elastic modulus of the matrix. When the fiber content is small, J_{tip} can be estimated as K_{Ic}^2/E_m.

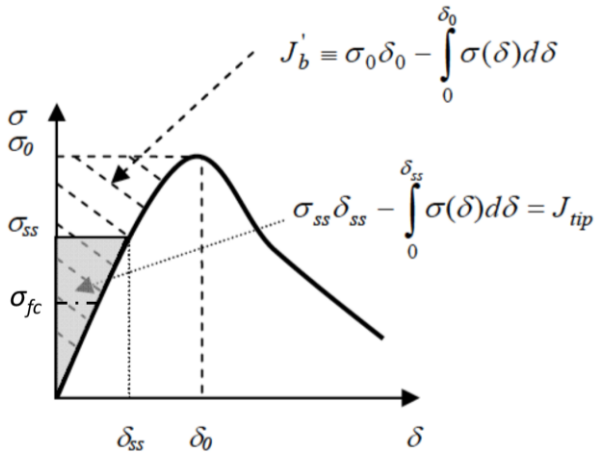

Figure 2.7 The representative fiber bridging stress σ versus crack opening width δ relationship for a single crack bridged by fibers [77].

In Equation (2.2), the term $\sigma_{ss}\delta_{ss}$ is the work done onto the crack body during the crack propagation process. Part of this energy, i.e., $\int_0^{\sigma_{ss}}\sigma(\delta)d\delta$, is consumed by fiber bridging when the crack opens from width 0 to the steady-state crack opening width δ_{ss}. The remaining energy is dissipated at the crack tip to break down the matrix material (i.e., J_{tip}). The left-hand side of Equation (2.2) is defined as the complementary energy J_{comp}, the value which corresponds to the shaded area in Figure 2.7. Since the fiber bridging stress σ has a peak value σ_0, J_{comp} will hence have a maximum value of J_b'. This value corresponds with the hatched area in Figure 2.7. In other words, to guarantee that the condition in Equation (2.2) is satisfied, the following criterion in Equation (2.3) should be met. This criterion is known as the energy-based pseudo strain-hardening (PSH) criterion.

$$J_{tip} \leq \sigma_0\delta_0 - \int_0^{\delta_0}\sigma(\delta)d\delta \equiv J_b' \tag{2.3}$$

where J_b' represents the maximum complementary energy.

2.3.2 Micromechanics-based model

Li et al. developed a micromechanics-based constitutive model to relate the micromechanical parameters in the individual fiber bridging behavior to the macroscopic composite behavior [78]. Li's model has been further modified and extended by other researchers [65, 79, 80]. This theoretical model takes into consideration all the influencing factors to achieve the strain-hardening behavior of composites. The idea behind the model is that the composite mechanical behavior is governed by the pull-out behavior of individual bridging fibers [66]. The output of the micromechanical model is the σ-δ relationship, which represents the uniaxial tensile stress σ carried by a matrix crack with uniform opening δ (Figure 2.7). The randomness of fiber location and fiber orientation also plays a role in the determination of the σ-δ relationship. This is achieved by adopting probability density functions that describe the distribution of the fibers. Mathematically, the constitutive law of the σ–δ relation is expressed as follows:

$$\sigma(\delta) = \frac{V_f}{A_f}\int_{\varphi_0}^{\varphi_1}\int_{z=0}^{(L_f/2)\cos(\varphi)} P(\delta, L_e)g(\varphi)p(\varphi)p(z)dzd\varphi \tag{2.4}$$

where V_f is the fiber volume fraction; A_f is the cross-sectional area of one fiber; the term V_f/A_f is equivalent to the number of fibers per unit area of the crack plane with φ=0; φ is the inclination angle of fiber to the perpendicular direction of the crack plane; L_f is the fiber length; z is the distance between the fiber centroid and the crack plane; L_e is the fiber embedment length.

In Equation (2.4), $P(\delta, L_e)$ represents the load carried by a single fiber aligned perpendicular to the crack plane (i.e., φ=0) with the embedment length of L_e (shown in Figure 2.8 (a)). The load $P(\delta, L_e)$ depends predominantly on the initial fiber embedment length L_e, fiber properties (fiber length L_f, fiber diameter d_f, and the fiber elastic modulus E_f), and the fiber/matrix interface bonding properties (such as chemical bonding energy G_d, the frictional bonding properties τ_0, etc.).

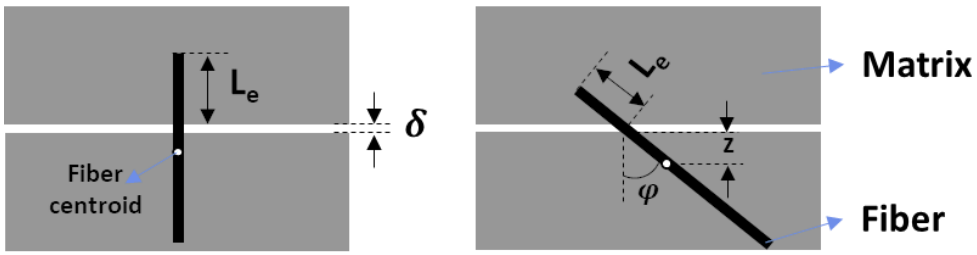

Figure 2.8 (a) One fiber normal to the crack plane bridging a single crack, (b) one inclined fiber bridging a single crack.

The fibers that are inclined to the matrix crack plane as shown in Figure 2.8 (b) also influence the fiber bridging relationships $\sigma(\delta)$ by both the mechanical effect and the geometric effect:

- The mechanical effect: when a fiber is inclined from the normal to the crack plane, additional frictional force occurs at the exit point of the fiber from the matrix [81]. This mechanical effect, also known as the “snubbing effect”, is taken into account by the term $g(\varphi)$. $P(\delta, L_e)$, together with $g(\varphi)$, thus represents the pull-out behavior of a single fiber with arbitrary embedment length L_e and inclination angle φ.

- The geometric effect refers to the random distribution of fibers in the composite. This is taken into account by the probability density functions (PDFs): $p(\varphi)$ determined by fiber inclination angle φ and $p(z)$ determined by the location of fiber centroid z.

The double integral in Equation (2.4) calculates the total load carried by all bridging fibers in the crack plane with various orientation angles φ and centroid locations z. The upper and lower bounds of φ integration are limited between φ_0 and φ_1 depending on the dimension of the specimen. For 2D random fiber distribution, φ varies from 0 to $\pi/2$. The upper bound of z integration is calculated as $(L_f/2)\cos(\varphi)$.

The micromechanical model also considers three additional mechanisms that can influence the σ-δ relationships, i.e., the matrix micro-spalling, Cook-Gordon effect, and two-way fiber pullout (when fibers have a large slip-hardening coefficient β). The complete mathematical derivation for these three mechanisms is given in Appendix A.

- Matrix micro-spalling: the matrix micro-spalling happens when an inclined fiber is pulled out from the matrix. The stress concentration can occur at the bearing point, leading to local failure of the matrix (indicated by the light grey area in Figure 2.9). This happens more often in brittle matrices with low tensile strength. Due to the micro-spalling, the fiber inclination angle φ becomes smaller during the crack opening, which increases the crack opening width δ. In this way, the fiber rupture is delayed and the maximum bridging stress is increased [82].

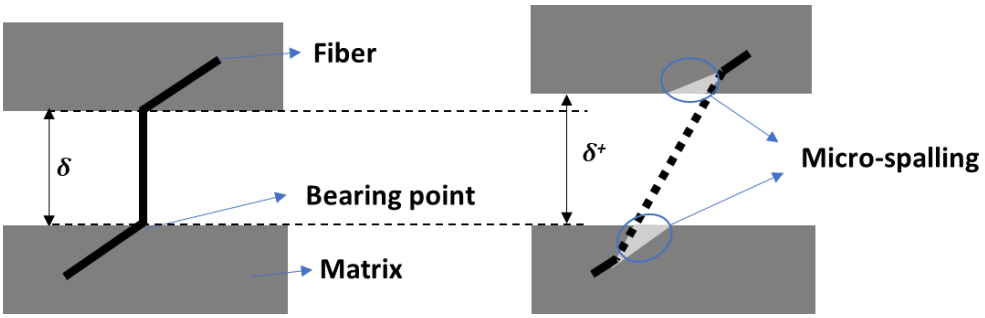

Figure 2.9 Schematic illustration of matrix micro-spalling

- Cook-Gorden effect: the Cook-Gordon effect, or pre-debonding of the fibers, refers to the debonding of a weak fiber/matrix interface at the location near a blunt crack tip in a fiber-reinforced composite (Figure 2.10). This means a when a fiber intersects a matrix crack, a small segment of the fiber/matrix interface at the crack plane has already been debonded [83], which leads to an increase in the crack opening width δ.

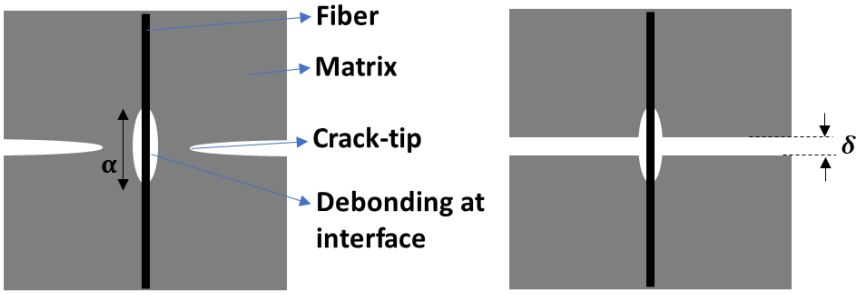

Figure 2.10 Schematic illustration of the Cook-Gordon effect

- Two-way fiber pullout: since the PVA fiber in the geopolymer matrix has a significant slip-hardening behavior, its pull-out load thus can be much higher than the debonding load. Consider the crack in Figure 2.5 is bridged by only one PVA fiber, after the completion of debonding at the short embedment side, the long embedment side may continue debonding and eventually enter the pullout stage such that two-way fiber

pull-out occurs. The contributions from both sides of the fiber across the crack to the total crack opening δ can then be calculated.

Finally, the fiber-bridging stress at a crack plane, i.e., $\sigma(\delta)$, can be calculated using Equation (2.4) for given parameters of fiber, matrix, and fiber/matrix interface properties. The complete mathematical derivation of $P(\delta, L_e)$, $g(\varphi)$, $p(\varphi)$, and $p(z)$ is also given in Appendix A.

In essence, the micromechanics-based constitutive model enables systematic design and tailoring of the parameters to achieve desired tensile properties of the composite. In previous studies, researchers have used the model and the simulated σ-δ relationship in Equation (2.4) for mixture development and optimization purposes [77]. This is done by the modification of parameters to satisfy the strength/energy criterion for steady-state multiple-cracking, or to achieve higher tensile strength or smaller crack width of the composite.

2.3.3 Application of the strain-hardening criteria and the micromechanics-based model

The strength- and energy-based PSH criteria can be applied to evaluate whether a composite has the potential for significant strain-hardening and multiple-cracking behaviors. To quantitatively evaluate if the PSH criteria are met, two performance indices namely pseudo strain-hardening strength index (PSH_s) and energy index (PSH_e) were introduced by Kanda and Li [79] as follows:

$$PSH_s = \frac{\sigma_0}{\sigma_{fc}} \tag{2.5}$$

$$PSH_e = \frac{J_b{}'}{J_{tip}} \tag{2.6}$$

To ensure strain-hardening and multiple-cracking behavior, both PSH_s and PSH_e indices have to theoretically exceed unity. The higher the values of the performance indices, the greater the possibility of saturated strain-hardening and multiple-cracking behavior, and eventually lead to higher tensile strain capacity of the composite. Unsaturated PSH behavior often results in small tensile strain capacity and large variation in tensile ductility of the composite [79, 84].

Considering the inevitable material variability, e.g., the heterogeneous fiber dispersion as well as the flaw distribution, sufficient margins between σ_{fc} and σ_0, J_{tip} and J_b' have to be maintained to ensure that strain-hardening behavior occurs [84]. It has been demonstrated experimentally that for PSH_s > 1.3 (sometimes 1.5 [20]) and PSH_e > 2.7 (sometimes 3.0), saturated PSH behavior is ensured in most of the ECC/SHCC reinforced with PVA fiber [21, 79, 85, 86]. For FRCC prepared with other fibers, different values of PSH indices apply. For example, FRCC made with polyethylene (PE) fibers needs PSH_s >1.2 and PSH_e> 3.0 for a saturated PSH behavior [87]. While for FRCC prepared using polypropylene (PP) fibers, the requirements change to PSH_s > 2.0 and PSH_e > 3.0 [85].

2.4 General introduction to alkali-activated materials (AAMs) and geopolymer

Alkali-activated materials (AAMs), including geopolymer binders, are the broadest classification for any binder system derived from the reaction of an alkali source (solid or dissolved) with a solid (calcium) aluminosilicate precursor [8, 9]. The concept of AAMs dates back to 1908 [14]. The first systematic study on AAMs began in the 1940s when Purdon analyzed clinker-free cement made from slag and NaOH [88]. A significant breakthrough was made by Glukhovsky et al [89] in 1967. His study focused on binders from low calcium or calcium-free aluminosilicate (clay) and alkaline metal solutions with binders named “soil cement”. In the 1970s, Davidovits coined the terminology of ‘geopolymer’ to describe specifically a aluminosilicate inorganic polymer, initially developed as a refractory material as an alternative to organic thermosetting polymers [9]. The research on AAMs, including geopolymers, has reflourished since the 1990s, with the intention to develop sustainable alternatives to OPC-based binders [90].

The precursors to produce AAMs can be a wide range of by-products or wastes from industrial productions, mining operations, and agricultural activities. A series of natural aluminosilicate minerals can be used as precursors as well [90]. In fact, any aluminosilicate precursor with enough vitreous Si phases could be used as the solid precursor for geopolymer concrete [91]. The most widely used precursors nowadays are blast furnace slag, coal fly ash (either Class F or Class C), and metakaolin [92]. The alkali sources, i.e., the alkaline activator, are essentially any soluble substance that can supply alkali metal cations, raise the pH of the reaction mixture and accelerate the dissolution of the solid precursor [93]. They contain a wide range of materials, including caustic alkalis (NaOH, KOH), silicates ($M_2O{\cdot}nSiO_2$), weak base salt (Na_2CO_3, Na_2SO_4, etc), alkaline earth products (CaO, $Ca(OH)_2$, etc), and possible synergic utilization of above options [94]. Currently, the most frequently studied version is the caustic alkalis and/or alkaline silicates [90].

A conceptual model of the alkali activation process is shown in Figure 2.11. Generally, AAMs are defined in two categories: (I) high-Ca AAMs and (II) low-Ca content AAMs. The mechanisms governing the chemical reactions between precursors and alkaline activators are different. The high-Ca AAMs in category (I) mainly use Ca-rich material, e.g., blast furnace slag, as the solid precursor. The main reaction product is a calcium aluminosilicate hydrate (C-A-S-H) gel, with the incorporation of the alkali cations. It has a similar structure to the calcium silicate hydrate (C-S-H) gel as that from cement hydration, but with a much lower Ca/Si ratio [95]. A common secondary reaction product hydrotalcite is normally found to coexist with C-A-S-H gel due to the presence of Mg in precursors such as slag. In category (II), the low-Ca AAMs are normally made from metakaolin or type F fly ash precursors. This type of AAM is also named geopolymers. The main reaction product is an M-A-S-H gel (M being alkaline cations Na, K) [96]. Alkaline activation is considered a promising approach to transform different wastes and industrial by-products into cement-free building materials. Compared with conventional cementitious binders, AAMs are environmental-friendly with a considerable reduction of global warming potential and embodied energy [10, 97, 98]. Meanwhile, AAMs as binder material for concrete could maintain comparable mechanical properties and even better durability concerning chloride migration resistance, chemical resistance, and high-temperature resistance [99-102]. Therefore, AAMs serve as a promising alternative binder material for

sustainable construction and perfectly meet the Sustainable Development Goals of the United Nations.

Among all AAMs, the ones based on blast furnace slag, class F fly ash, and their blends are most intensively studied due to the large quantity as well as the relatively stable chemical compositions [6-9]. Previous studies on the slag/fly ash-based AAMs system, namely alkali-activated slag/fly ash (AASF), have focused on microstructure development, nature of reaction products, and mechanical properties [91, 103-106]. The application of AASF for engineering practices has also been greatly promoted [107].

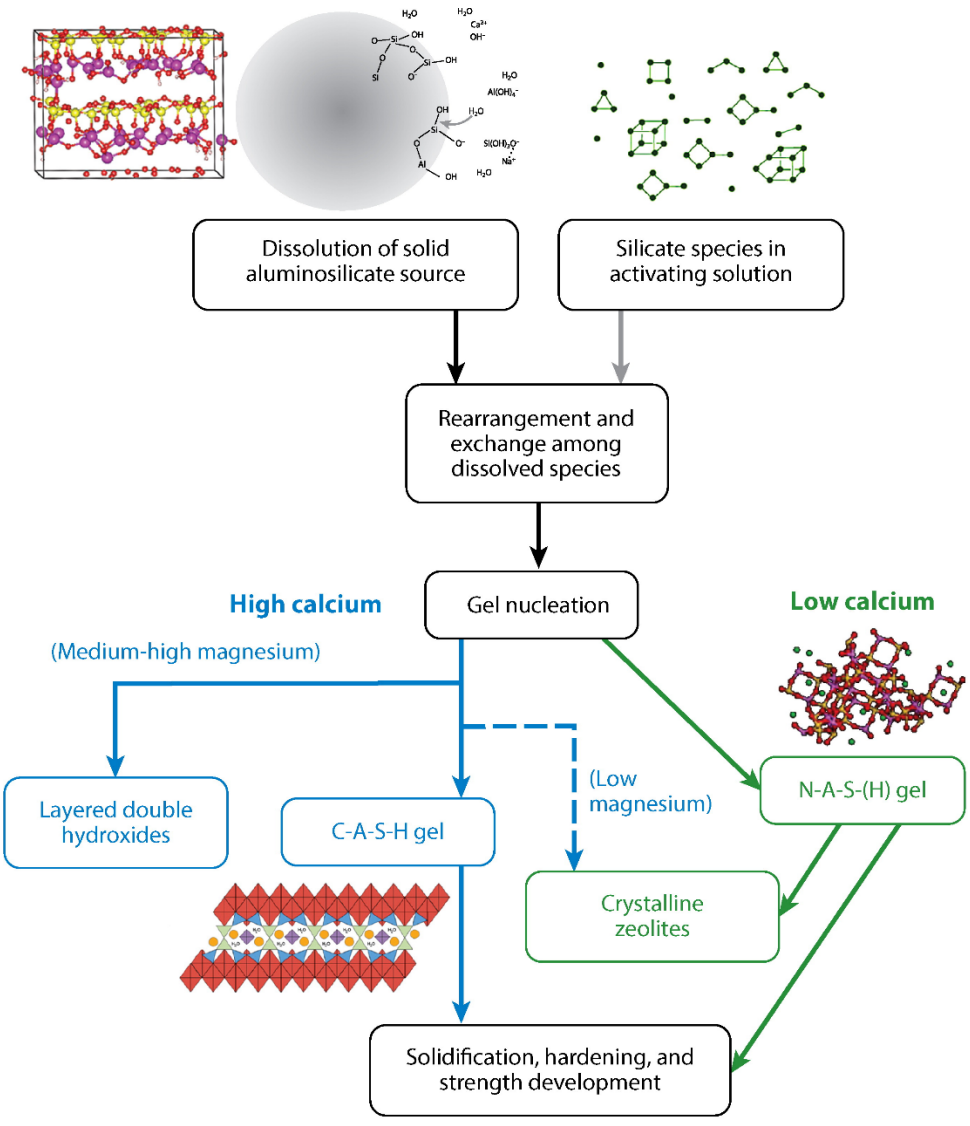

Figure 2.11 Conceptual reaction model of high calcium and low calcium alkali-activated materials [97].

2.5 Development of strain-hardening geopolymer composite (SHGC)

Recently, several types of strain-hardening geopolymer composite (SHGC) developed using different mineral precursors have been described in the literature. Considering the raw materials and curing temperature used during their preparation, these SHGCs can be classified into two categories: (1) a heat-cured fly ash-based and metakaolin-based SHGC, and (2) an ambient temperature cured slag/fly ash-based SHGC. It is important to note that, by definition, the term geopolymer strictly relates to a synthetic alkali aluminosilicate material, which is characterized by its three-dimensional aluminosilicate network [9]. However, it seems that the term geopolymer is more frequently used by civil engineers for AAMs, especially in the studies concerning the development of strain-hardening composite. In this thesis, the term SHGC is always used.

2.5.1 Heat-cured fly ash-based SHGC

Ohno and Li [21, 24] first studied the feasibility of strain-hardening fly ash-based geopolymer composite and developed a ductile engineered geopolymer composite (EGC) based on two kinds of fly ashes and PVA fiber. Furthermore, they also proposed an integrated design method, which includes the statistic design method for the matrix, micromechanical modeling for the composite behavior, and determination of sustainability performance [21]. Nematollahi et al. [25, 86] also developed several fly ash-based SHGCs by heat curing PVA fibers and PE fibers. Farooq et al. [108] investigated the tensile performance of several types of fly ash-based SHGC reinforced with different micro-fibers, which were named eco-friendly ductile geopolymer composite (EDGC). Significant strain-hardening was achieved with PVA fibers EDGC. The above-mentioned SHGCs all exhibit good strain-hardening behavior (>3%) and multi-cracking characteristics. Recently, researchers also tried to improve the strain-hardening capacity of fly ash-based SHGC by adopting metakaolin [109], red mud [110], and municipal incineration solid wastes (MSWI) ash [111]. Using the strain-hardening criteria (Section 2.3.1), they have also proposed possible mechanisms to explain the differences in strain-hardening performance based on the study of fracture properties of the matrix and also the fiber/matrix interface properties.

Notably, researchers found that heat curing at a temperature between 40 to 80 °C is required for fly ash-SHGC to achieve satisfactory mechanical properties. However, the use of heat curing is not preferred because of the energy consumption needed for the autoclave/oven [21]. Nematollahi et al. also point out that heat-cured SHGC seems not suitable for in-situ applications such as structural retrofitting or repair [23].

2.5.2 Ambient temperature cured slag-based and slag/fly ash-based SHGC

The higher reactivity of blast furnace slag than Class F fly ash in AAMs has been confirmed in many previous studies [91, 103]. Based on this, several researchers have developed slag-based SHGC cured at ambient temperature. Lee et al. [112] developed a slag-based alkali-activated mortar using PVA fiber with tensile strain up to 4.5% and ultimate tensile strength of 4.7 MPa. Choi et al. [113] prepared slag-based SHGC with a tensile strain of up to 7.5% and

tensile strength of 13.1 MPa by using mixed activator ($Ca(OH)_2$ and Na_2SO_4) and PE fibers. They found that adding slag in SHGC can provide higher elastic modulus and ultimate tensile strength. However, adding slag also increases the first crack strength and the fracture toughness of the matrix, which is not beneficial for a saturated strain-hardening behavior [112].

To address the above problem, researchers incorporated Class F fly ash to develop slag/fly ash-based SHGC mixtures. Nematollahi et al. [23] developed a slag/fly ash-based SHGC cured at ambient temperature using PVA fibers. In addition, Nematollahi et al. [114] also developed a one-part SHGC using high modulus polyethylene (HMPE) fiber. The one-part mixture helps the material handling and preparation in practical applications. Alrefaei and Dai [115] investigated the tensile performance of both slag-based and slag/fly ash-based one-part SHGC incorporating hybrid combinations of steel and PE fibers (total fiber volume at 2%). In both systems, while the first crack strength is greatly influenced by the steel fiber content, the strain-hardening capacity is found to be directly related to the content of PE fiber. Zhong and Zhang [116] developed a slag/fly ash-based SHGC with PVA fiber and recycled tire polymer (RTP) fiber. SHGC with 1.75% PVA fiber and 0.25% RTP fiber showed acceptable strain-hardening properties including a tensile strain capacity of around 2.5%, while the material cost and the environmental impact were lowered. All the above-mentioned SHGCs exhibit good strain-hardening behavior (>3%) and multiple-cracking characteristics.

2.5.3 The use of the micromechanics-based model in the development of SHGC

The micromechanical model described in Section 2.3.2 has been used in previous studies on the development of SHGC [23, 117]. Researchers used the micromechanics-based model mainly for two purposes. First of all, they used the model to explain the origin of strain-hardening behavior [109, 111]. Second, the model was used for optimization purposes. Nematollahi et al. [117] optimized SHGC using a micromechanics-based model to study the effects of fiber length, fiber volume, and matrix fracture toughness. However, rarely has the micromechanical model served as a predictive tool to guide the development of SHGC.

Compared to the development of SHCC, more influencing factors in SHGC can affect the geopolymer matrix and related fiber/matrix interface properties [21]. For example, instead of the water-to-binder (w/b) ratio in SHCC, the corresponding factors in SHGC are the Na_2O, SiO_2, and water content in the alkaline activator. As a result, the development of SHGC using the conventional trial-and-error method is inefficient and time-consuming [86, 118, 119].

2.6 Influencing factors on the strain-hardening behavior of SHGC

According to previous studies, several factors can affect the strain-hardening behavior of SHGC. The most important factors from a materials perspective are (1) the selection of fiber (fiber properties), (2) the fracture properties of the matrix, and (3) the fiber/matrix interface bonding properties [120, 121].

2.6.1 Type and properties of fiber

Several types of fiber have been applied by researchers to develop SHGC mixtures. The physical and mechanical properties of these fibers are summarized in Table 2.2.

Table 2.2 Physical and mechanical properties of fibers in SHGC [24, 108, 112-115, 120, 122-125].

Fiber types	Density (g/cm3)	Elastic modulus (GPa)	Tensile strength (GPa)	Length (mm)	Diameter (μm)
PVA	1.3	41	1.6	8, 12	39
HMPE	0.97	88 to 123	2.7 to 3.5	12, 18	12 to 24
PP	0.91	3 to 3.5	0.6 to 0.7	12	50
PET	1.37	11.5	1.16	12	38
Steel	7.85	200	2.3 to 2.5	6 to 13	160 to 180

The most widely applied fibers for the development of SHGC are PVA fibers and high modulus polyethylene (HMPE) fibers. PVA fiber (RECS-15) with a proper oil coating on the fiber surface is the most often used to develop SHGCs [121]. The oil coating at the PVA fiber surface guarantees a proper chemical bond between the PVA fiber and the matrix. This results in dramatically enhanced complimentary energy J_b' and thereby a better strain-hardening behavior [84]. Another frequently used fiber is the HMPE fiber. Compared to normal polyethylene (PE) fiber, HMPE fiber has much higher tensile strength and elastic modulus. HMPE fiber has a hydrophobic nature so that no chemical bond is formed between HMPE fiber and SHGC matrix [51, 113]. Due to its very high tensile strength, however, the maximum fiber bridging capacity is significantly improved [49]. This eventually leads to higher ductility compared to SHGC [114].

Other fibers like steel fiber, polypropylene (PP) fiber [108], and polyethylene terephthalate (PET) fiber [123] were also studied. Farooq et al. [108] studied the strain-hardening behavior of fly ash-based SHGC with PP fiber, high-strength steel fiber, steel wool, and PVA fiber. Only SHGC prepared with PVA fiber was found to have good ductility. Steel fiber/wool in SHGC can only increase the first crack strength of the mixture but does not lead to superior tensile ductility. In fact, it is very difficult to achieve strain-hardening using only steel fiber [120]. SHGC with PP fibers only exhibits a higher tensile strain capacity and a very low tensile strength of 0.5 to 0.7 MPa, due to its lower modulus (3 to 4 GPa), leading to extremely high elongation when ruptures (25%). Instead of strain-hardening, mixtures prepared with steel fiber show only deflection-hardening behavior, similar to other studies [115].

Natural fibers such as luffa [124], jute, sisal, and curaua fibers [125], have also been applied to develop SHGC. However, Wei and Meyer [126] found that the cellulose in natural fibers could easily be damaged by the high-alkali environment. Hence, the long-term durability of the SHGC prepared with natural fibers needs to be considered.

Recently, the so-called fiber hybridization has been applied to develop SHGC. The hybridization can be PVA or PE fiber replaced with other fibers, such as recycled fibers RTP [116], steel fiber [115], and natural fibers [125]. These studies showed that the main role of PVA and PE fibers is to control the tensile strain capacity and multiple-cracking, whereas steel

fiber can increase the tensile strength of the SHGC. This conclusion is similar to what has been found for SHCC systems [127].

2.6.2 Fracture properties of the matrix

The fracture properties of the matrix, such as fracture toughness K_{Ic} (J_{tip}) and first crack strength σ_{fc}, significantly influence the crack initiation, propagation, crack-bridging, and consequently the strain-hardening and multiple-cracking behavior of SHGC [20, 21]. According to linear elastic fracture mechanics (LEFM), the first crack strength σ_{fc} of the matrix is uniquely related to its fracture toughness K_{Ic} (J_{tip}) [43, 128]. This makes the K_{Ic} (J_{tip}) the most important fracture property of the matrix in the design of SHGC. However, studies on the fracture properties of AAMs and geopolymers are still quite limited compared with those on cementitious systems. Only very few studies have reported the fracture properties of AAMs and geopolymers. A summary of both K_{Ic} and J_{tip} of SHGC matrices versus their compressive strength is shown in Figure 2.12.

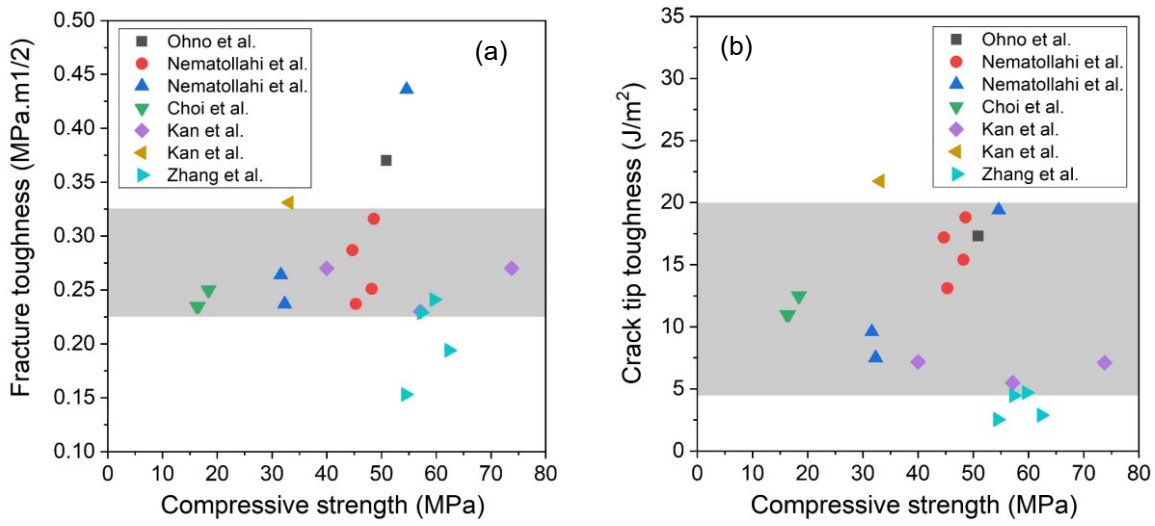

Figure 2.12 (a) Fracture toughness K_{IC} and (b) crack tip toughness J_{tip} of SHGC matrix in existing studies as a function of the compressive strength [21, 86, 109, 111, 129-131].

Most of the existing studies are limited to the experimental testing of K_{Ic} (J_{tip}) to determine the crack propagation resistance of the matrix [21, 86, 109, 111, 129-131]. These parameters were tested for the design of SHGC. In these studies, researchers found that the K_{Ic} (J_{tip}) of the SHGC matrix is influenced by aluminosilicate material [109, 115, 132], the cations in the activator (Na or K) [130], and the silicate modulus of the activator [129]. Unfortunately, these studies did not explain the mechanism behind the change in fracture toughness. Furthermore, the addition of fine aggregate also influences the K_{Ic} (J_{tip}) of the SHGC matrix. The K_{IC} (J_{tip}) increases by adding micronized quartz sand [133] and inert fine aggregates, such as zeolite [132] and MSWI ash [111] in the SHGC matrix. Increasing the content and the particle size of fine aggregate in the SHGC matrix also leads to higher K_{IC} (J_{tip}) [86, 108]. These conclusions are similar to what we know from cementitious systems [134]. Since excessively large K_{IC} (J_{tip}) leads to violation of the energy criterion and poor strain-hardening of SHGC, the amount of fine aggregate in SHGC should be carefully controlled.

The other sets of studies are related to the investigation of the fracture properties of alkali-activated concrete (AAC). Nath and Sarker [135] studied the ambient temperature cured AASF-based concrete and found that it was comparable with OPC concrete regarding their load-deflection behavior. Besides, the fracture toughness (K_{Ic}), which is comparable to that of OPC concrete under similar compressive strength, shares a similar trend with the flexural strength. Ding et al. [16] reported the fracture properties of ambient temperature cured AASF-based concrete. They found that the fracture behavior of AASF-based concrete is also affected by different material parameters, including the alkali concentration, the silicate modulus of activator, the slag/fly ash ratios as well as the liquid to binder ratio. They also found that the Bazant & Becq-Giraduon model predicts the fracture energy of AASF-based concrete as a function of compressive strength better than the CEB/FIP model. Other studies on fracture properties of AAMs concern heat-cured fly ash-based AAC. Pan et al. [15] measured the fracture properties of fly ash-based geopolymer paste and concrete and found they have lower characteristic lengths and higher brittleness compared to OPC counterparts. Interestingly, all the above studies found that fracture energy (G_F) is positively related to compressive strength.

2.6.3 Interface bonding properties

After a first crack occurs in fiber-reinforced composite like SHGC, its load-bearing capacity mainly depends on the pullout behavior of the bridging fibers during crack propagation. Since the pullout behavior is determined by the interactions between the fiber and matrix, the interface bonding properties have a prominent effect in determining the composite behavior of SHGC. To determine the interface bonding properties, the single-fiber pullout test has been widely used [136]. The test set-up of the test is shown in Figure 2.13.

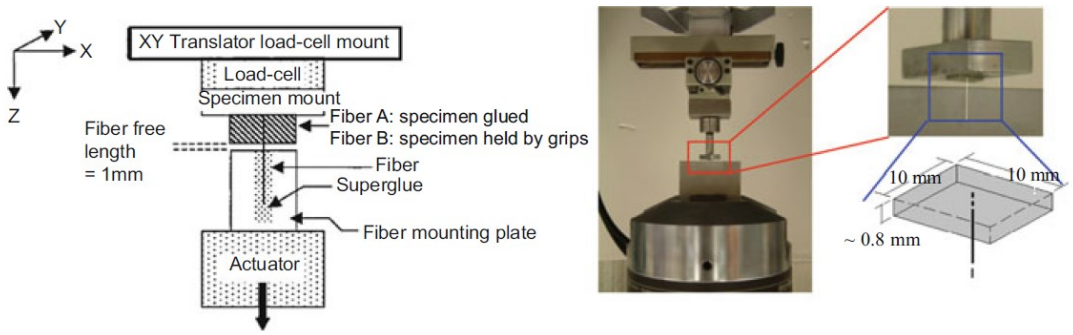

Figure 2.13 Test setup of the single fiber pullout experiment [137].

Up till now, only a few studies focused on the characterization and modification of fiber/matrix interface properties in SHGC [46, 138, 139]. The general profile of single-fiber pullout curves is presented in Figure 2.14. According to Redon et al. [138], it comprises three main regimes:

- Initially, a stable fiber debonding process occurs along the fiber/matrix interface. The load increases up to P_a when the debonded length equals the fiber embedded length L_e. The fiber is then debonded over its entire length (L_d=L_e), but the fiber end was not yet moving.

At this point, the displacement only consists of the elastic stretching of the debonded fiber segment and the free length of the fiber.

- Then the load decreases from P_a to P_b. This load drop normally indicates that the chemical bond is broken between the fiber and matrix. The strength of the chemical bonding can be revealed by the magnitude of the load drop [140, 141]. For instance, hydrophobic fibers like PE fibers have no chemical bonding to the matrix, so in this case, P_a equals P_b.
- Finally, the fiber starts to slide in the slippage phase from load P_b. From this point onwards, the pullout is resisted by frictional forces. In the majority of cases, the friction force increases linearly with increasing pullout distance. This increasing pullout resistance is referred to as the slip-hardening effect and is characterized by the slip-hardening coefficient β (β>0) [142].

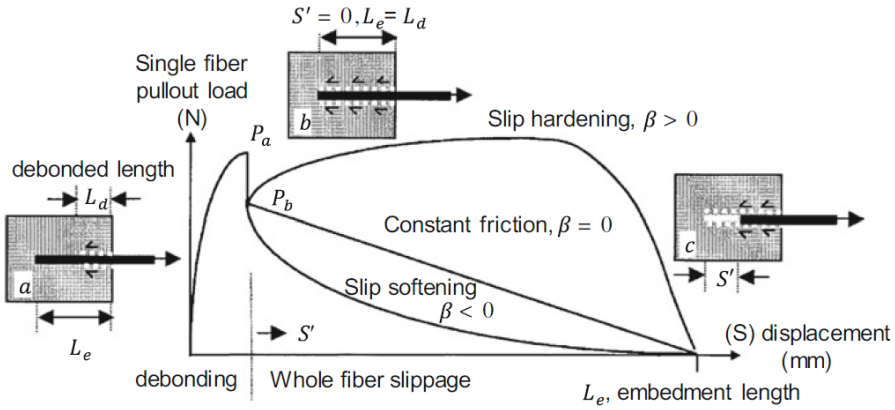

Figure 2.14 Typical pullout load P-displacement S relationship in single fiber pullout tests [137].

Generally, three important interface bonding properties including the chemical bonding strength G_d, the friction bonding strength τ_0 at initial fiber slippage, and the slip-hardening coefficient β can be determined from the single fiber pullout curves. Using a fiber debonding/pullout model, Lin et al. [143] derived the following Equations (2.7) to (2.9):

$$G_d = \frac{2(P_a - P_b)^2}{\pi^2 E_f {d_f}^3} \tag{2.7}$$

$$\tau_0 = \frac{P_b}{\pi d_f L_e} \tag{2.8}$$

$$\beta = \frac{d_f}{L_e}\left(\frac{(\Delta P/\Delta S \,|\Delta S \to 0)}{\pi \tau_0 d_f} + 1\right) \tag{2.9}$$

where E_f and d_f are the elastic modulus and diameter, $\Delta P/\Delta S$ is the initial slope of the pullout load P vs displacement S. P_a is the load when the fiber is fully debonded (i.e., debonded length L_d = embedded length L_e) and P_b is the load when the fiber begins to slip.

Ohno and Li [21] studied the interface properties of PVA fiber in a fly ash-based geopolymer matrix after strength optimization. They found that the value of G_d in SHGC is almost 5 times higher than that in PVA-based SHCC, whereas the frictional bond τ_0 and the tendency for slip-hardening behavior (indicated by coefficient β) is considerably lower. Nematollahi et al. [130] tested the interface properties of PVA fiber/matrix properties in alkali-activated fly ash mixtures. The influence of both sodium (Na) and potassium (K) silicate-based activators and the surface oil treatment on the interface properties were addressed. They concluded that the Na-based geopolymer matrix has advantageous properties in terms of higher mechanical properties, lower chemical bonding, high friction bond, and more significant slip-hardening compared K-based matrix. Additionally, Nematollahi et al. [23] concluded that the strong chemical bonding of PVA fiber could effectively enhance the fiber-bridging strength (i.e., ultimate tensile strength) of SHGC. Zhang et al. [129] investigated the interface properties of PVA fiber within AASF matrices and reported that G_d is predominantly related to microstructure and the chemistry of the reaction product, which could be effectively modified by changing the silicate modulus M_s of the alkaline activator. Some other studies focused on testing the interface bonding properties of HMPE fibers in SHGC. Compare to PVA fibers, HMPE fibers show no chemical bonding with the SHGC matrices (G_d=0). The friction bond τ_0 of HMPE fibers is also significantly lower than that in PVA-SHGC and is significantly lower than that of PE-SHGC [114]. Instead of slip-hardening, HMPE fibers show typical slip-softening behavior as indicated in Figure 2.14.

Studies have shown that, compared to those in SHCCs, the values of G_d and the τ_0 of slag-based or slag/fly ash-based SHGC are about 1.5 to 3 times and 2 to 3 times higher than those of SHCC, respectively. However, for fly ash-based SHGC, although G_d is 5 times higher, τ_0 is considerably lower. In both types of SHGCs, the slip-hardening behavior is much weaker than that in SHCCs (indicated by lower β values) [21, 23, 129]. Researchers suggested that the above significantly different fiber/matrix interface properties in SHGC and SHCC should be mainly determined by the microstructure and the chemical composition of reaction products [129]. Currently, no published studies can be found on this topic.

2.7 Environmental impact of SHGC

One of the important motivations for the development of SHGC is related to its better sustainability performance in comparison to conventional SHCC materials. As discussed in Section 2.5, many researchers have successfully developed SHGC based on different solid precursors and microfibers. All these SHGC mixtures exhibit good strain-hardening behavior (>3%) and multi-cracking characteristics. However, environmental impact assessments of SHGC have rarely been conducted.

Using heat curing for 1 day at 60 °C, Ohno and Li [21] evaluated the CO_2 equivalent emission and embodied energy (EE) of several fly ash-based EGCs. The optimized EGC with 1.5 vol.% PVA fiber has 55 % lower CO_2 equivalent emission and 11% lower EE than a standard version of ECC (i.e., ECC M45) [44]. The result is shown in Figure 2.15. Similar findings were reported by Nematollahi et al. [144]. Using similar heat curing conditions (1 day at 60 °C), they investigated the CO_2 equivalent emission and the EE of a fly ash-based lightweight SHGC. The CO_2 equivalent emission and the EE of the lightweight SHGC are found to be 52% and 17% lower than those of ECC M45, respectively. Additionally, Nematollahi et al. [23] also evaluated the CO_2 equivalent emission and the EE of a one-part slag/fly ash-based SHGC

cured at ambient temperature. This SHGC mixture offers a 76% reduction in CO_2 equivalent emission and a 36% reduction of EE compared to ECC M45. Zhong and Zhang [116] calculated the CO_2 equivalent emission (embodied carbon) and the EE of an ambient-temperature-cured slag/fly ash-based SHGC reinforced with recycled tire polymer (RTP) and PVA fiber. It was found that the CO_2 equivalent emission is approximately 48.83% lower than that of ECC M45. The EE of SHGC reduced gradually with increasing RTP fiber replacement and the reduction was in the range of 4.0 to 16.2% compared to PVA SHGC. This reduction is mainly ascribed to the lower EE of the recycled fibers.

All the above-mentioned studies found that the developed SHGC brings significant environmental benefits because of the considerably reduced CO_2 equivalent emissions compared to conventional SHCC (e.g., ECC M45) [21, 23, 116, 144] and SHCC with SCMs (e.g., High volume fly ash ECC [43]). However, it is important to note that the environmental impacts considered in these studies are only limited to CO_2 equivalent emissions and embodied energy. According to Centrum voor Milieukunde Leiden (CML) [145], more than 10 environmental impact categories need to be evaluated to reflect the overall environmental impact of a certain product. The CO_2 equivalent emissions related to the global warming potential (GWP) are only one of the impact categories. Focusing on CO_2 equivalent emissions alone is a crude approach that may lead to misleading conclusions about the impacts in certain cases [146]. Thus, a more thorough life-cycle assessment (LCA) using multiple environmental impact indicators is needed to give a complete picture of the sustainability performance of SHGC.

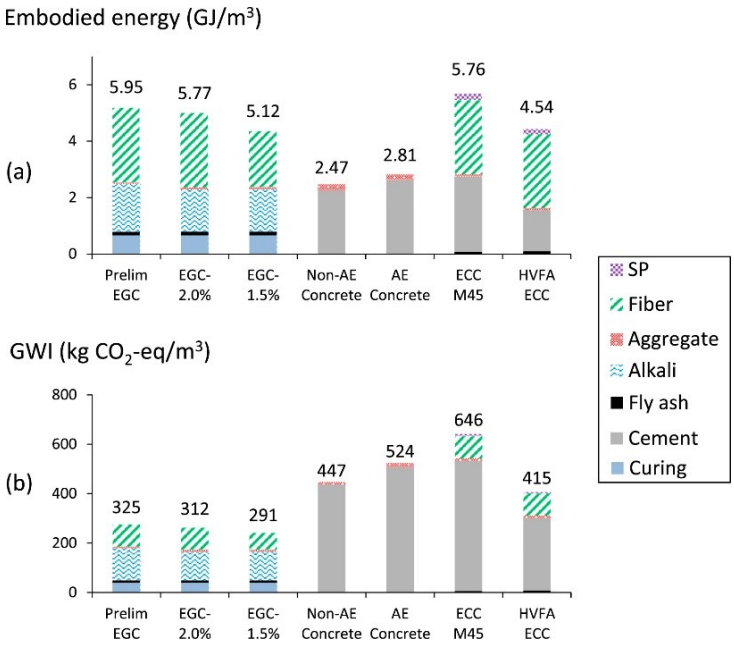

Figure 2.15 (a) Embodied energy and (b) global warming intensity for engineered geopolymer composite (EGC), concrete, and ECC materials [21].

Besides the confirmed environmental benefits of SHGC, almost all previous studies have pointed out that the major environmental impact of SHGC is due to the use of PVA fiber and the alkaline activator. Furthermore, SHGC cured at ambient temperature is found to be even more sustainable because the energy-intensive heat curing process is avoided.

2.8 Challenges in the development of SHGC

Up till now, much effort has been put into the development of conventional SHCC. However, scientific and technical knowledge of SHGC is still in the very early stage of development. Based on the literature survey, several major challenges and knowledge gaps can be identified:

- The knowledge of the fracture properties of the SHGC matrix is largely unknown. Furthermore, there is also a knowledge gap between the study of the chemical composition of reaction products and the study of fracture properties.

- The effects of different influencing parameters (solid precursors, alkaline activator composition, etc.) on mechanical properties, especially the fracture properties, of geopolymer matrices are not yet investigated. These properties are crucial for the development of SHGC.

- The fiber/matrix interface bonding properties in SHGC are still largely unknown. The lack of knowledge on the bonding mechanism of fiber to AAMs/geopolymer matrix also hinders the development of SHGC when interface bonding turns out to be crucial for the further development of this material.

- Considering SHGC has more influencing parameters in mixture design when compared with conventional SHCCs, the trial-and-error method is no longer suitable for the development of SHGC. However, very few studies have been devoted to a systematic design methodology (such as using micromechanics-based modeling) for SHGC.

- Ambient temperature-cured SHGCs with high tensile ductility and multiple-cracking behaviors are scarcely developed. Up till now, only a limited number of studies were conducted regarding the development of SHGC [21, 23-25].

- The environmental impact of SHGC has not been systematically studied yet. Only a limited number of studies have been conducted on the environmental impact of SHGC. Almost all of them only focused on CO_2 equivalent emissions (global warming potential) and embodied energy. Hence, it cannot provide the whole picture of the environmental profile of SHGC.

Chapter 3

Fracture properties and microstructure formation of hardened alkali-activated slag/fly ash matrix[3]

3.1 Introduction

The performance of a high-performance composite, e.g., a strain-hardening geopolymer composite (SHGC), is governed by its three main components: the matrix, the fiber, and the fiber/matrix interface. Besides the influence of the mechanical properties of the fiber, both matrix fracture properties and the fiber/matrix interface properties will substantially influence the crack-bridging and crack propagation, and consequently the strain-hardening and multiple-cracking behavior of SHGC [20, 21]. For the development of a slag/fly ash-based SHGC, the fracture properties play equally important roles as strength development. For this reason, this chapter aims to experimentally investigate the fracture properties of hardened AASF paste as the matrix of SHGC. To this end, the fracture toughness K_{Ic}, crack-tip toughness J_{tip}, and fracture energy G_F of AASF pastes were studied using three-point bending tests. Other mechanical properties, including compressive strength (f_c), splitting tensile strength (f_{st}), and elastic modulus (E_m) of hardened AASF pastes were tested as well.

Additionally, since the fracture resistance relates intimately to the material's microstructure [147], comprehensive knowledge of the microstructure of AASF is crucial for an effective design and/or tailoring of the fracture properties. Up till now, not only the number of studies concerning fracture properties of AASF is limited, but studies on fracture-related microstructural aspects are also missing. Therefore, multiple techniques were applied for the microstructure characterization regarding the chemical composition, the pore structure, and the amount of reaction product in hardened AASF pastes.

Finally, these microstructural aspects are further correlated with tested fracture properties and mechanical properties. Based on this, the fracture mechanism of hardened AASF paste is investigated and discussed.

[3] This chapter is based on:

Zhang, S., Li, Z., Ghiassi, B., Yin, S., & Ye, G. (2021). Fracture properties and microstructure formation of hardened alkali-activated slag/fly ash pastes. Cement and Concrete Research, 144, 106447.

Zhang, S., Li, Z., Ghiassi, B., Yin, S., & Ye, G., 2019. Effect of alkali activator modulus on fracture properties of alkali-activated slag/fly ash pastes. 15th Congress on the Chemistry of Cements, Prague, Czech Republic.

The results and conclusions obtained in this chapter enable effective modification of the fracture properties by simply adjusting the mixture design of AASF. Furthermore, the experimentally acquired fracture properties (K_{Ic} and J_{tip}), along with the splitting tensile strength f_{st} and the elastic modulus E_m of the matrix will serve as an important input for the micromechanical modeling to guide the development of the SHGC in Chapter 6.

3.2 Materials and methods

3.2.1 Materials

The solid precursors used in this study were ground granulated blast furnace slag and Class F fly ash according to ASTM 618 [148]. Both of them are produced locally in the Netherlands. The material density of slag and fly ash are 2890 kg/m^3 and 2440 kg/m^3, respectively. The particle size distribution (PSD) of solid precursors is determined using laser diffraction and is shown in Figure 3.1. The d_{50} particle size is 17.88 μm for slag and 33.19 μm for fly ash. The chemical compositions determined by X-ray Fluorescence along with other properties of the solid precursors (including the LOI at 950 °C) are shown in Table 3.1.

Table 3.1 Chemical compositions and properties of raw materials

Oxide (wt %)	SiO_2	Al_2O_3	Fe_2O_3	CaO	MgO	SO_3	TiO_2	Na_2O	K_2O	LOI
Slag	32.91	11.84	0.46	40.96	9.23	1.60	1.00	-	0.33	1.15
Fly ash	52.90	26.96	6.60	4.36	1.50	0.73	1.14	0.17	-	3.37

LOI: loss on ignition

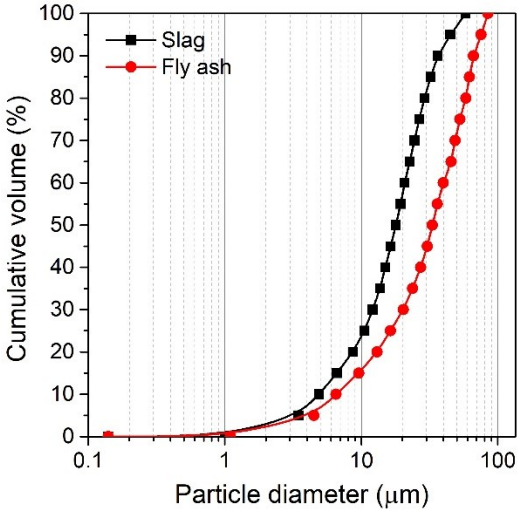

Figure 3.1 Particle size distribution of solid precursors slag and fly ash

The crystalline phases were determined using powder X-ray diffraction (XRD). The XRD patterns of slag and fly ash are shown in Figure 3.2. The major crystalline phases in fly ash are quartz, mullite, and hematite, while the blast furnace slag contains mainly amorphous phases. Both precursors contain considerable amorphous contents indicated by the humps in the XRD patterns (from 17° to 35° for fly ash and from 25° to 35° for slag). The reactivity of

slag is indicated by its abundant amorphous content (over 98%). The high reactivity of slag in the alkaline environment has been confirmed previously using isothermal calorimetry [91]. The reactivity of fly ash is assessed by its reactive silica content of 43.04% and reactive alumina content of 14.51%, as reported in a previous study [91].

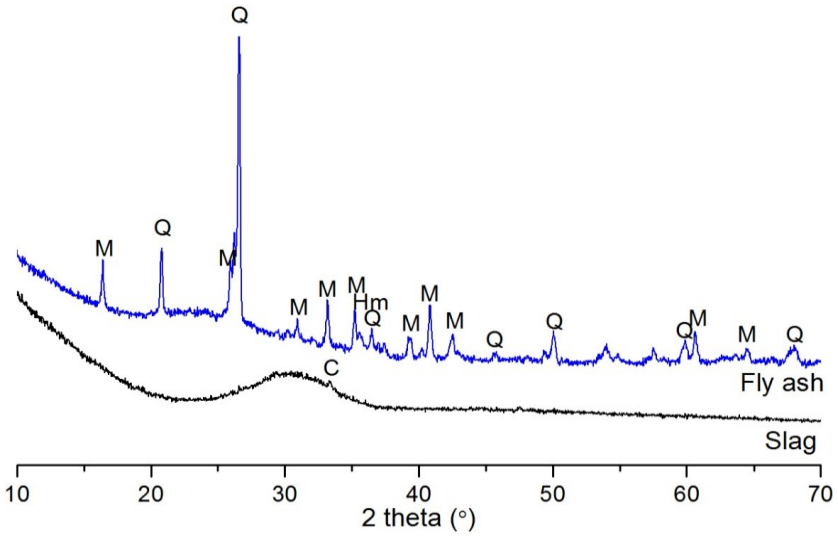

Figure 3.2 XRD patterns of solid precursors (Q: quartz, M: mullite, Hm: hematite, and C: calcite)

The alkaline activator solutions with different silicate modulus (M_s) were prepared by mixing sodium hydroxide pellets (analytical grade, purity ≥ 98%) and concentrated liquid sodium silicate solution (Na_2O: 8.25 wt.%, SiO_2: 27.50 wt.%, and H_2O: 64.25 wt.%) in distilled water. The activator solutions were cooled down to room temperature (20 °C) before mixture preparation.

3.2.2 Mixture design and sample preparation

The starting point for the mixture design is an AASF mixture with good mechanical properties and workability [149]. It has been reported that the microstructure and reaction kinetics of AASF is significantly influenced by the Ca and Si contents [91, 103, 150]. As a result, both the slag/fly ash content and the silicate modulus (M_s being the SiO_2/Na_2O molar ratios) of the activator play important roles in the mechanical properties of the mixture [95, 151]. Hence, the slag content and the M_s of the alkaline activator were selected as the main variables in this study. The detailed mixture proportions are shown in Table 3.2. Two types of binder composition with different slag content (S30 and S50) and activator with different silicate moduli M_s (0-1.5) are given. The w/b ratio was kept constant at 0.32 in all mixtures to ensure adequate workability. The Na_2O content in the activator is 4% of the slag/fly ash binder mass. According to the type of activator, the samples were categorized into two systems: sodium hydroxide-activated system (with no soluble silicate in the activator) and sodium silicate-activated system (with soluble silicate in the activator).

The solid precursors were first dry mixed for 5 min using a HOBART® mixer at a low speed. Alkaline activator solution was then gradually added and the batches were mixed for an

additional 5 min at a medium speed (285 rpm). The fresh paste mixtures were cast in polystyrene prism molds (40 x 40 x 160 mm^3), compacted on a vibration table, and then sealed with a plastic wrap. The samples were demolded after 1 day and were cured in a climate room (20 °C and ≥98% RH) until the moment of testing.

Table 3.2 Mixture proportions of alkali-activated slag/fly ash pastes

Mixture*	Precursor (wt.%)		Alkaline activator (wt.%)			
	Slag	Fly ash	Water	Na_2O	SiO_2	Silicate Modulus (M_s)
S30M0	30	70	32	4.0	0	0
S30M0.5					1.94	0.5
S30M0.8					3.1	0.8
S30M1.0					3.88	1.0
S30M1.2					4.65	1.2
S30M1.5					5.8	1.5
S50M0	50	50	32	4.0	0	0
S50M0.5					1.94	0.5
S50M0.8					3.1	0.8
S50M1.0					3.88	1.0
S50M1.2					4.65	1.2
S50M1.5					5.8	1.5

*****Mixture notations: S indicates the weight percentage of slag in the slag/fly ash binder. M indicates the silicate modulus M_s (the SiO_2/Na_2O molar ratio) of the alkaline activator used for mixture preparation.

3.2.3 Testing procedures

3.2.3.1 Compressive strength and elastic modulus test

The compressive strength of AASF specimens cured for 28 days was measured according to NEN 196-1 standard [152]. The 28-day elastic modulus was obtained using 40 x 40 x 160 mm^3 prismatic specimens following ASTM C496 [153]. Four loading-unloading cycles with stress ranging from 5% to 15% of the compressive strength were applied. During the tests, the strain was measured using four LVDTs attached to each side of the prism. At least three specimens for each mixture were tested and the elastic modulus was calculated using the data obtained in the 2^{nd} to 4^{th} loading processes. The tests were conducted on a close-loop INSTRON machine using load-control with a loading rate of 0.1 MPa/s.

3.2.3.2 Three-point bending test on single notched beam

The fracture toughness K_{Ic} of the AASF paste was determined using single-edge notched specimens shown in Figure 3.3. The specimen has 40 mm in depth (W), 40 mm in width (B), and 160 mm in length. The single-edge notches with 1.5 mm in width, 40 mm in length, and 12 mm in notch depth (a) were prepared using a diamond cutting saw. The relative notch depth ratio α ($\alpha = a/W$) was 0.3. The three-point bending (3PB) tests were performed on a closed-loop INSTRON machine with the crack mouth opening displacement (CMOD) rate of 0.01 mm/min. The CMOD was controlled using two LVDTs, which were attached to the two sides of the notch on the side surfaces of the prism. The prism was supported over a load span (S) of 120 mm. At least 6 3PB tests were conducted for each mixture.

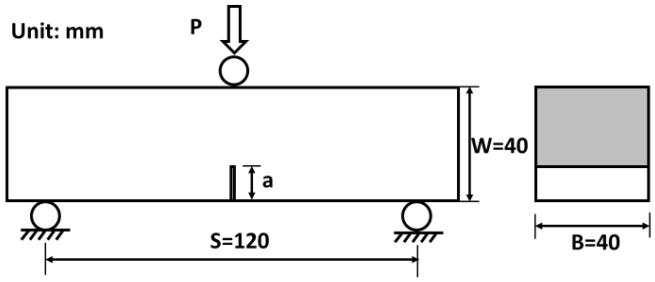

Figure 3.3 Three-point bending test configuration for single-edge notched prism specimen **[129]**

The fracture toughness K_{Ic}, i.e., mode I critical stress intensity factor, can be calculated with Equation (3.1). It also considers the specimen-related shape function $f(\alpha)$ determined using two-dimensional plane stress analysis. For $0.05 \leq \alpha \leq 0.8$, $f(\alpha)$ is given in Equation (3.2) as used in previous studies and recommendations [15, 21, 129, 154, 155].

$$K_{Ic} = \frac{1.5\, P_{Max}\, S\, \sqrt{\pi a}}{B\, W^2}\, f(\alpha) \tag{3.1}$$

$$f(\alpha) = \frac{0.68 - 0.744\alpha}{1 - 2.155\alpha + 1.161\alpha^2} + 0.36 - 2.088\alpha + 4.611\alpha^2 - 6.499\alpha^3 + 4.232\alpha^4 \tag{3.2}$$

where P_{Max} is the highest applied load [N], B is the specimen width [mm], W is the specimen depth [mm], S is the loading span [mm], a is the notch depth, and α is the relative notch depth ratio.

The crack tip toughness J_{tip}, i.e., the critical strain energy release rate, is calculated with Equation (3.3) and provides insights from an energy perspective:

$$J_{tip} = \frac{{K_{Ic}}^2}{E_m} \tag{3.3}$$

where E_m is the elastic modulus of the paste [GPa].

The fracture energy G_F based on work-of-fracture is calculated according to RLIEM recommendation by TC-FMC [156]:

$$G_F = \frac{W_0 + mg\ \delta_0}{A_{lig}} = \frac{\int_0^{\delta_0} P(\delta)\, d\delta + \ mg\ \delta_0}{W\ (B - a)} \tag{3.4}$$

where W_0 is the area under the load-CMOD curves [J] (see Figure 3.5), m is the mass of the beam between support [kg], g is the gravity constant [m/s^2], δ_0 is the final mid-point deflection [μm], and Al_{ig} is the ligament area calculated from the size of the specimen [m^2]. It is worth noting that in this study W_0 is calculated using CMOD instead of mid-point deflection δ_0 [157].

The calculation is based on the linear relationship that exists between the CMOD and the mid-point deflection in 3PB tests on single-edge notched prismatic specimens [158-160].

3.2.3.3 Microstructure characterization

All microstructure characterization tests were performed on AASF paste samples cured for 28 days. Before testing, the samples were crushed into small pieces. Further chemical reactions of the samples were stopped using isopropanol following the solvent exchange method. Afterwards, the samples were dried under vacuum.

The chemical compositions of reaction products were characterized by environmental scanning electron microscopy (ESEM) and energy dispersive X-ray (EDX) analysis, using a Philips-XL30-ESEM equipped with a Thermofisher UltraDry EDX detector. After the reaction stoppage, the samples were impregnated using low viscosity epoxy resin and then polished down to 0.25 µm using ethanol [161]. The polished samples were then coated with carbon. The EDX measurement was conducted at an accelerating voltage of 15 kV in high vacuum mode. It should be noted that the atomic number, absorption, and fluorescence (ZAF) corrections were made in each EDX measurement using the Pathfinder software. ZAF corrections convert apparent concentrations (raw intensities) into corrected concentrations to eliminate inter-element matrix effects. This makes it possible for semi-quantitative comparisons of element ratios.

Thermogravimetry and differential thermogravimetry (DTG) was performed in a TG-449-F3-Jupiter instrument for analysis of the reaction products. The powder of samples was put in a small aluminum oxide crucible and heated from 40 °C to 1100 °C at 10 °C/min in an argon protective atmosphere. The flow speed of argon gas was set at 50 µL/min.

The chemical bonds formed in the reaction products were determined by Fourier-transform infrared spectroscopy (FTIR) using a Spectrum TM100 Optical ATR-FTIR spectrometer. The tests were performed over the wavelength range of 600 cm^{-1} to 4000 cm^{-1} with a resolution of 1 cm^{-1}.

The pore volume and pore size distributions were measured by nitrogen gas adsorption using a Gemini VII 2390 instrument. The relative pressure defined as the equilibrium vapor pressure divided by the saturation vapor pressure (p/p_0) ranges from 0.05 to 0.99, which corresponds to a pore size from 0.002 to 0.1 µm. The pore size distribution is derived using Barrett-Joyner-Halenda models.

3.3 Results and discussions

3.3.1 Compressive strength and elastic modulus

The compressive strength and the elastic modulus of AASF pastes at 28 days are plotted as a function of the activator silicate moduli M_s ranging from 0 to 1.5 in Figure 3.4 (a) and (b), respectively.

Regardless of the alkaline activators used, higher slag contents, from 30 wt.% to 50 wt.%, yielded both higher compressive strength and elastic modulus at 28 days. Slag as an

aluminosilicate precursor with a higher content of amorphous phases has higher reactivity than fly ash. The Ca in the slag also promotes early-age reaction rates and is beneficial for rapid strength development [106]. Furthermore, the effect of the activator M_s on both mechanical properties is also significant. As depicted in Figure 3.4, the sodium hydroxide-activated systems (M_s=0) have substantially lower compressive strength and elastic modulus than the sodium silicate-activated systems (M_s=0.5 to 1.5). The compressive strength of both S30 and S50 show clear dependency on M_s. With increasing M_s, they first increase and then decrease after reaching a maximum at M_s=1.0. The 28-day maximum compressive strength of S30 and S50 mixtures are 62.6 MPa and 80.3 MPa, respectively. For the 28-day elastic modulus, the maximum values are achieved with M_s=0.5. The maximum elastic modulus of S30 and S50 mixtures are 14.3 GPa and 17.4 GPa, respectively.

The influence of M_s is due to the availability of soluble silica from the activator. Increasing M_s results in more available Si from the activator and alters the geopolymerization process. As a result, the reaction product formation is promoted and this consequently leads to superior mechanical properties. These findings are further confirmed by a higher amount of reaction products (See Section 3.3.3.4) and are also in line with previous studies [150, 162]. However, an excessive amount of silica is not favorable for strength development. This is because too much silica can retard the dissolution of slag as well as the further polycondensation reaction [150, 162, 163]. Therefore, optimum activation conditions for AASF could only be achieved using mixtures with moderate M_s, i.e., values between 0.5 and 1.0. Either too low or too high M_s is not favorable for the compressive strength development.

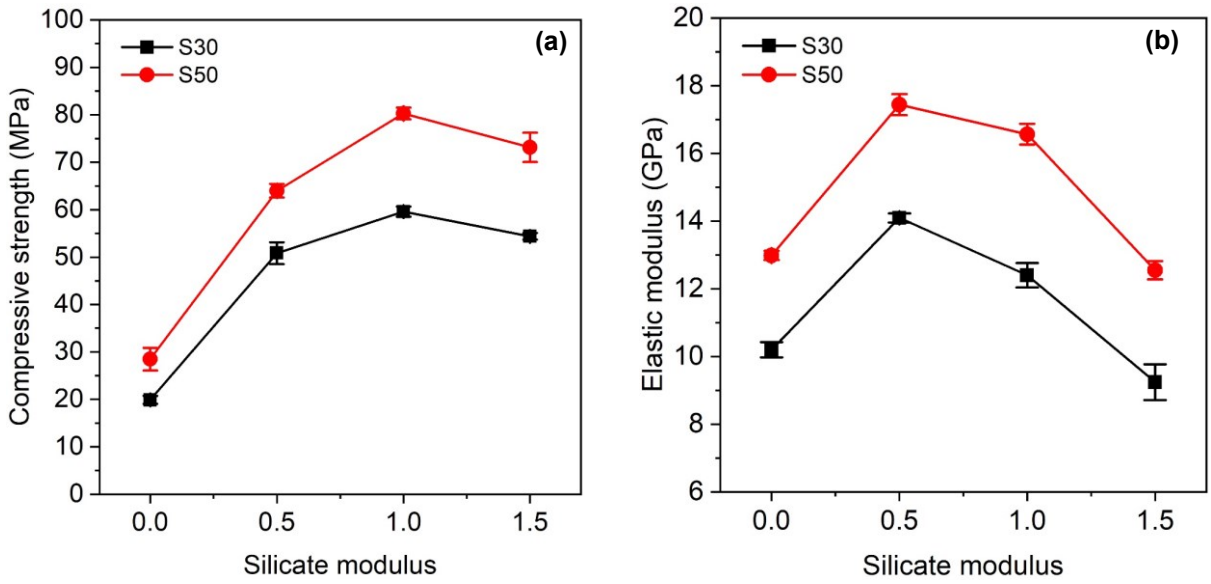

Figure 3.4 (a) Compressive strength and (b) elastic modulus of AASF pastes at 28 days as a function of activator silicate modulus 0, 0.5, 1.0, and 1.5.

Different trends of the compressive strength and elastic modulus as a function of M_s are observed. The compressive strength peaks at a M_s of 1.0, while the elastic modulus peaks at M_s of 0.5. These differences are reasonable since the compressive strength and elastic modulus are not determined by exactly the same factors. The AASF paste, like cementitious

paste, is a heterogeneous porous material. Its compressive strength is very often governed by its porosity [164]. However, the elastic modulus is not dependent on the porosity only. The elastic moduli of other reaction products also play important roles [165]. Consequently, the maximum compressive strength and elastic modulus are achieved at slightly different M_s.

3.3.2 Fracture properties

The fracture properties of AASF pastes, including K_{Ic}, J_{tip}, and G_F derived from 3PB tests on single-edge notched prismatic specimens, are discussed in this section. The representative load vs CMOD curves of all AASF pastes are shown in Figure 3.5 (a) and (b). The load-CMOD curve of AASF paste has similar characteristics to that of cementitious material. It consists of a linear elastic part followed by an elastic-plastic stage before reaching the peak load P_{max}. After reaching P_{max}, the paste went through a strain-softening stage as the crack continuously propagated. This characteristic relates closely to the brittleness of the AASF pastes. It should be noted that the post-peak softening branch of S50M0 and S50M0.5 pastes could not be obtained by controlling CMOD. This is possibly due to their higher inherent brittleness than that of other AASF pastes.

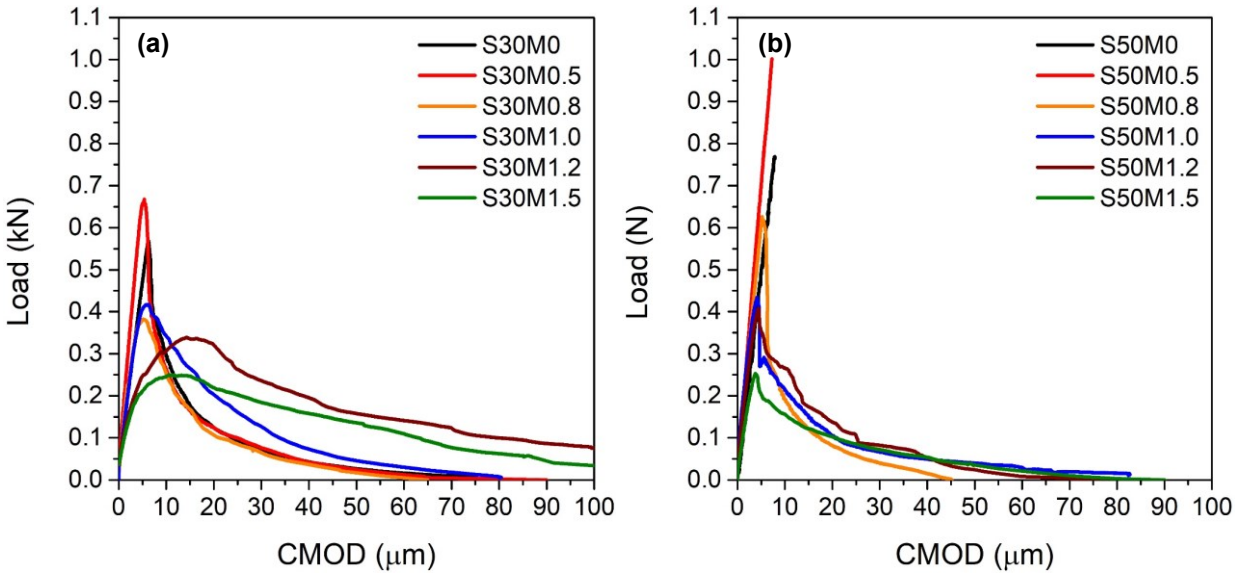

Figure 3.5 Representative Load-CMOD curves for (a) S30 pastes and (b) S50 pastes

3.3.2.1 Fracture toughness and crack tip toughness

The fracture toughness K_{Ic} generally increases with M_s from 0 to 0.5 and then gradually decreases with increasing M_s as shown in Figure 3.6 (a). Similar to compressive strength results, S50 mixtures have higher K_{Ic} than S30 mixtures. Except for S50M0 and S50M0.5 mixtures, the K_{Ic} of AASF paste in general falls in the range of 0.13 to 0.36 MPa·m$^{1/2}$. These values are comparable to the K_{Ic} of OPC pastes (0.2 to 0.6 MPa·m$^{1/2}$) [155, 166, 167], the K_{Ic} of AASF reported by Nematollahi et al. [86], and the K_{Ic} of fly ash-based geopolymer pastes reported by Pan et al. [15] and Ohno et al. [15, 21]. The highest values of K_{Ic} are observed at the M_s of 0.5. They reach 0.36 MPa·m$^{1/2}$ and 0.61 MPa·m$^{1/2}$ for S30 and S50 mixtures, respectively.

As shown in Figure 3.6 (b), the crack tip toughness J_{tip} with increasing M_s reveals a similar trend as K_{Ic}. This consistency reflects the effectiveness as well as the suitability of using 3PB for fracture testing of AASF paste. In linear elastic fracture mechanics (LEFM), the fracture toughness K_{Ic} and the J_{tip} (i.e., the strain energy release rate) are uniquely related. Therefore, the similar trend of J_{tip} and K_{Ic} with increasing M_s also indicates that the use of LEFM to determine the fracture properties of AASF paste is justified.

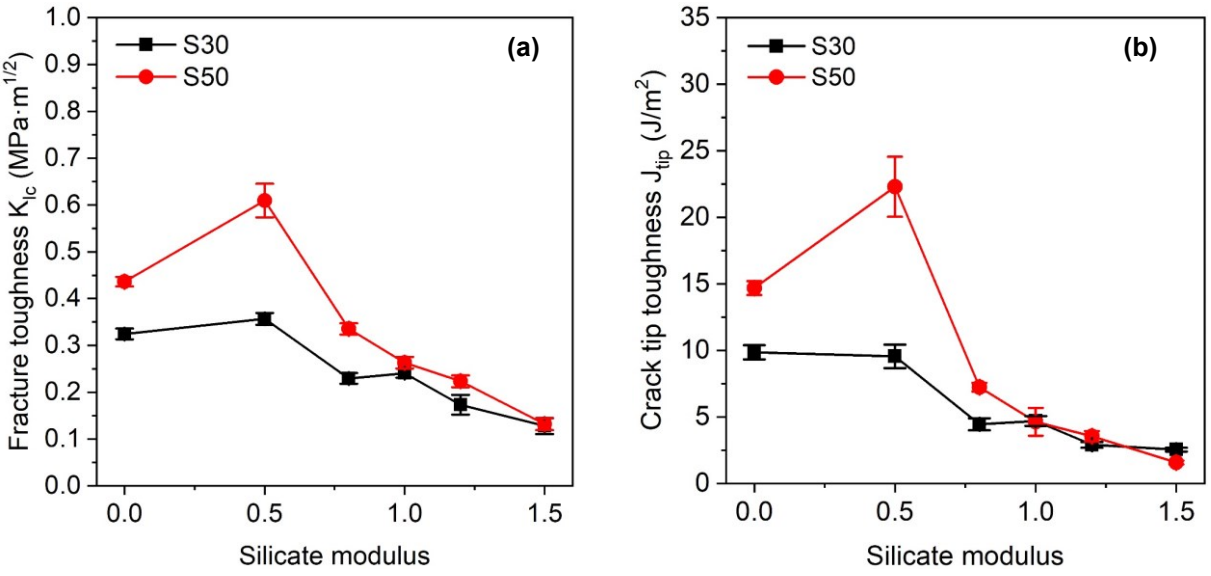

Figure 3.6 Fracture toughness K_{Ic} and crack tip toughness J_{tip} of AASF pastes at 28 days as a function of activator silicate modulus 0, 0.5 1.0, and 1.5.

Finally, both K_{Ic} and J_{tip} follow a different trend compared to compressive strength. With increasing M_s, the fracture properties (Figure 3.6) and the compressive strength (Figure 3.4 (a)) peak at different values. It seems that these two properties are determined by different factors. Furthermore, they could not be modified consistently by changing M_s only. It has been reported that the K_{Ic} is mainly affected by the size, texture, and angularity of aggregate particles as well as the microstructure of the paste [15]. In previous studies, a strong correlation was also found between K_{Ic} and the fracture surface roughness (R_{fs}) of the cement paste [168], the latter being a characteristic determined by the microstructure [169]. It is plausible that the K_{Ic} and J_{tip} are also governed by different microstructures of AASF pastes and possibly the chemical composition of the reaction products. Further discussion will be given in Section 3.3.4.3.

3.3.2.2 Fracture energy based on the work-of-fracture

The fracture energy G_F, based on the work-of-fracture of all investigated AASF pastes, is shown in Figure 3.7. In most cases, mixtures with less slag exhibit higher G_F. The G_F of S30 and S50 mixtures peaks at M_s of 1.2 and 1.0, respectively. The values of G_F within the range of 6 to 15 J/m^2 are comparable to G_F values reported by Pan et al. [15]. Most of them are lower than G_F values normally found for cementitious systems (15 to 30 J/m^2) [167]. These lower values of G_F indicate that AASF pastes are inherently more brittle than their cementitious counterparts with similar compressive strength. For an ideal brittle material, G_F based on the work-of-fracture equals the crack tip toughness J_{tip}. However, the trend of G_F with increasing M_s shown in Figure 3.7 differs from that of J_{tip} Figure 3.6 (b). This is because G_F based on the

work-of-fracture not only relies on the peak load but also heavily relies on the softening curves after the peak load. The latter is very sensitive to the test configuration, the tortuosity of the crack, as well as the porosity of the specimen [164]. In fact, both the fracture energy G_F and the compressive strength of S30 and S50 pastes reached the maximum for M_s around 1.0. At this M_s value, the AASF pastes also have the lowest porosity (See Section 3.3.3.3). Despite the clear influence of the porosity, the fracture energy G_F based on the work-of-fracture still serves as a valuable parameter to evaluate the brittleness of AASF materials.

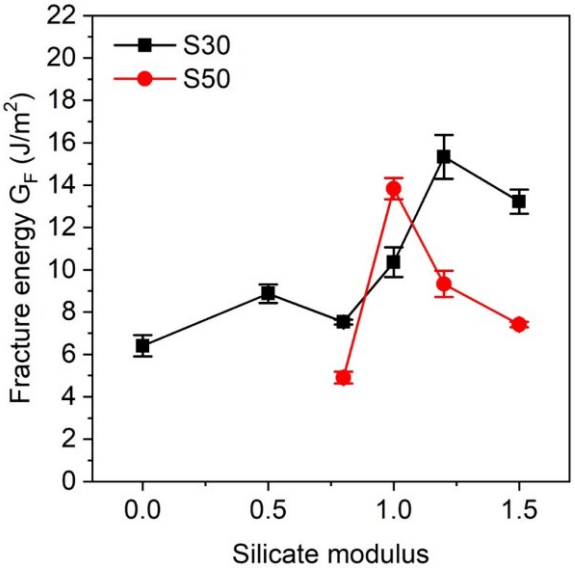

Figure 3.7 Work-of-fracture based G_F of AASF pastes at 28 days as a function of activator silicate modulus.

3.3.3 Microstructural characterization

3.3.3.1 ESEM and EDX analysis

EDX point analysis was carried out in both S30 and S50 AASF pastes at 28 days to determine the chemical compositions of the reaction products. The CaO-SiO_2-Al_2O_3 ternary diagram of S30 and S50 mixtures are plotted in Figure 3.8. The Ca, Al, and Si are normalized to 100% on an oxide basis. All EDX data points fall well in the region corresponding to C-A-S-H gel formed in alkali-activated slag (AAS) [151, 170, 171] and in AASF systems [103-105, 150, 172-174]. This finding suggests that C-A-S-H gel is the main reaction product. Considering the large amount of Na from the alkaline activator, the C-A-S-H gel should be a C-(N-)A-S-H gel due to the Na incorporation into its structure. Furthermore, no EDX data points are found anywhere near the SiO_2-Al_2O_3 axis. This suggests that EDX does not detect any signal of “pure” N-A-S-H gel. Considering the density of the reaction product, the electron beam under an acceleration voltage of 15 kV can reach about 1.0 to 2.5 µm below the sample surface [175]. The segregation of the EDX signals from the intermixed phases is rather difficult due to the limited resolution of EDX and lacking high-resolution techniques [103]. Therefore, it is not feasible to eliminate the possibility of gel intermixing of C-(N-)A-S-H, N-A-S-H, and possible (N, C)-A-S-H phases. As a result, the presence of N-A-S-H gel in the reaction product cannot be excluded completely. However, considering that the EDX signal is dominated by C-A-S-H gel, it can still be inferred from the ternary diagram that the amount of N-A-S-H gel formed in AASF paste is

insignificant in comparison to that of C-(N-)A-S-H gel. The above evidence indicates that the main reaction product in AASF pastes is C-(N-)A-S-H gel, which is in line with many previous studies [91, 103-105, 150, 176, 177]. Finally, the formation of the hydrotalcite phase rich in Al and Mg is also possible considering the high Mg in slag [91, 178].

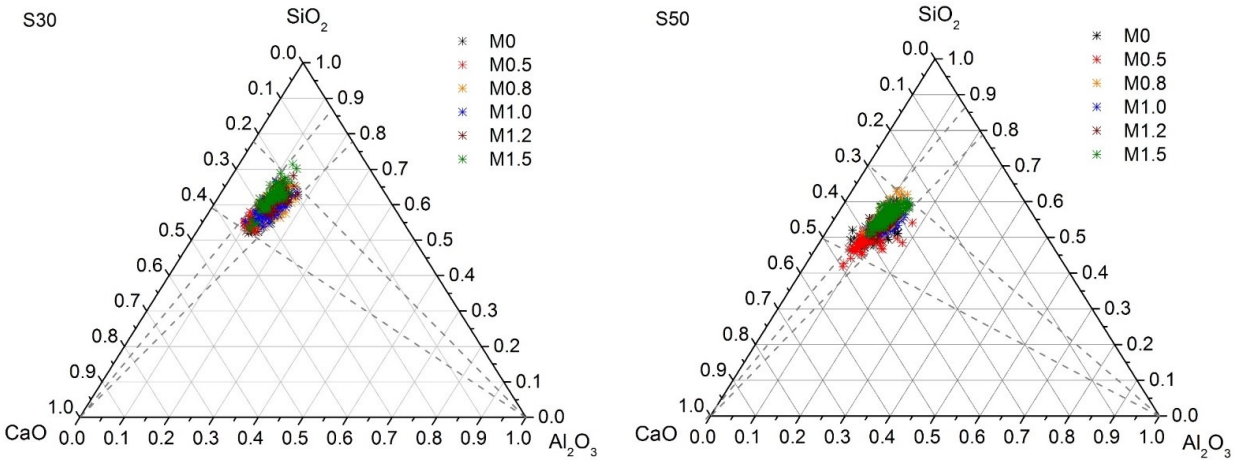

(a) S30 AASF pastes (b) S30 AASF pastes

Figure 3.8 Ternary diagram of CaO-SiO_2-Al_2O_3 of EDX spot analysis for the reaction products in (a) S30 and (b) S50 AASF pastes at 28 days.

The C-(N-)A-S-H gel contains aluminosilicate chains arranged similarly to the disordered tobermorite-like C-S-H gel [179]. The Ca/Si ratio of C-(N-)A-S-H gel is thereby used to indicate its chemical composition [180, 181]. In this study, the Ca/Si ratios were determined from the EDX analyses on flat-polished samples. The results were further examined and fitted using the simple Gaussian curve with the minimization of the least squares by Origin Software. All Ca/Si ratios of investigated mixtures fitted Gaussian distribution quite well. Two representative histograms of Ca/Si ratios in S30M1.2 and S50M1.2 are given in Figure 3.9 (a) and (b), respectively. Besides, the corresponding Ca/Si box plots are also shown. According to the central limit theorem in statistics, a good fit with Gaussian distribution indicates that the results are affected by a large number of independent random variables. In this case, the random error was induced by the experimental equipment or due to the intermixing of multiple phases in the reaction products. Consequently, the mean values of Ca/Si ratios (S30 and S50) determined by EDX analysis serve as a good approximation of the chemical composition of the main reaction products (C-(N-)A-S-H gel) in each AASF matrix.

The box plots of Ca/Si ratios of the main reaction products (C-(N-)A-S-H gel) of S30 and S50 AASF pastes are shown in Figure 3.10 (a) and (b). For the same M_s, S50 pastes always have higher Ca/Si ratios than S30 ones because more Ca is present with increasing slag content. Additionally, the average Ca/Si ratio in silicate-activated systems declines in both S30 and S50 mixtures with increasing activator M_s (0.5-1.5). Using sodium silicate in the activator brings abundant Si species in the pastes for further polymerization. As a result, the Ca/Si ratio of the reaction products decreases [182]. Notably, the mean Ca/Si ratio (in a range of 0.44-0.83) is consistent with previous studies of AASF [103, 104, 183]. Due to the presence of fly ash, the

Ca/Si ratios are also considerably lower than those of the C-(N-)A-S-H gel in sodium-silicate activated slag [174, 184].

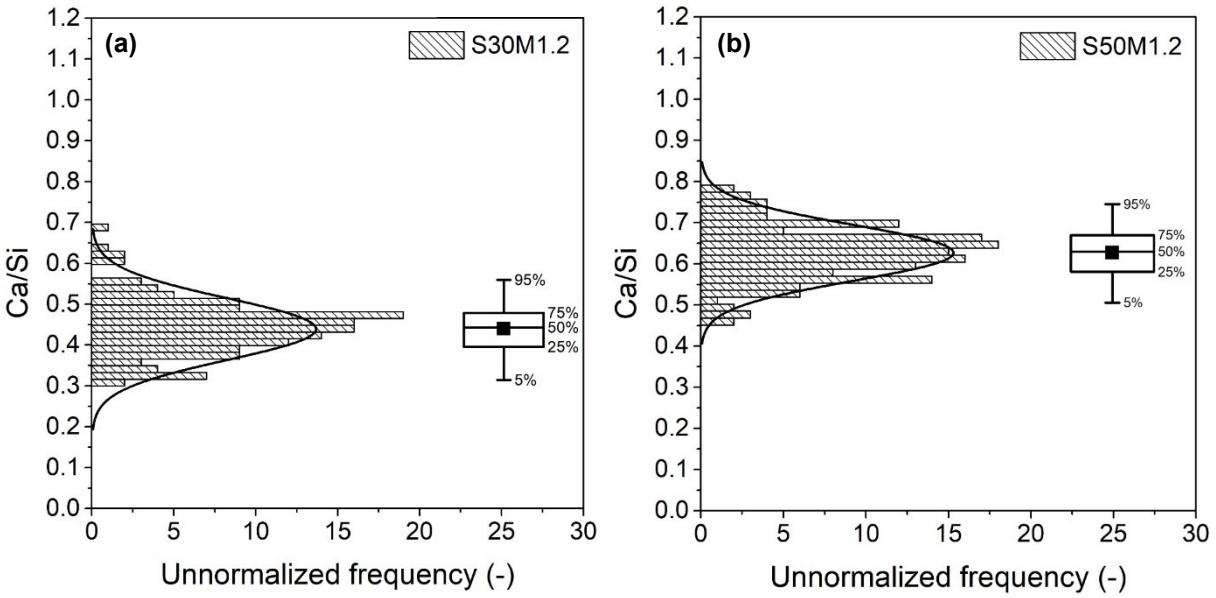

Figure 3.9 Histogram and box plot of EDX data points (Ca/Si ratio) of the reaction products in (a) S30 and (b) S50 AASF pastes at 28 days. In the box plot, the median value(-), the mean (■), the values at 25% and 75% (box edges), and the values at 5% and 95% (whiskers) are illustrated.

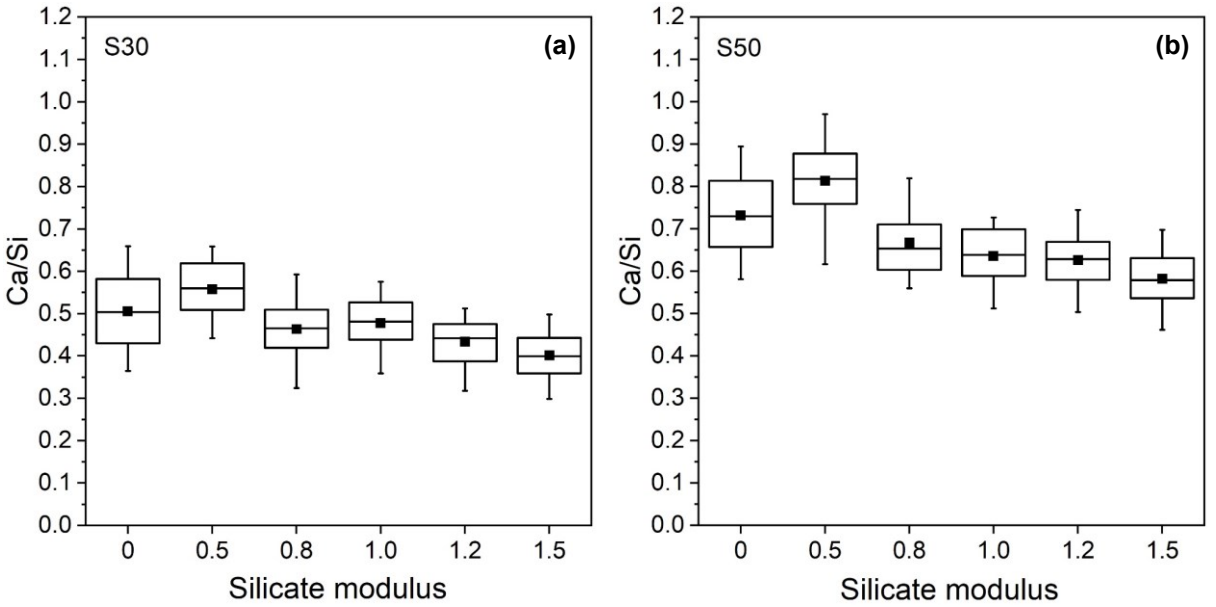

Figure 3.10 Box plot of Ca/Si ratio of main reaction products in (a) S30 and (b) S50 AASF pastes at 28 days. In the box plot, the median value(-), the mean (■), the values at 25% and 75% (box edges), and the values at 5% and 95% (whiskers) are illustrated.

Notably, the sodium hydroxide-activated systems (mixture S30M0 and S50M0), show relatively lower Ca/Si ratios than the silicate-activated systems (mixtures S30M0.5 and S50M0.5). In comparison to a sodium silicate-based activator, the sodium hydroxide-based activator with

the same Na_2O content has higher alkalinity (higher pH). At high pH, the dissolution of Ca is significantly inhibited [185, 186]. At the same time, the alkaline environment also facilitates the dissolution of Si species from solid precursors, especially from fly ash [182, 186]. These are the main reason why the reaction product in S30M0 and S50M0 mixtures has lower Ca/Si ratios.

Finally, with increasing M_s, the Ca/Si ratio of reaction products in Figure 3.10 and K_{Ic} (J_{tip}) in Figure 3.6 show a similar trend. This finding could indicate that the fracture properties of AASF are related to the chemical composition of the reaction product, for instance, its Ca/Si ratio. Further discussion will be given in Section 3.3.4.3.

3.3.3.2 FTIR analysis

The FTIR is an effective tool to study the structure of reaction products by analyzing the presence of different chemical bonds. Since any fracture process is ultimately related to the rupture of chemical bonds, the FTIR analysis can thereby help understand the fracture processes in AASF pastes.

The FTIR spectra of S30 and S50 AASF pastes at 28 days within the wavenumber range of 600 to 2000 cm^{-1} are shown in Figure 3.11 (a) and (b), respectively. Both series of spectra indicate traces of quartz as the remnant crystalline phases from fly ash particles at 777 cm^{-1} and 796 cm^{-1} [187]. The bands located near 660 cm^{-1} can be assigned to the vibrations of Si-O-Si bonds, which have fewer crosslinking or stretching vibrations than the Si-O-Al bonds [188, 189]. The peak shoulder at 893 cm^{-1} is believed to be associated with the stretching of Si–O with one non-bridging oxygen (NBO) per SiO_4 tetrahedral in both unreacted slag and fly ash [190]. In addition, the peaks at 720 cm^{-1}, 874 cm^{-1} and the relatively broad humps at 1420 cm^{-1} and 1465 cm^{-1} are associated with the presence of carbonate (CO_3^{2-}) with different vibration modes, such as $v_4[CO_3]^{2-}$ for 720 cm^{-1}, $v_2[CO_3]^{2-}$ for 874 cm^{-1}, and $v_3[CO_3]^{2-}$ for 1420 cm^{-1} and 1465 cm^{-1} [191]. Additionally, the vibration bands detected near 3400 cm^{-1} and 1650 cm^{-1} are related to the bending vibrations of molecular water and symmetric and asymmetric stretching of O-H bonds, respectively. Figure 3.11 only shows the bands near 1650 cm^{-1} (1640 cm^{-1}).

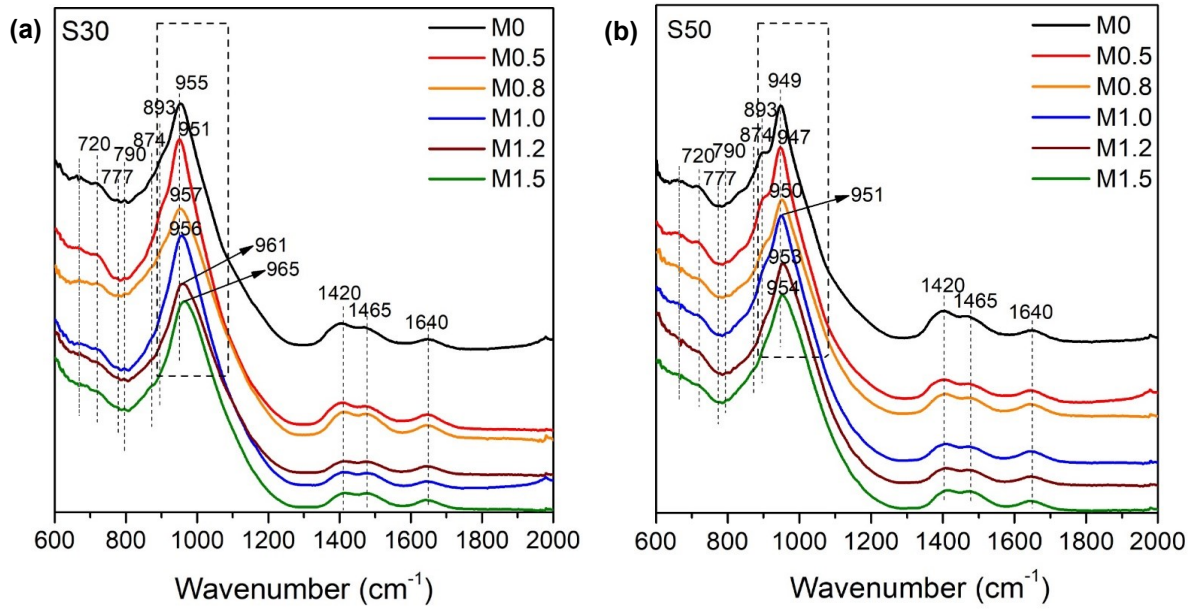

Figure 3.11 FTIR spectra of (a) S30 and (b) S50 AASF pastes at 28 days

More importantly, the overall broad band of interest is located between 800 and 1200 cm^{-1} because of phase overlapping from both precursors and reaction products. This band is widely accepted in the literature as the main T–O asymmetric stretching band and is used to study the changes in the amorphous gel structure in AAMs [91, 192-194]. Despite the influence of slag content, the main band of all spectra is centered at approximately 950 cm^{-1}. The band near this wavenumber is often related to Si–O and/or Si–O–M bonds (M being alkali metal or alkali earth metal) [195]. More specifically, it could be associated with the Si–O–Si bonds of SiO_n units (n=2) [196], representing the structure of (alumino-)silicate chains-containing C-A-S-H gel. This finding is in line with the EDX analysis and confirms the formation of C-(N-)A-S-H gel as the main reaction product in all investigated AASF systems [103-105, 150]. Additionally, the FTIR results do not show evident signals of Si-O-T (T being either Si or Al) stretching with wavenumbers higher than 1000 cm^{-1}. These signals are normally attributed to the three-dimensionally structured N-A-S-H gels within fly ash and metakaolin-based geopolymers [197, 198]. N-A-S-H gel, if treated as a zeolite precursor, is stable in a highly alkaline environment. However, it behaves pozzolanicly in cementitious systems due to the abundance of Ca [199]. Previous compatibility studies also suggest that N-A-S-H is only stable at low pH values (<12) in Ca-rich alkali-activated systems [193]. The presence of N-A-S-H together with C-A-S-H leads to the degradation of N-A-S-H and its transformation to C-A-S-H until equilibrium conditions are reached [194]. Considering the high amount of Ca^{2+} introduced by slag, the formation of N-A-S-H gel in the AASF system is thereby not favored in comparison to C-A-S-H gels [194].

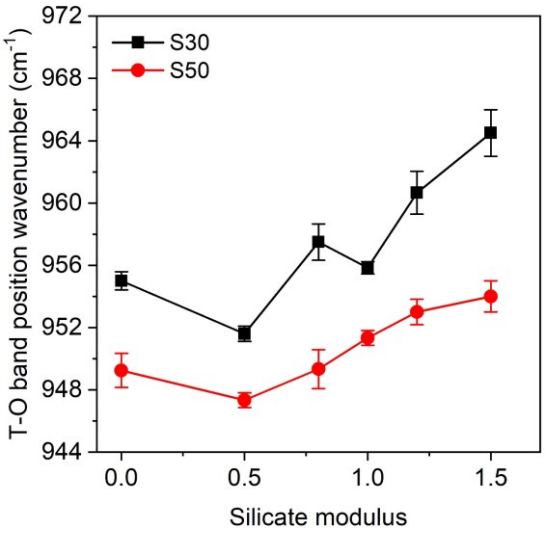

Figure 3.12 Changes in wavenumber of the main T-O band for S30 and S50 AASF pastes as a function of activator silicate modulus.

From the analysis of the main T–O band positions near 950 cm^{-1}, the shifts of the main T-O band are detected and the results are depicted in Figure 3.12. Higher slag content in AASF is in general associated with the T-O band with a lower wavenumber, which indicates a less polymerized structure of the C-A-S-H gel [198, 200]. Furthermore, the activator M_s also has a substantial influence on the position of the main T-O band of AASF paste. The wavenumber of the main T-O band increases with lower slag content but does not monotonically increase with increasing M_s. It first decreases from M_s value of 0 to 0.5 and then gradually increases.

The above-mentioned position changes could be related to (i) the different levels of Al incorporation into the reaction product; and/or (ii) the different Ca/Si ratios in the C-(N-)A-S-H gel as the main reaction product [91]. Indeed, the substitution of Si by Al in the Si-O-Si bonds in the reaction product results in the main T-O band shifting to lower numbers [91, 198, 201]. However, the first assumption is highly improbable since by increasing slag content, i.e., decreasing the fly ash content, the reactive alumina content in the binder does not change significantly. The more significant variations lie in the available Ca^{2+} content from slag and the available silica content from activator. In fact, the amount of available silica (monomer in particular) and the pH of the activator change remarkably with different activator M_s [202, 203]. The variations in the available Ca^{2+} and silica have a major influence on the early-age dissolution of solid precursors. They also effectively alter the apparent activation energy and the polymerization process of the C-(N-)A-S-H gel [176]. Eventually, C-(N-)A-S-H gel with different Ca/Si ratios is formed (Section 3.3.3.1).

From the above discussion, the shifting of the main T-O band is due to the different polymerization degrees and/or higher cross-linking of its silica network in C-(N-)A-S-H gel. In fact, the shifting of the main band to higher wavenumbers is also reported in cementitious systems as hydration proceeds. This indicates the formation of C-S-H gel and C-A-S-H gel with a higher polymerization degree and/or higher cross-linking of the silica network [91, 200] and also increases in mechanical properties [204].

Interestingly, with increasing M_s, the trend of the main T-O band position has exactly the opposite trend with the K_{Ic} and J_{tip} (Figure 3.6), as well as the Ca/Si ratio (Figure 3.10). The M0.5 mixtures with the lowest T-O band wavenumber, i.e., lowest polymerization degree, actually have the highest Ca/Si ratio as well as the highest K_{Ic} and J_{tip}. This finding contradicts the conclusions in previous studies that the intrinsic properties of C-S-H and C-A-S-H gel are higher with a higher polymerization degree [205-207]. Further discussions on the contradiction will be given in Section 3.3.4.1 and Section 3.3.4.3.

3.3.3.3 Pore structure analysis

From the preliminary study using mercury intrusion porosimetry (MIP) and other research techniques [175], we learned that AASF paste has a very fine pore structure. Capillary pores larger than 0.1 μm are hardly found, particularly not in silicate-activated systems. The nitrogen adsorption method can assess the pore size from 0.002 to 0.1 μm. It thereby matches well with the pore size range of AASF pastes.

The pore volume of S30 and S50 pastes derived from nitrogen adsorption are shown in Figure 3.13 (a) and (b), respectively. AASF paste with higher slag content shows lower cumulative pore volume with the pore size ranging from 0.002 to 0.1 μm. Furthermore, in both S30 and S50 pastes, the cumulative pore volume reaches a minimum value at M_s 0.5. The pore size distribution of S30 and S50 pastes are shown in Figure 3.13 (c) and (d), respectively. The pore structures of both pastes are finer in mixtures with higher M_s from 0 to 1.5. This is reflected by the shifts of critical pore size[4] [208] to smaller values in the pore size distribution curves.

[4] The critical pore size represents the grouping of the largest fraction of interconnected pores. It corresponds to the steepest slope of the cumulative porosity curve and the maximum in the pore size distribution curve.

Notably, the pore structure of M0 and M0.5 mixtures is dominated by capillary pores larger than 0.01 μm. In contrast, the majority of pores in M1.0 and M1.5 mixtures are gel pores smaller than 0.01 μm.

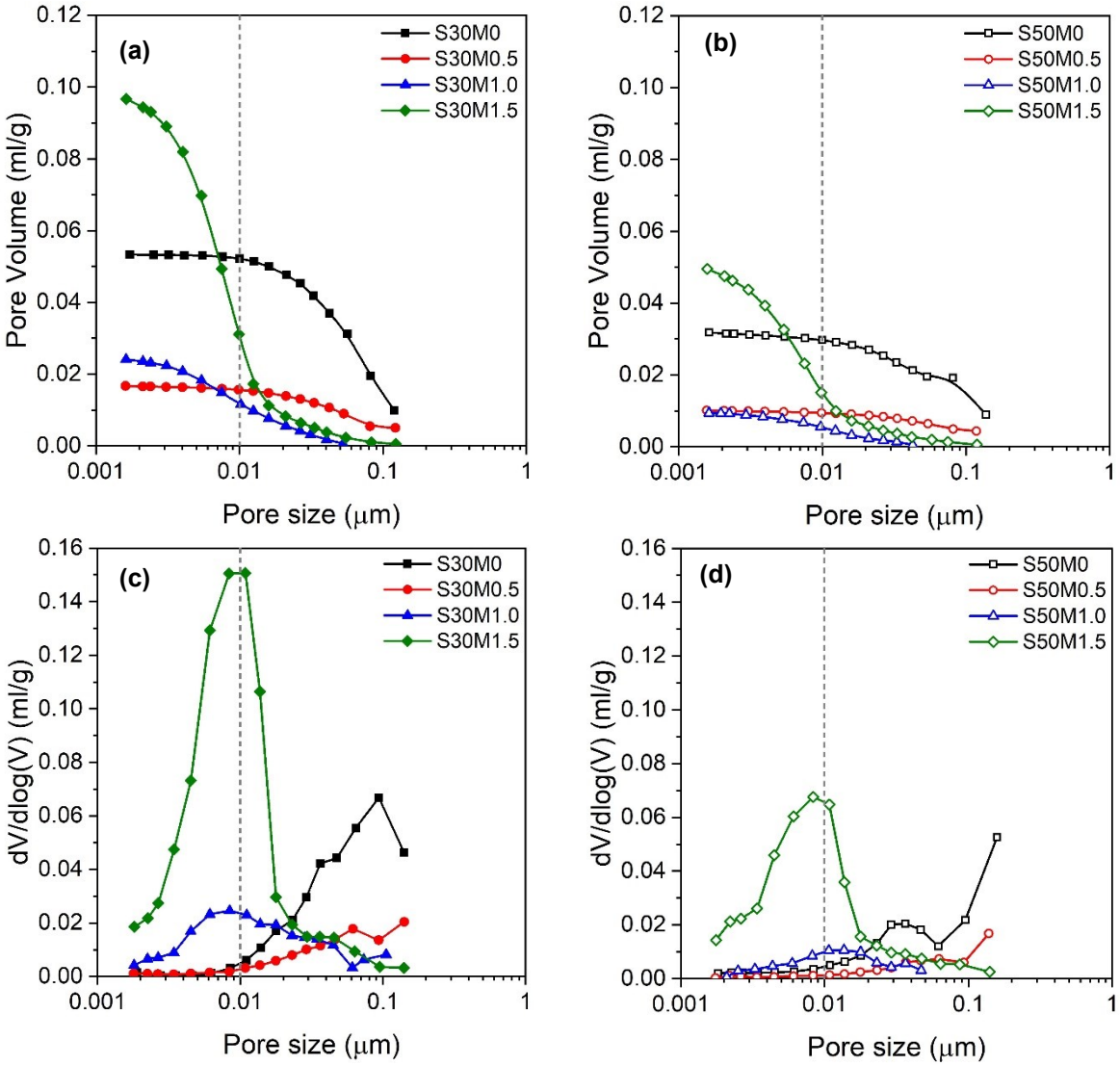

Figure 3.13 Cumulative pore volume of (a) S30 and (b) S50 AASF pastes at 28 days; pore size distribution of (c) S30 and (d) S50 AASF pastes at 28 days.

The pore volume of AASF pastes with pore size larger than 0.01 μm is shown in Figure 3.14. With increasing M_s, the trend of pore volume (>0.01 μm) coincides well with the 28-day compressive strength shown in Figure 3.4 (a). This result indicates that the capillary pores with a size above 0.01 μm have a major impact on the compressive strength of AASF pastes, which is in line with the previous study by Young et al. [209]. The strong correlation between the compressive strength and the porosity of mixtures will be further discussed in detail in section 3.3.4.2.

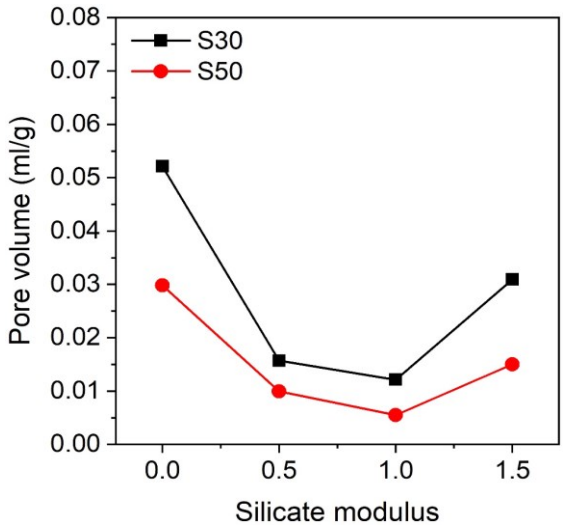

Figure 3.14 Pore volume (>0.01 µm) (a) and (b) critical pore size diameter of AASF pastes at 28 days as a function of activator silicate modulus 0, 0.5, 1.0, and 1.5.

3.3.3.4 Thermogravimetric analysis

Thermogravimetry (TG) is used to determine the amount of reaction product formed in AASF pastes at 28 days. This provides another angle to study the microstructure of AASF pastes and helps to better understand the mechanical properties, especially those depending on the porosity.

The mass loss of the reaction product is determined by TG and the corresponding differential thermogravimetry (DTG) results are presented in Figure 3.15. Since the physically bound water has been removed by the isopropanol solvent exchange, the mass loss within the range of 40 °C to 105 °C is negligible. In all AASF pastes, major DTG peaks are found between 105 and 300 °C. These peaks are associated with the decomposition of the main reaction product. Considering that C-(N-)A-S-H gel is the main reaction product (EDX analysis in Section 3.3.3.1), the mass loss within this temperature range is due to the decomposition of the C-(N-)A-S-H gel. This range has previously been found for the decomposition of C-S-H gel [210, 211] and C-A-S-H gel [194, 212] in cementitious systems, as well as C-(N-)A-S-H gel in AAS [176, 213] and AASF system [91, 103, 150].

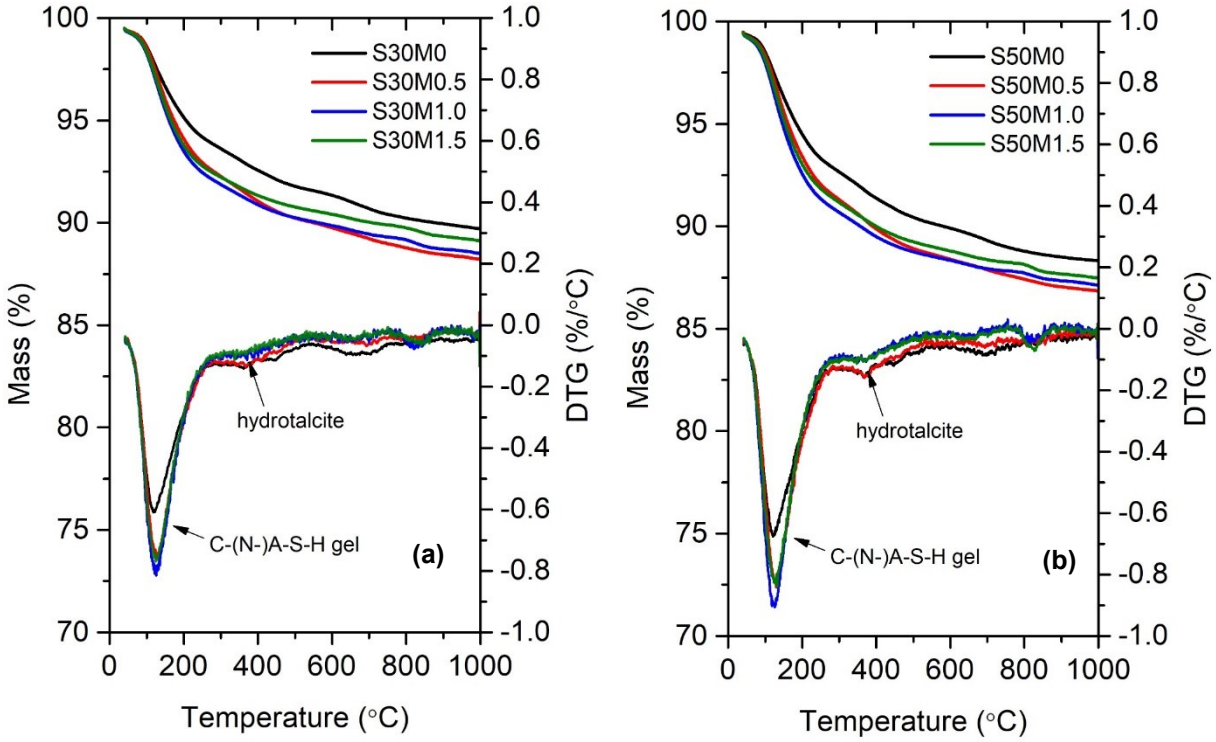

Figure 3.15 Thermogravimetric (TG) and differential thermogravimetric (DTG) curves of (a) S30 and (b) S50 paste mixtures at 28 days.

Additionally, the minor DTG peaks in Figure 3.15 at around 300 to 400 °C are attributed to the dehydration process of the hydrotalcite phase [103, 214, 215]. Its major mass loss happens due to the dehydration of the Mg-Al layer at approximately 400 °C [91, 103, 176, 177]. Finally, weak peaks observed between 500 to 800 °C are due to either the carbonate phases in the precursors or possibly the carbonation of C-(N-)A-S-H gel. Above 800 °C, new phases start to crystallize under high temperatures. This process is dominated by the formation of akermanite or other related melilite phases [216].

Considering that C-(N-)A-S-H gel is the dominant binding phase in AASF, its amount could be inferred from the mass loss from 105 to 300 °C on the thermogravimetric (TG) curves in Figure 3.15. These mass losses, which are related to the chemically bound water of C-(N-)A-S-H gel, are presented in Figure 3.16. AASF pastes with higher slag content exhibit higher mass loss at the same M_s. With increasing M_s, the mass loss first increases, peaks at M_s value of 1.0, and then decreases. This trend somehow shows similarity to that of the compressive strength of AASF pastes with increasing M_s (Figure 3.4 (a)). Further discussions will be given in Section 3.3.4.2.

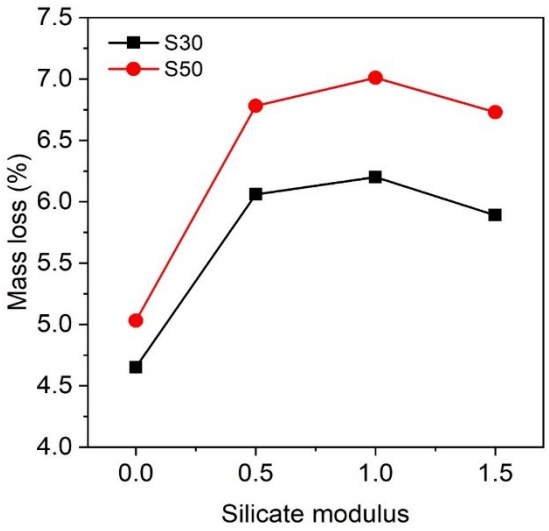

Figure 3.16 Mass loss of the main reaction products within temperature range 105 to 300 °C in AASF pastes at 28 days

3.3.4 General discussion

From the experiments, several strong correlations between microstructural properties and mechanical properties can be inferred. Although correlation does not always imply a direct causal relationship, those between microstructural aspects and the mechanical properties help us to better understand the fracture and mechanical properties of AASF. Along with references to experimental evidence and theories verified by previous researchers, the fracture mechanism of hardened AASF paste is explored and discussed.

3.3.4.1 Polymerization degree of C-(N-)A-S-H gel in AASF pastes

Clear correlations were observed between the Ca/Si ratio of the reaction products and the position of the main T-O band as shown in Figure 3.17. The position of the main T-O band, as an indication of the polymerization degree of the C-(N-)A-S-H gel, exhibits a hyperbolic decrease with an increasing Ca/Si ratio. Notably, it shares a similar trend with the mean chain length (MCL) vs the Ca/Si ratio in the previous experimental study on C-S-H by Chen et al. [217] and thermodynamics modeling C-(N-)A-S-H gel in AAS by Meyers et al. [218]. This is because the higher Ca/Si ratio normally indicates a less polymerized structure of the reaction product with shorter MCL of aluminosilicate chains (Q^2) as well as fewer crosslinking cites (Q^3) [219]. This relationship between the Ca/Si ratio and the polymerization degree of C-(N-)A-S-H has also been found for the decalcification of the carbonation in AAS and AASF pastes [183]. Together with the above-mentioned previous experimental evidence, the correlations depicted in Figure 3.17 thus strongly indicate that the polymerization degree of C-(N-)A-S-H gel in AASF pastes is also substantially governed by its Ca/Si ratio.

It should also be noted here that the observed correlation between polymerization degree and Ca/Si ratio reflects what is believed to be the intrinsic property of the C-(N-)A-S-H gel. Hence, the relationship holds for all AASF pastes in this study, regardless of the slag content and the activator M_s.

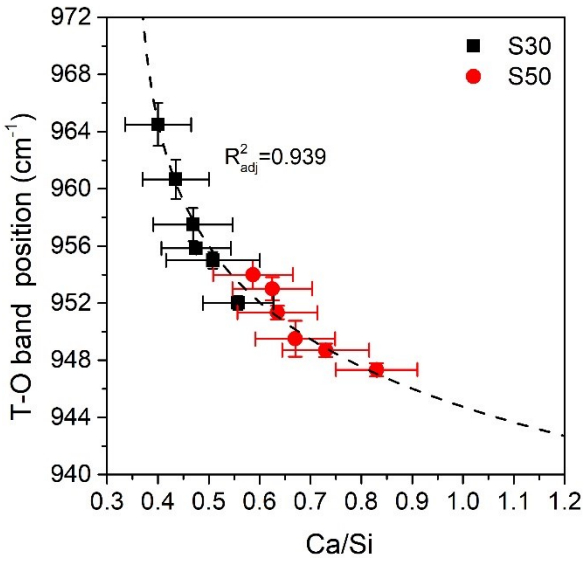

Figure 3.17 Correlations of the average Ca/Si ratio of C-(N-)A-S-H gel and the related position of the main T-O vibration band in FTIR as an indicator of the polymerization degree.

3.3.4.2 Compressive strength and the porosity of AASF pastes

The compressive strength versus porosity (>0.01 µm) relationship of AASF pastes is plotted in Figure 3.18 (a). The relationship was fitted using the Ryshkevitch exponential model [220]. A correlation coefficient R_{adj}^2 = 0.825 indicates that the compressive strength is strongly related to the porosity of AASF paste.

Furthermore, a strong linear relationship is found between the mass loss of C-(N-)A-S-H gel from 105 to 300 °C in TG tests and the compressive strength of AASF pastes. This relationship is illustrated in Figure 3.18 (b). A higher amount of C-(N-)A-S-H gel thus leads to lower total porosity and a higher gel/space ratio. This finally results in a higher compressive strength [221, 222]. Therefore, the porosity-based strength theory is appropriate to explain the compressive strength development of AASF paste [223, 224].

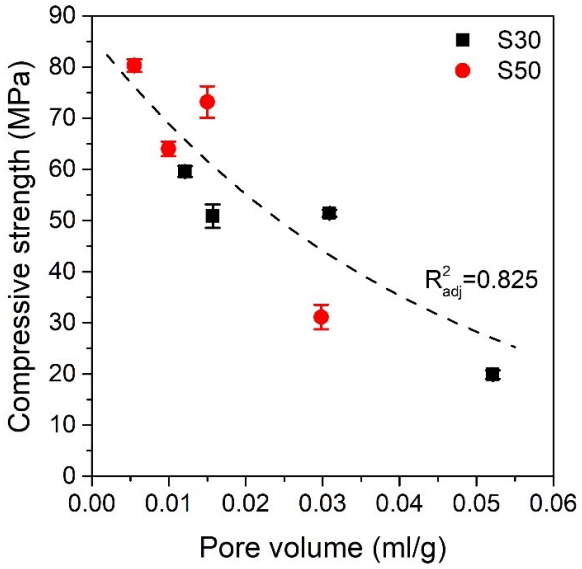

(a) compressive strength vs porosity (>0.01 μm)

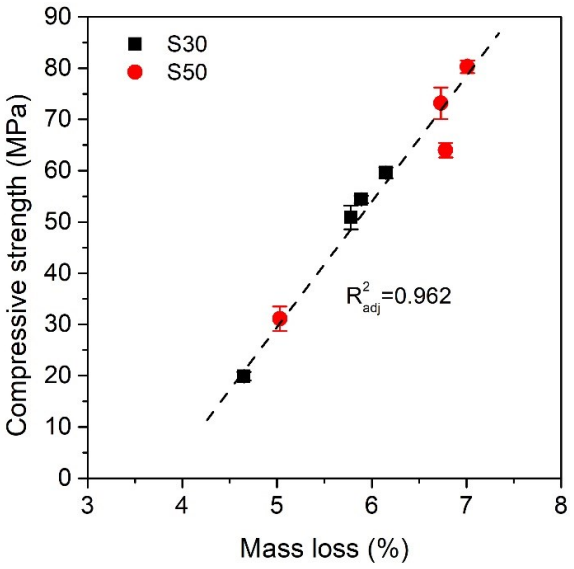

(b) the compressive strength vs the mass loss from 105 to 300 °C of the main reaction product

Figure 3.18 (a) Relationship between the compressive strength and the porosity (>0.01 μm) and (b) between compressive strength and the mass loss of the main reaction products in AASF pastes when heated from 105 to 300 °C.

3.3.4.3 Fracture properties of AASF pastes and the Ca/Si ratio of the reaction products.

In previous studies, several hypotheses have been proposed on factors that determine the mechanical properties of cementitious materials. These factors are (I) the porosity, (II) the phase assemblage, and (III) the interparticle cohesion and/or adhesion [225]. The fracture properties of AASF pastes should be determined by one or more of the above factors.

Although the porosity-based strength theory could explain the compressive strength development, it seems invalid to explain the fracture toughness K_{Ic} and crack tip toughness J_{tip}. At least, no strong correlations between the fracture properties and porosities of AASF pastes were found in this study. This suggests that the porosity is not the major factor to determine the fracture properties of AASF pastes.

The influence of phase assemblage on the mechanical properties of cementitious pastes can be assessed by the mechanical properties and chemical composition of the principal phase, i.e., the C-S-H gel [226, 227]. In AASF pastes, the C-(N-)A-S-H gel is the only principal binding phase. To study the influence of phase assemblage of AASF pastes, the fracture properties K_{Ic} and J_{tip} are plotted against the chemical composition (Ca/Si ratio) of the C-(N-)A-S-H gel in Figure 3.19 (a). Here, the Ca/Si ratio rather than the Ca/(Si+Al) ratio is used to indicate the chemical composition of C-(N-)A-S-H gel. This is to avoid the influence of Al by the unreacted precursor particles and the hydrotalcite formed as secondary reaction products. A strong linear relationship was found between K_{Ic} and the Ca/Si ratio of C-(N-)A-S-H gel in AASF pastes. Besides, Figure 3.19 (b) shows a good hyperbolic relationship between J_{tip} and the corresponding Ca/Si ratio. Both these two relationships suggest that the fracture properties of AASF pastes (K_{Ic} and J_{tip}) are positively related to the Ca/Si ratio of C-(N-)A-S-H gel.

This finding is related to the fracture properties of AASF pastes at the mesoscale. When it comes to the influence of the chemical composition (Ca/Si ratio) on the intrinsic mechanical properties of C-(N-)A-S-H gel, however, the conclusions are exactly the opposite. A lower Ca/Si ratio of C-(N-)A-S-H gel leads to a higher polymerization and/or crosslinking degree (Figure 3.17) and also a longer mean chain length (MCL) [228]. According to previous studies, C-S-H and C-A-S-H gel with longer MCL, i.e., lower Ca/Si ratios, exhibits higher nanoscale intrinsic mechanical properties, e.g., tensile strength and elastic modulus [205-207]. Such total disparity indicates that the phase assemblage does not govern the fracture properties (K_{Ic} and J_{tip}) of AASF pastes. Factors other than the chemical composition and the nanoscale structure of C-(N-)A-S-H gel seem to play more dominant roles.

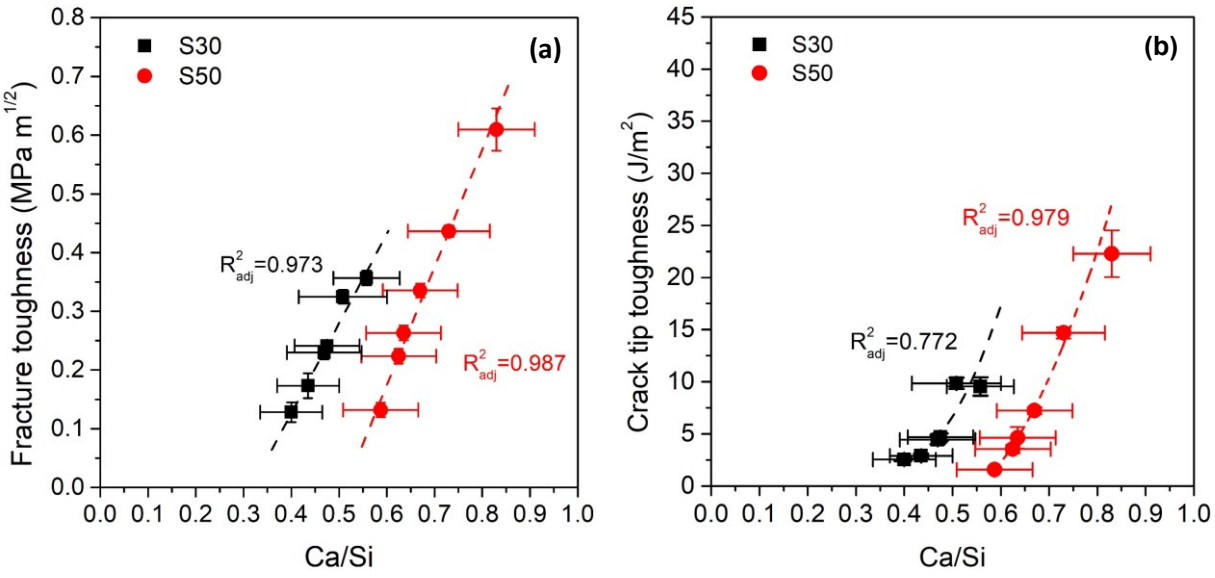

Figure 3.19 Correlation of (a) fracture toughness K_{Ic} and (b) crack tip toughness J_{tip} as a function of the Ca/Si ratio of C-(N-)A-S-H gel as main reaction products of AASF pastes.

Consequently, it is only reasonable to hypothesize that the fracture properties (K_{Ic} and J_{tip}) of AASF pastes are determined by an interparticle cohesion and adhesion-based mechanism. This could be the cohesion between the C-(N-)A-S-H gel particles (globules), and/or partially by the adhesion properties between the C-(N-)A-S-H gel particles (globules) and the remnant slag and fly ash particles [229]. The terminology “particles (globules)” used here is adopted from the colloid model of C-S-H by Jennings [230]. The above hypothesis is supported by indirect experimental evidence as well as verified theories by previous researchers [229, 231]. Both the cohesion and/or the adhesion have also been experimentally confirmed using atomic force microscopy [232] and zeta potential measurements [233]. In AASF pastes, these interactions are believed to be similar to those between C-S-H particles (globules) in cement pastes. Treating the surface of C-(N-)A-S-H gel particles as homogeneously charged walls, the strong interaction is a result of ion-ion interactions caused by very high negatively charged C-(N-)A-S-H gel particles and the presence of Ca^{2+} as divalent counterions [229, 232]. Based on this, a schematic representation of cohesion between C-(N-)A-S-H gel particles is illustrated in Figure 3.20. C-(N-)A-S-H gel with a higher Ca/Si ratio also has a higher negatively surface charge density [234]. This effectively enhances the cohesion between the C-(N-)A-S-H gel particles under the presence of freely moveable Ca^{2+} ions. Consequently, C-(N-)A-S-H gel with

a higher Ca/Si ratio has a higher resistance to crack initiation and propagation process, which is reflected by the higher K_{Ic} (J_{tip}) of AASF pastes.

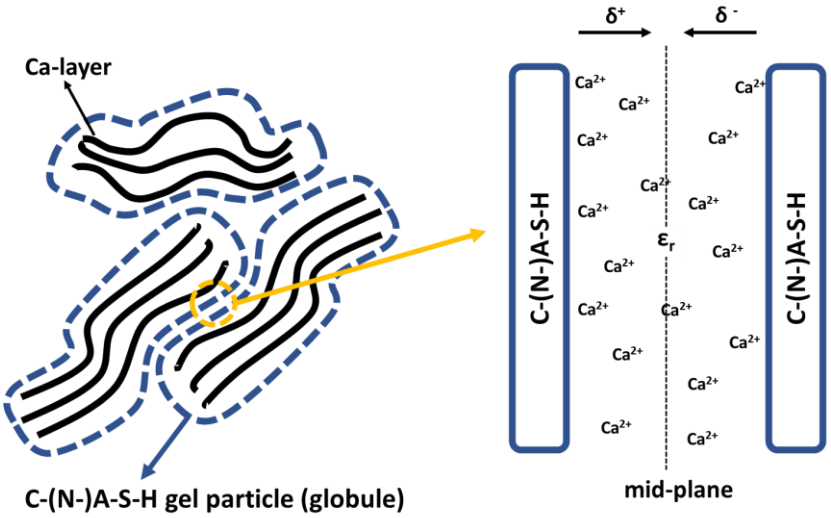

Figure 3.20 Schematic representation of cohesion mechanism between C-(N-)A-S-H particles (globules). Their atomic structure is ignored and represented by uniformly charged walls separated by a dielectric continuum in which Ca^{2+} cations are free to move (adopted from [235]).

Furthermore, the unreacted precursor particles, mainly crystalline quartz and mullite phases in fly ash particles, have similar surface charge properties as C-S-H [233, 236]. Based on this, the adhesion between C-(N-)A-S-H gel particles and unreacted precursor particles, like the cohesion between C-(N-)A-S-H gel particles, is also enhanced with increasing Ca/Si ratio. This has been confirmed in previous studies on the adhesion between filler (quartz) and C-S-H gel particles [233]. Still, it is worth noting here that the gel porosity (<0.01 μm) of C-(N-)A-S-H gel could affect the cohesion and adhesion because the gel pores and the elementary C-(N-)A-S-H gel particles have similar size [237]. However, the correlation between the K_{Ic}(J_{tip}) and the gel porosity (<0.01 μm) is much weaker than that between the K_{Ic}(J_{tip}) and the Ca/Si ratio of C-(N-)A-S-H gel. Consequently, cohesion and adhesion are still considered the dominating mechanism for fracture properties of AASF pastes.

Finally, the relationship between Ca/Si ratio and K_{Ic} (J_{tip}) gives guidance on how to change the fracture properties by modification of the mixture design. These modifications could be achieved by changing the activator M_s (Si) as well as the slag content (Ca). To fully substantiate the hypothesized cohesion and adhesion-based mechanism, molecular dynamics (MD) simulations and direct measurements of ion-ion correlation interactions between C-(N-)A-S-H particles (globules) as well as C-(N-)A-S-H particles (globules) and remnant precursor particles are recommended for future research.

3.4 Observations and conclusions

This chapter presents an experimental investigation of the fracture properties and microstructure formation of hardened AASF pastes. The paste mixtures were prepared with different slag/fly ash mass ratios and silicate modulus (M_s) of the alkaline activator. Strong

correlations between the chemical composition (Ca/Si ratio) of the reaction product and fracture properties of AASF pastes were identified. The following observations and conclusions are given:

- A higher slag content is beneficial for the mechanical properties of AASF pastes, including compressive strength, elastic modulus, as well as fracture toughness K_{Ic} and crack tip toughness J_{tip}.

- In comparison to the sodium hydroxide-based activator (M_s=0), the sodium silicate-based activator (M_s=0.5-1.5) effectively enhances the mechanical properties of AASF. However, AASF pastes with increasing alkaline activator M_s do not show a monotonic increase in mechanical properties. The optimal activation condition is achieved by using moderate M_s (0.5-1.0).

- The compressive strength of AASF pastes exhibits a clear correlation with the capillary porosity (>0.01 μm) and the amount of reaction product, supporting that the empirical porosity-based strength theory is valid for AASF pastes.

- In slag/fly ash-based AASF pastes, the main reaction product is C-(N-)A-S-H gel. No significant amount of N-A-S-H gel is formed.

- The polymerization degree of C-(N-)A-S-H gel, reflected by the position of the main T-O band of AASF paste, is substantially governed by the Ca/Si ratio of the gel.

- Very strong positive correlations are identified between the Ca/Si ratio of C-(N-)A-S-H gel and the fracture properties K_{Ic} (J_{tip}).

- The fracture properties K_{Ic} (J_{tip}) of AASF pastes are not governed by the intrinsic mechanical properties of the C-(N-)A-S-H gel. Rather, they are most probably dominated by interparticle cohesion and adhesion, either by the cohesion between the C-(N-)A-S-H gel particles (globules), and/or partially by the adhesion properties between the C-(N-)A-S-H gel particles (globules) and the remnant slag and fly ash particles.

The fracture properties of AASF pastes studied in this chapter are crucial for determining the composite behavior of strain-hardening geopolymer composite (SHGC). The other set of important factors relates to the interface bonding between the fiber and AASF matrices, which will be further studied in Chapter 4. This chapter provides promising guidance for the design and modification of the fracture properties of AASF pastes. Furthermore, it also contributes to the development of SHGC in Chapter 6.

Chapter 4

Experimental characterization of polyvinyl alcohol (PVA) fiber/matrix interface properties[5]

4.1 Introduction

Besides the fracture properties of the matrix studied in Chapter 3, the interface properties of PVA fiber in the alkali-activated slag/fly ash (AASF) matrix also determine the composite behavior. Therefore, a better understanding of the interactions between PVA fiber and AASF matrix helps the development of fiber-reinforced composites, such as strain-hardening geopolymer composite (SHGC). However, most previous studies on the PVA fiber/matrix interface properties were conducted in cementitious systems. Studies concerning the interface properties of PVA fiber in AASF are still rare. Only a few experimental studies on the interface bonding properties of PVA fiber in alkali-activated matrices could be found [21, 23, 130]. All the above-mentioned studies focused on the interface bonding properties by single-fiber pullout tests [46, 138, 139]. In these studies, the influence of the reaction product chemistry on the interface bonding properties was usually neglected. Furthermore, the studies on the interfacial transition zone (ITZ) between the PVA fiber and AASF matrix have been rarely reported. Since the main reaction products in a cementitious matrix and an alkali-activated matrix are not the same, the influence of reaction product chemistry on the interface properties of PVA fiber, as well as its interaction mechanism with the AASF system, is worth to be studied in more depth.

In this chapter, the execution and the results of a systematic experimental study of the interface properties of PVA fiber in AASF matrices are presented. The interface bonding properties concerning chemical bonding energy G_d, initial frictional bond τ_0, and slip-hardening coefficient of PVA fiber to the AASF matrix were systematically investigated using single fiber pullout tests. The influence of PVA fiber on the microstructure of the ITZ and the chemical composition of the reaction products within the ITZ were characterized and discussed. Furthermore, the relationship between G_d and the chemical composition of the reaction products, the origin of the initial frictional bond, and the mechanism of the slip-hardening behavior were discussed. The experimental findings described in this chapter provide a basis for the molecular dynamics study on the adhesion mechanism of PVA fiber to the AASF matrix (Chapter 5) and also generate important input for micromechanics-guided development of SHGC (Chapter 6).

[5] This chapter is based on:

Zhang, S., He, S., Ghiassi, B., van Breugel, K., & Ye, G. Interface properties of polyvinyl alcohol (PVA) fiber in alkali-activated slag/fly ash pastes. Manuscript in preparation.

4.2 Materials and methods

4.2.1 Materials

The solid precursors used in this chapter were the same as in Chapter 3. Their chemical and physical properties were given in Section 3.2.1. The polyvinyl alcohol (PVA) fiber (RECS 15, Kuraray) with 1.2% oiling treatment on the surface was used. The chemical structure of the PVA fiber is shown in Figure 4.1. The PVA polymer is primarily composed of the vinyl group (C-OH) with a minor content of the acetate group (C-OCOCH3). According to the supplier, the acetate group is introduced by the synthesis process, although it is the vinyl group that determines the surface property of the fiber.

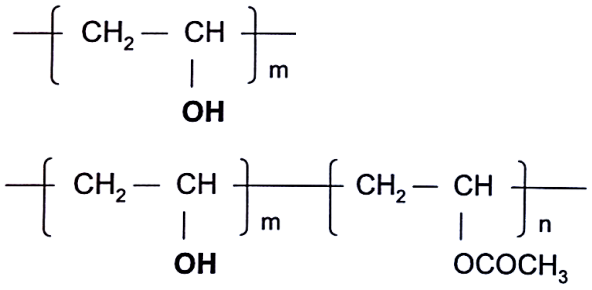

Figure 4.1 Structure of PVA polymer according to the fiber supplier

The physical and mechanical properties of PVA fiber are presented in Table 4.1. A filament-type PVA fiber with a diameter of 40 μm was used to test the interface bonding properties. For better characterization of the ITZ, PVA fiber with a diameter of 300 μm was used. The alkaline activator was a sodium-based silicate solution prepared by dissolving NaOH pellets (analytical grade, purity≥98%) and sodium silicate (Na_2O: 8.25 wt.%, SiO_2: 27.50 wt.%) in distilled water. The activator solution was cooled down to room temperature before mixture preparation.

Table 4.1. Physical and mechanical properties of PVA fiber

Fiber	Diameter (μm)	Density (g/cm^3)	Length (mm)	Strength (MPa)	Elastic modulus (GPa)
PVA	40, 300	1.30	Filament	1640	41.1

4.2.2 Mixture design

The chemical composition and microstructure of AASF matrices have been investigated already in Chapter 3. The same mixture designs are used for the matrix for studying the fiber/matrix interface bonding properties (See Table 3.3).

4.2.3 Determination of interface bonding properties

The interface bonding properties of PVA fiber AASF matrices were tested experimentally by single-fiber pullout tests with the set-up also used by Redon et al [138]. The set-up is shown in Figure 4.2 (a). A mold equipped with two-layer polyethylene bricks developed by Katz and Li [136] was used. A PVA fiber was cut, aligned, and fixed onto the PE brick using double-sided tape. Then, the fresh AASF paste was poured around the fibers. The specimens were put on a vibration table to remove entrapped air before sealing them with plastic wrap. After 24 hours, the specimens were demolded and transferred to a climate room (20°C and 95% RH) until 28 days. At 28 days, the hardened specimens were cut into very thin sliced samples using a low-speed saw (Minitom, Struers). As shown in Figure 4.2 (b), the cutting leaves the fiber on one side of the sample. The thickness of the sample, i.e., the embedded length (L_e) of PVA fiber, was approximately 1 mm, which is short enough to avoid fiber rupture during the fiber pullout process.

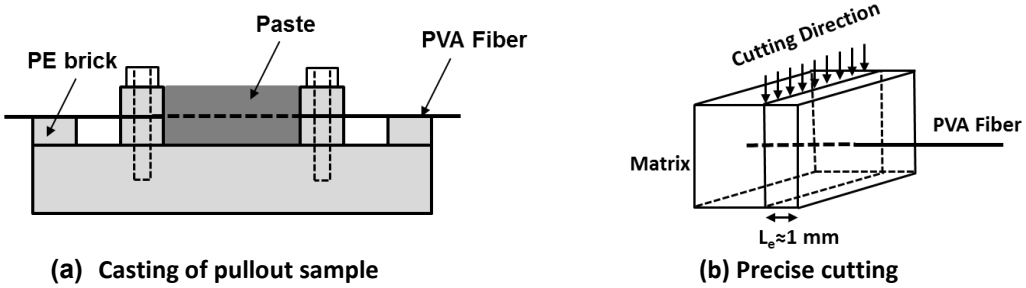

Figure 4.2 Pullout sample preparation methods: (a) casting and (b) precise cutting.

For the single-fiber pullout tests, a micro tension-compression testing device (manufactured by Kammrath & Weiss) was used as shown in Figure 4.3. Both the surface of the thin-sliced sample and the free end of the PVA fibers were glued to two small metal blocks. The fiber is aligned vertically to the matrix surface to avoid the influence of matrix spalling on the testing result. A hex nut was applied in between the cut surface and the metal block to avoid gluing the fiber ends onto the cut surface. Then, the two metal blocks with the pullout sample were mounted on the testing device and were further fixed to an actuator and a load cell. A 10 lb (44.48 N) load cell was used to measure the pullout load with an accuracy of 0.1%. The pullout tests were conducted using displacement control. A constant displacement rate of 0.01 mm/s was used to avoid fiber rupture while revealing information about the frictional force. At least 20 tests were conducted for each fiber/matrix combination.

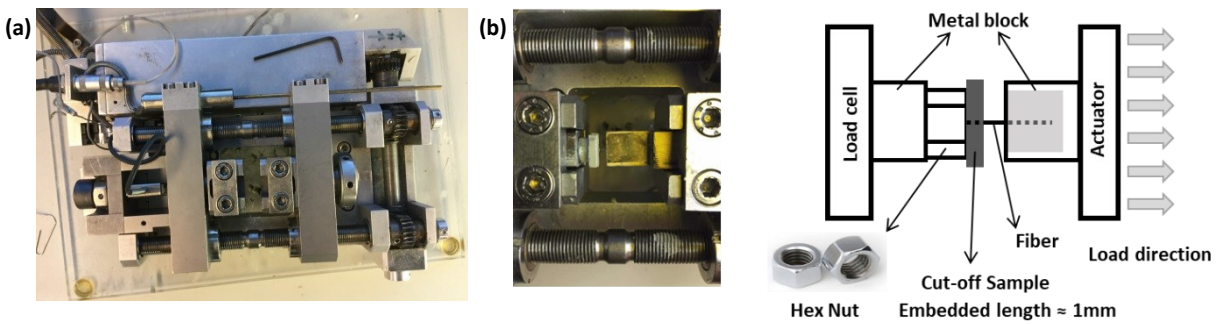

Figure 4.3 Single-fiber pullout test: (a) Micro tension-compression device, (b) schematic tests set-up.

As shown in Figure 4.3 (b), the fiber has a free segment of approximately 1 mm between the actuator and the pullout sample. Although this free length could influence the pullout displacement measurement due to the elastic deformation of the fiber, the displacement readings do not need any corrections. This is because of the following two reasons: (i) the chemical bonding and initial frictional bond are calculated using only pullout load readings; and (ii) the calculation of the slip-hardening coefficient requires both pullout load and displacement readings, but it only uses the later portion of the pullout curve when the elastic stretching of the free fiber segment has already attained its final value.

4.2.4 Microstructural characterizations

The microstructure and the chemical compositions of reaction products in AASF bulk matrices and the ITZ around PVA fiber were characterized. All characterizations were conducted at 28 days using environmental scanning electron microscopy (ESEM) and energy dispersive X-ray (EDX) analysis. An ITZ thickness of approximately 30 µm was assumed. This thickness is considered appropriate to study the influence of PVA fiber on the reaction product formation at the fiber/matrix interface (see also [238]).

For the characterization of the reaction product composition in AASF bulk matrices, mixtures including S30M0-M1.5[6] were used. The element distribution of reaction products in the ITZ around a PVA fiber was only studied on S30M1.2 and S50M1.0 samples. The samples were prepared following the method for single fiber pullout tests as described in Section 4.2.3.

Before the ESEM/EDX tests, the chemical reaction in hardening pastes was stopped by solvent exchange using isopropanol. After vacuum drying, the samples were impregnated using low viscosity epoxy resin. After the hardening of the epoxy resin, the samples were polished until reaching a surface roughness of 0.25 µm. Backscattered electron (BSE) images and secondary electron (SE) images were taken at an accelerating voltage of 15 kV and 5 kV, respectively. The polished samples were coated and then the EDX measurements were conducted at an accelerating voltage of 15 kV in the high vacuum mode.

The ESEM/EDX-based spectral imaging (SI) was performed to study the chemical compositions of the reaction products. Both EDX spot analysis and line analysis were carried out. In each EDX measurement, corrections on the characteristic X-ray intensity were made by taking into account the atomic number, absorption, and fluorescence excitation effect. These corrections convert apparent concentrations (raw intensities) into corrected concentrations to eliminate inter-element matrix effects.

The automated phase mapping was used to study the different phases formed in the ITZ. For this purpose, the COMPASS™ as a built-in function in the Pathfinder software (Thermo Fisher Scientific) was applied. The phase mapping is based on the analysis of spectral imaging (SI) data using principal component analysis (PCA). With a multivariate statistical approach, COMPASS analyzes the spectrum at each pixel location and groups the pixels with similar spectra together into principal components [239]. These principal component maps are translated into phase maps using the same types of intensity threshold algorithms used for traditional element-based phase mapping. The phase spectrum is thus the summation of the

[6] For sample notation, see Table 3.2.

spectra from each pixel within the phase [239, 240]. The final results are a list of chemically unique phase spectra and phase maps. In this way, the hidden phases could be also revealed, regardless of the inevitable intermixing of the phases and the noise signals from unreacted precursor particles [241]. For one automated phase mapping analysis, 300 frames of EDX element mapping were taken on the selected area containing both the PVA fiber and the ITZ.

4.3 Results and discussions

4.3.1 PVA fiber/matrix interface bonding properties characterization

4.3.1.1 Single-fiber pullout behavior

The single-fiber pullout behavior, i.e., the load-displacement relationship of PVA fibers embedded in the AASF matrix, is shown in Figure 4.4. The PVA fiber debonding and pullout behavior in the AASF matrix is similar to that of PVA fiber in the cementitious matrix [138, 242].

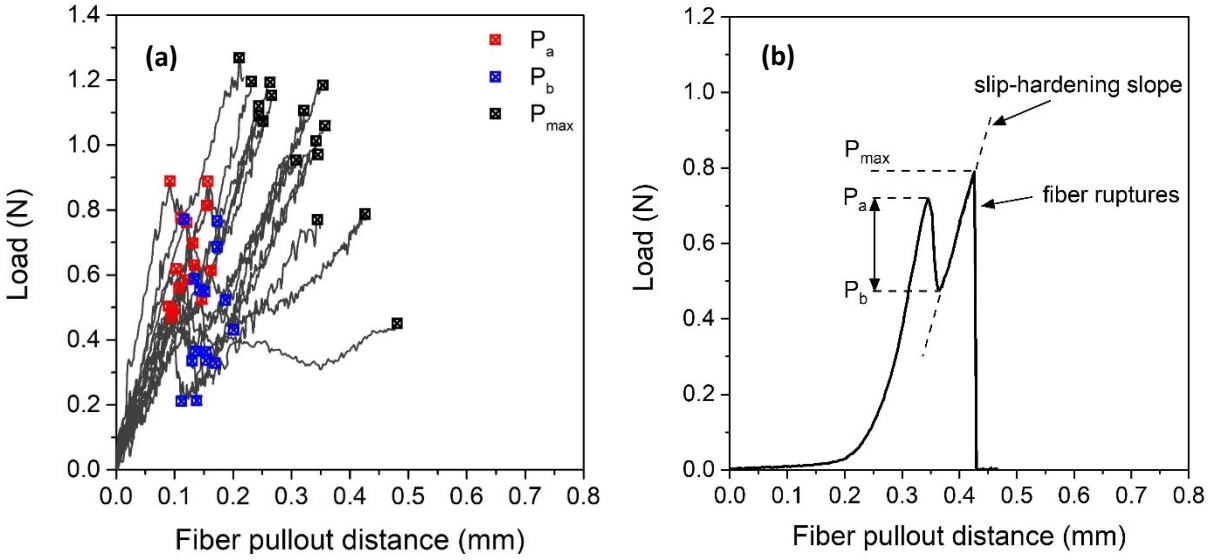

Figure 4.4 (a) Representative pullout curve of PVA fiber in AASF matrix; and (b) schematic illustration of fiber pullout process.

As illustrated in Figure 4.4, the general profile of a single-fiber pullout curve can be decomposed into three main regimes [138]. Initially, a stable debonding process occurs along the fiber/matrix interface. In this process, the load increases up to P_a until the moment when the debonded length equals the fiber embedded length. Then, the fiber was debonded over its entire length, but the fiber end was not yet moving. At this point, the displacements consisted of only the elastic stretching of the debonded fiber segment and the free length of the fiber. Finally, the fiber starts to slide in the slippage phase from load P_b. From this point onwards, the pullout is resisted by frictional forces only. In the majority of cases of PVA fiber pullout, the friction force increases linearly with increasing pullout distance up to the maximum load P_{max} before the fiber ruptures. The increasing pullout resistance is referred to as the slip-hardening effect and is characterized by the slip-hardening coefficient β (β>0) [142].

To quantitatively determine the interface properties, the chemical bonding energy G_d, initial frictional bond τ_0, and slip-hardening coefficient β were derived from the single fiber pullout curves with Equations (2.7) to (2.9). All these equations are derived from a fiber debonding/pullout model by Lin et al. [143]. In formula form:

$$G_d = \frac{2(P_a - P_b)^2}{\pi^2 E_f {d_f}^3} \tag{4.1}$$

$$\tau_0 = \frac{P_b}{\pi d_f L_e} \tag{4.2}$$

$$\beta = \frac{d_f}{L_e}\left(\frac{(\Delta P/\Delta S\,|\Delta S \to 0)}{\pi \tau_0 d_f} + 1\right) \tag{4.3}$$

where E_f, d_f, and L_e are the elastic modulus, diameter, and embedded length of PVA fiber respectively. $\Delta P/\Delta S$ is the initial slope of the pullout load P vs displacement S. P_a is the load at the moment when the fiber is fully debonded (debonded length L_d = embedded length L_e) and P_b is the load when the fiber begins to slip. The results of all calculated interface bonding properties are given in Table 4.2.

Table 4.2 PVA fiber/matrix interface bonding properties

Interface	Chemical bonding energy G_d (J/m^2)	Initial frictional bond τ_0 (MPa)	Slip-hardening coefficient β
S30M0	2.77±1.11	2.13±0.77	0.31±0.01
S30M0.5	4.01±1.41	3.38±1.03	0.42±0.08
S30M0.8	1.97±0.92	1.81±0.78	0.33±0.11
S30M1.0	3.12±1.26	3.00±0.76	0.39±0.12
S30M1.2	2.86±1.08	4.01±1.16	0.26±0.09
S30M1.5	2.53±1.04	3.13±0.90	0.25±0.06
S50M0	4.61±1.21	2.29±0.56	0.34±0.05
S50M0.5	6.15±1.49	4.09±1.14	0.43±0.08
S50M0.8	4.92±1.27	3.22±0.81	0.47±0.13
S50M1.0	3.74±1.31	3.41±0.84	0.44±0.10
S50M1.2	3.29±1.34	3.21±0.82	0.40±0.08
S50M1.5	2.62±0.88	2.96±0.97	0.35±0.09

4.3.1.2 Chemical bonding energy G_d

According to previous studies, the debonding process in the fiber pullout test is assumed to be a tunnel crack propagation along the fiber/matrix interface. The pullout of the fiber is resisted by the debonding fracture energy of the tunnel-shaped crack [143]. The fracture energy is also known as the chemical bonding energy G_d between PVA fiber and matrix and is calculated with Equation (2.7) [138]. The chemical bonding energy G_d of PVA in S30 and S50 AASF

matrices is presented in Figure 4.5 (a) and (b), respectively. Similar to what has been found in previous studies, the standard deviations (STDs) for G_d are relatively large. They generally fall between 25% to 40% of the mean value of G_d. Such large STDs are the result of the heterogeneity of reaction products around PVA fibers.

The plot of the average values of G_d versus the activator silicate modulus (M_s) shows a clear trend (Figure 4.5). The values of G_d vary from 2.0 to 4.0 J/m^2 in S30 matrices and from 2.6 to 6.2 J/m^2 in S50 matrices with the activator silicate modulus ranging from 0 to 1.5. Knowing that the G_d normally ranges from 1 to 2 J/m^2 [139] in conventional strain-hardening cementitious composite (SHCC) and from 0.5 to 1.5 J/m^2 in high-volume fly ash SHCC [46], the chemical bonding of PVA fiber (with 1.2% oiling) in AASF matrices is stronger than those reported in cementitious systems. In fact, the average values of G_d in SHGC matrices are generally 1.5 to 2.5 times higher than those in conventional SHCC [46, 139, 141].

The S50 mixtures have higher chemical bonding energy G_d than S30 mixtures. This effect is more prominent at lower activator silicate moduli (M_s). Furthermore, in both S30 and S50 matrices, G_d first increases, peaks at M_s of 0.5, and then gradually decreases (despite the anomaly found in S30M0.8).

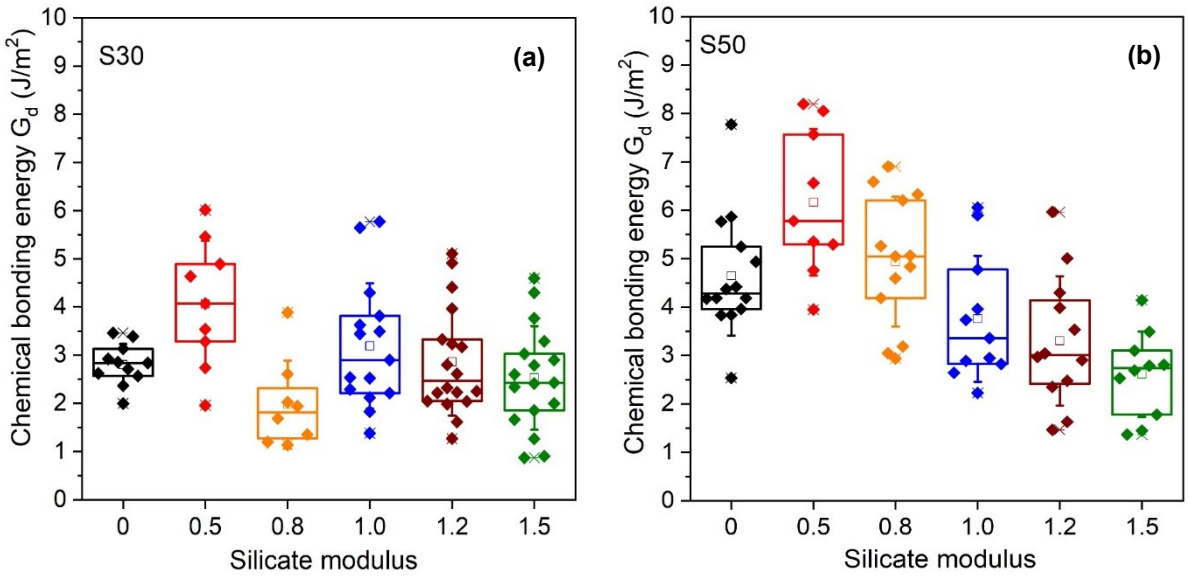

Figure 4.5 Box plot of chemical bonding energy (G_d) of PVA fiber in (a) S30 and (b) S50 AASF matrices with different activator silicate modulus. The box plot illustrates the median value (-), the mean (□), the values at 25% and 75% (box edges), and the standard deviation (Whiskers). Each of the box plots is derived from at least 16 individual pullout tests.

4.3.1.3 Initial frictional bond τ_0

The initial frictional bond τ_0, calculated with Equation (4.2), stands for the friction between the PVA fiber and the matrix. As shown in Figure 4.6, the initial friction bond τ_0 for AASF mixtures for M_s from 0 to 1.5 follows a somewhat different trend than G_d. It reaches a maximum value for S30 mixtures at M_s1.2 and S50 mixtures at M_s 0.5. Notably, the average τ_0 is found to be about 2 to 3 times higher than those in cementitious systems [46, 141].

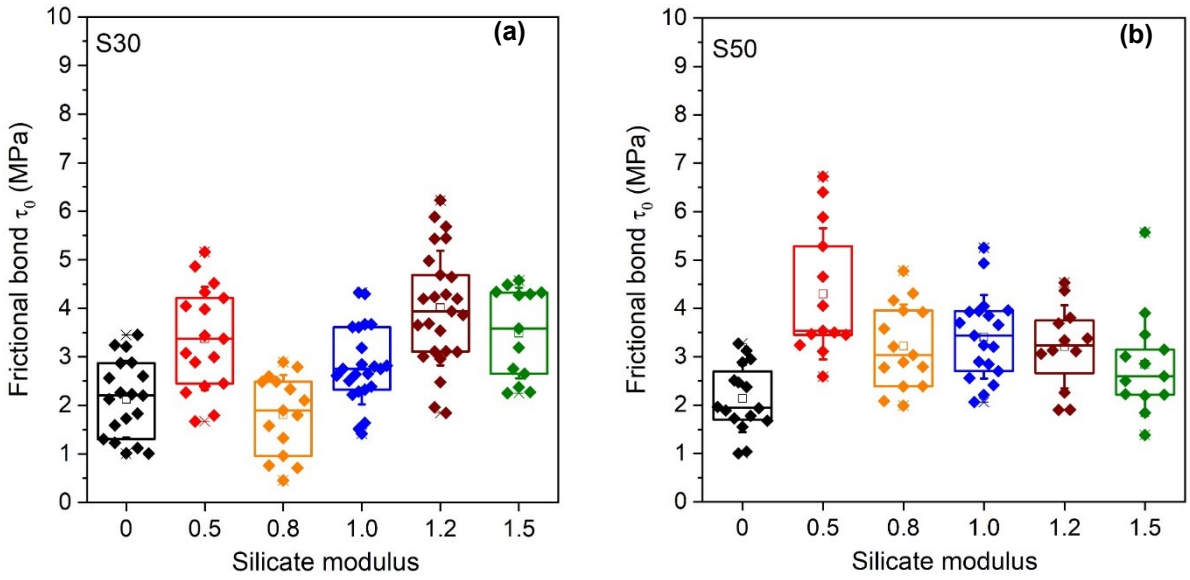

Figure 4.6 Box plot of the initial frictional bond (τ_0) of PVA fiber in (a) S30 and (b) S50 AASF matrices with different activator silicate modulus. The box plot illustrates the median value (-), the mean (□), the values at 25% and 75% (box edges), and the standard deviation (Whiskers). Each of the box plots is derived from at least 16 individual pullout tests.

4.3.1.4 Slip-hardening coefficient β

The slip-hardening effect is indicated by the slope of the pullout load versus displacement curve (Figure 4.4), while the slip-hardening coefficient β is calculated with Equation (4.3). A significant slip-hardening is beneficial for steady-state crack propagation and can reduce the critical fiber volume required for multiple-cracking (strain-hardening) of the composite [142].

The slip-hardening coefficients β of the AASF S30 and S50 mixtures are shown in box plots in Figure 4.7 (a) and (b), respectively. The average values of β are in a range of 0.26-0.42, which are much lower than those found in conventional SHCC (1.15) [139] and high volume fly ash-based SHCC (0.58-0.63) [80]. The average values of β in the S30 series in Figure 4.7 (a) show a similar trend as the chemical bonding energy G_d and the fracture toughness K_{Ic} (J_{tip}) in Figure 3.6. The average values of β in the S50 series in Figure 4.7 (b), however, do not reveal such clear similarities.

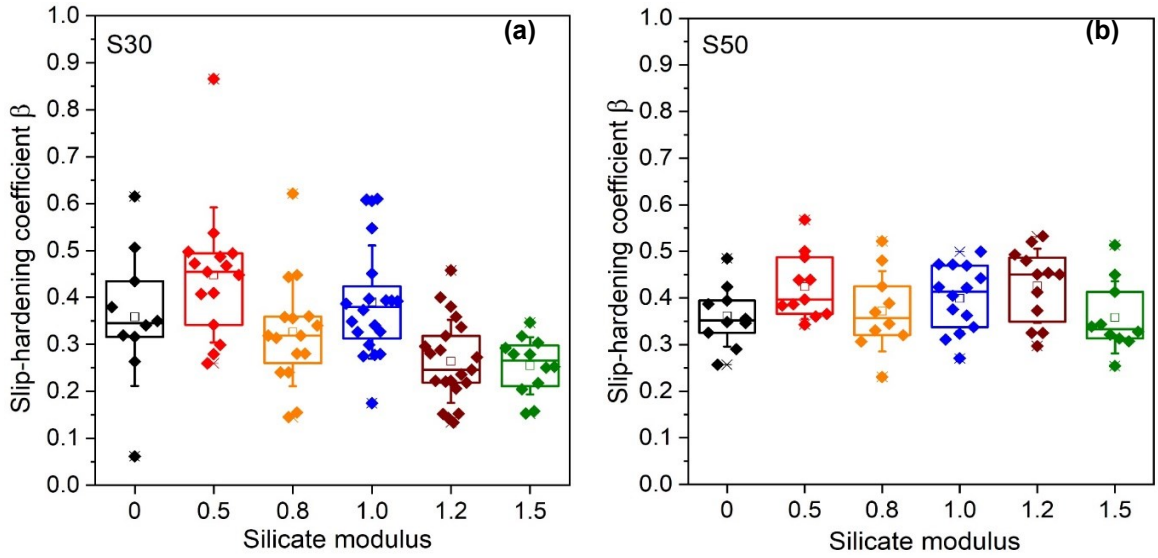

Figure 4.7 Box plot of slip-hardening coefficient β of PVA fiber in (a) S30 and (b) S50 AASF matrices with different activator silicate modulus. The box plot illustrates the median value (-), the mean (□), the values at 25% and 75% (box edges), and the standard deviation (Whiskers). Each of the box plots is derived from at least 16 individual pullout tests.

4.3.2 Microstructural characterization of ITZ

To further understand the interface properties, the ITZ between PVA fiber and the AASF matrix was systematically characterized. The aspects to be discussed are: (1) the morphology of the PVA fiber/matrix interface, (2) the element distribution around the PVA fiber, and (3) the chemical composition of the reaction products in the ITZ.

4.3.2.1 Morphology of PVA fiber/matrix interface

The morphology of the PVA fiber/matrix interface was observed using backscattered electron imaging on polished sections. Figure 4.8 (a) and (b) show typical BSE micrographs of the cross-section of both the PVA fiber and the ITZ in AASF (S50M1.0). The grey level contrast in both BSE micrographs distinguishes among different constituents, i.e., the PVA fiber, reaction products, the remnant slag and fly ash particles, as well as the micro-cracks and pores.

The presence of a relatively large PVA fiber (300 μm) could disturb the packing of slag particles. This is known as the wall effect and can increase the local liquid-to-solid ratio near the PVA fiber [243]. Compared to the bulk AASF matrix at 28 days (S50M1.0), an ITZ around PVA fiber (300 μm) is observed to be only slightly more porous. This observation seems to be consistent with previous studies on the ITZ around the fine sand particle (300 μm) in alkali-activated slag (AAS) mortar, which was found to be dense with very low porosity [244, 245]. Figure 4.8 thus suggests that the wall effect around a 300 μm PVA fiber in the AASF matrix is not significant.

Furthermore, the reaction products in the ITZ appeared to be firmly attached to the surface of the PVA fiber. Unlike the finding of the portlandite phase formed around PVA fiber in the cementitious system [246], no newly-formed crystalline phases are observed. This observation will be further discussed in Section 4.3.2.3.

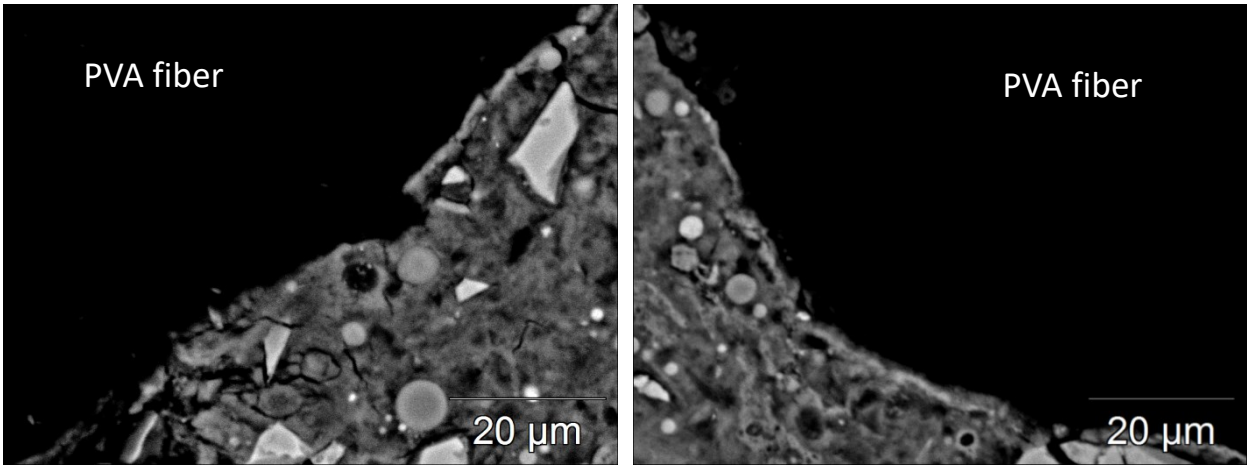

(a) the ITZ of PVA fiber in AASF matrix S50M1.0

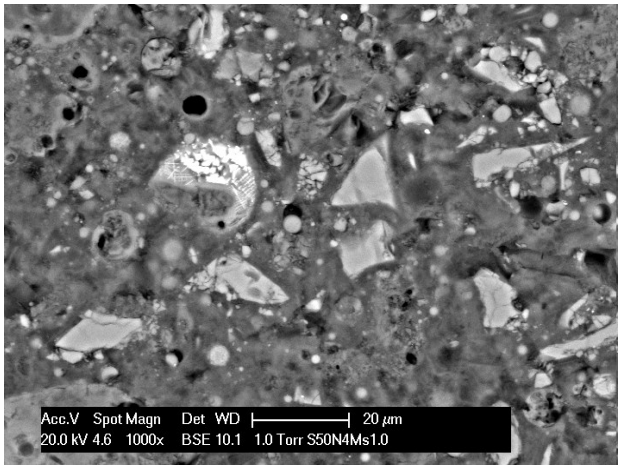

(b) the AASF matrix S50M1.0

Figure 4.8 Comparison of typical SEM micrographs of (a) the ITZ of the AASF S50M1.0 at 28 days and (b) AASF matrix S50M1.0 at 28 days.

4.3.2.2 Element distribution around PVA fiber

The EDX element mapping (Na, Mg, Al, Si, and Ca in atomic %) of the reaction products around PVA fiber is illustrated in Figure 4.9. A higher brightness represents the higher atomic concentration of a certain element. Slag particles rich in Ca and Mg, and fly ash particles rich in Si and Al can be identified. Furthermore, Ca, Na, Al, and Si are distributed more homogeneously than Mg. This is due to the low mobility of Mg ions during the reaction process [247]. Interestingly, the Ca map depicts a rim of reaction products around the PVA fiber. It has a much higher brightness than the rest of the reaction product in the bulk matrix. This indicates the formation of a Ca-rich reaction product at the fiber/matrix interface. Other elements, including Si and Al, do not show preferential distributions.

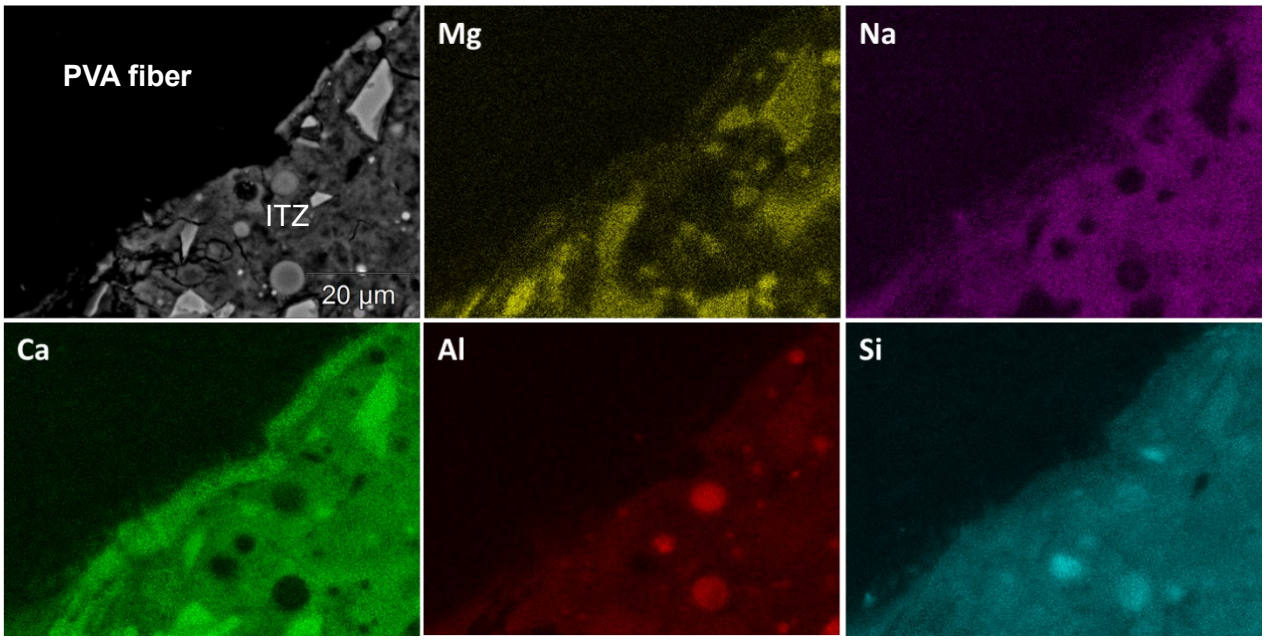

Figure 4.9 EDX element mapping (Na, Mg, Al, Si, and Ca in atomic %) of reaction products around PVA fiber in the S50.

EDX spot analyses were conducted on the Ca-rich reaction product to further determine their chemical composition in comparison to that of the bulk matrix. The results are presented in a CaO-SiO_2-Al_2O_3 ternary diagram in Figure 4.10 (a) and (b). In both S30 and S50 systems, the Ca-rich reaction products have evidently higher Ca/Si ratios than those formed in the bulk matrix. However, both of them have similar Al/Si ratios. Despite its high Ca content, the Ca-rich reaction products show the characteristic chemical composition of C-(N-)A-S-H gel.

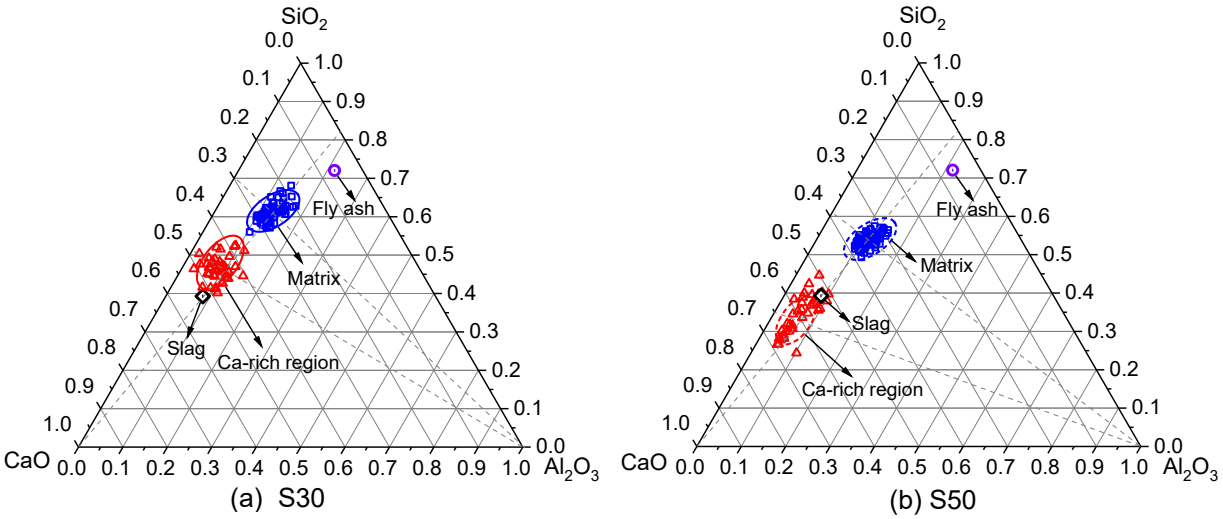

Figure 4.10 Ternary diagram of CaO-SiO_2-Al_2O_3 of EDX spot analysis for reaction product in the matrix and the Ca-rich region in the ITZ in (a) S30 and (b) S50

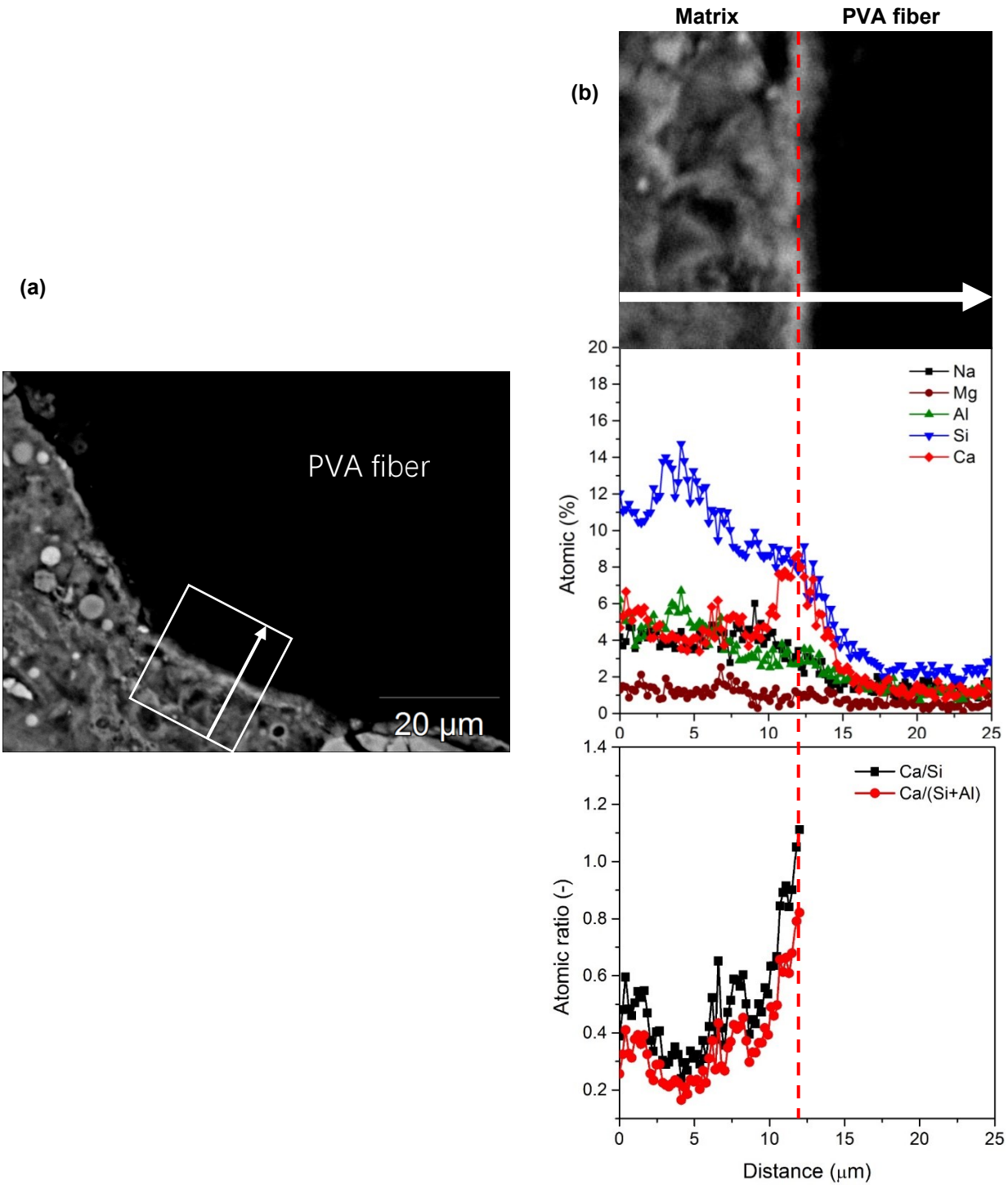

Figure 4.11 Elemental distributions of Na, Mg, Al, Si, Ca, Ca/Si, and Ca/(Si+Al) ratios of the reaction products in the ITZ. The distance corresponds to the length of the line scan across the fiber/matrix interface.

Additionally, several carefully selected EDX Line scans from the AASF matrix to the PVA fiber were performed. The line scan can reveal the influence of PVA fiber on the element distribution in the reaction products within the ITZ. Figure 4.11 shows a representative line scan result of

the change in atomic percentage of Na, Mg, Al, Si, and Ca, which are plotted against the length of the line scan (x-axis).

The concentration of Na, Mg, Al, and Si decreases progressively from the bulk side of the ITZ to the PVA fiber surface. Particularly, a substantial decline of Si along the line into the PVA fiber region is observed. The concentration of Ca, however, experiences a marked increase along the line scan, reaches a maximum at the PVA fiber surface, and then continuously decrease into the fiber region. Accordingly, the Ca/Si and Ca/(Si+Al) ratios are significantly higher in the ITZ region than in the bulk matrix. Both ratios also reach the maximum precisely at the PVA fiber surface as shown in Figure 4.11 (b). Considering that the Mg concentration in the ITZ does not change significantly, it is not possible that the marked increase of the Ca concentration is due to the accumulation of unreacted slag particles at the interface. It is reasonable to believe that a Ca-rich reaction product is formed near the PVA fiber surface.

In previous studies, the reaction product around aggregate particles in AAS mortar has a lower Ca/Si ratio than that in the bulk matrix due to the “wall effect” [245]. The higher Ca/Si ratio of the reaction product near the PVA fiber thus indicates that the physical “wall effect” is not dominating in this case. Instead, the chemical characteristics of the PVA fiber surface could play a more significant role in the formation of Ca-rich reaction products. This could also be the reason for the differences between the chemical bonding energy of PVA fiber in AAMs systems and cementitious systems [21, 129, 130].

4.3.2.3 Reaction product formation in the ITZ

To further assess the reaction product formed in the ITZ, the automated phase mapping based on the chemical composition of different phases is applied using a principal component analysis (PCA) approach. The results are illustrated in Figure 4.12 and Figure 4.13 for the S30 and S50 systems, respectively.

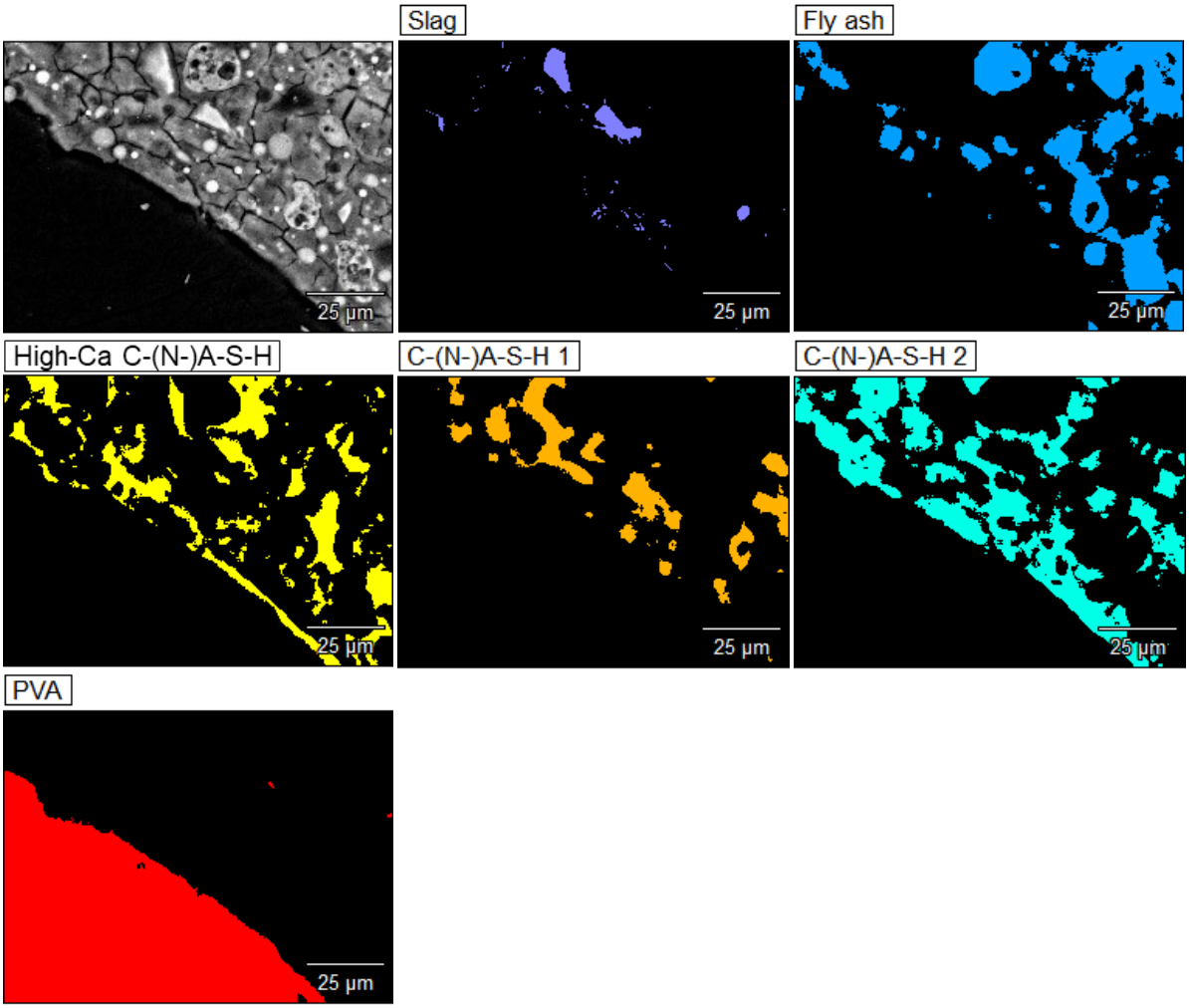

Figure 4.12 Phases mapping using principal component analysis (in atomic %) of reaction products in the ITZ of S30

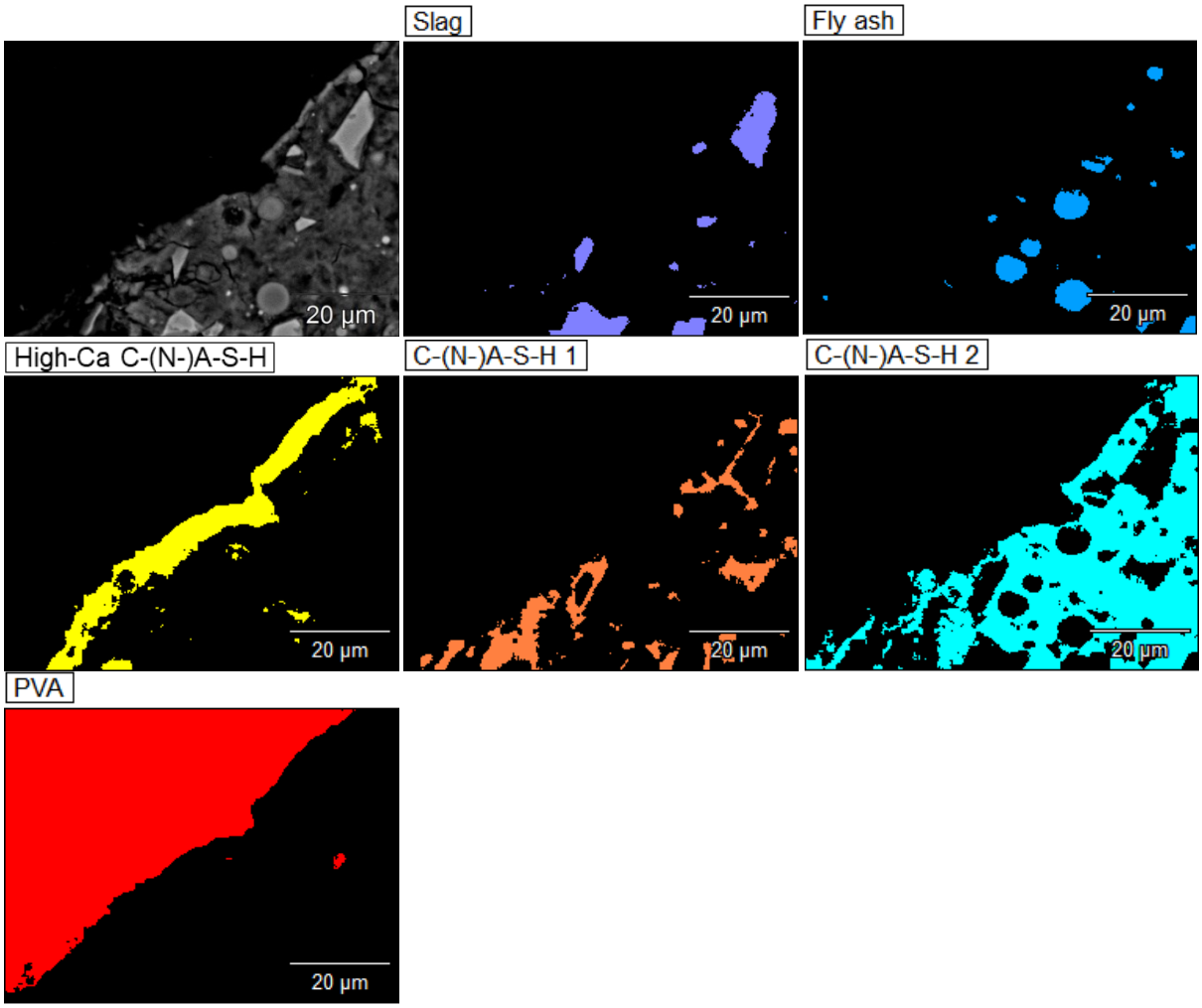

Figure 4.13 Phases mapping using principal component analysis (in atomic %) of reaction products in the ITZ of S50

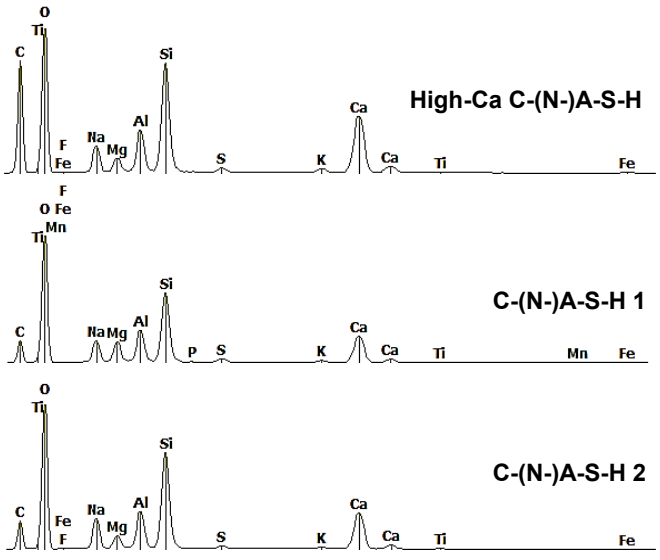

Figure 4.14 EDX spectra for three C-(N-)A-S-H phases identified by automated COMPASS phases mapping: High-Ca C-(N-)A-S-H, C-(N-)A-S-H 1, and C-(N-)A-S-H 2.

The unreacted slag particles, unreacted fly ash particles, and PVA fiber can be effectively identified by phase mapping. Furthermore, phase mapping also helps to identify at least three chemically distinct reaction products. These three phases, named by their chemical compositions, are high-Ca C-(N-)A-S-H, C-(N-)A-S-H 1, and C-(N-)A-S-H 2. Their representative EDX spectra are given in Figure 4.14 and the chemical compositions of these phases (atomic ratios) are given in Table 4.3.

Table 4.3 Atomic ratios of the reaction products determined by EDX spot analysis

	Reaction product	Ca/Si	Ca/(Si+Al)	Al/Si	Mg/Ca	Mg/Si
S30	High-Ca C-(N-)A-S-H	1.00±0.16	0.72±0.13	0.35±0.09	0.13±0.10	0.13±0.09
	C-(N-)A-S-H 1	0.39±0.07	0.26±0.05	0.42±0.06	0.82±0.06	0.32±0.06
	C-(N-)A-S-H 2	0.33±0.07	0.25±0.05	0.39±0.06	0.35±0.06	0.12±0.06
S50	High-Ca C-(N-)A-S-H	1.82±0.53	1.44±0.30	0.34±0.06	0.12±0.03	0.13±0.03
	C-(N-)A-S-H 1	0.61±0.03	0.43±0.05	0.42±0.05	0.50±0.11	0.31±0.11
	C-(N-)A-S-H 2	0.61±0.04	0.43±0.05	0.40±0.05	0.24±0.11	0.15±0.11

Note: Hydrotalcite phases as secondary reaction products are intermixed with the main reaction product C-(N-)A-S-H gel in all cases, although the amount of hydrotalcite differs according to the mixture as well as the region for EDX testing as can be reflected by the Mg/Ca and Mg/Si ratio.

As shown in Table 4.3, the Ca/Si and Ca/(Si+Al) ratios of the high-Ca C-(N-)A-S-H phase are much higher than those of the C-(N-)A-S-H 1 and 2 phases. The high-Ca C-(N-)A-S-H in S50 mixtures also has higher Ca/Si and Ca/(Si+Al) ratios than that in S30 mixtures due to the higher amount of available Ca that is present in slag. All three C-(N-)A-S-H phases have a higher Al/Si ratio (0.35~0.42) than the C-A-S-H gel in AAS [248] and the synthetic C-A-S-H gel [249]. Additionally, the high-Ca C-(N-)A-S-H phases have a lower Al/Si ratio than the other two C-(N-)A-S-H phases in both S30 and S50 pastes. Further discussions on the reaction products formed in the ITZ are given in Appendix B.

4.3.3 General discussions

4.3.3.1 Chemical bonding energy G_d and chemical composition of C-(N-)A-S-H gel

As discussed in Chapter 3, the main reaction products were characterized to be C-(N)-A-S-H gel [250]. By changing the slag content and activator M_s, the availability of both Ca and silica species was effectively altered. This changed the global reaction and chemical nature of the reaction products [151, 163, 251]. Such effects lead to the formation of C-(N-)A-S-H gel with various Ca/Si and Ca/(Si+Al) ratios. As shown in Figure 4.15 (a), a strong linear relationship was also confirmed between chemical bonding energy G_d and the Ca/Si ratio of the C-(N-)A-S-H gel in AASF pastes. Besides, a good linear relationship also exists between G_d and the Ca/(Si+Al) ratio as shown in Figure 4.15 (b). This implies that, similar to the fracture toughness K_{Ic} (J_{tip}) of the matrix, the chemical bonding energy G_d is also dominated by the chemical composition of C-(N-)A-S-H gel.

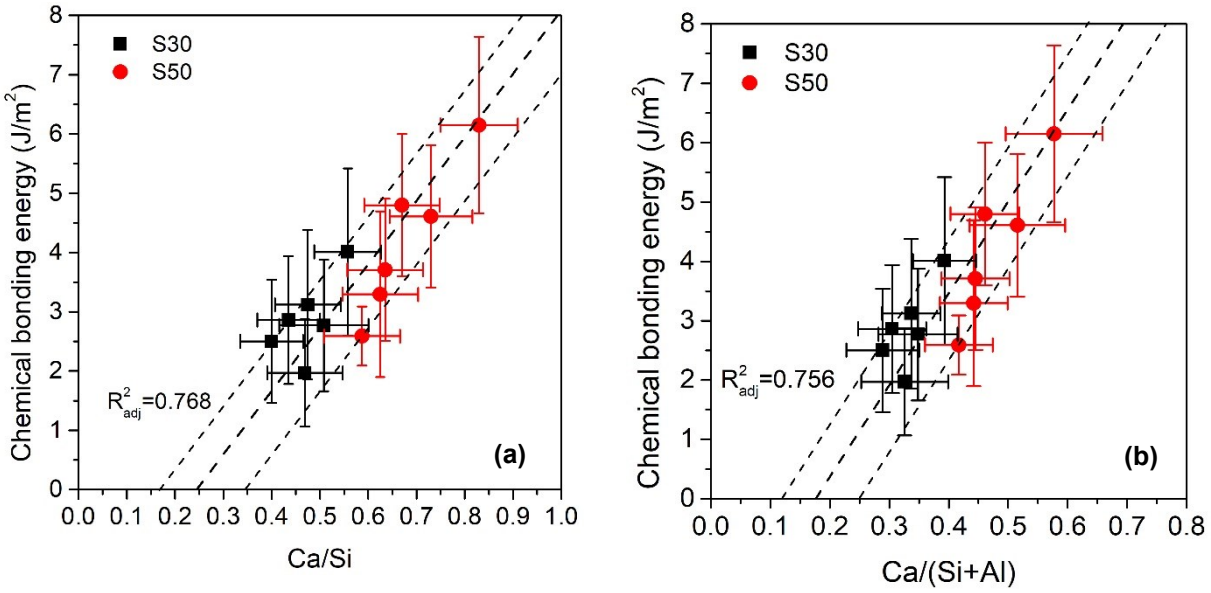

Figure 4.15 Correlation of chemical bonding energy G_d as a function of (a) Ca/Si ratio, and (b) Ca/(Si+Al) ratio of C-(N-)A-S-H gel as main reaction products of AASF pastes. The error bar indicates the standard deviations (STDs).

The reason for the strong correlations between chemical bonding energy G_d and the Ca/Si and Ca/(Si+Al) ratios of the C-(N-)A-S-H gel could be the following. First of all, the hydroxyl group (-OH) in PVA fiber has a strong polarity due to the high electronegativity of the oxygen atom. It thus serves as a favorable oxygen site provider for the formation of electrostatic interactions. Secondly, similar to C-S-H gel, C-(N-)A-S-H gel with high Ca/Si or Ca/(Si+Al) ratios presents a high negative surface charge density [234]. Under such circumstances, the formation of the electrostatic $O_{C\text{-}(N\text{-})A\text{-}S\text{-}H}$-Ca-$O_{PVA}$ bonds is highly feasible [252, 253]. These electrostatic interactions could account for the strong chemical bonding energy G_d. Secondly, it is believed that the hydroxyl group at the surface of PVA fiber provides oxygen sites for the formation of hydrogen bonds [252]. Consequently, the higher charge density of C-(N-)A-S-H gel with higher Ca/Si or Ca/(Si+Al) ratio can effectively enhance both the electrostatic interaction and the formation of hydrogen bond between the C-(N-)A-S-H gel and PVA fiber surface. These stronger interactions finally result in a higher chemical bonding energy G_d.

Further to the foregoing reasoning, it is worth noting that the strong polarity of PVA can also attract freely moving cations, such as Ca^{2+}, to accumulate near the PVA fiber surface. Some experimental evidence of this has been found in the ITZ of PVA fibers in AASF matrices. A preferential Ca distribution near the PVA fiber surface, as well as the formation of the high-Ca C-(N-)A-S-H phase in the ITZ, have been observed. (see also discussions in Section 4.3.2.2 and Section 4.3.2.3). It is suggested that the chemical bonding is governed by the surface interactions or adhesion between the PVA fiber and the C-(N-)A-S-H gel. Since further insights into the fundamental adhesion mechanism are not possible at the microscale (i.e., the length scale considered in this chapter), molecular dynamic simulation at the nanoscale will be conducted in Chapter 5 to give further insights into the adhesion mechanism.

4.3.3.2 Origin of initial frictional bond τ_0

A schematic representation of the possible origin of the initial frictional bond τ_0 is illustrated in Figure 4.16. The figure depicts the fiber/matrix interface at the end of the fiber debonding process, i.e., at the starting point of the slippage phase. This is also the moment when the pullout load drops from P_a to P_b in Figure 4.4 (b). With the completion of the debonding process, the initially intact fiber/matrix interface could be considered as two solid surfaces in contact with each other. Compared with chemical bonding energy G_d, the origin of τ_0 is more complicated. Three possible surface contact scenarios after the fiber debonding process can be considered:

(1) Scenario I: the contact is between the PVA fiber to the matrix fracture surface due to the adhesive failure at the interface (PVA-matrix)

(2) Scenario II: the contact is between two fracture surfaces of the matrix due to the cohesive failure of the matrix in the ITZ (matrix-matrix);

(3) Scenario III: the contact is a combination of both scenario I and II due to the combined adhesive-cohesive failure [254].

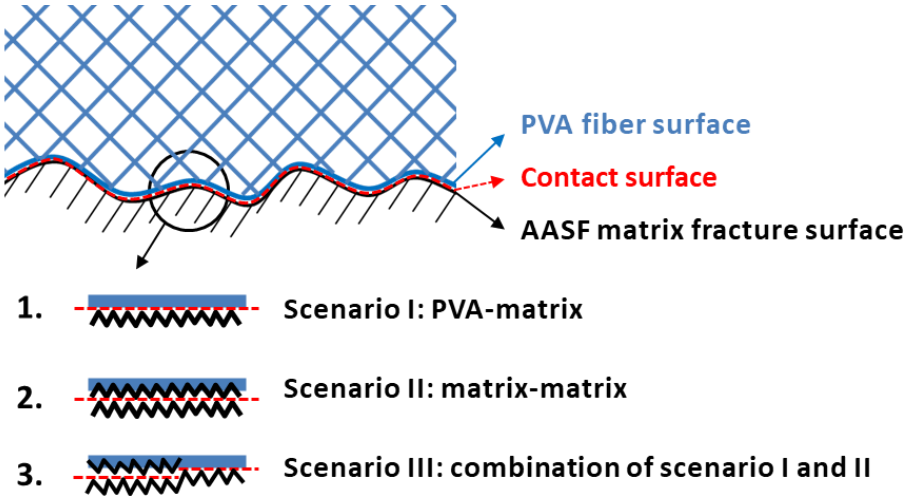

Figure 4.16 Schematic representation of the surface contact scenarios for the initial frictional bond.

According to previous studies, the surface contact according to scenario I normally holds for hydrophobic polymeric fiber (e.g., PE, PP, PLA, etc.). These fibers have negligible chemical bonding (adhesion) with the reaction product in the matrix [50, 114, 242]. During pullout, the tunnel crack propagates exactly along the fiber surface. The adhesive failure at the interface determines that the friction will be between the fiber and the matrix [255]. This is also the reason why the friction between the hydrophobic fibers and the matrix could be substantially improved by increasing the surface roughness of the fibers [50, 256, 257].

In contrast, surface contact according to scenario II occurs normally when a hydrophilic fiber (e.g., PVA, nylon, etc.) strongly adheres to the matrix. Under such circumstances, the adhesion between fiber and matrix is stronger than the cohesion in the matrix. As a result, the tunnel

crack tends to propagate in the matrix near the PVA fiber leading to the cohesive failure of the matrix in the ITZ.

Finally, scenario III happens when the chemical bonding between fiber surface and matrix, i.e., adhesion, is about equal to the cohesion in the matrix. The tortuous tunnel crack propagates partially along the fiber surface but also in the matrix, which leads to an adhesive-cohesive failure in the ITZ.

From the previous studies [139, 258], surface contact according to scenario II and III have been observed in PVA fiber reinforced cementitious matrices. In this study, the PVA fiber surface after pullout appears to be almost fully covered with matrix residue (Section 4.3.2). Considering that the chemical bonding energy G_d of PVA fiber in AASF matrices is 2 to 3 times higher than that in cementitious materials, the surface contact is most probably dominated by scenario II [259, 260]. The initial friction can thus be described as “dry friction” between two solid surfaces and the classic coulomb-type friction law is assumed to be applicable. The initial frictional bond τ_0 is then determined by (1) the surface properties of the two contact surfaces (normally characterized by the friction coefficient) and (2) the residual stress of the surrounding matrix onto the fiber surface [141, 261].

Firstly, the initial friction bond is stronger with a higher friction coefficient, which could be achieved by a higher fracture surface roughness of the AASF matrix. According to Lange et al. [168], the fracture surface roughness is positively related to the matrix fracture toughness (K_{Ic}). Since K_{Ic} has also a strong positive linear relationship with the Ca/Si ratio of the C-(N-)A-S-H gel (see Chapter 3), AASF matrices with high Ca/Si ratios thus have a higher friction coefficient. This contributes to a stronger initial friction bond.

Secondly, the residual stress of the surrounding matrix onto the fiber surface may also significantly affects the initial friction bond τ_0 [262]. This residual stress is caused by shrinkage of the AASF matrix, e.g., autogenous shrinkage and possible drying shrinkage. Furthermore, it is also affected by the creep and relaxation behavior of the AASF matrix. Given the fact that the shrinkage and creep are governed by various factors (such as the pore structure, the mechanical properties, and most likely the chemical composition of the reaction products [263, 264]), further insight into the mechanism of shrinkage and creep in AASF systems is needed to better understand the residual stress and the related friction behavior.

4.3.3.3 Mechanism of slip-hardening behavior

The slip-hardening behavior results from the lower rigidity of the PVA fiber in comparison to the surrounding AASF matrix. The difference in rigidness leads to severe abrasion between the PVA fiber and the surrounding rough AASF matrix tunnel. The abrasion thus results in “micro-excavation” damage to the PVA fiber surface, leaving the fiber debris in the form of stripped fibrils [142]. As shown in the SEM micrograph in Figure 4.17, the surface of the pulled-out PVA fiber has a substantial amount of fibrils. Figure 4.17 also shows clearly the spalled micro-debris from the matrix attached to the fibrils. With increasing fiber pullout displacement, the accumulation of these fibrils (with matrix micro-debris) promotes the formation of a “locking front”, which increases the pullout resistance [265]. This effect is also referred to as the “jamming effect” [139, 142]. The slip-hardening behavior may lead to a tensile load exceeding the fiber tensile strength causing rupture of the fiber. This rupture happens when the pullout load reaches the maximum P_{max} as shown in Figure 4.4 (b).

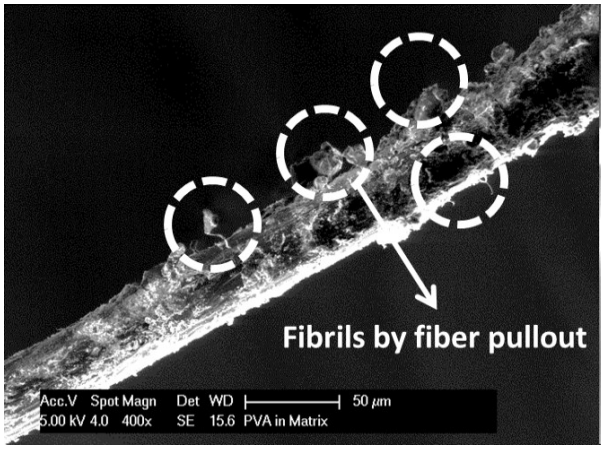

Figure 4.17 Fibril's on PVA fiber surface after single fiber pullout test

The slip-hardening behavior is determined by the following three factors:

1. The chemical bonding between PVA fiber and the matrix: A strong chemical bonding between PVA fiber and AASF matrix (Section 4.3.3.1) prevents the occurrence of adhesive failure at the fiber/matrix interface. As shown in Figure 4.17, the roughened surface of the PVA fiber after pullout suggests a cohesive failure of the matrix in the ITZ after debonding, i.e., a surface contact according to scenarios II. A strong chemical bonding thus promotes a more significant slip-hardening process.

2. The surface roughness of the matrix: A rougher surface of the tunnel crack, i.e., a higher matrix fracture toughness (K_{Ic}) [168], can promote the "micro-excavation" damage initiation at the fiber surface. This leads to a more severe fiber-matrix interaction and hence a higher resistance during the pullout process.

3. Shrinkage-induced residual stress onto the fiber surface: As previously shown in Figure 4.4 (b), the pullout load keeps increasing from the load P_b (when the friction starts) until the load P_{max} (when the fiber ruptures). This suggests that the fiber surface is still under residual stress before the fiber rupture. As a result, the residual stress enables the accumulation of fibrils (matrix micro-debris) to form the "locking front" and increases the pullout resistance. As discussed in Section 4.3.3.2, the magnitude of the residual stress depends on many factors. Further studies on the effect of residual stress are beyond the scope of this thesis.

4.4 Conclusions

In this chapter, a systematic experimental investigation of the PVA fiber/matrix interface properties in AASF pastes is presented. Three important interface bonding properties, i.e., the chemical bonding energy (G_d), the initial frictional bond strength (τ_0), and slip-hardening behavior (β) were determined using single-fiber pullout tests. To further understand the influence of PVA fiber on the interface bonding properties, the microstructure of the interfacial transition zone (ITZ) and the chemical composition of the reaction products within the ITZ were also characterized. Based on the results and discussions, the following conclusions can be drawn:

- The chemical bonding energy G_d between PVA fiber and AASF matrix increases with increasing Ca/Si and Ca/(Si/+Al) ratio of C-(N-)A-S-H gel, where the latter is the main reaction product in AASF pastes.

- The initial frictional bond τ_0, unlike the chemical bonding energy G_d, is not only determined by the chemical composition of the reaction products. A synergistic mechanism of the fracture surface roughness of the matrix (positively related to K_{Ic}) and shrinkage-induced residual stress determines the magnitude of the frictional resistance.

- The hydrophilic nature of PVA fiber promotes the formation of the high-Ca C-(N-)A-S-H phase in the ITZ near the PVA fiber surface. The high-Ca C-(N-)A-S-H phase has considerably higher Ca/Si and Ca/(Si+Al) ratios, lower Al/Si ratios, and lower Mg/Ca ratios compared to the C-(N-)A-S-H phases in the bulk matrix.

- Two kinds of C-(N-)A-S-H phases were formed in the bulk matrix of AASF paste. The main difference between them is their different Mg content. This is most probably due to the different amounts of hydrotalcite intermixed within C-(N-)A-S-H phases.

- Due to the strong chemical bond between PVA fiber and AASF matrix, the debonding process is dominated by the *cohesive* failure that happened within the ITZ rather than the *adhesive* failure along the PVA fiber surface. As a result, the initial friction bond τ_0 is most likely determined by the interaction between the fracture surfaces of the AASF matrix and not between PVA fiber and the AASF matrix.

- The slip-hardening behavior of PVA fiber in the AASF matrix is caused by a ‘jamming’ effect. The accumulation of the stripped fibrils (along with matrix micro-debris) on the fiber surface increases the pullout resistance.

- The residual stress onto the fiber surface plays an important role in the initial friction bond τ_0 and slip-hardening behavior in the pullout of PVA fiber from the AASF matrix. Studies on the influence of shrinkage and creep behavior of the AASF matrix on the residual stress are recommended.

The study provides important insights into the interface bonding properties of PVA fiber to the AASF matrix. The experimental evidence suggests that the PVA fiber has a significant impact on the chemical bond and the formation of the Ca-rich C-(N-)A-S-H phase. To further understand the above-mentioned aspects, molecular dynamic simulation at the nanoscale will be conducted to give further insights into the adhesion mechanism in Chapter 5. Data of the interface bonding properties will be used as input for the micromechanics-based development of SHGC, as will be discussed in Chapter 6.

Chapter 5

Molecular dynamics simulation on the adhesion mechanism of polyvinyl alcohol (PVA) fiber to alkali-activated slag/fly ash matrix[7]

5.1 Introduction

The results in Chapter 4 reveal the formation of a unique Ca-rich C-(N-)A-S-H gel in the interfacial transition zone (ITZ) of polyvinyl alcohol (PVA) fiber in the AASF matrix. The interface properties are also found to be different in comparison to those in cementitious matrices. All of these indicate that the adhesion mechanism of PVA fiber to the AASF matrix is different from that to the cementitious matrix. Due to the hydrophilic surface characteristic, the adhesion between PVA fiber and the AASF matrix leads to characteristic features of the single fiber pullout behavior as discussed in Chapter 4. The fiber/matrix adhesion can determine the chemical bonding energy G_d and is also indirectly responsible for the frictional bonding τ_0 as well as the slip-hardening coefficient β. Since the interface properties play important roles in the composite behavior, the understanding of the adhesion mechanism is pivotal for the development of strain-hardening geopolymer composite (SHGC).

Due to the limitations of current experimental techniques at the nanoscale, observation of the interaction between PVA fiber as an organic matter and the inorganic matrix of AAMs is not possible. As an alternative, computational simulation methods, like molecular dynamics (MD), can be applied to provide a better understanding of the experimental findings concerning the adhesion at micro/meso scales [266]. In most of the previous research, the adhesion properties were studied by the use of MD to calculate critical values of the interaction energy (including adsorption enthalpies). Besides, the interfacial adhesion mechanism could be also unravelled by investigating the interaction between organic matter and inorganic matrix using different force fields. These interactions can be simulated accurately, provided that suitable force fields are applied [267, 268]. Several studies can be found concerning the adhesion between the cementitious matrix and different organic matter, including polymer fiber [269], polymer additives [253, 270], and epoxy resin [271, 272]. However, as explained in Chapter 4, the main reaction product in an alkali-activated matrix is different from that of the cementitious matrix. Currently, the studies on adhesion between PVA fiber and alkali-activated matrix are still rare.

[7] This chapter is partially based on:

Zhang, S., Duque-Redondo, E., Kostiuchenko, A., Dolado, J. S., & Ye, G. (2021). Molecular dynamics and experimental study on the adhesion mechanism of polyvinyl alcohol (PVA) fiber in alkali-activated slag/fly ash. Cement and Concrete Research, 145, 106452.

This chapter aims to provide better insights into the PVA fiber/AASF matrix adhesion mechanism through MD simulation and intensive experimental testing. The adhesion (at the nanoscale) of the PVA fiber to C-(N-)A-S-H type reaction products are simulated with a PVA molecule embedded in C-(N-)A-S-H structure with different chemical compositions. The schematic illustration is shown in Figure 5.1. It gives an idea about the length scale considered in the simulation. In the MD simulation, the adhesion mechanism is investigated by the study of the interaction between the PVA molecule with different C-(N-)A-S-H structures. The strength of adhesion (in the form of adsorption enthalpy) is also calculated. Finally, these simulation results were compared with experimental results.

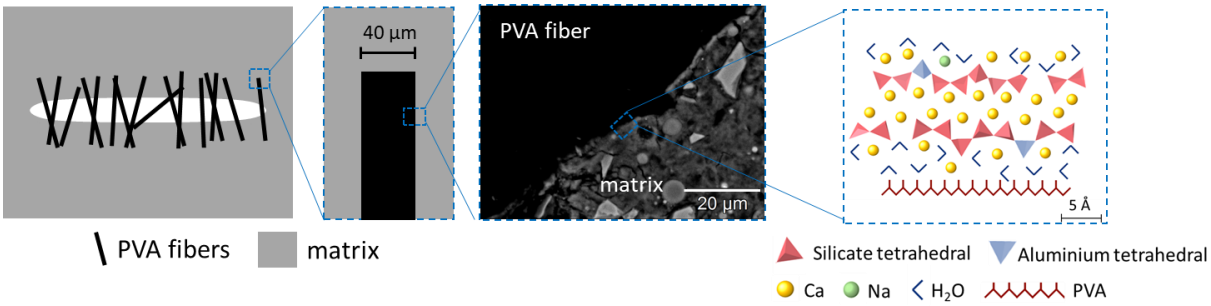

Figure 5.1 Schematic illustration of the interaction between PVA fiber (molecule) with the reaction product at the different length scales

5.2 MD simulation details

To study the interaction between PVA molecules and C-(N-)A-S-H and the underlying adhesion mechanism at the nanoscale, MD simulation was performed in this chapter. The PVA molecule and C-(N-)A-S-H structure was first constructed to build PVA/C-(N-)A-S-H composites. The MD simulation details are given in the subsequent sections.

5.2.1 Construction of the PVA molecule

The Avogadro Builder [273] was employed for the creation of the PVA molecule formed by 100 monomeric units of vinyl alcohol as shown in Figure 5.2. The structure of the PVA molecule was equilibrated by performing MD simulations using the LAMMPS simulation package [274]. CHARMM[8] force field [275] was used to describe the bonding and non-bonding interactions in

[8] CHARMM (Chemistry at Harvard Macromolecular Mechanics) is a widely used set of force fields for molecular dynamics simulation. It primarily focuses on molecules of biological interest but is also suitable for the simulation of polymers.

the PVA molecule. The atomic charges were derived by electrostatic potential (ESP) analysis of density-function theory (DFT) results using the CHELPG[9] scheme [276].

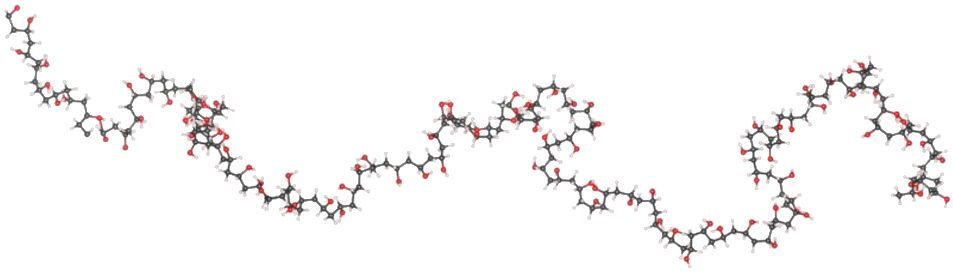

Figure 5.2. Atomic structure of the PVA molecule.

First, energy minimization was performed to get the position of atoms in the molecule and its simulation box with their minimum energy conformation. Then, the structure of the PVA molecule was equilibrated in the canonical ensemble (NVT) at 300 K during 2.5 ns, with a time step of 0.5 fs and a thermostat coupling constant of 0.1 ps. Finally, the atoms and the volume of the simulation box were further relaxed in the isobaric-isothermal ensemble (NPT) at 300 K and 1 atm for another 2.5 ns with a thermostat and barostat coupling constants of 0.1 ps.

5.2.2 Chemical composition of the C-(N-)A-S-H structures

The chemical composition of the C-(N-)A-S-H structures is based on EDX spot analysis in the AASF matrices shown in Figure 3.10. Two Al/Si ratios of 0.25 and 0.5 and five Ca/(Si+Al) ratios from 0.5 to 1.3 were selected to cover the chemical composition of the C-(N-)A-S-H gel. The procedures to determine the chemical composition of the C-(N-)A-S-H structures are given in detail in Appendix C. Notably, the Ca/(Si+Al) ratio was extended up to 1.3 to cover the chemical composition of C-(N-)A-S-H gel formed in AAS [151, 170, 171] and AASF with high slag content [103-105, 150, 172, 174]. In this way, the conclusions from the MD simulation are also suitable for Ca-rich binders.

5.2.3 Construction of the PVA/C-(N-)A-S-H composites

The construction procedures of PVA/C-(N-)A-S-H composites are shown schematically in Figure 5.3 in 4 steps. In the first step, C-(N-)A-S-H structures were created by modifying the structure of tobermorite 14 Å minerals described by Bonaccorsi et al. [277], following the procedure described by Pellenq et al. [278] and refined by Qomi et al. [279]. In the construction of the C-(N-)A-S-H structures, the restrictions imposed by Kovačević et al. [280] and Kumar et al. [281] in their procedures were also considered. These restrictions concern the distribution of dimeric and pentameric silicates to avoid the presence of monomeric species. In this way, they help the construction of more accurate C-(N-)A-S-H structures. The unit cell of this mineral

[9] CHELPG (CHarges from ELectrostatic Potentials using a Grid-based method) is an atomic charge calculation scheme developed by Breneman and Wiberg. The atomic charges are fitted to reproduce the molecular electrostatic potential (MESP) at a number of points around the molecule.

was replicated to obtain a simulation box with defined dimensions in the x, y, and z directions of 5.2 x 6.2 x 3.3 nm^3, respectively. In the simulation process, periodic boundary conditions (PBC) were applied to approximate an infinite system.

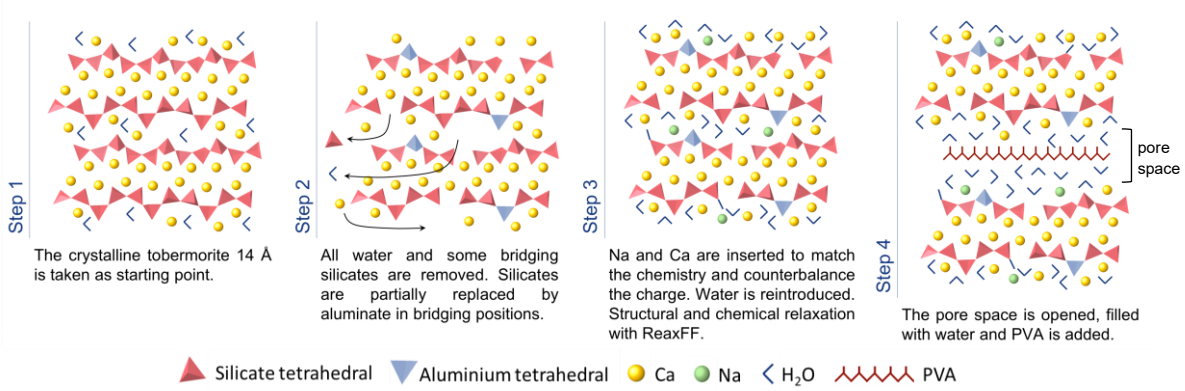

Figure 5.3. Schematic procedure of the construction of the C-(N-)A-S-H structures and the PVA/C-(N-)A-S-H composites.

In the second and third steps, the chemical composition of the tobermorite mineral was modified to reach the desired composition of the C-(N-)A-S-H gel. To achieve this, all water molecules were removed from the interlaminar spaces and some bridging silicate groups were removed randomly. The remaining bridging silicates were partially substituted by aluminates to adjust the Al/Si ratio to values between 0.25 and 0.5. The negative charge resulting from the replacement of Si^{4+} by Al^{3+} is compensated by inserting one Na ion per Al. Additionally, Ca was added to match the Ca/(Si+Al) ratio, increasing it from 0.83 (the typical value of tobermorite 14 Å minerals) to 1.0, 1.1, and 1.3, respectively. Meanwhile, no silicate monomers were generated [280, 281]. To reach the Ca/(Si+Al) ratio below 0.83 (0.5 and 0.75), the interlaminar Ca was replaced by Na ions.

Once the Ca/(Si+Al) and Al/Si ratios were adjusted, water was reintroduced in the pore space using a geometry-based algorithm [282] up to a density of 1 g/cm^3, and the structure was equilibrated. The LAMMPS code [274] and the reactive force field (ReaxFF) [283] were used to perform energy minimization and MD simulations in the isobaric-isothermal ensemble (NPT) at room conditions (300 K and 1 atm) for 5 ns with barostat and thermostat coupling constants of 0.2 and 1 ps, respectively. ReaxFF as a reactive force field allows the structural and chemical relaxation of the C-(N-)A-S-H structures. Thus, water molecules can dissociate into hydroxyl groups in the new Q^1 sites formed after removing the bridging silicate [284].

The construction of the PVA/C-(N-)A-S-H composite was done in the last step, i.e., step 4 in Figure 5.3. It comprises the expansion of the pore space (1.5 nm) to accommodate the PVA molecule. Then, the pore space was filled with water, and the PVA/C-(N-)A-S-H composite was equilibrated using a combination of CSHFF[10] [285] and CHARMM [275] force fields to

[10] CSHFF (C-S-H force field) [34] was developed to describe the interaction between atoms in cementitious systems. It has been widely applied in the C-S-H gel simulation and was successfully applied to describe its structure, energy and mechanical properties.

describe the C-(N-)A-S-H and the PVA fiber. An initial relaxation was conducted in the canonical ensemble (NVT) for 0.5 ns at 300 K with a thermostat coupling constant of 0.1 ps, followed by further equilibration in the isobaric-isothermal ensemble (NPT) at room conditions (300 K and 1 atm) with barostat and thermostat coupling constants of 0.2 and 1 ps, respectively. A final MD simulation was carried out in the canonical ensemble for 0.1 μs at 300 K. The lattice parameters and densities of the different PVA/C-(N-)A-S-H after equilibration are given in Table 5.1.

Table 5.1. Lattice parameters and densities for the PVA/C-(N-)A-S-H composites after MD equilibration at the studied Ca/(Si+Al) ratio with an Al/Si ratio of 0.5.

Ca/(Si+Al) ratio	0.5		0.75		1.0		1.1		1.3	
Al/Si ratio	0.25	0.5	0.25	0.5	0.25	0.5	0.25	0.5	0.25	0.5
L_x (nm)	5.181	5.179	5.272	5.215	5.083	5.037	4.972	5.013	4.925	4.877
L_y (nm)	6.062	5.983	6.158	5.973	5.828	5.747	5.790	5.696	5.688	5.544
L_z (nm)	2.975	3.183	2.918	3.061	3.451	3.375	3.061	3.161	2.949	2.911
ρ (g·cm^3)	1.670	1.577	1.697	1.711	1.376	1.526	1.664	1.696	1.758	1.912

5.2.4 Interaction between PVA molecule and C-(N-)A-S-H

In the MD simulations, the PVA/C-(N-)A-S-H composites are built by placing the PVA fibers in the center of the expanded pore space at about 0.7 nm from the C-(N-)A-S-H surface (Step 4 in Figure 5.3). Based on previous studies by Zhou et al. [270], three types of interactions between the PVA molecule and C-(N-)A-S-H in the PVA/C-(N-)A-S-H composite are possible. These interactions, as shown schematically in Figure 5.4, could be between the PVA molecule and the C-(N-)A-S-H through the Ca and Na cations as well as the formation of hydrogen bonds between the hydroxyl groups of the PVA molecule and the oxygen atoms from the C-(N-)A-S-H.

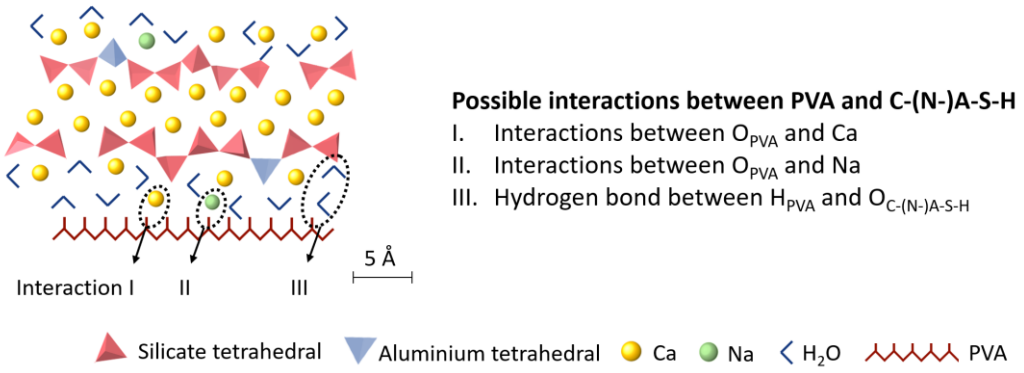

Figure 5.4 Schematic illustrations of possible interactions between the PVA molecule and C-(N-)A-S-H in the PVA/C-(N-)A-S-H composite.

To further understand the interaction, the radial distribution function (RDF) and the coordination number (CN) were determined. In particular, the RDFs and CNs of the hydroxyl groups of the PVA fibers were calculated with the cations (Ca and Na) and with the oxygen atoms from the C-(N-)A-S-H surfaces to analyze the effect of Ca/(Si+Al) and Al/Si ratios. Furthermore, the RDFs and CNs of the donor H atoms from the PVA molecule and acceptor oxygen atoms from the C-(N-)A-S-H surface were also calculated. This helps the understanding of the microscopic adhesion mechanism of the PVA fiber to C-(N-)A-S-H gel.

The RDF gives the probability of finding a certain type of particle from a reference particle as a function of a distance, between r and r+dr, as shown schematically in Figure 5.5. In this way, the density variation *g(r)* is described as a function of the distance r to a reference particle.

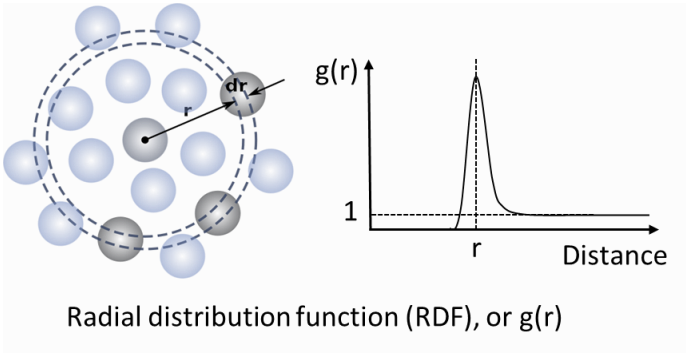

Figure 5.5 Schematic illustration of the radial distribution function (RDF), or g(r).

The radial distribution function (RDF), or *g(r),* is calculated using the following Equation 5.1 [286]:

$$g(r) = \frac{V}{N_A N_B T} \sum_{t=1}^{T} \sum_{i=1}^{N_A} \sum_{j=1}^{N_B} \langle \delta(r - |\vec{r}_i(t) - \vec{r}_i(t)|) \rangle_t \tag{5.1}$$

where N_A and N_B depict the number of arbitrary atoms A and B, r_i and r_j define the position vectors of the particle *i* and *j*; the Dirac delta function (δ function) can take the value 1 only in the interval [-*w, w*) (with *w* being the bin width), otherwise, it takes the value of 0; T indicates the number of frames taken from the trajectory of MD simulation.

The integration of the RDF provides the coordination number (CN), which can be defined as the total number of particles that a reference particle holds as neighbours within a shell between r_0 and *r*. r_0 is the rightmost position starting from r = 0 where g(r) is 0. The CN of a certain atom, or *n(r)*, is given by the following Equation 5.2:

$$n(r) = 4\pi\rho \int_{r_0}^{r} r^2 g(r) dr \tag{5.2}$$

where ρ is the atomic density.

To further evaluate the hydrogen bond, the angle distribution function (ADF) was also calculated using Equation (5.3):

$$f_{ABC}(\alpha) = \frac{1}{\sin(\alpha)\, N_A N_B N_C T} \sum_{t=1}^{T} \sum_{i=1}^{N_A} \sum_{j=1}^{N_B} \sum_{k=1}^{N_C} \langle \delta \left(\alpha - \sphericalangle\left(\mathrm{r}_j(t) - \mathrm{r}_i(t), \mathrm{r}_j(t) - \mathrm{r}_k(t) \right) \right) \rangle_t \qquad (5.3)$$

where $\sphericalangle$(x, y) depicts the angle between two vectors *x* and *y*; N_A, N_B, and N_C are the number of atoms A, B, and C, respectively; r_i, r_j, and r_k define the position vectors of the particle *i, j,* and *k*; sin(α) is the cone correction factor to account for the geometrical bias [287]; δ is the Dirac delta function (δ function); T indicates the number of frames taken from the trajectory of MD simulation.

By combining the RDF (Equation 5.1) and the corresponding ADF (Equation 5.3), the combined distribution functions (CDFs) can be determined. The CDFs were used to further analyze the most probable bond distances and angles for hydrogen bonds formed in the PVA/C-(N-)A-S-H composites.

5.2.5 In situ polymerization

An *in situ* polymerization of the C-(N-)A-S-H gel was simulated using monomeric species including $Ca(OH)_2$, $Si(OH)_4$, and $Al(OH)_4Na$. The polymerization process from these monomers to C-(N-)A-S-H gel and the potential reactions between PVA and the monomers are crucial factors for generating the microstructures of the matrix and the ITZ. The GULP software [288] was used to perform this *in situ* polymerization, which consists of placing a PVA fiber and the precursors $Ca(OH)_2$, $Si(OH)_4$, and $Al(OH)_4Na$ into a simulation box with dimensions 4 x 4 x 4 nm^3 in the x, y and z directions. This allows the formation of C-(N-)A-S-H gel around a PVA fiber. A combination of the reactive Garofalini potential [289] for the polymerization of the C-(N-)A-S-H gel and CHARMM force field [275] for the PVA molecule was employed. Here, the reactive Garofalini potential is a classical MD force field developed to create computational silica models. The systems were equilibrated in the canonical ensemble (NVT) at 1500 K for 5 ns, with a time step of 0.5 fs and a thermostat coupling constant of 0.5 ps, so that the equilibrium of the systems was reached.

5.2.6 Adhesion strength between PVA molecule and C-(N-)A-S-H

The adhesion strength between the PVA molecule and C-(N-)A-S-H is determined by calculating the difference in potential energy between the PVA/C-(N-)A-S-H composite and a system of individual PVA molecule and C-N-A-S-H. This energy thus equals the energy needed to completely remove the PVA molecule from the PVA/C-(N-)A-S-H composites. The functional form of the potential energy in the force fields (CSHFF [285] and CHARMM [275] force fields) employed in the MD simulations includes bond terms to describe the interactions of the atoms linked by covalent bonds and non-bonded interactions, the latter being the electrostatic interactions and the van der Waals forces between particles. Since the PVA molecule is not covalently linked to the C-(N-)A-S-H surface, the options for the interaction between them are then limited to electrostatic and van der Waals interactions (e.g., the formation of hydrogen bonds).

The adsorption enthalpy[11] of PVA molecule in C-(N-)A-S-H with different Ca/(Si+Al) and Al/Si ratios can be determined with Equation 5.4:

$$\Delta \boldsymbol{H_{ads}} = \Delta \boldsymbol{H_{PVA/C-(N-)A-S-H}} - \Delta \boldsymbol{H_{PVA}} - \Delta \boldsymbol{H_{C-(N-)A-S-H}} \quad (5.4)$$

where $\Delta H_{PVA/C\text{-}(N\text{-})A\text{-}S\text{-}H}$ is the enthalpy of the whole composite, ΔH_{PVA} *is* the enthalpy of the PVA molecule, and $\Delta H_{C\text{-}(N\text{-})A\text{-}S\text{-}H}$ is the enthalpy corresponding to the C-(N-)A-S-H without PVA molecule. According to this definition, a lower adsorption enthalpy indicates stronger interaction between PVA and C-(N-)A-S-H, and hence a thermodynamically more favorable state.

5.3 Results and discussions

5.3.1 The chemical composition of the simulated C-(N-)A-S-H structure and C-(N-)A-S-H gel in AASF

The chemical composition of the real C-(N-)A-S-H gel and the simulated C-(N-)A-S-H structures are compared in Figure 5.6. The ternary diagram shows the chemical composition of the simulated C-(N-)A-S-H structures with Al/Si ratios of 0.25 and 0.5, respectively. In addition, it also shows the chemical composition of the "pure" C-(N-)A-S-H gel in M0.5-M1.5 S50 AASF matrices determined by EDX analysis.

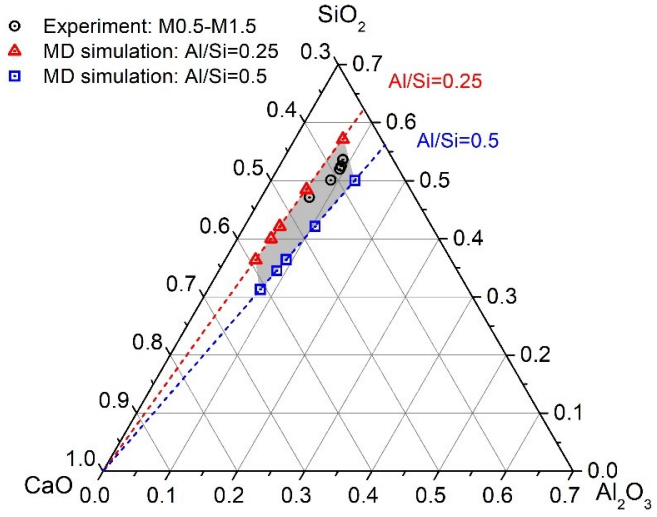

Figure 5.6 The $CaO\text{-}SiO_2\text{-}Al_2O_3$ ternary diagram of the chemical composition of "pure" C-(N-)A-S-H gel in the M0.5-M1.5 AASF matrices and the C-(N-)A-S-H structures for MD simulation (Al/Si=0.25 and Al/Si=0.5).

[11] In this case, the difference between the energy and the enthalpy is negligible because no significant volume change of the composite was observed after the equilibration and MD simulations. The adsorption enthalpy is considered as an indicator of the adhesion strength.

The ternary diagram shows that the Ca/(Si+Al) and Al/Si ratios of the simulated C-(N-)A-S-H structures agree well with the experimental data, in particular at low Ca/(Si+Al) ratios. The grey-shaded area within the dashed tie lines covers the chemical composition of C-(N-)A-S-H gel considered in the MD simulation. It is found that the proposed chemical composition of "pure" C-(N-)A-S-H gel with Ca/(Si+Al) ratio 0.50-0.69 and Al/Si ratio 0.30-0.36 fall well into the grey areas. Consequently, the chemical composition of the simulated C-(N-)A-S-H structures sufficiently cover that of the real C-(N-)A-S-H gel formed in AASF matrices. The reliability of the C-(N-)A-S-H structures as the basis for MD simulation is also substantiated.

5.3.2 Interactions between PVA molecule and C-(N-)A-S-H

The radial distribution functions (RDFs) of the oxygen atoms from the PVA molecule to Ca and Na cations (O_{PVA}-Ca and O_{PVA}-Na) and their corresponding coordination number (CNs) with five Ca/(Si+Al) ratios and two Al/Si ratios are shown in Figure 5.7.

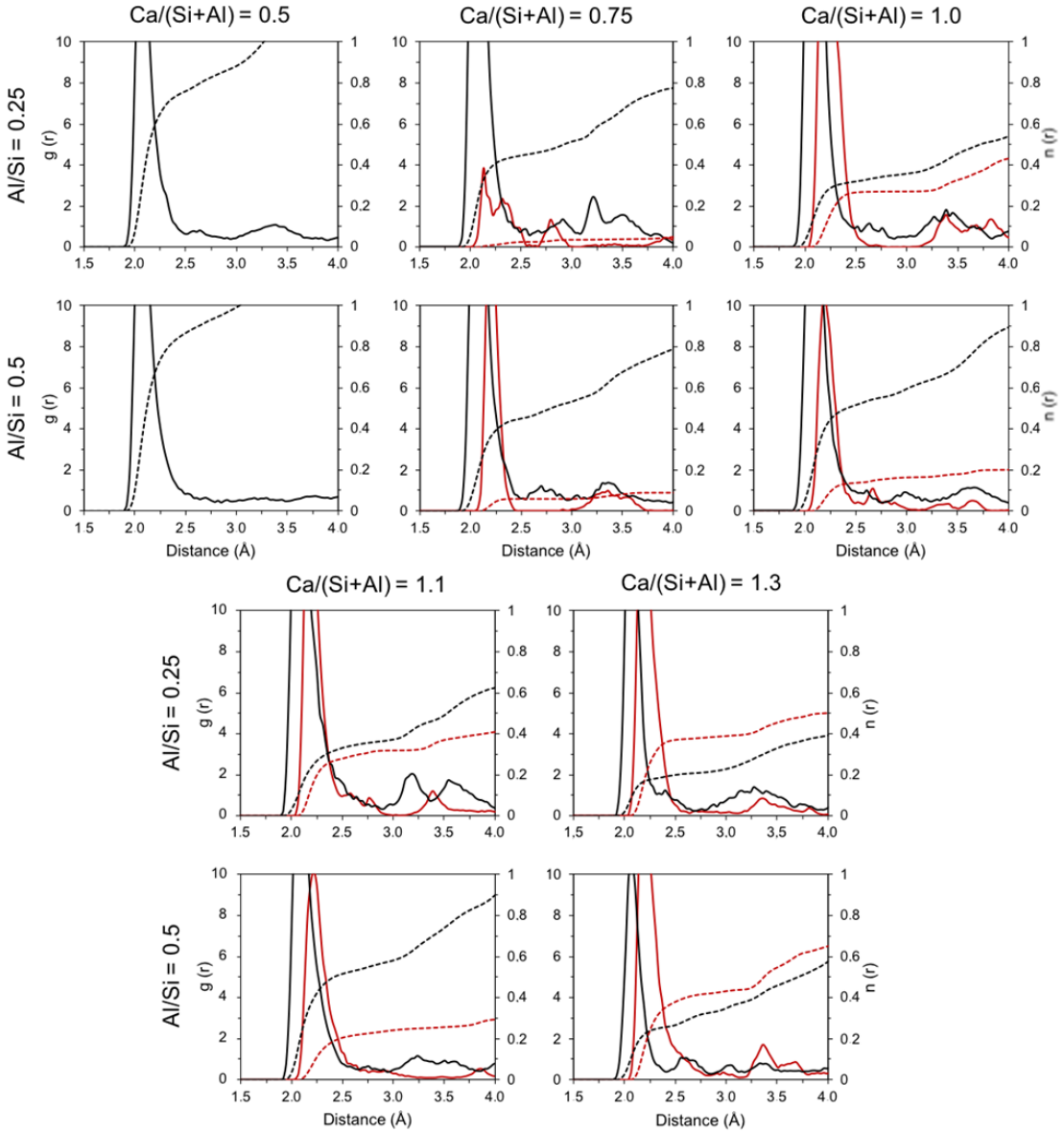

Figure 5.7 Radial distribution functions (continuous lines) and coordination numbers (dashed lines) for O_{PVA}-Na (in black) and O_{PVA}-Ca (in red) for the C-(N-)A-S-H with Ca/(Si+Al) ratios of 0.5, 0.75, 1.0, 1.1 and 1.3 at Al/Si ratios of 0.25 and 0.5.

The plots in Figure 5.7 show sharp peaks at distances around 2.2 Å and 2.0 Å for the RDFs of O_{PVA}-Ca (in red) and O_{PVA}-Na (in black), respectively. These peaks correspond to the first coordination sphere of the oxygen atoms of the PVA molecule (O_{PVA}) to the cations from C-(N-)A-S-H. The positions of the peaks indicate the interaction distances of O_{PVA}-Ca and O_{PVA}-Na. It must be noted that neither the Ca/(Si+Al) ratio nor the Al/Si ratio affects the O_{PVA}-Ca and the O_{PVA}-Na interaction distances. The sharp first peaks in the RDFs O_{PVA}-Ca and O_{PVA}-Na indicate the affinity of Ca and Na to the PVA molecules since the possibility of finding Ca and Na cations near the PVA molecule is much higher than elsewhere in the composite.

The coordination number (CNs) of the oxygen atoms from the PVA molecule to Ca and Na cations (O_{PVA}-Ca and O_{PVA}-Na) at the studied Ca/(Si+Al) ratios for two Al/Si ratios (0.25 and 0.5) are presented in Figure 5.8. With Ca/(Si+Al) ratios increasing from 0.75 to 1.3, the CNs of the O_{PVA}-Ca grow progressively from 0.03 to 0.43 Ca cations per O_{PVA}. The increasing CNs of O_{PVA}-Ca provokes a slight decrease in the CNs of O_{PVA}-Na as the Ca/(Si+Al) ratio rises. This is because Ca, compared to Na, is a divalent cation (Ca^{2+}) that has stronger electrostatic interactions with the negatively charged hydroxyl groups of the PVA fiber (OH^-). In this case, it is conceivable that the Ca cations could displace some of the Na cations. Notably, compared to other C-(N-)A-S-H structures, the C-(N-)A-S-H structure with a Ca/(Si+Al) ratio of 0.5 has a much higher CN of O_{PVA}-Na. Considering that the Ca/(Si+Al) ratio of 0.5 suggests the complete replacement of the interlaminar Ca by Na (1 Ca^{2+} by 2 Na^+) in the C-(N-)A-S-H structure, the higher CNs of O_{PVA}-Na are because of the higher total Na content compared to that in other C-(N-)A-S-H structures. Regarding the effect of the Al/Si ratio on CNs, the CNs of O_{PVA}-Na increase significantly due to the increasing amount of Na at high Al/Si ratios (0.5), whereas, the CNs of O_{PVA}-Ca are not affected significantly.

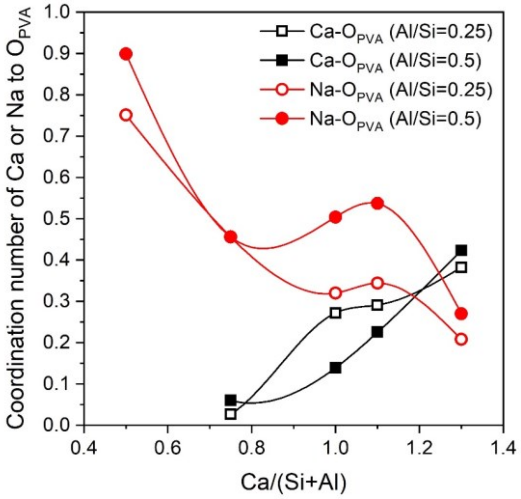

Figure 5.8 Coordination numbers of the oxygen atoms of PVA molecule O_{PVA} to Na (in red) and Ca (in black) for the studied PVA/C-(N-)A-S-H composites.

The affinity of Ca and Na to the PVA molecule in the PVA/C-(N-)A-S-H composite was further analyzed by performing an *in situ* polymerization of the C-(N-)A-S-H in the presence of a PVA molecule as shown in Figure 5.9 (a). It should be noted that the precursors are present in the appropriate proportion to reach the average Ca/(Si+Al) ratio of 1.3 and the Al/Si ratio of 0.5. The Ca/(Si+Al) ratio of the reaction product is monitored as a function of its distance to the

PVA molecule and the result is shown in Figure 5.9 (b). It can be seen that the Ca/(Si+Al) ratio is significantly higher around the PVA molecule than the average (1.3). This observation confirms that the incorporation of PVA polymer leads to the formation of a reaction product with higher Ca/(Si+Al) ratios.

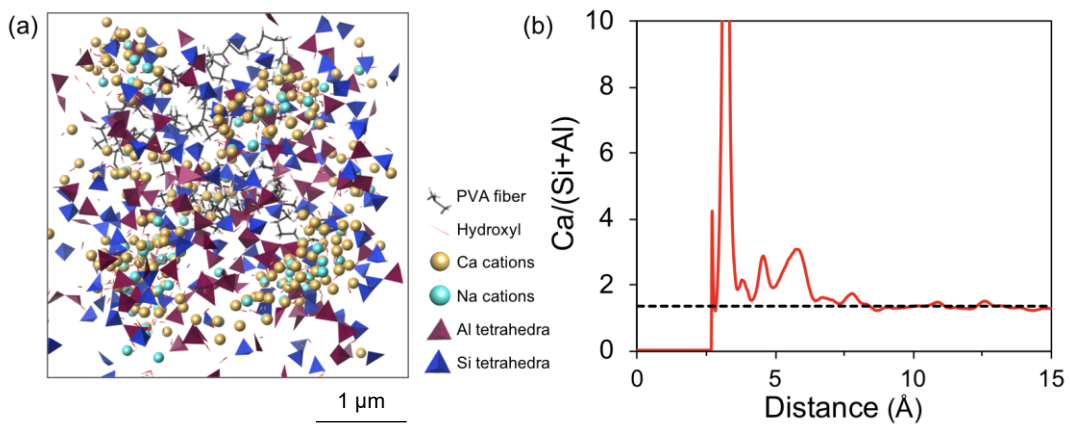

Figure 5.9 (a) Snapshot of the *in situ* polymerization process of C-(N-)A-S-H gel around a PVA molecule in a simulation box (4 x 4 x 4 nm^3) with an average Ca/(Si+Al) ratio of 1.3 and Al/Si ratio of 0.5. (b) Evolution of the Ca/(Si+Al) ratio as a function of the distance from the oxygen atoms of the PVA molecule. The black dashed indicates the average Ca/(Si+Al) ratio of 1.3.

5.3.3 Hydrogen bonds between PVA molecule and C-(N-)A-S-H surface.

Besides the interactions between the PVA molecule and the C-(N-)A-S-H surface through the Ca and Na cations, the formation of hydrogen bonds between the hydroxyl groups of the PVA molecule and the oxygen atoms from the C-(N-)A-S-H surface is also possible [270]. The RDFs and CNs of hydrogen atoms in the hydroxyl groups in the PVA molecule (H_{PVA}) to the oxygen atoms of the C-(N-)A-S-H surface ($O_{C\text{-}(N\text{-})A\text{-}S\text{-}H}$) are calculated and plotted in Figure 5.10. The main peak of the RDFs for H_{PVA} to $O_{C\text{-}(N\text{-})A\text{-}S\text{-}H}$ is found at a distance of around 1.8 Å. This distance matches the characteristic distance between the donor H atoms and the acceptor O atoms in hydrogen bonds [290, 291].

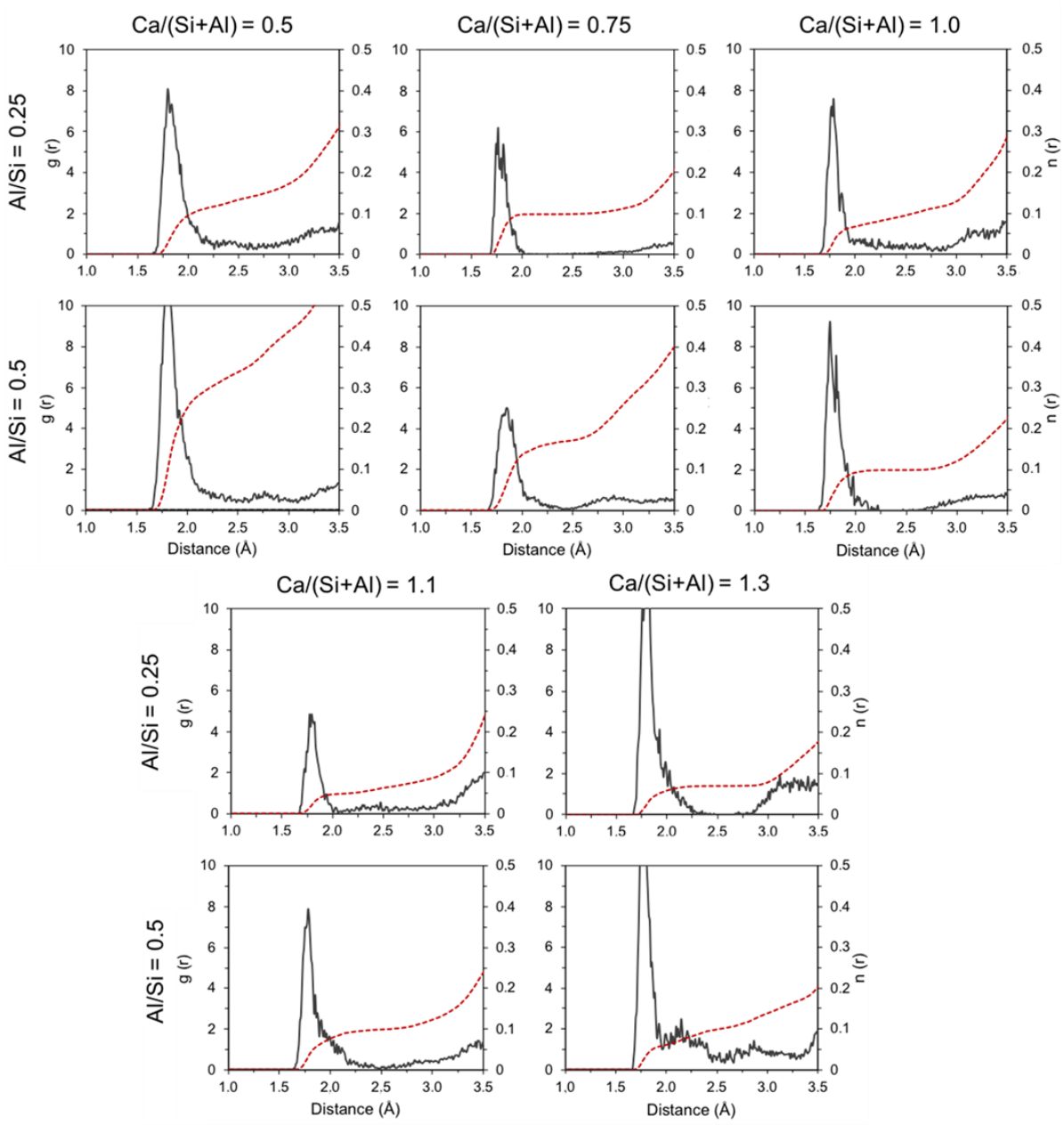

Figure 5.10 Radial distribution functions (black continuous lines) and coordination numbers (red dashed lines) for H_{PVA} to $O_{C\text{-}(N\text{-})A\text{-}S\text{-}H}$ with Ca/(Si+Al) ratios of 0.5, 0.75, 1.0, 1.1, and 1.3 at Al/Si ratios of 0.25 and 0.5.

As shown in Figure 5.11, the CNs of the donor H from the PVA molecule (H_{PVA}) to the acceptor O atoms from the C-(N-)A-S-H surface ($O_{C\text{-}(N\text{-})A\text{-}S\text{-}H}$) decrease with increasing Ca/(Si+Al) ratio. With the same Ca/(Si+Al) ratio, however, the CNs of H_{PVA} to $O_{C\text{-}(N\text{-})A\text{-}S\text{-}H}$ is found to be higher for a higher Al/Si ratio of 0.5. These findings suggest that there is a higher number of hydrogen bonds between the PVA molecule and the C-(N-)A-S-H at low Ca/(Si+Al) ratios and high Al/Si ratios. The reduction of CNs with increasing Ca/(Si+Al) ratios is attributed to the higher content of Ca cations. The presence of Na cations, on the other hand, does not hinder the formation of the hydrogen bonds between the PVA and the C-(N-)A-S-H surface. This is because Ca, compared to Na, is a divalent cation (Ca^{2+}) that has stronger electrostatic interactions with the negatively charged hydroxyl groups of the PVA fiber (OH^-). Higher Ca content could prevent

the formation of hydrogen bonds by their interaction with the hydroxyl groups of the PVA molecule.

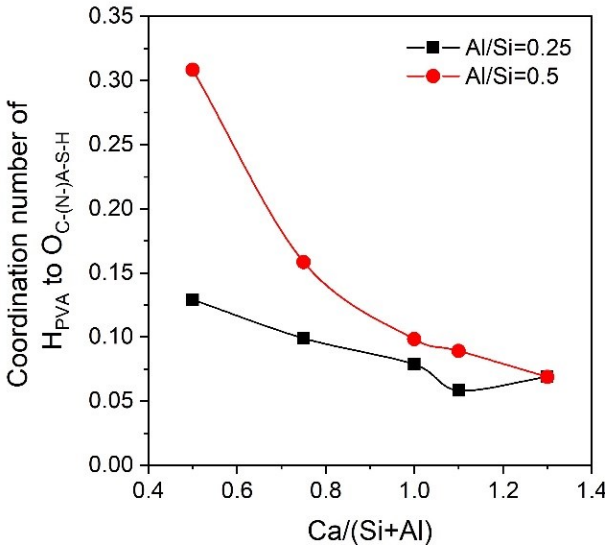

Figure 5.11 Coordination numbers of donor hydrogen atoms from PVA molecule (H_{PVA}) to the oxygen atoms of C-(N-)A-S-H surface ($O_{C-(N-)A-S-H}$) for the studied PVA/C-(N-)A-S-H composites.

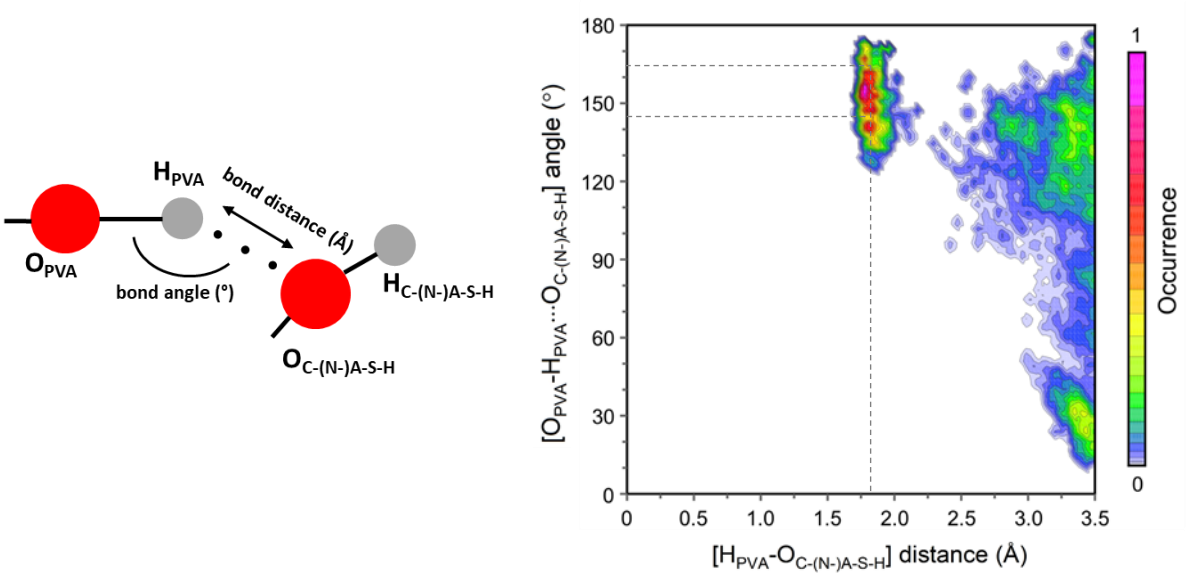

Figure 5.12 Combined distribution function (CDF) of hydrogen bond distances and angles between the PVA molecule and the C-(N-)A-S-H surfaces. The area in reddish colors corresponds to the most probable configurations, while the bluish ones are related to the less probable configurations.

The strength of these bonds is strongly dependent on the bonding angle [292]. It is important, therefore, to know the angle of the hydrogen bonds between the hydroxyl groups of the PVA molecule and $O_{C-(N-)A-S-H}$ at the C-(N-)A-S-H surface. The maximum strength is achieved when the three atoms involved in the hydrogen bond are aligned so that the donor H points directly to the acceptor electron pair [293]. To analyze the most probable distances and angles for

hydrogen bonding in the PVA/C-(N-)A-S-H composites, a combined distribution function (CDF) made of the RDF of $H_{PVA}\cdots O_{C\text{-}(N\text{-})A\text{-}S\text{-}H}$ and the ADF of the $O_{PVA}\text{-}H_{PVA}\cdots O_{C\text{-}(N\text{-})A\text{-}S\text{-}H}$ was determined. The CDF results, along with a schematic illustration of the hydrogen bond, are shown in Figure 5.12. The most probable distance between donor H_{PVA} atoms and acceptor $O_{C\text{-}(N\text{-})A\text{-}S\text{-}H}$ atoms is around 1.8 Å. On the other hand, the most probable angle defined by those atoms and the donor oxygen atom from PVA (O_{PVA}) is between 145° and 165°. Thus the $O_{PVA}\text{-}H_{PVA}\cdots O_{C\text{-}(N\text{-})A\text{-}S\text{-}H}$ atoms are not fully aligned with the bond angle of 180°. Despite the structural and chemical differences, the most probable distances and angles for the hydrogen bonds are in the same range for all the composites analyzed in this study.

5.3.4 Adhesion mechanism of PVA in C-(N-)A-S-H

To explore the adhesion mechanism of a PVA molecule to C-(N-)A-S-H, the adsorption enthalpy values for the PVA/C-(N-)A-S-H composites with different Ca/(Si+Al) ratios and Al/Si ratios of 0.25 and 0.5 were calculated. The results are shown in Figure 5.13 in two different units (kJ/m^2 and kJ/g). It can be seen that the adhesion of the PVA molecule to the C-(N-)A-S-H is more favorable for a higher Ca/(Si+Al) ratio for both Al/Si ratios (0.25 and 0.5). This can be attributed to the higher Ca content for higher Ca/(Si+Al) ratios, allowing the development of more electrostatic interactions between those cations and the PVA fibers. Additionally, stronger adsorption is observed with a lower Al/Si ratio, particularly when the Ca/(Si+Al) ratio is high (>1.0). The higher CNs of the PVA molecule to the Na ions at high Al/Si ratios may be responsible for the weakening of the adhesion. This is because the electrostatic interactions of the PVA molecule with Na, a monovalent cation, are much weaker than those with Ca, a divalent cation.

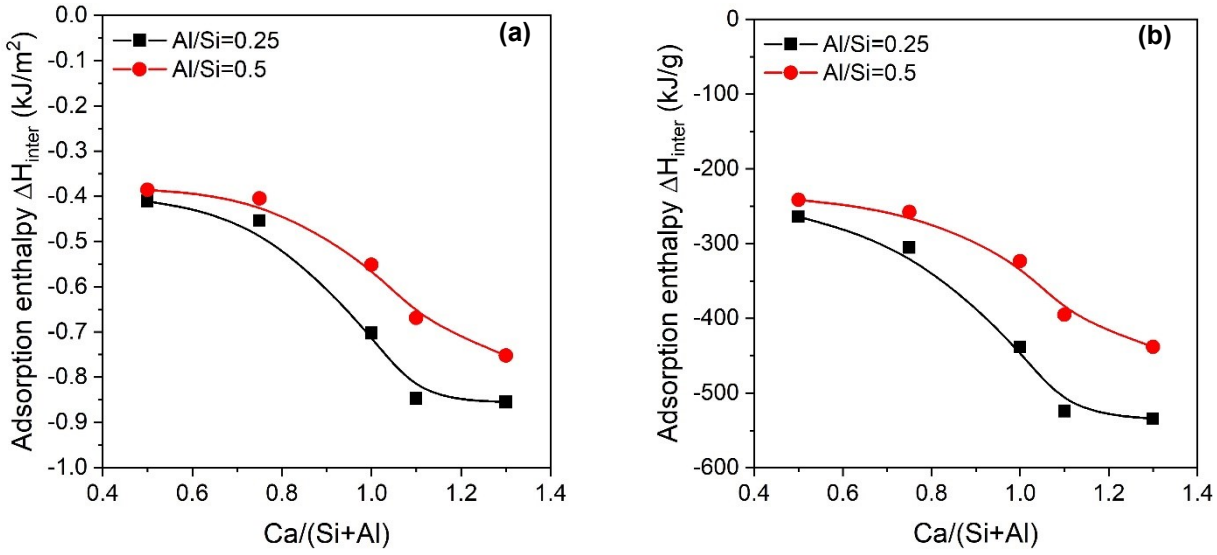

Figure 5.13 Adsorption enthalpies in (a) kJ/m^2 and (b) kJ/g of PVA molecule for the composites with Al/Si ratio of 0.25 (black squares) and 0.5 (red dots) at the considered Ca/(Si+Al) ratios.

In addition to the interaction of the PVA molecule with the cations, there are also hydrogen bonds between the oxygen atoms from the C-(N-)A-S-H surface and the hydroxyl groups of the PVA molecule. This study describes the hydrogen bonds as Van der Waals interactions.

Despite the lack of consensus on the nature of the hydrogen bonds, treating them as Van der Waals interaction helps to estimate the contribution of hydrogen bonds to the adsorption enthalpy. To this effect, the enthalpy of a single hydrogen bond for the most probable $H_{PVA}\cdots O_{C\text{-}(N\text{-})A\text{-}S\text{-}H}$ distance (1.8 Å) and $O_{PVA}\text{-}H_{PVA}\cdots O_{C\text{-}(N\text{-})A\text{-}S\text{-}H}$ angle (160°) according to Figure 5.12 was calculated to be -4.84 kcal mol^{-1}. This value is similar to the hydrogen bonds formed between water molecules (5.0 kcal mol^{-1}) and its strength is considered weak [292].

The adsorption enthalpy of the hydrogen bonds between the PVA molecule and C-(N-)A-S-H with different Al/Si and Ca/(Si+Al) ratios were also calculated by considering the number of the H_{PVA} atoms interacting with the $O_{C\text{-}(N\text{-})A\text{-}S\text{-}H}$ atoms. As shown in Figure 5.14, the adsorption enthalpy of the hydrogen bonds decreases as the Ca/(Si+Al) ratio rises regardless of the change in Al/Si ratio. However, this adsorption enthalpy is higher in PVA/C-(N-)A-S-H composite with a higher Al/Si ratio. Notably, these trends are in agreement with the CNs of H_{PVA} to $O_{C\text{-}(N\text{-})A\text{-}S\text{-}H}$ in Figure 5.11.

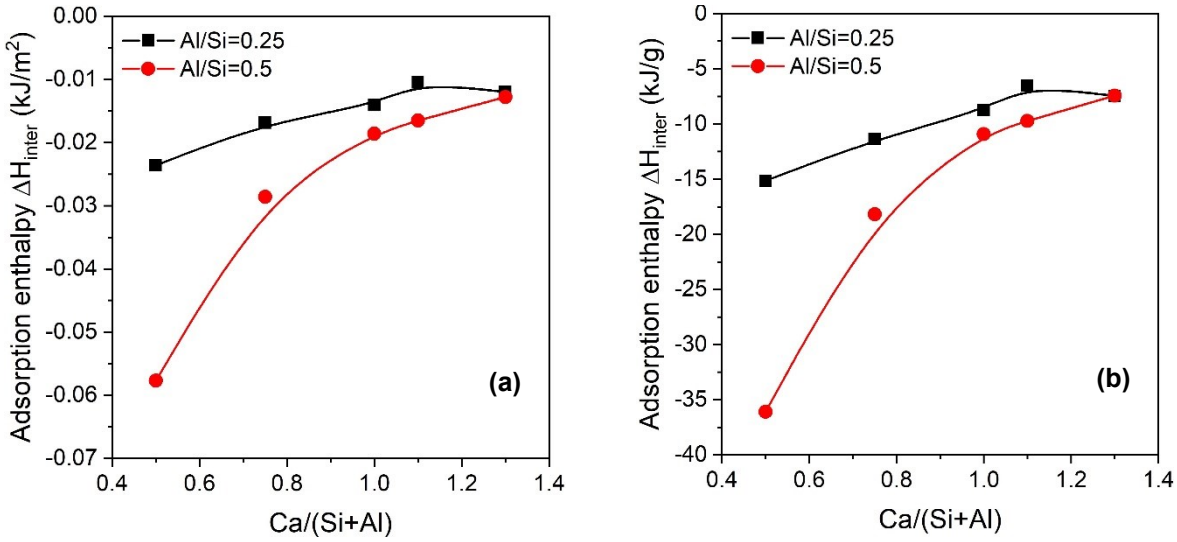

Figure 5.14 Adsorption enthalpies in (a) kJ/m^2 and (b) kJ/g attributed to the hydrogen bonds between the PVA molecule and the C-(N-)A-S-H for the composites with an Al/Si ratio of 0.25 (black squares) and 0.5 (red dots) at the considered theoretical Ca/(Si+Al) ratios.

The contribution of the hydrogen bonds to the total adsorption enthalpy ranges from 1.3% to almost 15%. The strongest hydrogen bonds are found in the composites with an Al/Si ratio of 0.5 and a Ca/(Si+Al) ratio of 0.5. Therefore, the contribution of the hydrogen bonds to the adhesion is only significant when the ionic concentration in the interlaminar space is low. This happens when the PVA/C-(N-)A-S-H composite has a low Ca/(Si+Al) ratio and high Al/Si ratio. At high Ca/(Si+Al) ratios, the adsorption of the PVA molecule in the C-(N-)A-S-H is almost exclusively electrostatic.

5.3.5 Experimental evidence of adhesion properties and mechanism

In this section, the high affinity of Ca^{2+} and Na^{+} cations to the PVA molecule is discussed and compared with the experimental results in Chapter 4 (i.e., the formation of Ca-rich reaction products in the ITZ). Furthermore, the adsorption enthalpy of PVA molecule in C-(N-)A-S-H

with different Ca/(Si+Al) and Al/Si ratios are compared with the chemical bonding energy G_d determined from single fiber pullout tests.

5.3.5.1 Ca-rich reaction product in the ITZ

As previously shown in Chapter 4, the reaction products and the element spatial distribution at the PVA fiber/matrix interface were studied by EDX element mapping of the ITZ. The EDX element mapping (see Figure 4.9) depicts a rim of Ca-rich reaction products with high brightness adjacent to the PVA fiber. This indicates a higher Ca content in the rim region. Other elements, including Si and Al, show no preferential spatial distribution at the PVA fiber/matrix interface. Furthermore, the EDX line analysis (see Figure 4.11) reveals the element spatial distribution and element ratios of reaction products within ITZ. A substantial decline of Si along the line into the PVA fiber region is observed. In contrast, the concentration of Ca experiences a marked increase in the ITZ before it continuously decreases into the fiber region. Accordingly, the atomic ratios of both Ca/Si and Ca/(Si+Al) increase significantly within the ITZ and reach the maximum exactly at the fiber/matrix interface.

The abovementioned experimental results coincide well with the MD simulation results of the RDF and CNs of Ca to O_{PVA} as well as the *in situ* polymerization results (Section 5.3.1). All of them indicate a strong affinity of Ca^{2+} cations to the PVA fiber. These changes consequently resulted in the formation of Ca-rich C-(N-)A-S-H gel in the ITZ, viz. the high-Ca C-(N-)A-S-H phase confirmed previously in Chapter 4 (see Section 4.3.2.3). Unlike Ca, Na does not show affinity to the PVA fiber in the experimental results. This could be due to the very abundant concentration of Na in the pore solution throughout the formation of C-(N-)A-S-H gel in the AASF matrix [79]. The accumulation of this high-Ca C-(N-)A-S-H gel around PVA fiber could effectively enhance the adhesion between PVA fiber and the AASF matrix and is thereby essential for interface modification for SHGC.

5.3.5.2 Chemical bonding energy between PVA fiber and AASF matrix

The adhesion between PVA fiber and the AASF matrix has been experimentally quantified with single-fiber pullout tests (Chapter 4). This adhesion, also widely known as the chemical bonding energy G_d between PVA fiber and matrix, can be calculated using Equation 5.4 [138] (See also Section 4.3.1.1).

$$G_d = \frac{2(P_a - P_b)^2}{\pi^2 E_f {d_f}^3} \tag{5.4}$$

where E_f and d_f are the elastic modulus and diameter of the PVA fiber, respectively. As shown by the representative single fiber pullout curve in Figure 4.5 (a), P_a is the load up to full debonded length and P_b is the load when the fiber begins to slip.

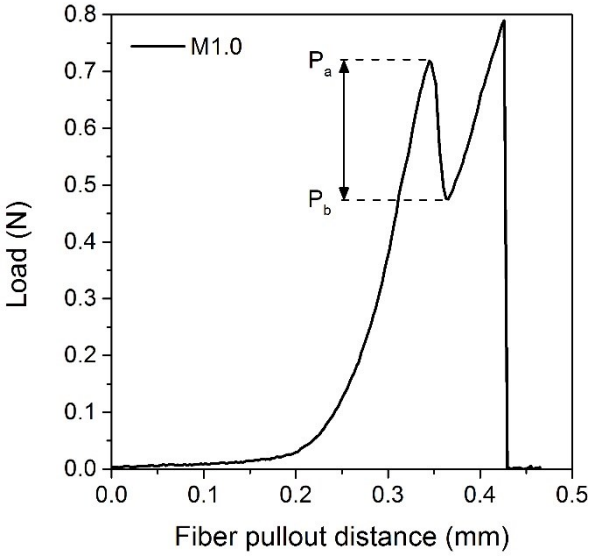

(a) Representative single fiber pullout curve

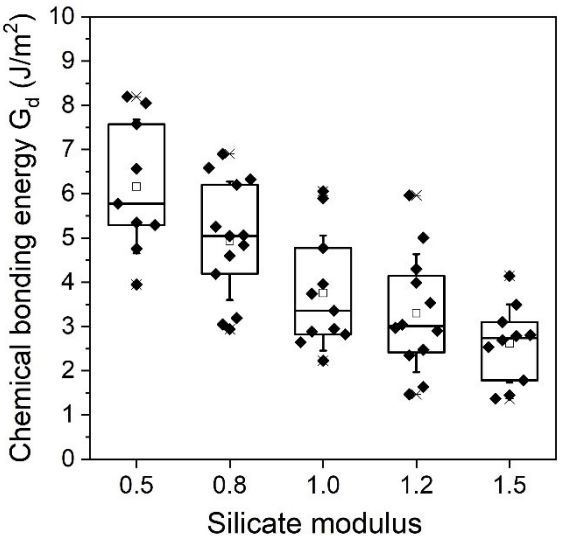

(b) Chemical bonding energy G_d from experiment

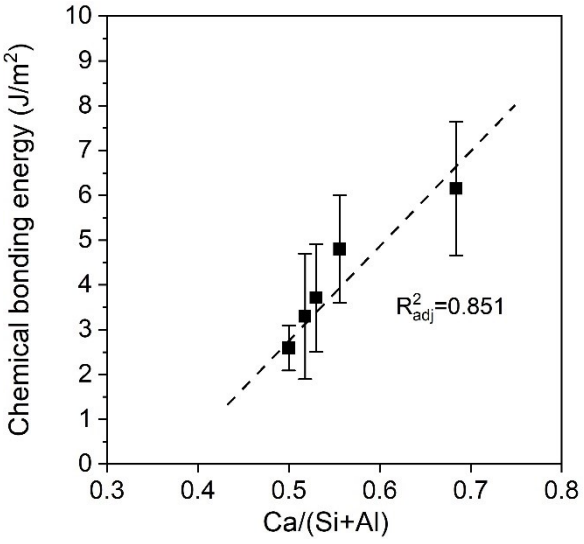

(c) G_d vs Ca/(Si+Al) ratio of C-(N-)A-S-H gel determined by EDX analysis

Figure 5.15 (a) Representative single-fiber pullout curves of PVA fiber in M1.0 AASF matrix; (b) Chemical bonding energy (G_d) of PVA fiber in M0.5-M1.5 S50 AASF matrices determined from at least 16 measurements. The box plot illustrates the median value (-), the mean (□), the values at 25% and 75% (box edges), the standard deviation (Whiskers); and (c) G_d as a function of the Ca/(Si+Al) ratio of C-(N-)A-S-H gel determined by EDX analysis.

The chemical bonding energy G_d of PVA fiber in M0.5-M1.5 S50 AASF matrices is summarized in Figure 4.5 (b). The chemical bonding energy G_d decreases from 6.2 to 2.9 J/m^2 with increasing silicate modulus M_s from 0.5 to 1.5. Notably, as shown in Figure 4.5 (c), the experimentally-attained G_d is found to be positively correlated with the Ca/(Si+Al) ratio of the C-(N-)A-S-H gel in matrices (see also Section 4.3.1.1).

This experimentally-attained G_d versus Ca/(Si+Al) ratio in Figure 4.5 (c) is then further compared with the adsorption enthalpy simulated by the MD simulation versus Ca/(Si+Al) ratio in Figure 5.13. The comparison is shown in Figure 5.16. It is clear that, with an increasing Ca/(Si+Al) ratio, G_d has a similar trend with the adsorption enthalpy. The latter also rises primarily with increasing Ca/(Si+Al) ratio of the simulated C-(N-)A-S-H structures.

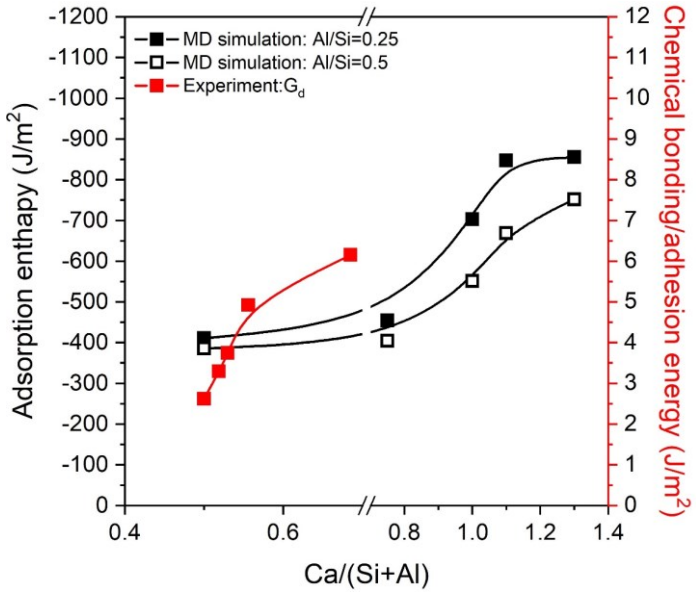

Figure 5.16 Comparison between experimental-attained chemical bonding energy G_d and MD simulated adsorption enthalpy of PVA fiber in C-(N-)A-S-H matrix.

Despite their similar trend, the values of the simulated adsorption enthalpy and the experimentally-attained G_d have a certain gap with a difference in magnitude of 100 times regardless of the Al/Si ratio of C-(N-)A-S-H structures. This difference between G_d and the corresponding adsorption enthalpy could be related to the coverage of C-(N-)A-S-H on the PVA fiber surface. In the MD simulation, all possible electrostatic interactions between Ca^{2+} from C-(N-)A-S-H to PVA molecule have been considered. Compared to the contribution of hydrogen bonding, they have the main contribution to adhesion. In reality, however, the PVA fiber surface is not fully covered by C-(N-)A-S-H gel. This is due to the heterogeneous distribution of reaction products. In addition, the oiling treatment (1.2%) on the fiber surface can hinder the coverage as well. In fact, the fiber/matrix ITZ is found to be more porous than the matrix (Section4.3.2.1). All the above-mentioned differences contributed to a low rate of effective coverage of C-(N-)A-S-H over the PVA fiber. The G_d acquired experimentally by single-fiber pullout test then only relates to the effective bonding energy per m^2 (J/m^2). Therefore, it is reasonable that the experimentally-attained G_d has a lower value in comparison to the simulated adsorption enthalpy. As a result, the direct linking of adhesion properties in MD simulation to the mesoscale bonding G_d is only possible with an essential upscaling process.

From the above discussion, the MD simulation proves to be a useful tool to study the adhesion of PVA fiber in C-(N-)A-S-H gel. It provides a fundamental understanding of the adhesion mechanism and helps to determine the most important factors that govern the adhesion properties, i.e., the electrostatic interaction between PVA fiber surface and C-(N-)A-S-H gel. Although the strength of the adhesion, i.e., the chemical bonding energy G_d, cannot be precisely predicted using MD simulation, the consistency between the experiment and MD simulation suggests that the chemical composition of C-(N-)A-S-H predominantly affects the PVA/C-(N-)A-S-H adhesion properties. These findings suggest that by the proper mixture design of AASF, the tailoring of the interface property can be achieved. Particularly, this information is important for the development of future PVA-based SHGC, the performance of which is largely governed by the adhesion properties.

5.4 Conclusions

This chapter aims to investigate the adhesion mechanism and the related adhesion properties of PVA fiber to C-(N-)A-S-H gel formed in alkali-activated slag/fly ash (AASF) matrix. Both the molecular dynamics (MD) simulation and the experimental characterization were carried out. Various Ca/(Si+Al) and Al/Si ratios of C-(N-)A-S-H gel were considered. Their impacts on the adhesion energy and the spatial distribution of elements of C-(N-)A-S-H to PVA were simulated and experimentally verified. Based on the results and discussions of this study, the following conclusions can be drawn:

- The origin of adhesion between PVA and C-(N-)A-S-H gel at high Ca/(Si+Al) ratios (> 1) is almost entirely due to the electrostatic interactions between the hydroxyl group (OH^-) in PVA and the Ca^{2+} and Na^+ cations within C-(N-)A-S-H gel. The contribution to the adhesion due to the hydrogen bonding between the PVA molecule and C-(N-)A-S-H gel is only significant at low Ca/(Si+Al) ratios (< 1).

- The polarity of the PVA molecule induced by the hydroxyl functional group and its interaction with C-(N-)A-S-H presents a high affinity of Ca^{2+} and Na^+ cations to the PVA molecule. Accordingly, the formation of Ca-rich C-(N-)A-S-H gel, with considerably higher Ca/(Si+Al) and Ca/Si ratios and similar Al/Si ratios, were detected at the ITZ near the PVA fiber in comparison to those of the AASF matrix.

- The experimentally-attained chemical bonding energy G_d coincides well with the adsorption enthalpy of PVA in C-(N-)A-S-H calculated by MD simulation. In both cases, the adhesion enhances primarily by increasing the Ca/(Si/+Al) ratio of C-(N-)A-S-H gel.

- The difference between the experimentally-attained chemical bonding energy G_d and simulated adhesion enthalpy can be explained by the effective coverage of C-(N-)A-S-H gel on the PVA fiber surface.

- MD simulation is a useful tool to clarify the adhesion mechanism of PVA fiber in C-(N-)A-S-H gel. It helps to understand the adhesion mechanism and at the same time helps to determine the most important factors that govern the adhesion properties.

The study in this chapter provides further insights into the adhesion mechanism of PVA fiber to C-(N-)A-S-H gel formed in the AASF system and contributes to the tailoring

strategies for the design of fiber-reinforced composites with enhanced performance through proper mixture design. These findings are particularly valuable for the development of PVA-based strain-hardening geopolymer composite (SHGC), which will be elaborated on in Chapter 6.

Chapter 6

Micromechanics-guided development of a slag/fly ash-based strain-hardening geopolymer composite (SHGC)[12]

6.1 Introduction

The performance of SHGC is governed by its three main components, which are the matrix, the fiber, and the fiber/matrix interface. Besides the influence of the mechanical properties of PVA fiber, both matrix fracture properties [294] and the fiber/matrix interface properties [139] play crucial roles in determining the crack-bridging and crack propagation, and consequently the strain-hardening and multiple-cracking behavior of SHGC [20, 21]. The research results in Chapters 3, 4, and 5 all indicate that both the fracture properties and the interface properties are governed by the chemical composition of the AASF. They are primarily determined by the Ca/Si and Ca/(Si+Al) ratio of the C-(N-)A-S-H gel. The chemical composition of the reaction products could be effectively altered by changing the silicate modulus M_s (Si) of the activator as well as the slag content (Ca). These findings already serve as important knowledge basis for effective modification of matrix and interface properties to achieve the required composite behavior of SHGC. However, challenges still exist regarding the mixture design of SHGC because it involves even more factors to be considered compared to traditional SHCC design [21]. As a multi-factor optimization problem, the development of SHGC using the conventional trial-and-error method is extremely inefficient and time-consuming.

The micromechanical model developed by Li et al. [30, 295], providing a solid theoretical design basis, has proven also effective in previous studies on SHGC [23, 117]. However, in most of these studies, this model was applied to earlier developed mixtures to explain the origin of strain-hardening behavior. Research on using the micromechanical model as an effective design tool to guide the development of SHGC from scratch is still very limited.

This chapter aims to develop a slag/fly ash-based SHGC following the guidance from micromechanical modeling for the composite mixture design. To this end, the experimentally-attained physical properties of fiber, matrix (Chapter 3), and fiber/matrix interface (Chapter 4) served as input for the micromechanical modeling. The micromechanical modeling was firstly conducted to assist in choosing suitable fiber volume and fiber length in the mixture design. Once they were chosen, the micromechanical model then served as a predictive tool to evaluate the strain-hardening potential of the designed SHGC mixtures. Finally, the

[12] This chapter is partially based on:

Zhang, S., Li, V.C., & Ye, G., 2020. Micromechanics-guided development of a slag/fly ash-based strain-hardening geopolymer composite. Cement and Concrete Composites 109, 103510.

performance of the designed SHGC mixtures was experimentally evaluated using uniaxial tensile tests. In this way, the feasibility and effectiveness of using micromechanical modeling for the development of SHGC are also demonstrated and experimentally verified.

6.2 Micromechanics-based design approach

6.2.1 The starting matrix designs

For the development of SHGC, the solid precursors are ground granulated blast furnace slag and Class F fly ash according to ASTM 618 [148], produced locally in the Netherlands. The chemical composition and physical properties of the solid precursors have been given in Section 3.2.1. The fiber is a polyvinyl alcohol (PVA) fiber (RECS 15, Kuraray) with a 1.2% oiling treatment on the surface. Its chemical structure and physical and mechanical properties have been given in Section 4.2.1.

As discussed in Chapter 3 and 4, the S50 mixtures (slag 50 wt.%) have generally higher chemical bonding energy G_d and fracture toughness K_{Ic} (J_{tip}) than the S30 mixtures (slag 30 wt.%). According to previous studies, high G_d and K_{Ic} (J_{tip}) are not favorable for the strain-hardening behavior of conventional SHCC [43]. Because of this, the mixture design in this study is limited to S30 mixtures. Since the silicate modulus M_s of the activator is an important factor that significantly affects both the fracture properties and almost all interface properties of the matrix, 6 different M_s (0, 0.5, 0.8, 1.0, 1.2, and 1.5) of alkaline activator are considered in this Chapter. The mixtures were named M0, M0.5, M0.8, M1.0, M1.2, and M1.5. These AASF matrices are identical to the ones studied in both Chapter 3 and 4. The Na_2O content (wt.%) with respect to binder mass was kept constant at 4%. The water-to-binder (w/b) ratio was kept constant at 0.32 to guarantee adequate workability of all mixtures. Mixture proportions of the AASF matrices are presented in Table 6.1.

Table 6.1 Matrix mixture proportions of AASF matrices for SHGC (with respect to total binder mass)

Mixture	Precursor (wt.%)		Alkaline activator (wt.%)		
	Slag	Fly ash	Na_2O	SiO_2	Water
M0	30	70	4	0	32
M1.5	30	70	4	1.94	32
M0.8	30	70	4	3.1	32
M1.0	30	70	4	3.88	32
M1.2	30	70	4	4.65	32
M1.5	30	70	4	5.8	32

For mixture preparation, the solid precursors were first dry-mixed for 5 min at a low speed using a HOBART® mixer. Alkaline activator solution was then added gradually into the mixer and the batches were mixed for an additional 5 min at medium speed. The fresh paste mixtures were cast in polystyrene prism molds (40×40×160 mm^3) or cylindrical molds of 55 mm in diameter (D) and 110 mm in length (L). All mixtures were then compacted by vibration and sealed with plastic wrap. The samples were cured in a climate room (20 °C and ≥98% RH) before testing.

6.2.2 Micromechanics criteria for composite strain-hardening

To ensure that strain-hardening occurs in SHGC reinforced with randomly oriented shortcut fibers, the strength- and energy-based PSH criteria proposed by Kanda and Li [79] have to be met. A more detailed introduction of these two PSH criteria is already given in Section 2.3.1.

1. Strength criterion for crack initiation

The first criterion is the strength-based criterion for crack initiation. It is formulated as Equation (6.1):

$$\sigma_{fc} \leq \sigma_0 \tag{6.1}$$

where σ_{fc} is the tensile strength of the matrix (first crack strength), σ_0 is maximum fiber bridging stress. When the fiber content is small, J_{tip} can be estimated as K_{Ic}^2/E_m.

2. Energy criterion for flat-crack propagation

The second criterion is the energy-based criterion to guarantee flat crack propagation. It is formulated as Equation (6.2):

$$J_{tip} \leq \sigma_0\delta_0 - \int_0^{\delta_0} \sigma(\delta)d\delta \equiv J_b' \tag{6.2}$$

where J_{tip} is the crack-tip toughness of the matrix, and J_b' is the complementary energy.

If the strength criterion is not met, the composite will fail after the initiation of the first crack. On the other hand, violating the energy criterion results in Griffith-type crack propagation. This type of crack propagation will lead to an uncontrolled increase in the crack width, which results in the tension-softening behavior of the composite. The violation of either criterion prevents the composite to exhibit the strain-hardening behavior, but rather promotes a conventional strain-softening behavior.

Considering the inevitable material variability, e.g., heterogeneous fiber dispersion and flaw distribution, sufficient margins between σ_{fc} and σ_0, J_{tip} and J_b' have to be maintained to ensure that strain-hardening behavior occurs. In previous studies on SHCC, two purely empirical PSH indices for both strength and energy criteria have been used to reflect the probability of saturated strain-hardening behavior, namely the strength PSH index ($PSH_s=\sigma_0/\sigma_{fc}$) and the energy PSH index ($PSH_e=J_b'/J_{tip}$) [79]. Although not related quantitatively, the higher values of these two PSH indices indicate a greater probability of saturated strain-hardening behavior, and hence a better tensile strain capacity of the composite. From previous studies, a saturated strain-hardening performance of SHCC requires a $PSH_s \geq 1.5$ and a $PSH_e \geq 3.0$ [21, 79, 85, 86]. In this study, these two criteria are also used to judge if the designed SHGC mixture has the potential for a saturated strain-hardening behavior.

6.2.3 Experimental determination of micromechanical parameter values for the micromechanical modeling

To apply the micromechanical model, the determination of micromechanical parameters σ_{fc} and J_{tip} of the matrix and the fiber bridging properties σ_0 and J_b' are needed. In this study, σ_{fc} is directly obtained from the splitting tensile test. J_{tip} (=K_{Ic}^2/E_m) is calculated using the result of the fracture toughness test (K_{Ic}) and elastic modulus test (E_m). σ_0 and J_b' are determined from the σ-δ relationship simulated by micromechanical modeling using the experimentally-attained interface property values as input. In this study, these interface properties are obtained using a single-fiber pullout test.

6.2.3.1 Determination of matrix parameter values

The fracture toughness K_{Ic} was determined using three-point bending tests on a single-edge notched paste prism as described in Section 3.2.3. The 28-day elastic modulus was obtained using 40 × 40 × 160 mm^3 prismatic specimens following a set-up modified from ASTM C469 [153] as described in Section 3.2.3. Additionally, the crack tip toughness J_{tip}, i.e., the critical strain energy release rate, is calculated with the following Equation (6.3):

$$J_{tip} = \frac{{K_{Ic}}^2}{E_m} \tag{6.3}$$

where K_{Ic} is the fracture toughness of the matrix [MPa·m$^{1/2}$] and E_m is the elastic modulus of the paste [GPa].

The splitting tensile strength f_{st} was tested and was considered as the first crack strength σ_{fc} of the matrix. The f_{st} was measured with the set-up described in ASTM C496 Standard [296]. The tests were conducted using cylindrical specimens with 55 mm in diameter (D) and 110 mm in length (L). The f_{st} is calculated with Equation (6.4):

$$\mathrm{f}_{st} = \frac{2P_{Max}}{\pi LD}\left(1-\left(\frac{b}{D}\right)^2\right)^{2/3} \approx \frac{2P_{Max}}{\pi LD} \tag{6.4}$$

where P_{max} [N] is the maximum load, b [mm] is the bearing width of the wood strip, L [mm] and D [mm] are the length and diameter of the specimen, respectively. Since the bearing width *b* is rather small in comparison to the diameter *D*, the shape coefficient $(1-(b/D)^2)^{2/3}$ is considered to be equal to 1.

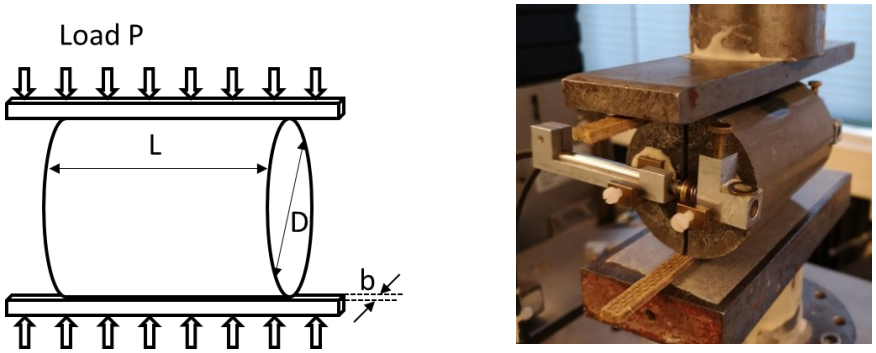

Figure 6.1 Splitting tensile test set-up.

The mechanical properties of the matrices as input parameter values at 28 days are summarized in Table 6.2.

Table 6.2 Matrix mechanical properties at 28 days as input parameters for micromechanical modeling

Mixture	Splitting tensile strength f_{st} (MPa)	Elastic Modulus E_m (GPa)	Fracture toughness K_{Ic} (MPa·m$^{1/2}$)	Crack tip toughness J_{tip} (J/m^2)
M0	2.6 ± 0.31	10.2 ± 0.23	0.325 ± 0.012	9.85 ± 0.54
M0.5	3.2 ± 0.38	14.1± 0.14	0.357 ± 0.013	9.54 ± 0.88
M0.8	2.9 ± 0.34	11.9 ± 0.33	0.229 ± 0.011	4.46 ± 0.45
M1.0	2.4 ± 0.27	12.4 ± 0.35	0.241 ± 0.009	4.70 ± 0.37
M1.2	2.0 ± 0.19	13.0 ± 0.30	0.194 ± 0.007	2.89 ± 0.21
M1.5	2.8 ± 0.47	9.2 ± 0.53	0.153 ± 0.004	2.54 ± 0.15

6.2.3.2 Determination of interface parameter values

The values of interface properties as input for the micromechanical model were determined using a single-fiber pullout test. The test set-up has been described in Section 4.2.3. The values of interface properties, i.e., chemical bonding energy G_d, initial frictional bond τ_0, and slip-hardening coefficient β, serve as input for the micromechanical model. The results are summarized in Table 4.2. Despite the data scatteredness, significant differences in interface properties (in particular G_d and τ_0) have been identified. Therefore, the average values of each interface property were used for micromechanical modeling.

Table 6.3 Fiber/matrix interface properties at 28 days as input parameters for micromechanical modeling

Mixture	Chemical bonding energy G_d (J/m^2)	Initial frictional bond τ_0 (MPa)	Slip-hardening coefficient β
M0	2.77 ± 1.11	2.13 ± 0.77	0.31 ± 0.01
M0.5	4.01 ± 1.41	3.38 ± 1.03	0.42 ± 0.08
M0.8	1.57 ± 0.84	1.81 ± 0.78	0.33 ± 0.11
M1.0	3.20 ± 1.26	2.80 ± 0.76	0.39 ± 0.12
M1.2	2.86 ± 1.08	4.01 ± 1.16	0.26 ± 0.09
M1.5	2.53 ± 1.04	3.13 ± 1.10	0.25 ± 0.06

6.2.4 Micromechanical modeling to guide the mixture design of SHGC

The micromechanical modeling was performed using a modified fiber bridging constitutive law developed by Yang et al. [80] and slightly modified by Ohno et al [21]. The model links the single fiber/matrix interaction to the fiber bridging behavior of a single crack. A brief introduction to micromechanical modeling has been given in Section 2.3.2. Additionally, a detailed derivation of the analytical scale-linking process of the micromechanical model is provided in Appendix A.

6.2.4.1 Input parameters for micromechanical modeling

The input parameters for the micromechanical model are summarized in Figure 6.2. The experimentally determined micromechanical parameter values of matrix and interface presented in Section 6.2.3 served also as modeling input.

In the simulation, the micro-spalling [82] and the Cook-Gordon effect [83] were not taken into consideration. This is because their effect on the simulated result was found to be insignificant in the preliminary parameter sensitivity study. The two-way pullout mechanism was considered here to improve the accuracy of the crack opening width prediction [85]. The fiber distribution in the matrix is considered two-dimensional. The apparent strength of the PVA fiber used for micromechanical modeling is lower than its true tensile strength, due to the surface damage caused by interaction with a rigid matrix during the debonding and pullout process [297]. This effect is considered using the strength reduction factor (f') [298]. Besides, the inclination angle (φ) of the fiber to the crack plane will also significantly influence the simulated σ-δ relationship. This effect can be reflected by the snubbing coefficient (f) [297]. In this study, the apparent strength of 1092 MPa of PVA fiber, f =0.33, and f'=0.2 were adopted from previous studies [21, 80, 139, 297, 298]. These values have been estimated from experimental results in cementitious systems and used in previous SHGC designs [21].

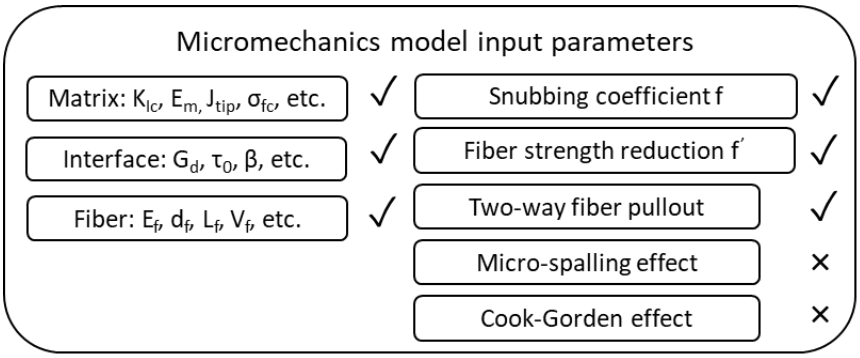

Figure 6.2 Input parameters for the micromechanical model. Input parameters values are given in Table 6.2 and Table 4.2.

6.2.4.2 Output of micromechanical modeling

The most important results from the micromechanical modeling are the fiber bridging stress versus crack opening (σ-δ) relationships of single crack bridged by fibers. In the simulated σ-δ relationships, the spatial randomness and the orientation of fiber are taken into consideration. This is achieved by adopting probability density functions that describe the spatial variability of

the fibers. Mathematically, the constitutive law of the σ−δ relationship is expressed as the following Equation (2.4):

$$\sigma(\delta) = \frac{V_f}{A_f}\int_{\varphi_0}^{\varphi_1}\int_{z=0}^{(L_f/2)\cos\varphi} P(\delta, L_e)g(\varphi)p(\varphi)p(z)dzd\varphi \tag{6.5}$$

where V_f is the fiber volume fraction; A_f is the cross-sectional area of fiber; the term V_f/A_f is the number of fibers per unit area of the crack plane with φ=0; φ is the inclination angle between the fiber orientation and the perpendicular direction of the crack plane; L_f is the fiber length; z is the distance between the fiber centroid and the crack plane; L_e is the fiber embedment length.

Based on the simulated σ−δ relationships, the corresponding complementary energy J_b', maximum fiber bridging stress σ_0, and crack opening width δ_0 for a certain type of SHGC mixture can be determined (See also Figure 2.7).

In this study, the micromechanical modeling assists the development of SHGC mixtures in the following two aspects:

(1) Choosing suitable fiber volume and fiber length

The physical and mechanical properties of fibers play significant roles in the performance of fiber-reinforced composites. Once a certain material of the fiber has been decided, two factors that can easily be adjusted in the composite mixture design are the fiber volume V_f and the fiber length L_f.

To find appropriate values of V_f and L_f, the critical fiber volume V_f^{crit} as a function of L_f to ensure saturated strain-hardening was determined by inputting all micromechanical parameter values (Table 6.2 and Table 4.2) into the micromechanical model and then check whether the two PSH criteria are met. In total 20 values of L_f are considered (1 mm, 2 mm, …, and 20 mm). For each L_f, two values of fiber volume V_f meet the minimum requirement of each PSH indices, respectively, i.e., the strength PSH index (σ_0/σ_{fc}) equals 1.5 and the energy PSH index (J_b'/J_{tip}) equals 3. These two V_f values are the critical fiber volume V_f^{crit} for this fiber length L_f. Following this approach, the V_f^{crit} vs L_f curve can be obtained by plotting the two V_f^{crit} vs L_f for each L_f value (1 mm to 20 mm). With the V_f^{crit} vs L_f curve, the lower bounds of V_f and L_f were defined.

For a proper SHGC mixture design, both V_f and L_f should be higher than the above lower bounds. Furthermore, high fiber volume and long fiber length also negatively influence the workability of the mixture and thus hinder proper fiber dispersion. Therefore, a fiber volume V_f up to 3% and a fiber length L_f up to 12 mm are set as upper bound values. In this way, the suitable V_f and L_f can be chosen for the SHGC mixture design.

(2) Evaluation of strain-hardening potential of the designed SHGC mixtures

With the chosen fiber volume fraction V_f and fiber length L_f, the complementary energy J_b' and the maximum fiber bridging stress σ_0 were determined from the simulated σ-δ relationships for each of the designed SHGC mixtures. Together with the experimentally determined values of σ_{fc} and J_{tip}, the strength and energy PSH indices ($PSH_s=\sigma_0/\sigma_{fc}$ and $PSH_e= J_b'/J_{tip}$) of each SHGC mixture were calculated to see if they meet both PSH criteria, i.e., $PSH_s \geq 1.5$ and $PSH_e \geq 3.0$. A larger margin between the calculated PSH indices and the required minimum values,

i.e., 1.5 and 3.0, indicates a better chance that the SHGC mixture exhibits good strain-hardening performance. These evaluations help to predict the final tensile behavior of the SHGC mixtures and in this way avoid the large number of trial-and-errors.

6.2.5 Validation of the strain-hardening behavior of designed SHGC

6.2.5.1 Uniaxial tensile tests

The tensile performance of the developed SHGC mixtures was finally evaluated by uniaxial tensile tests. The micromechanics-based design approach is considered to be effective if the most promising composite mixtures exhibit significant strain-hardening behavior, i.e., having a high tensile ductility of over 3%. The experimental set-up of the uniaxial tensile test is shown in Figure 6.3 (a). Dogbone-shaped composite specimens were used as shown in Figure 6.3 (b).

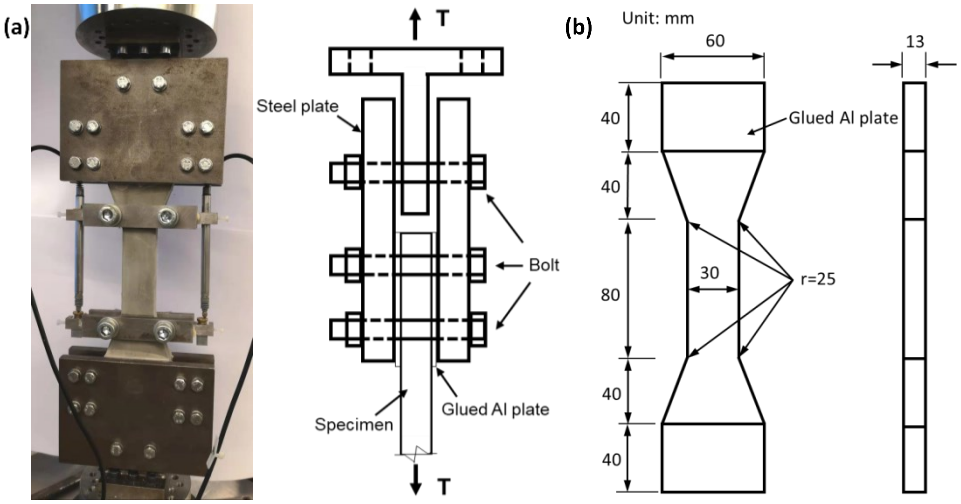

Figure 6.3 Uniaxial tensile test: (a) Experimental set-up and (b) dimensions of dogbone-shaped samples.

To prepare the composite specimens, the matrix mixtures were prepared first and the PVA fiber was slowly added. The fresh composite mixtures were then cast into dogbone-shaped molds and were sealed after compaction. All composite mixtures were cured under identical conditions for 28 days before testing. After 28 days of curing, the dogbone composite samples with a testing volume of 13×80×30 mm^3 were clamped using two pairs of steel plates with bolts. Four aluminum plates were glued on both sides of the specimen 1 day before testing. Two LVDTs were mounted on both sides of the specimen. Following RILEM recommendation [299], this set-up includes both rotationally fixed ends. The tests were conducted using displacement control by LVDTs at a rate of 0.01 mm/s. At least 4 samples were tested for each composite mixture.

6.2.5.2 Average crack width measurement of loaded specimens

After the uniaxial tensile tests, crack widths of the loaded specimens were measured on the mid-part of the dogbone specimens. The region of interest (ROI) has a size of 80 x 30 mm^2. Three lines parallel to the loading direction were drawn on the specimen surface within the ROI. These lines were uniformly spaced on the width of the specimen. Under the microscope, the number of cracks crossing each line was counted. The average crack number of each specimen was calculated by averaging the number of cracks crossing these three lines. The average crack width w_{avg} is calculated using Equation (6.6):

$$w_{avg} = \frac{\Delta L}{N} \tag{6.6}$$

where ΔL is the measured tensile elongation at the peak load during the uniaxial tensile tests and N is the number of cracks crossing each line in the ROI.

6.3 Results and discussions

6.3.1 Choosing suitable fiber volume and fiber length

To find a minimum fiber content to achieve saturated strain-hardening and multiple-cracking, the curves for the critical fiber volume V_f^{crit} as a function of fiber length L_f for mixtures M0-1.5 are determined and are shown in Figure 6.4 (a)-(f). All curves for V_f^{crit} vs L_f are concave upwards while decreasing. The points that fall on the curves indicate the critical fiber volume at a certain fiber length needed to meet the minimum strength (in red color) and energy PSH criteria (in black color). Accordingly, the V_f and L_f values in the area above both curves are considered to satisfy both PSH criteria. These areas are filled with grey color as shown in Figure 6.4 (a)-(f). As illustrated in all figures, increasing L_f leads to lower V_f^{crit} indicating that longer fibers are more effective to achieve strain-hardening. Furthermore, the V_f^{crit} versus L_f curves for mixtures M0-M1.5 are shown in Figure 6.5 (a). These curves also correspond to the lower boundaries of the abovementioned grey area for the V_f and L_f to be chosen.

As indicated by the direction of the arrow in Figure 6.5 (a), a higher fiber volume and a longer fiber length promote the fiber bridging capacity. However, it is recognized that higher fiber volume and longer fiber length also negatively influence mixture workability and hinder proper fiber dispersion in the matrix [300]. Here, a fiber volume V_f up to 3% and a fiber length L_f up to 12 mm are set as upper bound values.

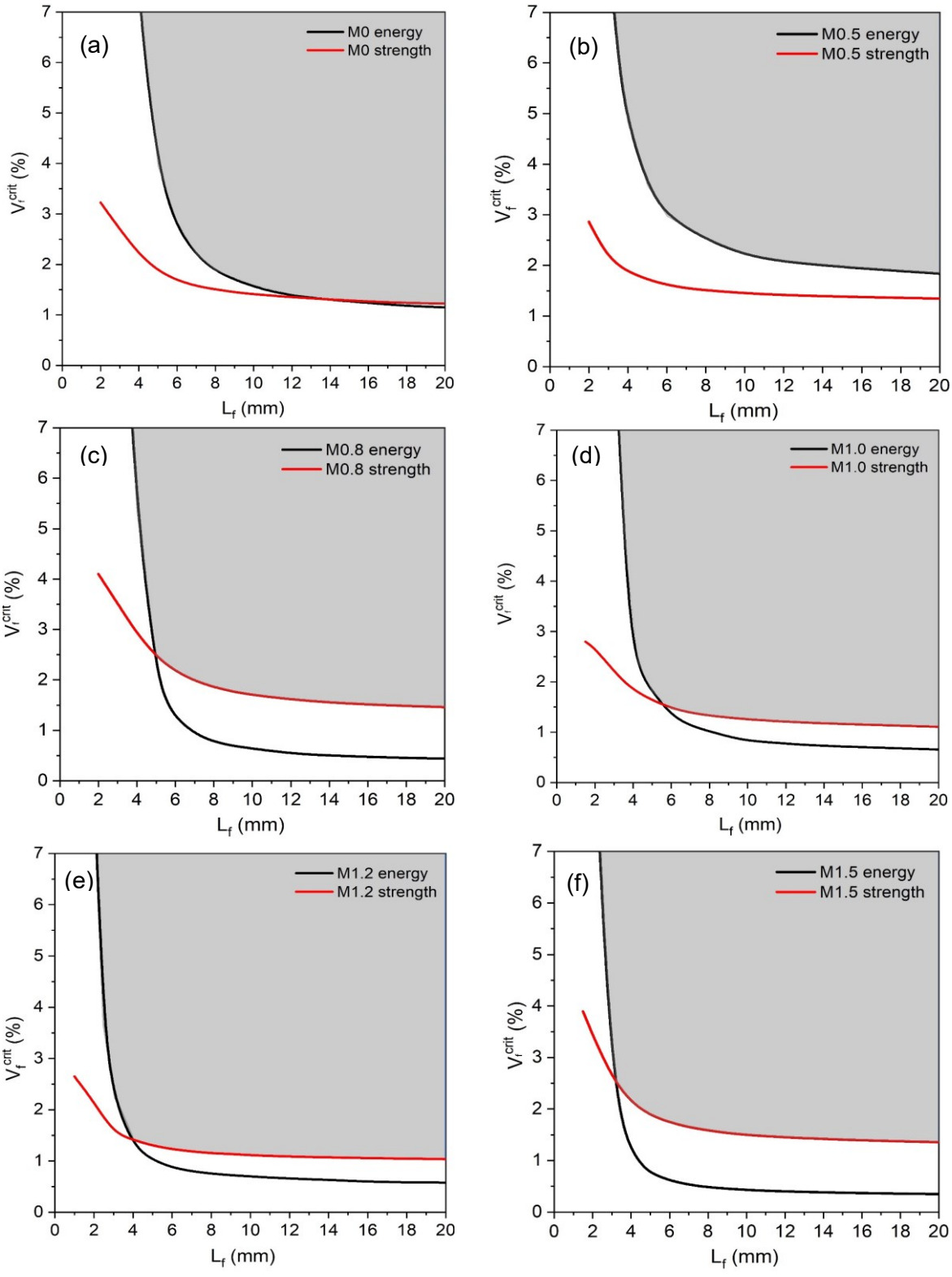

Figure 6.4 V_f^{crit} as a function of L_f determined by both energy criterion and strength criterion for (a) M0, (b) M0.5, (c) M0.8, (d) M1.0, (e) M1.0, and (f) M1.5

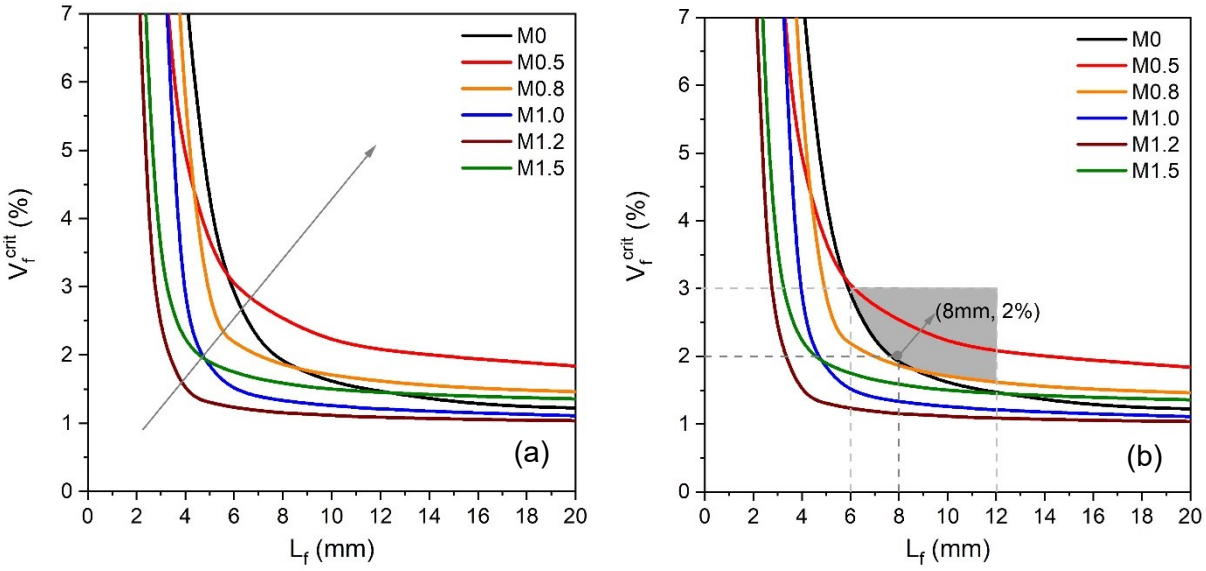

Figure 6.5 (a) The critical fiber volume V_f^{crit} for strain-hardening behavior as a function of fiber length L_f for SHGC mixture M0-M1.5; (b) Upper and lower bounds, and area (in grey color) for choosing L_f and V_f and to meet the PSH criteria for SHGC mixtures M0, M0.8, M1.0, M1.2, and M1.5.

Taking into consideration the upper and lower bounds for L_f and V_f, the grey area in Figure 6.5 (b) is marked where L_f and V_f could be chosen for most SHGC mixtures (all except for M0.5) to meet the PSH criteria. Mixture M0.5 is left out because Figure 6.5 (b) shows that it requires an evident higher L_f and V_f to meet the PSH criteria than other mixtures. Considering the commercial availability of the PVA fibers with a certain length, an L_f of 8 mm and a V_f of 2% were chosen for further studies. The corresponding point of (L_f, V_f) is also marked in Figure 6.5 (b). This point is the furthest away from the V_f^{crit} vs L_f curve of M1.2. This means that mixture M1.2 has the highest excess capacity to meet the PSH criteria and could be the most promising mixture for strain-hardening.

Finally, for the chosen value of the L_f of 8 mm and V_f of 2 vol.%, the mixture design for SHGC M0 to M1.5 is given in Table 6.4. The strain-hardening potential of these mixtures in tension is further evaluated using the output from micromechanical modeling and the results will be given in the following Section 6.3.2. Notably, although mixture M0.5 with the chosen L_f and V_f does not meet the PSH criteria (see Figure 6.5 (b)), it is still included in Table 6.4 for further comparison of its strain-hardening potential with other mixtures. This helps to evaluate the effectiveness of using micromechanical modeling for the development of SHGC.

Table 6.4 Mixture design of slag/fly ash-based SHGC

Mixture	Precursor		Fiber		Alkaline activator		
	Slag (wt.%)	Fly ash (wt.%)	V_f (vol.%)	L_f (mm)	Na_2O (wt.%)	SiO_2 (wt.%)	Water (wt.%)
M0	30	70	2	8	4	0	32
M0.5	30	70	2	8	4	1.94	32
M0.8	30	70	2	8	4	3.1	32
M1.0	30	70	2	8	4	3.88	32
M1.2	30	70	2	8	4	4.65	32
M1.5	30	70	2	8	4	5.8	32

6.3.2 Evaluation of strain-hardening potential using micromechanical modeling

Micromechanical modeling was employed to determine the σ-δ relationships to evaluate the strain-hardening potential of the SHGC mixtures listed in Table 6.4. The predicted maximum fiber bridging stress σ_0, the corresponding crack opening width δ_0, and the complementary energy J_b' could be obtained from the σ-δ relationships. The values of these output parameters are listed in Table 6.5.

Table 6.5 Predicted fiber bridging properties of the designed SHGC mixtures (see Table 6.4) from micromechanical modeling

Mixture	M0	M0.5	M0.8	M1.0	M1.2	M1.5
Maximum fiber bridging stress σ_0 (MPa)	5.6	6.4	5.4	5.9	6.5	5.8
Complementary energy J_b' (J/m^2)	31.7	23.8	32.8	27.5	22.5	28.4
Crack opening width δ_0 (μm)	32.3	21.2	35.5	23.8	18.9	26.5

The simulated σ-δ curves are presented in Figure 6.6 (a). As can be seen, σ-δ relationships for SHGC mixtures show clear differences. Four characteristics of σ-δ curves can be observed in Figure 6.6 (a) and (b). These characteristics are influenced by the fiber/matrix interface properties (Table 6.3) and are summarized as the following:

1. The y-intercept of the simulated σ-δ curves in Figure 6.6 (b) indicates that a certain stress level needs to be reached to initiate the debonding process. The magnitude of the y-intercept is positively related to G_d as shown in Figure 6.6 (c).

2. The height of the first peak in the simulated σ-δ curves corresponds to the maximum fiber bridging stress σ_0. Its value is influenced by both the initial frictional bond τ_0 as well as the slip-hardening behavior [298].

3. The position of the first peak in the simulated σ-δ curves corresponds to the predicted crack opening width δ_0. It is influenced by the chemical bonding energy (G_d). A higher G_d leads to a smaller δ_0.

4. The shape of the second peak/peak shoulder (if any) in the simulated σ-δ curves is influenced by the post-pullout process of the fiber during crack bridging. For PVA fibers, the post-pullout process can be determined by the magnitude of the slip-hardening coefficient β (given in Table 6.3).

SHGC mixtures have a relatively stronger frictional bond than conventional SHCC, which is beneficial for yielding a higher σ_0 and J_b'. On the other hand, SHGC compared to conventional SHCC has a relatively weaker slip-hardening behavior, i.e., lower slip-hardening coefficient β. This could lead to lower fiber bridging capacity σ_0. Compared to conventional SHCC, SHGC mixtures also have a lower predicted crack opening width of δ_0. This is because the stronger chemical bonding in SHGC results in stronger resistance to the crack opening during the strain-hardening stage, which typically leads to smaller crack opening width [21].

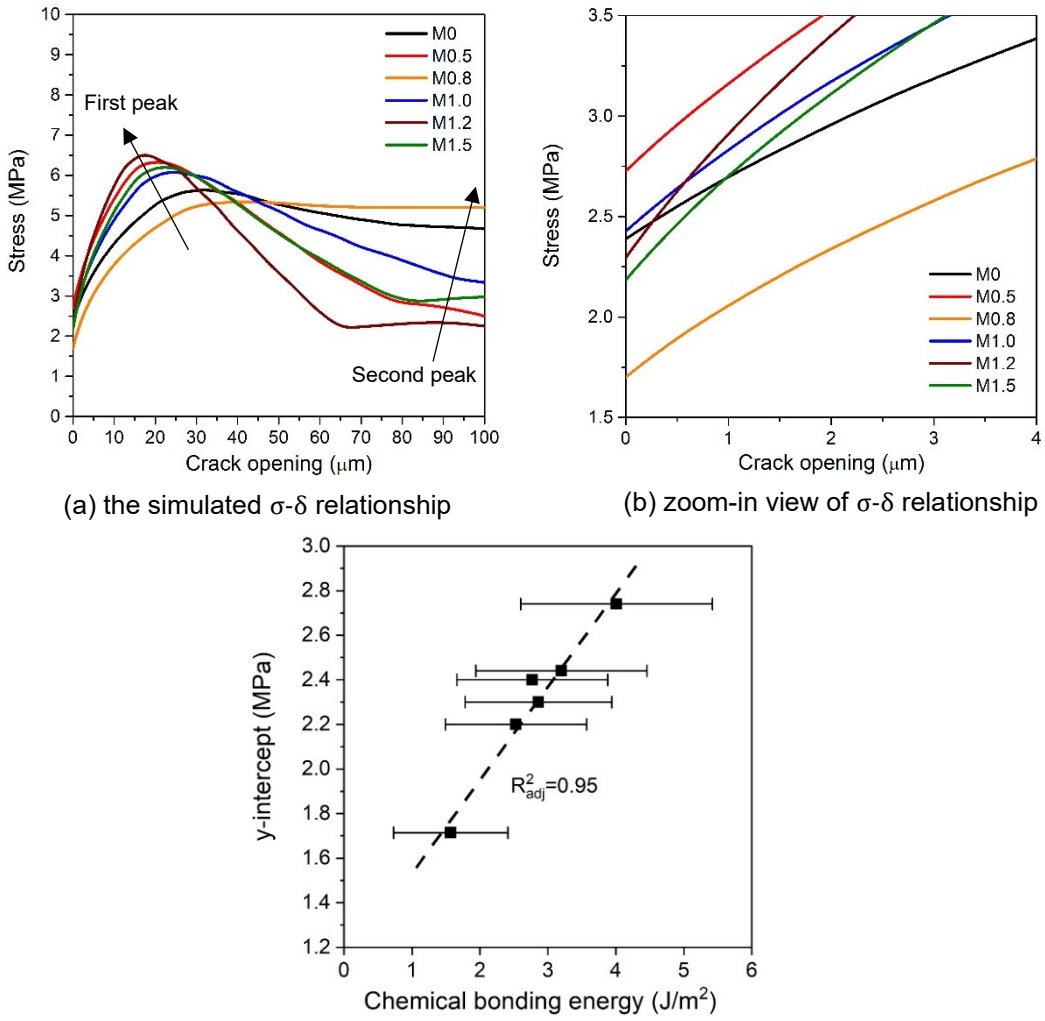

(a) the simulated σ-δ relationship

(b) zoom-in view of σ-δ relationship

(c) y-intercept in the simulated σ-δ curves vs the chemical bonding energy G_d

Figure 6.6 (a) Simulated σ-δ relationship for PVA SHGC; (b) zoom-in of simulated σ-δ relationship for PVA SHGC with the crack opening width from 0 to 4 μm; (c) y-intercept in the simulated σ-δ curves vs the chemical bonding energy.

To further assess the potential of SHGC to achieve strain-hardening and multiple-cracking, two PSH indices, i.e., the strength PSH index ($PSH_s=\sigma_0/\sigma_{fc}$) and the energy PSH index ($PSH_e=J_b'/J_{tip}$), were determined. They were calculated using the experimentally-attained matrix and interface properties (i.e., σ_{fc} and J_{tip}), and the output from micromechanical modeling (i.e., σ_0 and J_b'). Both values of the PSH indices of SHGC mixtures are summarized in Figure 6.7. As discussed previously in Section 6.2.4.2, two empirical values of the strength PSH index of 1.5 and the energy PSH index of 3.0 were taken as the lower bound for both PSH indices, respectively [21, 79, 85, 86]. A larger margin between the calculated PSH indices and the lower bounds (1.5 and 3.0) indicates a better chance that the SHGC mixture has a good strain-hardening performance.

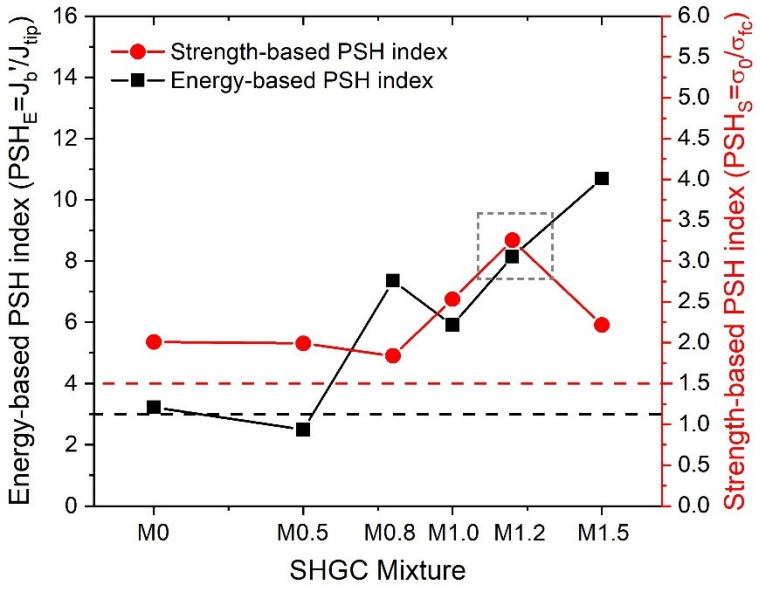

Figure 6.7 Strength and energy PSH indices for SHGC mixtures M0 to M1.5

Figure 6.7 shows that the strength PSH indices are greater than 1.5 for all the mixtures. This indicates that the strength criterion is well met for all mixtures. We also see that the energy PSH indices of all mixtures except M0.5 exceed the value of 3.0. Notably, the energy PSH indices for mixture M0 are only marginally higher than 3.0. Therefore, the results show that all designed mixtures, except M0 and M0.5 mixtures, could exhibit saturated tensile strain-hardening behavior with multiple-cracking. It is also noteworthy that these results do not strictly imply M0 and M0.5 mixtures could not exhibit strain-hardening and multiple-cracking behavior at all. According to the micromechanical modeling results, however, their strain-hardening potential is relatively low.

Furthermore, the mixtures M1.0 and M1.2 have both high energy and strength PSH indices. On the contrary, mixtures M0.8 and M1.5 only have high energy PSH indices, while their strength PSH indices are lower than those of other mixtures. It means that both mixtures M1.0 and M1.2 should have promising potential for saturated strain-hardening. Furthermore, compared with mixture M1.2, mixture M1.0 has a high strength PSH index of 2.3, while its energy PSH index of 5.7 is the lowest among mixtures M0.8-M1.5. Consequently, according to the micromechanical modeling, the mixture M1.2 is considered optimal with the highest potential for tensile strain-hardening and multiple-cracking behavior.

6.3.3 Uniaxial tensile properties of the designed SHGC mixtures

As explained in 6.2.5.1, uniaxial tensile tests on the mixtures SHGC M0-M1.5 were performed to validate the uniaxial tensile performance of the designed SHGC mixtures following the micromechanical-based design approach. The results of uniaxial tensile tests are shown in Figure 6.8. The SHGC mixtures M0.8, M1.0, and M1.2 exhibit evident strain-hardening behavior, although their tensile strain capacities vary significantly. In comparison, the SHGC mixtures M0 and M0.5, and M1.5 have lower tensile strain capacities.

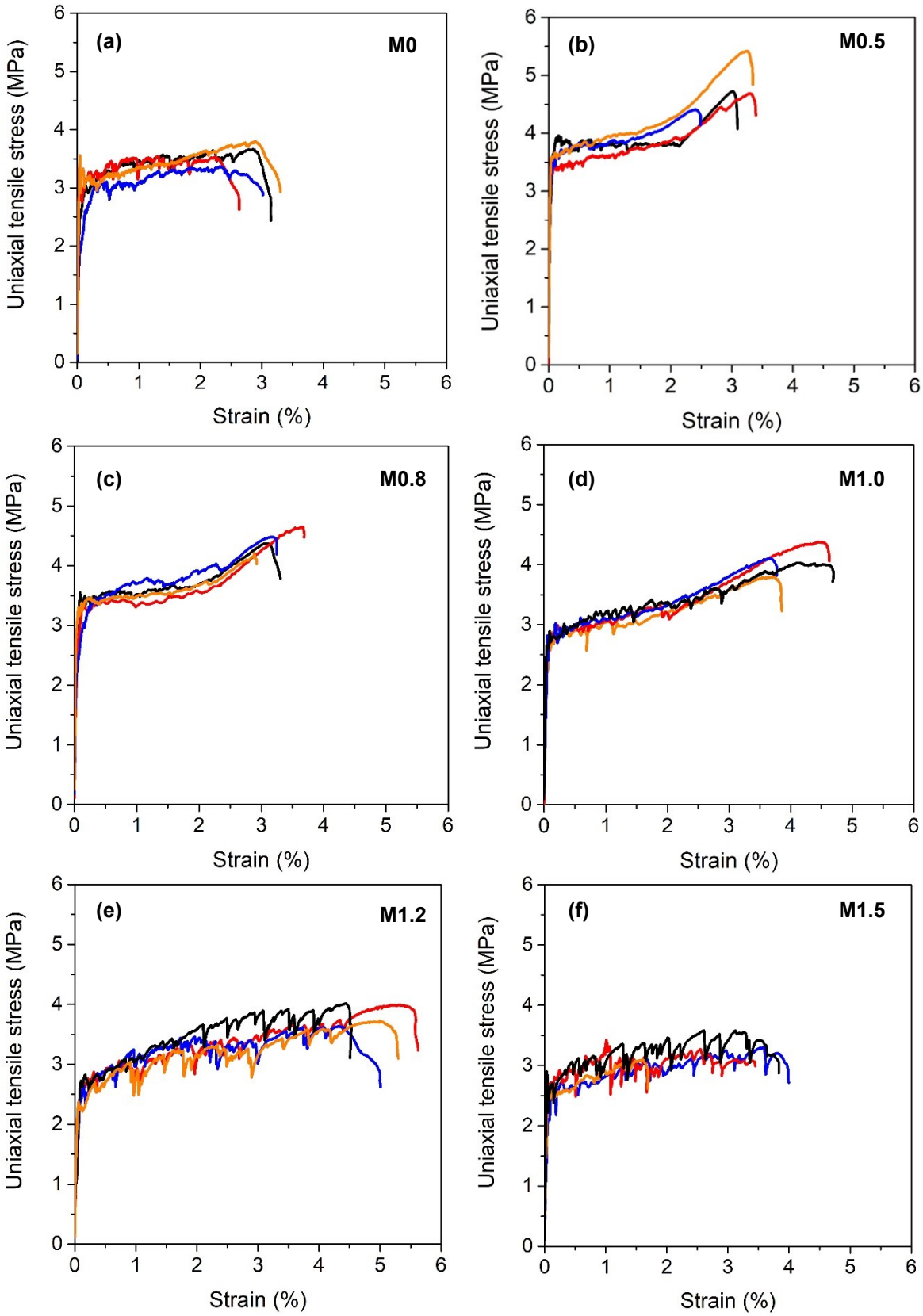

Figure 6.8 Uniaxial tensile stress-strain curves of SHGC mixtures: (a) M0, (b) M0.5, (c) M0.8, (d) M1.0, (e) M1.2, and (f) M1.5.

The uniaxial tensile test results confirm the prediction in Section 6.3.2 that mixture M1.2 exhibits the most significant strain-hardening behavior with high tensile ductility of 4.8% and ultimate tensile strength of 3.8 MPa. Four out of six SHGC mixtures fulfill the requirements of tensile ductility over 3% and ultimate tensile strength over 3 MPa. Such tensile performance is similar to conventional SHCC with moderate strain-hardening properties, e.g., the most intensively studied version of SHCC (ECC M45) [60], an SHCC containing a higher volume of fly ash with enhanced greenness (HVFA ECC) [46], and a slag cement based SHCC (Delft ECC) [47].

Table 6.6 The properties of designed SHGC in uniaxial tensile tests

Mixture	First crack strength σ_{fc} (MPa)	Ultimate tensile strength σ_{ult} (MPa)	Tensile strain capacity ε (%)	Average crack width w_{avg} (μm)
M0	3.3 ± 0.27	3.6 ± 0.17	2.6 ± 0.32	117 ± 18.1
M0.5	3.6 ± 0.27	4.8 ± 0.43	3.0 ± 0.41	61 ± 9.5
M0.8	3.4 ± 0.12	4.4 ± 0.19	3.2 ± 0.32	86 ± 8.4
M1.0	2.8 ± 0.08	4.2 ± 0.18	4.0 ± 0.38	58 ± 6.9
M1.2	2.6 ± 0.16	3.8 ± 0.19	4.8 ± 0.46	84 ± 1.1
M1.5	2.7 ± 0.15	3.4 ± 0.21	2.3 ± 1.22	77 ± 21.2

The results of the uniaxial tensile tests are also summarized in Table 6.6. The properties of the SHGC mixtures in tension are characterized by their first crack strength σ_{fc}, ultimate tensile strength σ_{ult}, tensile strain capacity ε, and average crack width W_{avg}. These characteristics will be discussed further one by one in the following subsections.

6.3.3.1 First crack strength

The first crack strength σ_{fc} of SHGC is defined as the stress at the moment when the first crack occurs under tension. In this study, the splitting tensile strength f_{st} of the matrix is assumed to be an estimation of the first crack strength σ_{fc} as input. In particular, f_{st} is used instead of σ_{fc} to calculate the strength PSH index (i.e., $PSH_s=\sigma_0/f_{st}$). This assumption is further discussed in this section by comparing the σ_{fc} obtained from uniaxial tensile tests and the splitting tensile strength f_{st} of the matrix (see Table 6.2).

As shown in Figure 6.9 (a), the splitting tensile strength f_{st} of the SHGC matrix has a similar trend as the first crack strength σ_{fc} with increasing M_s. The splitting tensile strength f_{st} is in general 10% to 20% lower than the σ_{fc}. Similar findings have been reported for conventional concrete [301-303]. Consequently, using f_{st} instead of σ_{fc} overestimates the strength PSH index ($PSH_s=\sigma_0/f_{st}$). In fact, the strength PSH index calculated with f_{st} (σ_0/f_{st}) is 12% to 23% higher than those calculated with σ_0 ($PSH_S=\sigma_0/\sigma_{fc}$).

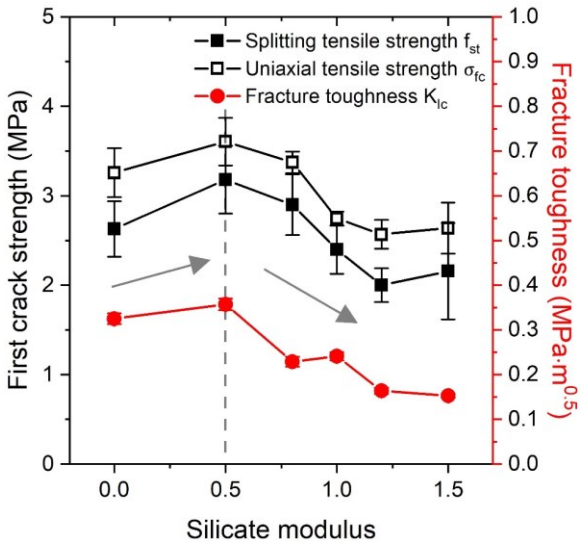

(a) The σ_{fc}, f_{st}, and K_{Ic} as a function of silicate modulus M_s

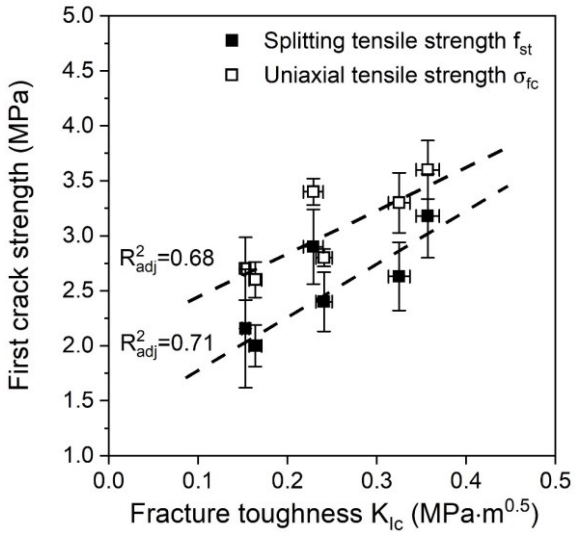

(b) The σ_{fc} and f_{st} vs K_{Ic}

Figure 6.9 (a) First crack strength σ_{fc}, splitting tensile strength f_{st}, and matrix fracture toughness K_{Ic} as a function of activator silicate modulus; (b) correlations of σ_{fc} vs K_{Ic} and f_{st} of vs K_{Ic}

Interestingly, Figure 6.9 (a) also shows that both the σ_{fc} and the K_{Ic} first increase and then decrease with increasing M_s. In Figure 6.9 (b), both the σ_{fc} and the f_{st} values are positively correlated with K_{Ic}. Similar findings were also found in a previous study by Xu et al. [128]. This positive correlation can be explained by the linear elastic fracture mechanics (LEFM) of brittle material. In LEFM, the tensile strength of a matrix in a uniform stress field is determined by the fracture toughness K_{Ic} and the size of the defects in the material as given in Equation (6.7) [304]:

$$\sigma_{fc} = \frac{K_{Ic}}{\sqrt{\pi r}} f\left(\frac{r}{a}\right) \tag{6.7}$$

where K_{Ic} is the matrix fracture toughness and f(r/a) is the shape correction factor of the defects.

In reality, the defects in SHGC could be air voids, restrained shrinkage-induced microcracks, relatively weak interfaces between reaction products, and unreacted particles or fibers. This offers another possibility to tailor the σ_{fc} by modifying the defects in the matrix [305, 306].

6.3.3.2 Ultimate tensile strength

In the uniaxial tensile tests, all SHGC mixtures exhibited moderate ultimate tensile strength σ_{ult} in the range of 3.4-4.4 MPa. The ultimate tensile strength σ_{ult} of SHGC is reached only when the tensile stress in the material exceeds the maximum fiber bridging capacity at each of the cracks. As a result, the ultimate tensile strength σ_{ult} theoretically is equal to the maximum fiber bridging stress σ_0 from the micromechanical modeling. However, the σ_{ult} from uniaxial tensile tests (Table 6.6) was found to be considerably lower than the corresponding maximum fiber bridging stress σ_0 from micromechanical modeling (Table 6.5). These discrepancies are related to the inhomogeneous fiber dispersion in the composite. In the micromechanical model,

the fibers are assumed to be randomly distributed within the matrix. In the experiments, however, the actual fiber dispersion is influenced by the processing details and may deviate from a perfect random dispersion. In the tests of the composite tensile behavior, the final failure happens at the crack with the lowest crack-bridging capacity, i.e., at the cross-section with the lowest fiber volume V_f [25, 80, 128]. This fiber volume, sometimes referred to as effective fiber volume, is often lower than the designed value. This leads to a low crack-bridging capacity, i.e., a lower σ_{ult} compared to σ_0.

In the micromechanical modeling, a higher fiber volume V_f leads to a higher maximum fiber bridging stress σ_0. To show this effect, the σ-δ relationships of SHGC mixture M1.2 with different fiber volume V_f were simulated using the micromechanical model. The values of the micromechanical input parameters were given in Table 6.2 and Table 4.2**.** In the modeling, the only variable was the fiber volume V_f (1.0%, 1.5%, and 2.0%). As shown in Figure 6.10, the maximum fiber bridging stress σ_0 indeed increases with increasing fiber volume V_f. The increased fiber volume increases the number of fibers in the cross-section of the specimen and thereby also increases the load-bearing capacity (higher σ_0). However, the corresponding crack opening width δ_0 remains almost unchanged with increasing V_f. This is because the crack bridging behavior fundamentally depends on how a single fiber behaves during the crack opening. The latter is determined by the tensile strength of the PVA fiber and the fiber/matrix interface properties rather than the V_f [43].

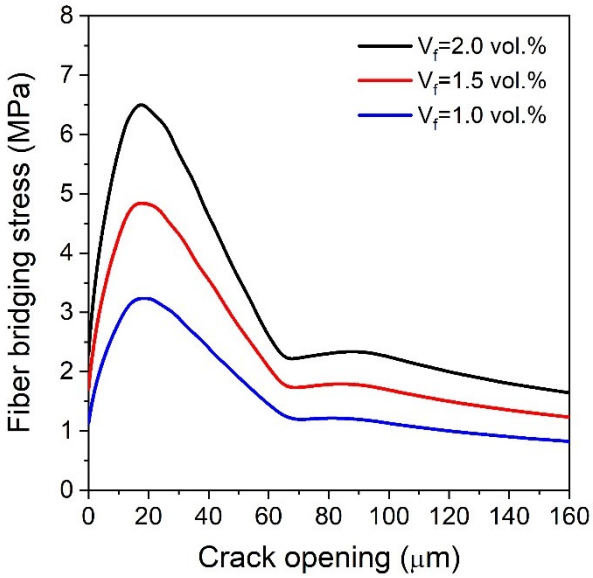

Figure 6.10 The simulated σ-δ relationship for mixture M1.2 with different fiber volumes (1.0, 1.5, and 2.0 vol.%) by micromechanical modeling

Furthermore, the effective fiber volume in SHGC can be estimated by comparing the ultimate tensile strength σ_{ult} and the maximum fiber bridging stress σ_0. To this end, the σ-δ relationships of other SHGC mixtures M0-M1.5 with V_f of 1.0%, 1.5%, and 2.0% were simulated and the corresponding σ_0 was determined. The σ_0 of all SHGC mixtures were then compared with their experimentally-attained σ_{ult} in Table 6.6. The results are shown in Figure 6.11. The shaded area covers the possible range of the predicted σ_{ult} for V_f ranging from 1.0% to 2.0%. The σ_{ult} normally lies between 70% to 75% of the σ_0. These findings confirm that the σ_{ult} of SHGC

mixtures is largely influenced by the fiber distribution. In most cases, the effective fiber volume only reaches 1.5 vol.% rather than the designed value (2 vol.%).

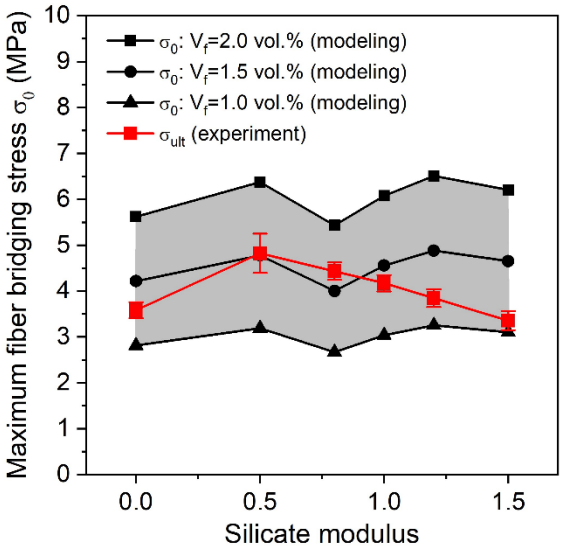

Figure 6.11 Comparison between simulated maximum fiber bridging stresses σ_0 with different fiber volumes (1.0, 1.5, and 2.0 vol.%) and the experimentally-attained ultimate tensile strength σ_{ult}.

The above findings also suggest that the tensile performance of all SHGC mixtures could be further improved by a more homogeneous fiber distribution. This could be achieved by either adopting suitable viscosity modification admixture (VMA) such as hydroxypropyl methylcellulose (HPMC) [307], or by adjusting the processing details such as mixing sequence [308] as suggested by previous research in SHCC.

6.3.3.3 Tensile strain capacity

As previously shown in Table 6.6, moderate to high tensile strain capacities of SHGC mixtures are found in the range from 2.3% to 4.8%. Mixture M1.2 shows promising strain-hardening behavior with the highest average tensile strain capacity up to 4.8%. Although mixture M1.5 yields the lowest tensile strain capacity (2.3%), it is still several hundred times higher than that of conventional concrete. Earlier in this section, the strength PSH index (PSH_s) is calculated using simulated maximum fiber bridging stress σ_0 and f_{st} as the first crack strength (Figure 6.7). Here, the PSH_s index is calculated again but using experimentally-attained σ_{ult} and σ_{fc} values as shown in Figure 6.12 (a). This experiment-based PSH_s is plotted against the tensile strain capacities in Figure 6.12 (b).

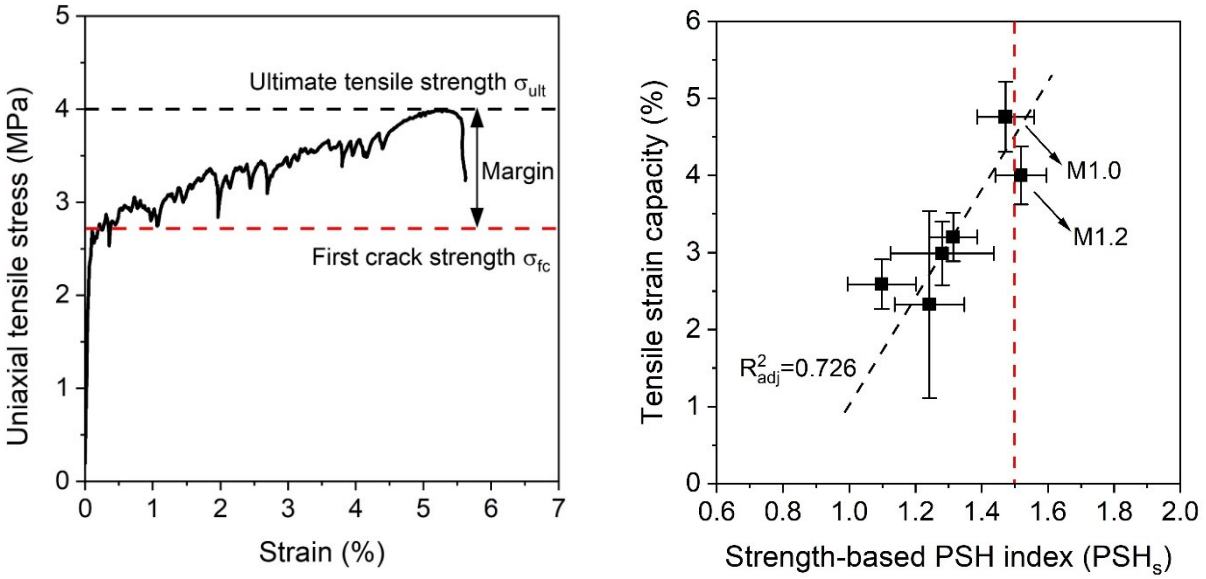

(a) The margin between σ_{ult} and σ_{fc}

(b) The tensile strain capacity vs experiment-based PSH_s

Figure 6.12 (a) The σ_{ult}, σ_{fc}, and the margin between σ_{ult} and σ_{fc} from the uniaxial tensile test results; (b) Relationship between the experiment-based strength PSH indices (PSH_s) and tensile strain capacities. The recommended strength PSH value of 1.5 is indicated with the red dashed line.

As depicted in Figure 6.12 (b), M1.0 and M1.2 mixtures with sufficiently high experiment-based PSH_s (i.e., PSH_s>1.5) also yield higher tensile strain capacities compared to other SHGC mixtures. The good correlation between the tensile strain capacities and the experiment-based PSH_s also suggests that the tensile performance of SHGC mixtures is governed by the strength PSH index. From Figure 6.12 (b), it can be inferred that the experiment-based PSH_s should be at least higher than 1.3 for the SHGC mixture to achieve a tensile strain capacity of 3%. This finding indicates the critical value of the strength PSH index (PSH_s) for achieving saturated strain-hardening of SHGC mixtures is lower than 1.5, most probably 1.3.

Therefore, further optimization of their tensile performance is possible through proper matrix tailoring. This could be achieved by improving the fiber dispersion to enhance the ultimate tensile strength as discussed in Section 6.3.3.2.

6.3.3.4 Average crack width

The average crack width w_{avg} was estimated using the tensile elongation and the number of visible cracks on the sample surface. The tensile elongation is calculated using the length of the area of interest (ROI) multiplied by the tensile strain capacity of the mixture.

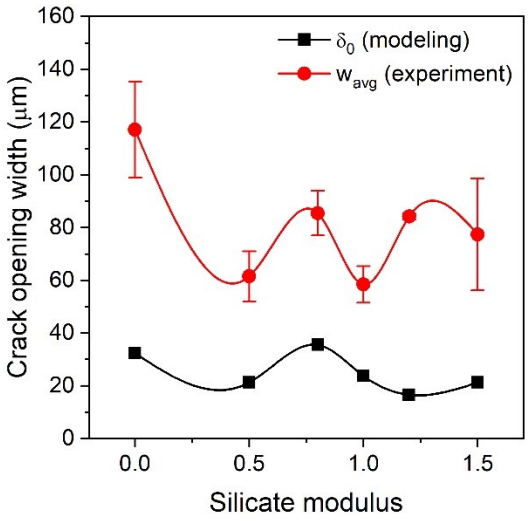

Figure 6.13 Simulated crack opening width δ_0 by micromechanical modeling and measured loaded crack width w_{avg} as a function of activator silicate modulus

The predicted crack opening width δ_0 of SHGC by micromechanical modeling is within a range of 18.9 to 35.5 μm (see also Table 6.5). With increasing silicate modulus M_s, the crack opening widths under tensile loading and the corresponding predicted crack widths follow similar trends. However, as shown in Figure 6.13, the experimentally-attained average crack width w_{avg} in a range of 58 to 117 μm does not perfectly match with the predicted crack opening width δ_0. According to Li et al. [45], the actual crack width under the tensile load should be smaller than the average crack width of the loaded specimens. This is because the actual number of cracks developed during the tensile loading of the specimen was higher than the number of visible cracks on the surface of the specimen after the load is removed.

6.4 Discussion on using the micromechanics-based approach for the development of SHGC

The development of SHGC is more complicated than that of SHCC because more parameters have to be considered during the mixture design. These parameters concern the chemistry of the alkaline activator (Na_2O%, silicate modulus M_s, water content) [95, 151, 309], the chemical/physical properties of solid precursors [103, 150], and also the temperature and the relative humidity during curing [310-312]. Up till now, the systematic approach for geopolymer concrete design is still not developed and the available literature concerning the development of SHGC is very limited. Due to the different origins and the large variances in the chemical composition of the solid precursors, it seems that the design of SHGC can only work on a case-by-case basis. In this context, the conventional trial-and-error method is not suitable for the development of SHGC. The design process would be very time-consuming and largely relies on the experience of the researcher rather than comprehensive scientific knowledge.

The micromechanics-based design approach, proposed in this study, is demonstrated to be more effective and practical for the development of SHGC systems. This approach is schematically illustrated in Figure 6.14. The input parameters for the micromechanical modeling, such as matrix fracture properties and interface bonding properties, are measured

first. Using the micromechanical modeling, the simulated results help to choose suitable fiber length (L_f) and fiber volume (V_f) for the mixture design. Based on the PSH indices determined using the simulation results, the strain-hardening potential of the selected mixtures can also be evaluated with the PSH criteria. This helps the selection of the most promising SHGC mixtures while saving a large number of trial-and-error tests.

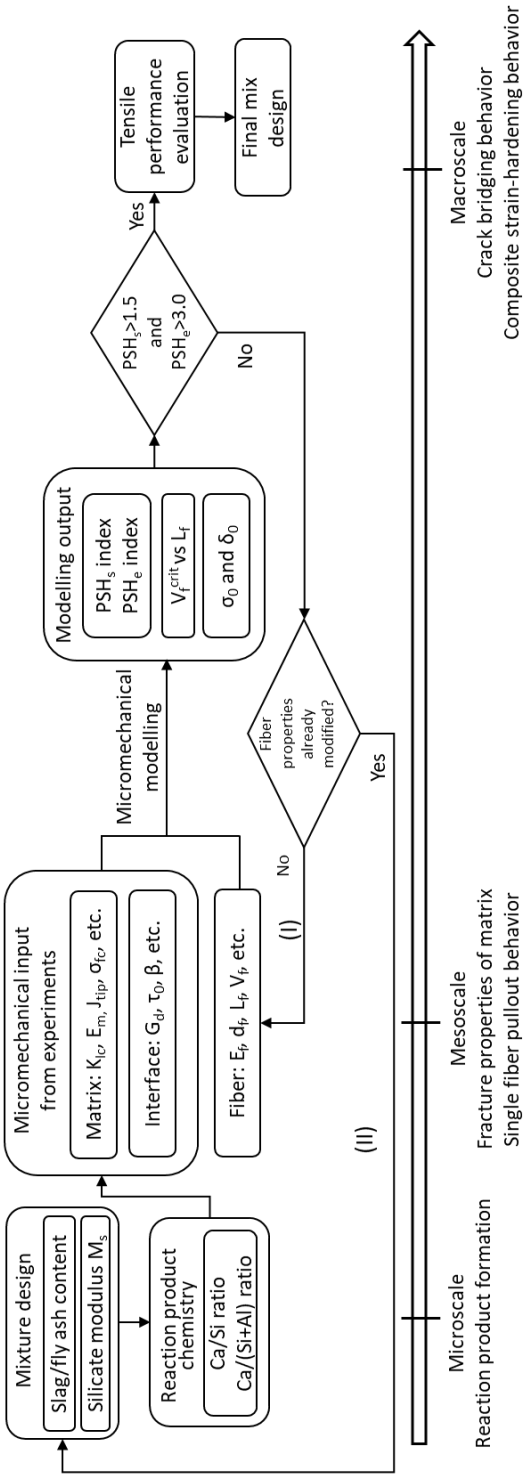

Figure 6.14 The Schematic flowchart of the micromechanics-based design approach for the development of slag/fly ash-based SHGC.

In case the PSH indices of the designed mixture do not satisfy the PSH criteria (i.e., $PSH_s \geq 1.5$ and $PSH_e \geq 3.0$), modification of micromechanical parameters is needed. Two possible routes are given in Figure 6.14: (I) modification/re-selection of L_f, V_f, fiber surface treatment, and even application of a different type of fiber; (II) modification of the mixture design. By combining the micromechanics-based modeling and the knowledge gained from Chapter 3 and 4, the development process of SHGC can be guided systematically.

Furthermore, the values for both energy and strength PSH indices in this study were harvested from the purely empirical values from conventional SHCC. These values are found compatible to be utilized in the development of SHGC. Finally, certain discrepancies do exist between the predicted and experimentally-attained ultimate tensile strength σ_{ult}. The main reason for these discrepancies is the variation in fiber dispersion. However, the prediction of the potential for high tensile strain capacity is considered satisfactory and offers useful guidance for the development of SHGC.

Besides, the SHGC mixtures developed in this chapter, for instance, M1.0 and M1.2, still have room for improvement concerning their mechanical properties, i.e., first and ultimate tensile strength. As discussed in Section 6.3.3.2 and 6.3.3.3, a higher first crack strength σ_{fc} can be achieved through further matrix tailoring, while the ultimate tensile strength σ_{ult} could be improved with a more homogeneous fiber distribution.

6.5 Conclusions

Several types of slag/fly ash-based strain-hardening geopolymer composite (SHGC) with low slag content have been successfully developed in this chapter following the micromechanics-based design approach. The optimal mixtures showed excellent strain-hardening and multiple-cracking performances following the guidance from micromechanical modeling. Based on the results and discussions of this study, the following conclusions can be drawn:

- The optimal SHGC mixture M1.2, with 30 wt.% slag and 70 wt.% fly ash activated by sodium-based silicate solution, exhibits promising tensile strain capacity up to 4.8% and ultimate tensile strength of 3.8 MPa. The performance of the mixture is considered satisfactory compared to that of conventional SHCC materials.

- The silicate modulus M_s of the alkaline activator directly influences the matrix and interface properties and hence the final strain-hardening properties of SHGC. This study confirms that for a mixture with a given slag/fly ash ratio, changing the M_s is an efficient way to modify the strain-hardening behavior of SHGC.

- Compared to conventional SHCC, SHGC demonstrates significant differences in interface properties, viz. a stronger chemical bond, and frictional bond, but a lower slip-hardening coefficient. According to the micromechanical modeling, this leads to higher fiber bridging stress and smaller crack opening width.

- From the micromechanical modeling, increasing the fiber volume in SHGC enhances the maximum fiber bridging stress, but does not significantly influence the crack opening width.

- The effective fiber volume in SHGC mixtures is lower than the designed value (2 vol.%) due to inhomogeneous fiber dispersion. This leads to a lower ultimate tensile strength than that predicted by the micromechanical model.

- Compared to the energy PSH index, the strength PSH index is a better indicator for the strain-hardening potential of SHGC.

- The empirical values of the critical energy and strength PSH indices derived from conventional SHCC are found to be valid for SHGC as well. For SHGC, the value of the critical strength PSH index is lower than 1.5, most probably 1.3.

- The micromechanics-based design approach, linking micromechanical and composite properties, is an effective tool for the development of SHGC. It assists in choosing suitable fiber properties, helps to predict the potential tensile performance, and offers guidance for formulating the design/tailoring strategy.

Chapter 7

Cradle-to-gate life cycle assessment (LCA) of the slag/fly ash-based strain-hardening geopolymer composite[13]

7.1 Introduction

In chapter 6, several mixtures of slag/fly ash-based strain-hardening geopolymer composite (SHGC) have been successfully developed and tested. Among them, mixture M1.2 has the most promising strain-hardening capacity, ultimate tensile strength, and average crack width. Although many studies concluded that geopolymer concrete is a promising alternative to ordinary Portland cement (OPC) concrete, the environmental impact assessment of SHGC has rarely been systematically conducted. Up till now, only Ohno et al. [21] and Nematollahi et al. [23] extended their research on the environmental aspects of SHGC. Their works prove that SHGC brings significant environmental benefits with considerably lower embodied energy and carbon equivalent emissions in comparison with typical SHCC (e.g., ECC M45 [44]) and a greener version of SHCC with SCMs incorporation (e.g., High volume fly ash ECC [43]) [21, 23].

In this chapter, the environmental impacts of the slag/fly ash-based SHGC are evaluated based on a life-cycle assessment (LCA). The most promising mixture SHGC M1.2 was selected for this evaluation. The LCA was conducted within the cradle-to-gate system boundaries. A total of 11 environmental impact indicators and the embodied energy (EE) of the composite materials were determined. In addition, the contribution of each raw material to the environmental impact, such as global warming potential (GWP), human toxicity potential (HTP), marine aquatic ecotoxicity potential (MAETP), and EE was calculated and compared with those of conventional SHCC materials. Recommendations were finally given for the improvement of sustainability of next-generation SHGC.

[13] This chapter is based on:

Zhang, S., van Breugel, K., & Ye, G., 2020. A comparative life-cycle assessment of strain-hardening geopolymer and cementitious composites. Manuscript in preparation.

Zhang, S., Feng, Q., Wang, D., & Ye, G., 2020. Environmental impact of a sustainable slag/fly ash-based strain-hardening geopolymer composite (SHGC). 11th ACI/RILEM International Conference on Cementitious Materials and Alternative Binders for Sustainable Concrete, Toulouse, France.

7.2 The LCA Methodology

The environmental impacts of the optimum SHGC mixture M1.2 are selected for evaluation using Life-cycle assessment (LCA). In addition, three types of most widely adopted conventional cement-based SHCCs were considered in this comparative LCA study. Considering that the matrix of SHGC is slag/fly ash based, the SHCCs were selected to include these two raw materials as well. These mixtures include a most intensively studied SHCC (ECC M45) based on OPC and fly ash [60], an SHCC containing a high volume of fly ash with enhanced greenness (HVFA ECC) [46], and a slag cement-based SHCC (Delft ECC) [47]. The LCA follows the general requirements from ISO14040 [313], EN15804 [314], and the Environmental Performance Assessment Method recommended by the Dutch construction industry [315]. The LCA contains the following four phases:

1. Definition of goal and scope of the analysis
2. Life-Cycle Inventory analysis (LCI-phase)
3. Life-Cycle Impact Assessment (LCIA-phase)
4. Results interpretation phase

These four phases will be explained and discussed in detail in the following sub-sections.

7.2.1 Goal and scope of this study

The goal of this study is to evaluate the environmental impacts of slag/fly ash-based SHGC compared to those of conventional cement-based SHCC materials. The LCAs were conducted following the EN 15804 (2012) standard, which is one of the latest publications in the field [314]. The EN15804 standard distinguishes four stages to cover the full life cycle (“cradle-to-grave”) of a material. These four stages are [314]:

1. Product stage: the raw material extraction, processing, transport, and finally the manufacturing of the product.
2. Construction process stage: the transport of the product to the building site and its installation on site.
3. Use stage: the use, maintenance, repair, replacement, and refurbishment of the product during its service life.
4. End-of-life stage: the demolition, disposal, and reuse/recovery/recycling of the product.

In addition to these four stages, and the view of quantitative evaluation of the environmental impact of materials, the *system boundaries* and the *functional units* of the analyses have to be defined.

7.2.1.1 System boundary

For a reliable comparative LCA, the definition of the system boundary is vital. Since SHGC is a newly developed material, assumptions and simplifications are necessary due to limited data for each of the aforementioned stages. This study, like many previous works [21, 23, 316, 317],

focuses on the product stage (“cradle-to-gate”) only. A “cradle-to-gate” assessment concerns the part of the product life-cycle from resource extraction (cradle) to the factory gate (i.e., before it is transported to the consumer) [314]. It also frequently served as the basis for environmental product declarations (EPDs). Notably, more than 75% of the LCA studies on geopolymer concrete up to 2019 were also conducted considering this system boundary [98, 318]. The system boundaries of the comparative LCA are then given in Figure 7.1.

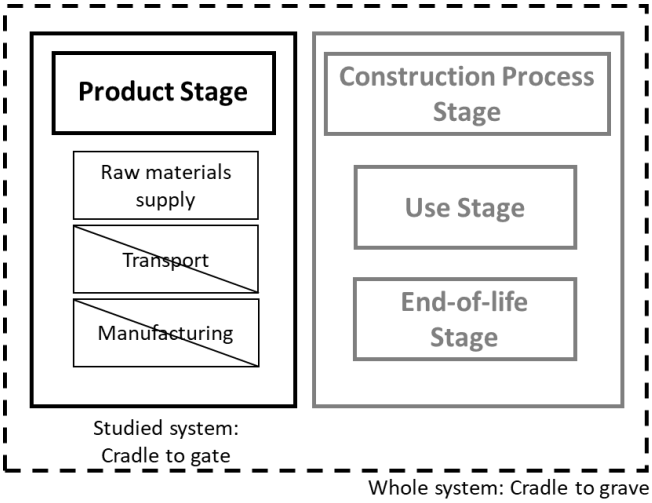

Figure 7.1 System boundary of the comparative LCA in this study

For the production of cost-effective building materials, local availability of raw materials is preferred. This helps to minimize the environmental impact of raw materials because of the minimum need for material transportation [319]. To make fair comparisons, this study assumes that all raw materials for both SHGC and SHCC are locally available, and the transportation-related impact was not considered in the assessment. Notably, the manufacturing process of SHGC compared to that of SHCCs does require additional processes for the preparation of the alkaline activator solution. However, this additional process does not introduce a significant environmental impact, because the homogenous state of the activator solution could be easily achieved without extra heating [320]. Consequently, the comparative LCA was limited to the environmental impacts related to raw materials supply in the product stage.

7.2.1.2 Functional units and basis for comparative LCA

According to EN 15804, the comparison of LCA results is only meaningful when the studied objects have comparable functionality [314]. In this specific case of strain-hardening materials, the compared materials should have similar mechanical properties and tensile ductility at 28 days. Therefore, the functional unit is chosen to be 1 m^3 of strain-hardening materials with comparable compressive strength (MPa), ultimate tensile strength (MPa), and tensile strain capacity (%).

Three conventional cement-based SHCCs were selected carefully so that comparable performance to SHGC M1.2 was ensured. The mechanical properties and tensile ductility of SHGC and the three SHCCs are given in Table 7.1. All mixtures in Table 7.1 exhibit extraordinary strain-hardening behavior and multiple-cracking behavior. When compared with conventional SHCC materials, SHGC M1.2 has a comparable or a bit lower ultimate tensile

strength (3.8 MPa), while exhibiting superior tensile ductility (4.8%). Among the four mixtures, SHGC M1.2 also has the highest compressive strength. Hence, SHGC has a similar level of functionality to the three types of conventional SHCC materials. It thus fulfills the requirements for a comparative LCA.

Table 7.1 Mechanical properties of SHGC and conventional SHCC materials

Mixture	Compressive strength (MPa)	Ultimate tensile strength (MPa)	Tensile strain capacity (%)
SHGC M1.2*	59.6 ± 1.1	3.8 ± 0.18	4.8 ± 0.4
ECC M45 [43]	52.6 ± 0.2	4.8 ± 0.47	2.49 ± 0.6
HVFA ECC [46]	35.2 ± 1.3	3.8 ± -	3.0 ± 0.7
Delft ECC [47]	40.1 ± 1.2	4.6 ± 0.5	3.1 ± 0.7

*The SHGC mixture M1.2 was developed in Chapter 6.

7.2.2 Life-Cycle Inventory

The second phase of an LCA concerns the Life-Cycle Inventory (LCI). This phase concerns the data needed to meet the goals of the LCA under consideration. In the present study, this involved the environmental performance of several strain-hardening materials. The mixtures to be considered are slag/fly ash-based SHGC M1.2 and three types of conventional cement-based SHCCs (ECC M45, HVFA ECC, and Delft ECC). The mixture compositions of these four mixtures are presented in Table 7.2

Table 7.2 Mixture compositions of SHGC and conventional SHCC materials

Composition	SHGC M1.2 (kg/m^3)	ECC M45 (kg/m^3)	HVFA ECC (kg/m^3)	Delft ECC (kg/m^3)
CEM I 52.5 N	-	571	324	-
CEM III/B 42.5 N	-	-	-	790
Blast furnace slag	405	-	-	-
Fly ash	945	685	906	-
Limestone powder	-	-	-	790
Fine sand	-	456	456	-
Superplasticizer (30-45 wt.%)	-	5.5	5.5	7.9
Sodium silicate solution (48 wt.%)	94	-	-	-
Sodium hydroxide solution (50 wt.%)	29	-	-	-
PVA fiber	26	26	26	26
Water	304	332	320	411

The environmental impact data for the LCI were collected from various sources, including environmental product declaration (EPD) reports from industry bodies such as manufacturers [321-323], relevant research literature [324], and the NIBE EPD database [325] (partially based on the ecoinvent 3.5 databases [326]). The data were selected considering the system boundaries, assumptions, data reliability, and significance in the research field. In this study, the NIBE EPD database served as the main data source of the life-cycle inventory (LCI). The

LCI data of different ingredients used for SHGC and conventional SHCCs preparation are summarized in Table 7.3.

The data for CEM I and CEM III/B cement, sand, and superplasticizer (35-45 wt.%) were collected from the NIBE EPD database [325]. The alkaline activator solutions were prepared using sodium hydroxide solution (50 wt.%) and sodium silicate solution (48 wt.%). Both of them are most frequently used to prepare alkaline activator solutions and their data were collected from the NIBE EPD database as well [325]. Notably, the data on sodium silicate solution is still based on an LCA study by Fawer et al. [327]. It has been intensively cited by researchers working on the LCA of alkali-activated materials/geopolymers. All the above impact data in the NIBE EPD database are derived directly from ecoinvent 3.5 [326].

Like most of the previous studies, the blast furnace slag and fly ash are treated as industrial by-products rather than wastes. Their environmental impact data were gathered from the EPDs supplied by their manufacturers (Vliegasunie B.V. [322] and Orcem B.V. [321]).

Finally, the environmental impact data of PVA fiber was gathered from the literature [324]. Due to the currently lacking EPD documents on PVA fiber production, some of the data were also taken from the EPD for hydropol polymer pellets using PVA as the main input raw material [323].

Table 7.3 Life cycle inventory data of 1 kg of different ingredients in SHGC and conventional SHCC materials

Environmental impact category	Abbr.	Unit	CEM I 52.5 N [325]	CEM III/B 42.5 N [325]	Blast furnace Slag [321]	Fly ash [322]	Limestone powder [325]	Fine sand [325]	Superplasticizer without water [325]	Sodium hydroxide without water, 50 wt.% solution [325]	Sodium silicate without water, 48 wt.% solution [325]	PVA fiber [323, 324]
Abiotic depletion potential-elements	ADPE	Kg Sb Equiv.	7.91E-07	5.22E-07	1.94E-07	8.52E-10	2.55E-08	*5.61E-09*	0.00E+00	6.16E-06	7.36E-06	2.76E-06
Abiotic depletion potential--fossil fuels	ADPF	MJ	3.01E+00	2.08E+00	4.70E-01	4.86E-02	4.59E-01	*3.95E-02*	1.68E+01	1.34E+01	1.22E+01	1.01E+02
Global warming	GWP	kg CO_2 Equiv.	8.23E-01	3.53E-01	3.03E-02	3.26E-03	3.10E-02	*2.56E-03*	7.24E-01	9.03E-01	8.25E-01	3.43E+00
Ozone layer depletion	ODP	kg CFC-11 Equiv.	5.44E-09	6.02E-09	3.47E-09	2.56E-10	2.96E-09	*2.87E-10*	9.60E-08	8.24E-07	3.76E-07	2.85E-07
Photochemical oxidants creation	POCP	kg Ethene Equiv.	1.04E-04	7.88E-05	5.68E-06	1.20E-06	9.74E-06	*1.50E-06*	1.41E-03	2.88E-04	2.70E-04	3.74E-03
Acidification of soil and water	AP	kg SO_2 Equiv.	1.30E-03	8.20E-04	1.17E-04	1.54E-05	1.06E-04	*1.22E-05*	9.67E-03	5.50E-03	4.08E-03	1.16E-02
Eutrophication	EP	kg PO_4^{3-} Equiv.	3.28E-04	1.59E-04	1.67E-05	3.45E-06	2.24E-05	*2.79E-06*	4.55E-04	8.92E-04	6.16E-04	3.64E-03
Human toxicity	HTP	kg 1.4 DB Equiv.	3.92E-02	3.09E-02	1.12E-02	6.73E-04	5.46E-03	*9.82E-04*	7.44E-02	3.72E-01	4.32E-01	1.15E+00
Ecotoxicity. freshwater	FAETP		1.41E-03	7.23E-04	2.20E-04	2.05E-05	1.28E-04	*1.31E-05*	2.94E-02	6.55E-03	6.58E-03	3.22E-02
Ecotoxicity. marine water	MAETP		8.40E+00	5.14E+00	3.97E+00	2.14E-01	4.80E-01	*4.46E-02*	9.10E+00	2.95E+01	3.11E+01	1.30E+02
Ecotoxicity. terrestrial	TETP		1.58E-03	9.61E-04	2.62E-04	7.35E-06	5.03E-05	*1.07E-05*	3.44E-04	1.43E-02	2.30E-03	1.86E-02
Renewable primary energy		MJ	1.44E+00	0.00E+00	0.00E+00	2.25E-03	3.21E-02	*0.00E+00*	0.00E+00	2.53E+00	1.04E+00	0.00E+00
Non-renewable primary energy			4.21E+00	2.18E-00	4.83E-01	5.12E-02	4.55E-01	3.96E-02	2.07E+01	1.75E+01	1.18E+01	1.01E+02

7.2.3 Life-Cycle Impact Assessment (LCIA)

A total of 11 environmental impact indicators are considered in assigning LCI results, namely:

1.	Abiotic depletion potential-elements	ADPE	[Kg Sb Equiv.]
2.	Abiotic depletion potential--fossil fuels	ADPF	[MJ]
3.	Global warming potential	GWP	[kg CO2 Equiv.]
4.	Ozone layer depletion potential	ODP	[kg CFC-11 Equiv.]
5.	Photochemical oxidants creation potential	POCP	[kg Ethene Equiv.]
6.	Acidification potential	AP	[kg SO_2 Equiv.]
7.	Eutrophication potential	EP	[kg PO_4^{3-} Equiv.]
8.	Freshwater aquatic ecotoxicity potential	FAETP	[kg 1.4 DB Equiv.]
9.	Human toxicity potential	HTP	[kg 1.4 DB Equiv.]
10.	Marine aquatic ecotoxicity potential	MAETP	[kg 1.4 DB Equiv.]
11.	Terrestrial ecotoxicity potential	TETP	[kg 1.4 DB Equiv.]

All the above environmental indicators are evaluated based on the mid-point impact categories formulated by the Centrum voor Milieukunde Leiden (CML) 2015 [145]. The CML method is a classical impact assessment method that is widely adopted because of its robustness [328]. They provide information on the environmental issues associated with inputs and outputs of the product system [313]. The method limits uncertainties in the final output by restricting quantitative modeling to the early stages in the cause-effect chain [329].

Besides the 11 impact indicators, the embodied energy (EE [MJ]) of the composite materials is also evaluated. In this study, the EE refers to the total primary energy consumed in the direct and indirect processing operations, which are associated with the composite materials under the “cradle-to-gate” scope [330]. This energy is calculated as the summation of the total renewable primary energy [MJ] and total non-renewable primary energy [MJ].

7.2.3.1 Environmental impact calculation

Each of the 11 environmental impacts associated with 1 m^3 of composite material is calculated with Equation (7.1).

$$C_i = \sum C_j \cdot M_j \tag{7.1}$$

where C_i is the environmental impact indicator of one specific composite material, C_j is the environmental impact of one specific component listed in Table 7.3 and M_j is the mass fraction of the component (kg/m^3) as presented in Table 7.2.

The embodied energy EE_i of all four materials is calculated with Equations (7.2) and (7.3) as the sum of the primary energy consumption related to both the renewable ($E_j^{Renewable}$) and non-renewable ($E_j^{Non\text{-}renewable}$) resources as mentioned in Table 7.3. In formula form:

$$EE_j = E_j^{Renewable} + E_j^{Non-renewable} \tag{7.2}$$

$$EE_i = \sum EE_j \cdot M_j \tag{7.3}$$

7.2.3.2 Environmental impact normalization

To highlight the relative significance of the environmental impact of SHGC and SHCCs in an LCA, a normalization procedure was performed. Normalization of environmental impact results helps to interpret these results by providing information about the relative significance of individual impact categories [331, 332]. This study used the *external* normalization method [333, 334]. In this method, the normalized impact N_i of a specific impact category i is obtained by dividing the environmental impact indicator C_i of that impact category by a normalization factor R_i. In formula form:

$$N_i = \frac{C_i}{R_i} \tag{7.4}$$

The reference values R_i are generally based on the total yearly emissions in a reference year in a reference region. In this study, the reference values were taken from the CML-IA database [335], which considers the total yearly emissions at the global level in the reference year of 2000 [333]. The reference values for all 11 impact categories are shown in Table 7.4.

Table 7.4 Global equivalents reference values for the estimated environmental impact of each impact category from the CML-IA database [335].

Environmental impact category	Abbr.	Unit	Normalization factor R_i (CML-IA)
Abiotic depletion potential-elements	ADPE	Kg Sb Equiv. /year	3.61E+08
Abiotic depletion potential--fossil fuels	ADPF	MJ /year	3.80E+14
Global warming	GWP	kg CO_2 Equiv. /year	4.22E+13
Ozone layer depletion	ODP	kg CFC-11 Equiv. /year	2.27E+08
Photochemical oxidants creation	POCP	kg Ethene Equiv. /year	3.68E+10
Acidification of soil and water	AP	kg SO_2 Equiv. /year	2.39E+11
Eutrophication	EP	kg PO_4^{3-} Equiv. /year	1.58E+11
Human toxicity	HTP	kg 1.4 DB Equiv. /year	2.58E+12
Ecotoxicity. freshwater	FAETP		2.36E+12
Ecotoxicity. marine water	MAETP		1.95E+14
Ecotoxicity. terrestrial	TETP		1.09E+12

The normalized impact N_i of all four strain-hardening mixtures defined in Table 7.1 will also be compared to the normalized impact of the global warming potential (GWP) N_i/N_{GWP}. The underlying assumption here is that, if GWP is considered an important environmental impact indicator, any impact that is more significant than GWP (i.e., $N_i/N_{GWP}>1$), should be studied as well. In this way, the environmental impact of the composite materials could be further analyzed.

7.2.3.3 Environmental impact weighting

Understanding the LCIA results is not always easy and interpreting environmental impacts needs experience. Most LCA end-users, including policymakers, would prefer to have only one single indicator to assess the overall environmental impact of a product or a process [336]. An example of a single indicator is the EU energy efficiency label for electrical products [337]. Most LCAs, however, do not use a single indicator to evaluate the overall environmental impact. This causes problems when the contribution of certain individual environmental impacts needs to be compared or ranked. For example, it is not possible to compare the relevance of the global warming potential (GWP) directly with other environmental impacts since they use different units (see also Table 7.4). A possible solution to this problem is to assign different weights to different environmental impacts. This makes it possible to assess and compare the seriousness of the environmental impact across different categories. In this way, the total environmental impact can also be calculated by summation of all individual weighted environmental impacts to obtain a single score indicator for an LCA.

Table 7.5 Weighing factor values (€/kg equivalent) for the estimated environmental cost of each impact category from the SBK assessment approach [315].

Environmental impact category	Abbr.	Unit	The environmental cost weighting factor [€/kg equivalent]
Abiotic depletion potential-elements	ADPE	Kg Sb Equiv.	1.60E-01
Abiotic depletion potential-fossil fuels	ADPF	MJ	7.70E-05
Global warming	GWP	kg CO_2 Equiv.	5.00E-02
Ozone layer depletion	ODP	kg CFC-11 Equiv.	3.00E+01
Photochemical oxidants creation	POCP	kg Ethene Equiv.	2.00E+00
Acidification of soil and water	AP	kg SO_2 Equiv.	4.00E+00
Eutrophication	EP	kg PO_4^{3-} Equiv.	9.00E+00
Human toxicity	HTP	kg 1.4 DB Equiv.	9.00E-02
Ecotoxicity. freshwater	FAETP		3.00E-02
Ecotoxicity. marine water	MAETP		1.00E-04
Ecotoxicity. terrestrial	TETP		6.00E-02

In previous studies *monetization* of environmental impacts has been proposed for quantitative weighting of the environmental impact of construction materials [338, 339]. In this study, a simple monetization approach will be used to transform all the potential costs of environmental impact into *shadow prices*, sometimes referred to as “green taxes”. This approach is recommended by the Dutch Stichting Bouwkwaliteit (SBK) to support the decision-making of both construction materials suppliers and customers [315]. The environmental cost indicators (ECI) of all 11 impact categories can be calculated using Equation (7.5).

$$ECI_i = \sum ECI_j \cdot M_j \tag{7.5}$$

where ECI_i is the environmental cost indicator of one specific composite material, ECI_j is the environmental cost of one specific component [€/kg equivalent] given in Table 7.5, and M_j is the mass proportion of the component in the mixture [kg/m^3] presented in Table 7.2.

7.2.3.4 Contribution analysis of raw materials

To further interpret the results of a life cycle impact analysis (LCIA), it is essential to find the main contributor to the most significant environmental impacts by decomposing the total environmental impact into the individual contribution from raw materials/processes [340]. These analyses help to identify the major contributions from the raw materials and can guide further optimization of strain-hardening materials towards more advanced sustainable performance.

7.3 Results and discussion

7.3.1 Environmental impact of SHGC

All environmental impacts and the embodied energy (EE) of the slag/fly ash-based SHGCs were used to quantitatively assess the sustainability of the newly developed SHGC in comparison to conventional SHCCs. The environmental impact assessment for 1 m^3 of composite material is given in Table 7.6.

Table 7.6 Environmental impact of SHGC and conventional SHCCs

Effect	Abbr.	Unit	SHGC M1.2	ECC M45	HVFA ECC	Delft ECC
Abiotic depletion potential-elements	ADPE	Kg Sb Equiv.	9.18E-04	5.27E-04	3.31E-04	5.04E-04
Abiotic depletion potential-fossil fuels	ADPF	MJ	2.11E+00	2.16E+00	1.80E+00	2.29E+00
Global warming	GWP	kg CO_2 Equiv.	2.12E+02	5.66E+02	3.64E+02	3.98E+02
Ozone layer depletion	ODP	kg CFC-11 Equiv.	6.33E-05	1.14E-05	1.00E-05	1.53E-05
Photochemical oxidants creation	POCP	kg Ethene Equiv.	1.37E-01	1.66E-01	1.40E-01	1.78E-01
Acidification of soil and water	AP	kg SO_2 Equiv.	8.95E-01	1.11E+00	7.95E-01	1.11E+00
Eutrophication	EP	kg PO_4^{3-} Equiv.	1.83E-01	2.88E-01	2.08E-01	2.42E-01
Human toxicity	HTP	kg 1.4 DB Equiv.	8.14E+01	5.37E+01	4.41E+01	5.93E+01
Ecotoxicity. freshwater	FAETP		1.69E+00	1.82E+00	1.47E+00	1.74E+00
Ecotoxicity. marine water	MAETP		7.98E+03	8.40E+03	6.37E+03	7.89E+03
Ecotoxicity. terrestrial	TETP		1.26E+00	1.40E+00	1.01E+00	1.29E+00

In the next sections the following topics will be addressed:
- Environmental impact of SHGC M12 relative to that of ECC M45 (Section 7.3.1.1);
- The normalized environmental impact (Section 7.3.1.2);
- The overall environmental impact using the environmental cost indicator (Section 7.3.1.3).

7.3.1.1 Environmental impact of SHGC relative to ECC M45

The environmental impact of new slag/fly ash-based SHGC and conventional SHCCs relative to that of ECC M45 are shown in Figure 7.2. Among all impact categories, 8 out of 11 impacts in SHGC score lower than those in ECC M45 and are considered comparable to those in high volume fly ash ECC and Delft ECC. Particularly, SHGC has the lowest global warming potential (GWP), which is 63% lower than that of ECC M45. However, the impact categories ADPE, ODP, and HTP score higher in SHGC than in conventional SHCCs. Compared to that of ECC M45, the absolute impact values of ADPE, ODP, and HTP are 74%, 457%, and 51% higher, respectively. These findings are similar to those presented in several previous studies on the environmental impact of geopolymer concrete compared to OPC concrete [341, 342].

In the past, a very high value of ODP, between 11 to 17 times higher compared to that in OPC binders, has also been reported for geopolymer binders [341]. This high value of ODP, however, should be judged with care. Putting this value in perspective reference is made here following Passuello et al. [341], who used the LCA results in the LED light industry as a reference. The absolute value of ODP associated with 1000 kg of SHGC (3.28E-05 kg CFC-11 Equiv.) is similar to those emitted by a single incandescent 800-lumen household lamp operating for 1.16 years [343]. Even if we consider a yearly consumption of SHGC similar to that of OPC cement, i.e., 521 kg per capita [344] (which in reality should be several hundred times lower), the overall impact of the ODP associated with the use of SHGC will remain very low compared to other daily activities.

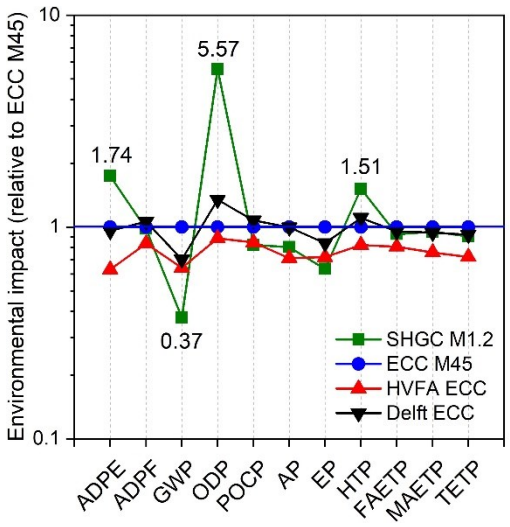

Figure 7.2 (Relative) environmental impacts of SHGC and conventional SHCCs compared to ECC M45. Environmental impact is shown in Table 7.6.

The scores of SHGC regarding ADPE and HTP seem unfavorable compared to those of conventional SHCCs. An explanation could be that the application of SHGC induces an

unfavorable environmental impact 'transfer' from GWP towards ADPE and HTP. Considering that the calculated environmental impact data are absolute values, further evaluation of those scores using an appropriate normalization and weighting process is recommendable and will be considered in Section 7.3.3.

7.3.1.2 Normalized environmental impact

Normalization of environmental impact scores helps to identify the most significant environmental impact categories. The normalized environmental impact N_i and the ratio N_i/N_{GWP} are shown in Figure 7.3 (a) and (b), respectively. The formalized impact factor N_i is based on the total yearly emissions at the global level in the reference year of 2000.

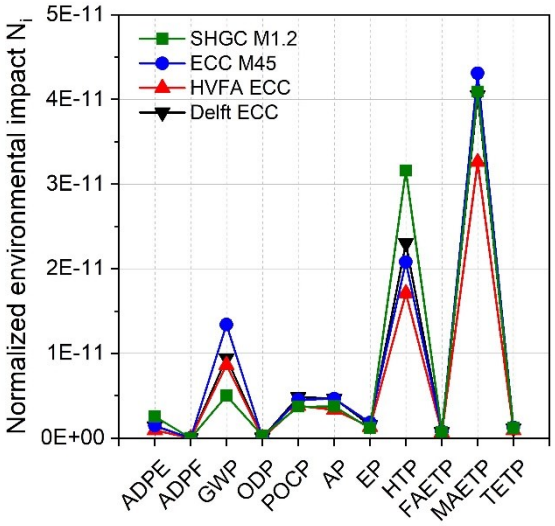

7.3 (a) Normalized environmental impact N_i

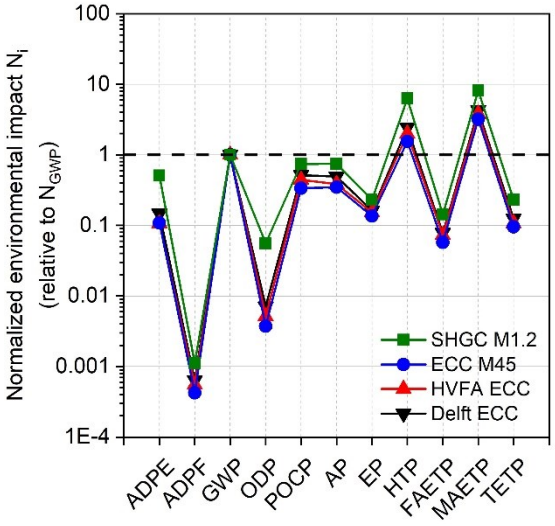

7.3 (b) Relative normalized environmental impact N_i/N_{GWP}

Figure 7.3 (a) Normalized environmental impact N_i and (b) Normalized environmental impact N_i relative to N_{GWP} of SHGC M1.2 and conventional SHCCs

The normalized impacts N_i in Figure 7.3 (a) indicate that in comparison to other SHCCs the environmental impacts of SHGC are only more significant in the categories HTP and MAETP. Although the abiotic depletion potential (ADPE) and the ozone layer depletion potential (ODP) stand out from the comparison of *absolute* impact values (Figure 7.2), their *normalized* impacts are not significantly different from other categories. On the other hand, the N_i/N_{GWP} ratio in Figure 7.3 (b) identifies the human toxicity potential (HTP) and the marine aquatic ecotoxicity potential (MAETP) as more significant impact categories than GWP ($N_i/N_{GWP}>1$). This means that if GWP is the impact indicator that determines the overall environmental profile of a product, it is then necessary to also include the above HTP and MAETP categories in the LCIA as well.

7.3.1.3 Environmental cost indicator (ECI)

The environmental cost of SHGC and conventional SHCCs is calculated using the weighing factor values (€/kg equivalent) for the estimated environmental impact of each impact category from the SBK assessment approach [315]. The ECI calculated here is a very simple monetized indicator. It reflects the total environmental impact of the composite materials. The lowest ECI for SHGC among all composite materials thus suggests its best sustainability performance. The results presented as environmental cost indicators (ECI) are shown in Figure 7.4. Among all composite materials, SHGC has the lowest ECI, which is 70.8%, 16.0%, and 36.2% lower than ECC M45, HVFA ECC, and Delft ECC, respectively.

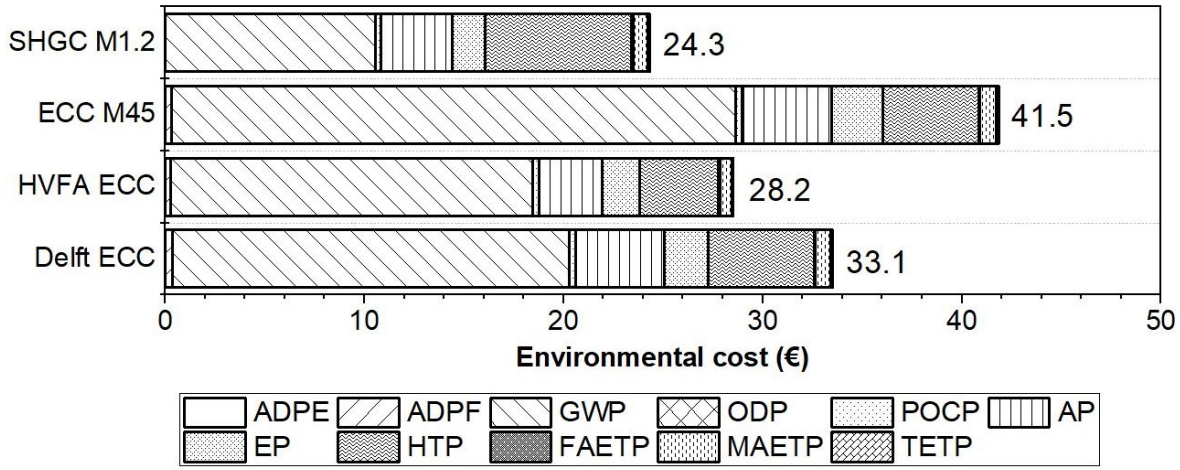

Figure 7.4 Environmental cost indicators (ECI) of SHGC in comparison to those of conventional SHCCs.

Among all environmental costs, the environmental cost for GWP is the highest for all composite materials. In line with the normalized results shown in Figure 7.3, the ADPE and ODP impact categories only have an insignificant contribution to the ECI. Interestingly, the top four major environmental impacts for all composite materials are GWP, AP, EP, and HTP. This finding is somewhat different from that previously reported for geopolymer concrete and conventional concrete. There, the four major impact categories were found to be ADP, GWP, AP, and MAETP [345]. This difference is due to the use of PVA fiber known for its high impact on HTP and EP as given in the LCI in Table 7.3. Still, SHGC generally has lower values for AP and EP than conventional SHCCs. Only the AP of HVFA ECC is 11.1% lower than that of SHGC. Considering that the normalized results do not reflect the significant sensitivity for either AP or EP, these two categories were not evaluated further in the following analysis.

7.3.2 Contribution analysis

As discussed in Section 7.3.1, a contribution analysis is necessary to identify the raw materials that significantly contribute to the environmental impact. Thus, the total result is decomposed into individual raw material contributions. The contribution analysis is conducted on GWP and EE since they are the most frequent environmental impacts considered in the previous LCA.

In addition, the analysis is also conducted on HTP and MAETP since they are identified as the most relevant impacts from the results of the normalization and weighting in Section 7.3.1.

7.3.2.1 Global warming potential (GWP)

The GWP is one of the most significant concerns in the construction industry due to the heavy dependency and large consumption of Portland cement-based concrete. The effect of greenhouse gases (e.g., methane (CH_4), nitrous oxide (N_2O), chlorofluorocarbons, etc.) on global warming potential is quantified relative to that of CO_2 (kg CO_2 Equiv.).

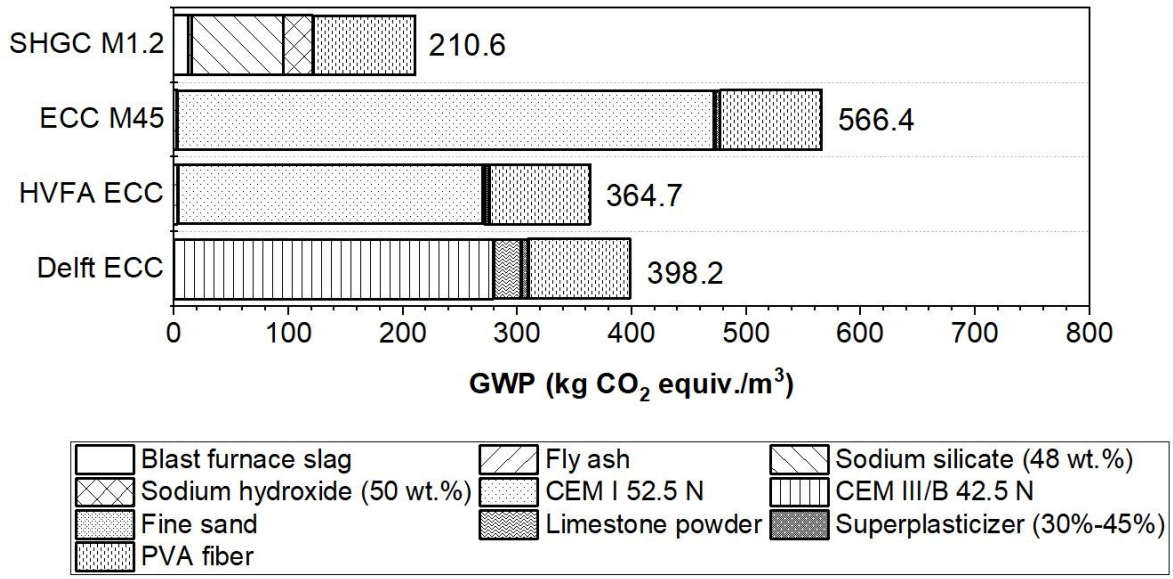

Figure 7.5 Contribution of different raw materials for global warming potential (GWP) of the SHGC and conventional SHCCs.

The contribution of raw materials to GWP of SHGC and conventional SHCCs is presented in Figure 7.5. The slag/fly ash-based SHGC has the lowest GWP among all four strain-hardening materials. Its GWP of 210.6 kg CO_2 equiv./m^3 is 63% lower compared to ECC M45. It is also 42% and 47% less compared with the GWP of the current green version of HVFA ECC and Delft ECC, respectively. The use of OPC accounts for the high GWP value of other SHCC materials. As previously reported, the production of 1 kg of OPC emits approximately 0.84-1.15 kg of CO_2 [346]. Therefore, a cement-free geopolymer matrix can significantly reduce the GWP of strain-hardening materials. The great advantages of this GWP reduction brought by SHGC are in line with most of the previous studies using similar “cradle-to-gate” system boundaries [342, 347, 348]. The only exception found is that McLellan et al. [348] also addressed the importance of the transport distance on the GWP of geopolymer.

The contribution of different raw materials for SHGC and conventional SHCCs to GWP was also assessed. As shown in Figure 7.5, the solid precursors, i.e., blast furnace slag and fly ash, contribute very little (<10%) to the GWP of SHGC. The major contributions to the GWP of SHGC come from the sodium-based silicate alkaline activator and PVA fiber, in line with previous LCA studies concerning SHGC [21, 23]. In fact, the alkaline activator in this study accounts for 50.3% GWP in SHGC. This major contribution to GWP originates from the high

GWP associated with sodium silicate and sodium hydroxide solutions used for the preparation of alkaline activators. On the other hand, the PVA fiber used also presents a substantial contribution to GWP (37.7%). Such high GWP is mainly caused by the manufacturing of vinyl acetate, a petroleum-based ingredient for PVA production [349, 350].

Notably, the findings here are well in line with two existing studies. Ohno and Li [21] reported similar benefits of a fly ash-based engineered geopolymer composite (EGC) reinforced with 1.5 vol. % PVA fiber, The GWP of SHGC is reduced by 55 % compared with ECC M45. Nematollahi et al. [23] reported a one-part slag/fly ash SHGC with an even higher reduction of GWP of 76%. Similar conclusions could also be found in earlier studies on geopolymer concrete. The geopolymer concrete can outperform OPC concrete in GWP reduction by a factor of 3 while having a similar impact on the depletion of resources and energy use [347].

7.3.2.2 Human toxicity potential (HTP)

Besides the GWP, the human toxicity potential (HTP) has been identified as an important environmental impact. The calculated raw materials contributions to HTP of SHGC and conventional SHCCs are illustrated in Figure 7.6.

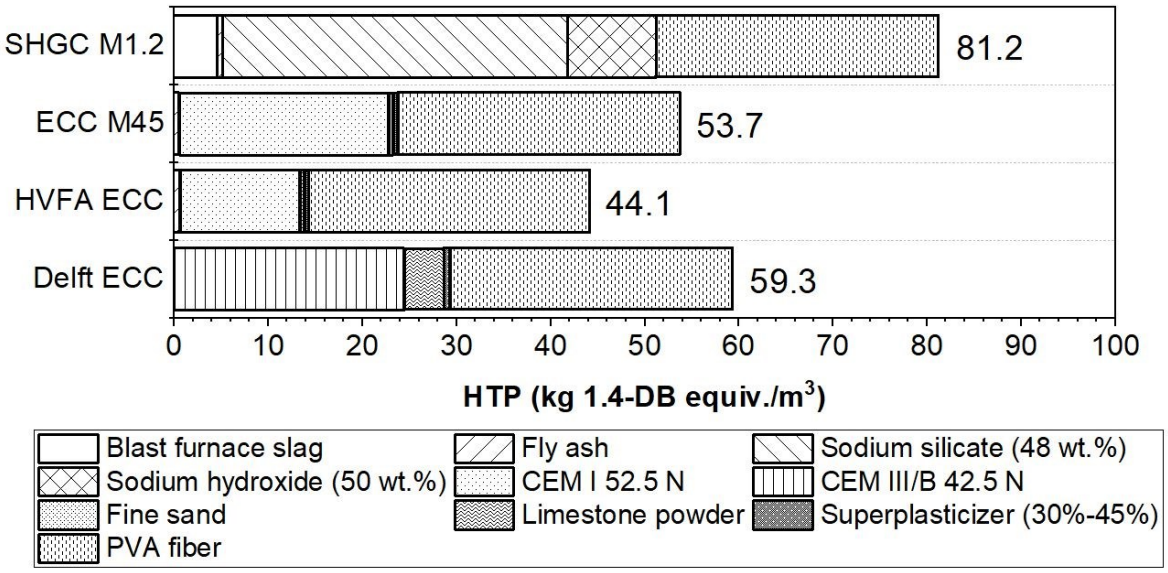

Figure 7.6 Contribution of different raw materials to the human toxicity potential (HTP) of the SHGC and conventional SHCCs.

Generally, the HTP of SHGCs is almost 1.5 times as high as those of conventional SHCCs. In both SHGC and SHCCs, the PVA fiber contributes to a large part of the HTP ranging from 36.8% to 68.0%. In conventional SHCCs, another major contribution to the HTP comes from the cement. It contributes to 41.7% HTP in ECC M45. The inclusion of fly ash as SCMs helps to decrease the HTP by 43.3 % in HVFA ECC. However, compared to ECC M45, the CEM III/B-based Delft ECC has a 9.1% higher HTP from the binder material due to the higher binder content. Another major contribution to the HTP in SHGC comes from the sodium hydroxide and sodium silicate solution. These two main components for the alkaline activator preparation account for 11.6% and 44.9% of the HTP in SHGC, respectively. This makes the alkaline activator the most significant contributor to the HTP in SHGC. These findings are in line with

previous LCA studies on geopolymer concrete, which claimed that the major environmental impact comes from the type and concentration of the alkaline activator [342, 348, 351, 352].

7.3.2.3 Marine aquatic ecotoxicity potential (MAETP)

The marine aquatic ecotoxicity potential (MAETP) is another relatively significant environmental impact. The contributions of different raw materials to the MAETP of SHGC and conventional SHCCs are illustrated in Figure 7.7.

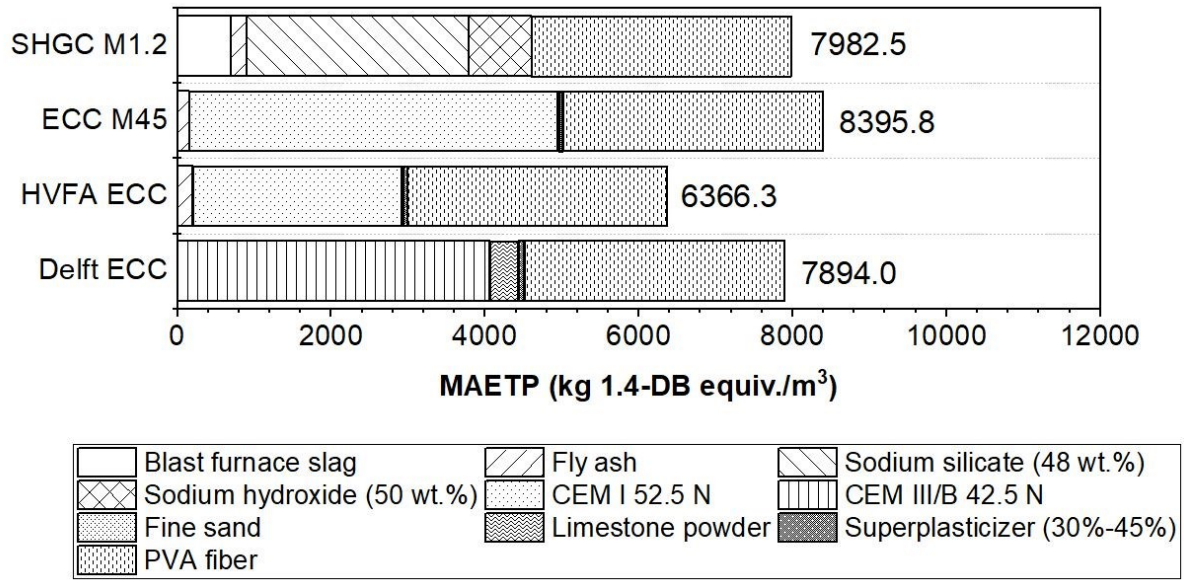

Figure 7.7 Contribution of different raw materials to the marine aquatic ecotoxicity potential (MAETP) of the SHGC and conventional SHCCs.

SHGC has a MAETP that is comparable to ECC M45 (4.4% lower) and Delft ECC (1.1% higher). The MAETP of HVFA ECC, however, is 20.2% lower than that of SHGC. In both SHGC and conventional SHCCs, the PVA fiber contributes to a large part of MAETP (40%-50%). In conventional SHCCs, the second major contribution comes from cement. In ECC M45, the cement contributes 51.4% of the MAETP. The inclusion of SCMs such as fly ash and slag helps to decrease the MAETP in HVFA ECC and Delft ECC by 41.0% and 17.9%, respectively.

The major contribution of MAETP in SHGC comes from the sodium hydroxide (10.1%) and sodium silicate solution (36.2%). These two main components of the activator account for almost half of the MAETP in SHGC. Notably, slag also has a non-negligible contribution (8.5%) to the MAETP in SHGC. This part of MAETP comes from the MAETP associated with the production of pig iron by iron ore smelting in blast furnaces. Since slag in this study is treated as a by-product rather than a waste from the steel-making industry, part of the MAETP associated with pig-iron production was allocated to slag.

7.3.2.4 Embodied energy (EE)

The embodied energy (EE) will be the last to be considered here in this section. The calculated raw materials EE contribution of SHGC and conventional SHCCs are presented in Figure 7.8. The slag/fly ash-based SHGC has lower or similar values of EE when compared with

conventional SHCCs. The EE of SHGC is 4.67 GJ/m^3, which is 21% lower than the EE of ECC M45. In addition, SHGC, HVFA ECC, and Delft ECC have almost similar EE. These findings indicate that SHGC is also competitive from the energy consumption perspective.

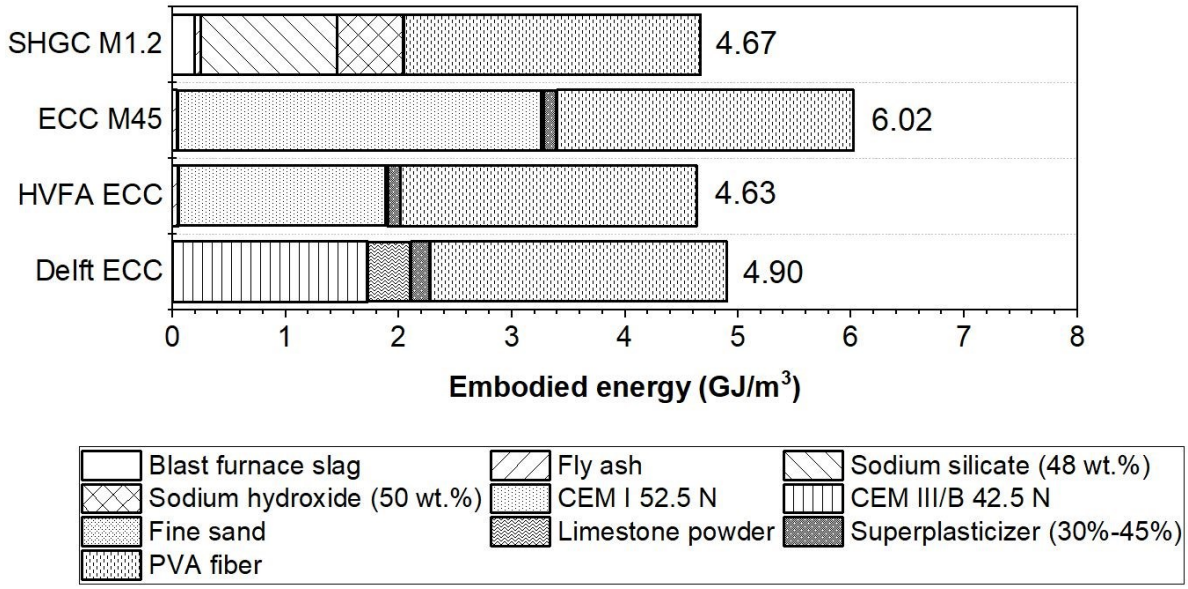

Figure 7.8 Embodied energy (EE) of the SHGC in comparison to those of conventional SHCCs.

The raw material contribution of SHGC and conventional SHCCs to the EE could also be assessed in Figure 7.8. The solid precursors, i.e., slag and fly ash, contribute very little (<10%) to the EE of SHGC. The major contributions come from the alkaline activator solution and PVA fiber, in line with previous LCA studies concerning SHGC [21, 23]. In fact, the sodium-based silicate alkaline activator in this study accounts for 37.5% EE in SHGC. This major contribution to the EE originates from the high EE associated with sodium silicate and sodium hydroxide solution used in alkaline activator preparation. On the other hand, the PVA fiber contributes to a major part of EE for SHGC (54%). This finding is reasonable since the production of PVA fiber, sodium silicate, and sodium hydroxide all involve energy-intensive processes.

The results of EE are in good agreement with two existing studies on SHGC. Nematollahi et al. [23] reported a one-part slag/fly ash SHGC with a reduction of 36% EE compared to that of ECC M45. Ohno and Li [21] reported similar benefits of a fly ash-based EGC reinforced with 1.5 vol. % of PVA fiber. An even higher EE reduction of 55% was achieved by the reduced fiber content.

7.3.3 Discussion on the use of alkaline activator and PVA fiber

The contribution analysis in the previous section indicates that the major environmental impacts and the embodied energy of SCGC come from two components: the alkaline activator solution and the PVA fiber. In this section, these two components are discussed in more detail.

7.3.3.1 Alkaline activator solution

Similar to previous studies, the findings in this chapter indicate the alkaline activator to be the major contributor to the environmental impact of SHGC [21, 23]. Most LCA studies on geopolymer materials have also identified that the environmental impacts (mostly GWP) and the EE are mainly affected by the type and concentration of alkali-activator solution [342, 348, 351-353]. In this study, the alkaline activator is prepared using sodium hydroxide solution and sodium silicate solution, and the environmental impacts and the EE are thus mainly associated with these two solutions.

As noticed in the life-cycle inventory in Section 7.1.1, the LCA data of sodium silicate by Fawer et al. [327] was published 20 years ago. The environmental impact of sodium silicate should have been most probably reduced by the energy consumption transition into using more renewable energy [354] and improvement in the production efficiency [355]. On the other hand, the environmental impact of sodium hydroxide (caustic soda) is also gradually getting lower. This is due to the continuing improvement in the emissions profile of the chlor-alkali industry and meanwhile the reduced reliance on mercury cells in alkali production [356]. Therefore, the actual environmental impacts should be lower than the ones reported in this chapter.

Still, the contribution analysis highlights the significance of the impacts from alkaline activators. Therefore, the dosage, composition, and origins of alkaline activators should be carefully considered to further reduce their environmental impacts of SHGC. Naturally, a lower environmental impact could be achieved by mixture optimization towards the reduced amount of activator. However, an even more effective approach is to use industrial by-products and waste residuals to produce alkaline activators instead of commercial chemicals. Studies have shown that as long as the industrial by-products and wastes contain an adequate amount of amorphous silica, it could be used as an alternative silica source for either alkaline activator solution [357] or solid precursors [91]. A range of options have been proved to be effective, e.g., rice husk ash [358], waste glass [91, 359], olivine silica [309], silica gel from chemical manufacturing processes [360], etc. Consequently, the environmental impacts and EE of the sodium silicate solution can be further reduced if these silica-containing waste and by-products are used. With regards to sodium hydroxide, a promising recent approach is to use the Bayer liquor from the bauxite refining process. The processed Bayer liquor has a concentration of about 230 g/L alumina and 400 g/L sodium hydroxide. Using Bayer liquor for the development of geopolymer concrete has proved to lower both the environmental impact and the embodied energy of the alkaline activator [361].

7.3.3.2 PVA fiber

PVA fiber has a substantial contribution to the environmental impact and embodied energy (EE) in SHCCs and SHGCs. The PVA is normally manufactured by the hydrolysis of polyvinyl acetate (PVAc) derived from vinyl acetate monomer. The high environmental impacts and EE are associated with their energy-intensive manufacturing process using petroleum-based ingredients as feedstock [362].

The environmental impacts and EE of SHGC could be lowered by using a lower amount of PVA fiber while keeping satisfactory performance in tension. This could be achieved using the micromechanics-based design approach as elaborated in Chapter 6. However, a more effective approach is to substitute PVA fiber with alternative fibers derived from waste streams

and/or synthetic materials with lower embodied energy. Research has been conducted to substitute or replace PVA fiber in conventional SHCC materials and comparable performance in tension is achieved. Some promising options include the use of renewable natural fiber [53], waste PET fiber [363], polyethylene (PE) fiber [349], and high tenacity polypropylene (HTPP) fibers [52]. Notably, the different chemical nature of these fibers will lead to different interface bonding behavior with the matrix. To use these “greener” fibers for the development of SHGC in the future, experiments on the interface bonding properties and molecular dynamics study on their adhesion mechanism to the matrix are recommended.

7.3.4 Discussion on the cradle-to-gate LCA of SHGC

To further discuss the sustainability of the newly developed SHGC evaluated by the cradle-to-gate LCA, the following aspects are addressed in this subsection.

- First of all, this study is limited to the environmental impact related to the product stage. Further study with a broader scope of LCA will be needed in the future when sufficient data concerning other life stages are available. Among those, durability can have large consequences on the LCA results. It is conceivable that a product with superior durability can outperform those less durable ones in the use stage. This is because superior durability leads to longer service life and also a reduced amount of work for maintenance and repair. Although this study does not take into consideration the durability aspects of SHGC, many researchers have reported that alkali-activated materials including geopolymer as binder material for concrete have similar or even better durability under certain exposure conditions. This is most probable when the temperature, the chemical attack aggressiveness (e.g., acidity), and the chloride content of the environment are high in the use stage [99-102]. Therefore, the SHGC has the potential to outperform conventional SHCC materials under these exposure conditions.

- Secondly, circularity aspects considered in the end-of-life stage also play an important role in the LCA of SHGC. In cementitious materials, the recovery of unreacted cement particles [364] and the reuse of demolition waste as recycled aggregates [365] have been already proved feasible. However, studies concerning demolition, recycling, and reuse of SHGC in the end-of-life stage are very limited. Future research is recommended on these aspects for further insights.

- Thirdly, another noteworthy aspect concerns the transportation cost and related environmental impact of the raw material for SHGC. Within the cradle-to-gate boundaries, the transportation of raw materials is assumed to be similar for both conventional SHCCs and SHGCs. However, this assumption is only valid when the SHGC, like conventional SHCCs, can be prepared effectively using local raw materials. Long-distance transportation can sometimes dominate the environmental impacts and embodied energy of the raw materials [348]. Therefore, it is crucial that SHGC is developed using locally available raw materials to ensure low environmental impacts.

- Additionally, as discussed in Section 7.3.3.1, the environmental impact data and embodied energy of sodium silicate and sodium hydroxide have raised some discussions. According to some researchers, they should have most probably been reduced with the development of technology [354, 355]. Unfortunately, there is currently still no up-to-date LCA on these

materials. As a result, updating the related data should be the priority in the near future to create an even clearer view of the LCA of SHGC. To achieve this, close collaboration between local industries and LCA experts is needed. In this way, the LCA studies can be conducted on primary data related to up-to-date production processes and will eventually lead to more reliable data on the related environmental impacts.

- Finally, the application of SHGC could induce an unfavorable environmental impact transfer from GWP towards other environmental impacts such as HTP and MAETP (Section 7.2.3.1). However, it is important to point out that the total environmental impact of the SHGC is still 16% to 70% lower depending on the choice of the SHCCs as reference. This means the major benefit from the GWP reduction is more than sufficient to offset the environmental burdens related to HTP, MAETP, etc. Consequently, the newly developed slag/fly ash-based SHGC is still considered a sustainable alternative for conventional SHCCs. It demonstrates a promising environmental profile with low environmental impacts, while at the same time an excellent technical performance is maintained.

7.4 Conclusions

In this Chapter, the environmental impacts of a newly developed slag/fly ash-based SHGC are evaluated and further compared with those of 3 conventional SHCCs. Through a cradle-to-gate LCA, a total of 11 environmental impacts, as well as the embodied energy of the composite materials, have been considered. The raw material accounting for the major environmental impacts and embodied energy in both SHGC and conventional SHCC materials are identified. Based on the results and discussions of this study, the following conclusions can be drawn:

- Compared to conventional SHCCs, the SHGC leads to a tremendous reduction of the global warming potential (GWP) by 42 to 63%. SHGC also has less significant or similar environmental impacts compared to conventional SHCC materials in all the impact categories except in human toxicity potential (HTP) and Marine aquatic ecotoxicity potential (MAETP).

- The major benefit of SHGC from the substantial GWP reduction is more than sufficient to offset the environmental burdens related to HTP and MAETP.

- The major environmental impacts and embodied energy come from sodium-based silicate alkaline activator in SHGC. In conventional SHCCs, they come from the use of OPC. Raw materials like sodium silicate and sodium hydroxide should be cautiously used.

- PVA fiber has a substantial contribution to the environmental impact and embodied energy (EE) in both SHGC and conventional SHCCs.

- The developed slag/fly ash-based SHGC demonstrates a very promising cradle-to-gate environmental profile together with excellent technical performance. Consequently, SHGC could serve as a promising alternative for SHCC materials with considerably lower environmental impacts.

Chapter 8

Conclusions, contributions, and future research

8.1 Conclusions

This PhD project aims to develop a cement-free strain-hardening geopolymer composite (SHGC) as high-value construction material using industrial wastes and by-products through alkaline activation technology. The research first focuses on the quantitative characterization of geopolymer matrix and fiber/matrix interface properties as a design basis for the development of SHGC (Chapter 3 and 4). The PVA fiber/matrix adhesion mechanism is also explored using molecular dynamics simulation (Chapter 5). Based on these results, the SHGC is then systematically developed following a micromechanics-based design approach (Chapter 6). The experimentally-attained matrix and interface properties were used as input and served as valuable input for the computational micromechanics model to simulate the crack bridging at the macroscale. Finally, the environmental impact of the developed SHGC with the most promising performance was also evaluated and compared with that of the conventional SHCC materials (Chapter 7).

The conclusions of this thesis are summarized as follows:

Fracture properties of AASF pastes are strongly related to the chemical composition of C-(N-)A-S-H gel as the main reaction product

- The fracture properties of AASF pastes are strongly related to the Ca/Si and the Ca/(Si+Al) ratio of C-(N-)A-S-H gel. The fracture properties K_{Ic} (J_{tip}) of AASF pastes are not determined by the porosity or intrinsic mechanical properties of the reaction product. Instead, they are most probably dominated by an interparticle cohesion and adhesion mechanism.
- A higher slag content and a moderate silicate modulus M_s of the activator are beneficial for the mechanical properties of AASF pastes.
- The empirical porosity-based strength theory is valid for AASF pastes.

SHGC has different fiber/matrix interface properties compared to SHCC. These interface properties are determined by the reaction products formed in the interfacial transition zone (ITZ)

- The chemical bonding energy G_d between PVA fiber and AASF matrix increases with increasing Ca/Si and Ca/(Si+Al) ratio of C-(N-)A-S-H gel. Hence, changing slag content and the alkali activator M_s proves to be an effective way to modify G_d.
- The initial friction bond τ_0 is most probably determined by the interaction between the fracture surfaces within the AASF matrix rather than between PVA fiber and the AASF matrix.

- The slip-hardening behavior of PVA fiber in the AASF matrix is due to the accumulation of the stripped fibrils (along with matrix micro-debris) on the fiber surface, which increases the pullout resistance.
- Unlike the formation of portlandite identified near the PVA fiber surface in SHCC, a high-Ca C-(N-)A-S-H phase is formed in the ITZ of SHGC. Compared to C-(N-)A-S-H phases formed in the bulk matrix, the high-Ca C-(N-)A-S-H phase in the ITZ has considerably a higher Ca/Si and Ca/(Si+Al) ratio, a lower Mg/Ca ratio, and a similar Al/Si ratio.

***The adhesion between PVA fiber and* C-(N-)A-S-H gel is primarily due to electrostatic interactions rather than van der Waals interactions**

- The origin of adhesion between PVA and C-(N-)A-S-H gel with high Ca/(Si+Al) ratios (> 1.0) is almost entirely due to the electrostatic interactions between the hydroxyl group (OH-) in PVA and the Ca^{2+} and Na^{+} cations within C-(N-)A-S-H gel.
- In contrast, the contribution to the adhesion from the hydrogen bonding (considered as van der Waals interactions) between the PVA molecule and C-(N-)A-S-H gel is only significant at low Ca/(Si+Al) ratios (< 1.0).
- The adhesion is quantified by the chemical bonding energy G_d (determined by the single-fiber pullout test) and the adsorption enthalpy of PVA in C-(N-)A-S-H (calculated by MD simulation). In both terms, the adhesion enhances primarily by increasing the Ca/(Si+Al) ratio of C-(N-)A-S-H gel.

The micromechanics-based design approach helps the systematic development of SHGCs

- The micromechanics-based design approach, linking micromechanical and composite properties, serves as an effective tool for the development of SHGC by assisting in the selection of suitable fiber volume and length, predicting the potential tensile performance, and offering guidance for formulating tailoring strategy.
- Changing the silicate modulus M_s of alkaline activator can effectively alter the matrix mechanical properties, fiber/matrix interface properties, and hence the final strain-hardening properties of SHGC.
- Compared to the energy PSH index, the strength PSH index is a better indicator for the strain-hardening potential of SHGC.

The developed SHGC has a promising cradle-to-gate environmental profile

- Compared to conventional SHCC, SHGC has a significant lower global warming potential (GWP). It also has less significant or similar total environmental impacts compared to conventional SHCC materials.
- The major environmental impacts and embodied energy of SHGC come from sodium-based silicate alkaline activator and PVA fiber in SHGC. These materials should be used cautiously for the development of SHGC.

8.2 Contribution of this study

The following contributions of this study were made to the science and engineering applications of SHGC and AAMs:

- The fracture properties of AASF pastes have been tested systematically by experiments. Considering the current lack of available data on fracture properties of AAMs, the obtained results are valuable for researchers and engineers working on the practical applications of AAMs. Furthermore, this study increases our understanding of the fracture mechanisms in AAMs. This provides a possibility for researchers to develop ultra-tough AAMs fundamentally from the material level. Besides, the strong relationship identified between the chemistry of C-(N-)A-S-H gel and fracture properties gives promising guidance for designing AAMs with required fracture properties. In particular, it contributes to the tailoring strategies for high-performance composite, like SHGC, through proper mixture design.

- This study provides further insights into the adhesion mechanism of PVA fiber to C-(N-)A-S-H gel formed in the AASF system. It also helps researchers to understand the adhesion between other polymeric fibers (with hydrophilic surface properties) to AAM and even to cementitious systems. Furthermore, the clarification of the adhesion mechanism suggests constructive ways to design and tailor the fiber/interface properties: (1) by modification of the fiber surface, (2) by changing the chemical composition of the C-(N-)A-S-H gel, and a combination of (1) and (2). These findings are also particularly valuable for the future development of SHGC.

- This study successfully developed a very sustainable slag/fly ash-based SHGC. It has a lower carbon footprint than SHCC and at the same time a good tensile performance. This newly developed material serves as a good example of the utilization of industrial by-products as secondary resources and at the same time contributes to building up a society with a circular economy.

- The micromechanics-based design approach proves valid for the development of SHGC. The application of this approach can help researchers and engineers to design and tailor future SHGC more efficiently than the commonly used trial-and-error method.

- The assessment of environmental impacts of SHGC is extended from only GWP and embodied energy to 11 impact categories. This gives a more convincing overview of the sustainability performance of SHGC compared to SHCC. It also gives recommendations for further improvements for future development.

8.3 Recommendations for future research

Based on this research there are still some very interesting aspects that are worth further investigation.

- In this thesis, only sodium hydroxide-based and sodium silicate-based alkaline activators were used. The development of SHGC using alternative activators, such as Na_2CO_3-based or Na_2SO_4-based ones, is recommended.

- The fracture mechanism of the SHGC matrix still needs further clarification. More experimental evidence is still needed to fully substantiate the hypothesized cohesion and adhesion-based mechanism. Molecular dynamics simulations and direct measurements

of ion-ion correlation interactions between C-(N-)A-S-H particles (globules) as well as C-(N-)A-S-H particles (globules) and remnant precursor particles are recommended.

- The shrinkage-induced residual stress (perpendicular to the fiber surface) plays an important role in both the initial friction bond τ_0 and the post-pullout behavior of the fiber (i.e., slip-hardening behavior). Since the residual stress is primarily related to the volume stability of the AAM matrix, studies on the influence of shrinkage and creep behavior of the AASF matrix on the residual stress are recommended.

- The origin of the initial friction bond between the PVA fiber and AAM matrix needs further clarification. The classical dry friction between PVA fiber and AAM matrix, determined by surface roughness and the residual stress onto the fiber surface, needs a more thorough experimental study.

- An experimental study on the fracture surface roughness of the AAM matrix is recommended to further confirm the relationship between the fracture surface roughness and the fracture toughness K_{Ic} in AAMs.

- A feasibility study on the application of SHGC, for instance, as repair and retrofitting of concrete structures, is recommended. A comparative study with commonly used repair materials is also recommended to evaluate the potential of SHGC in engineering practice.

- For the environmental impact assessment on AAMs, challenges still lie in the fair selection of up-to-date environmental data of raw materials. The scope of this study, like most existing studies, is still limited within the boundary of cradle-to-gate. A full life-cycle analysis (cradle-to-grave, or even cradle-to-cradle) on AAMs is recommended.

Appendix A

Micromechanics-based constitutive model

A.1 Numerical model for fiber debonding and pullout stages: the relationship between pullout load P and displacement u

A.1.1 Fiber debonding stage

The schematic fiber-debonding model is shown in Figure A.1. A single fiber with the diameter of d_f and the embedment length of L_e is loaded by an external load P. The debonding process is assumed to be a tunnel-crack propagation that initiates from the fiber exit point in the matrix. The model considers a scenario in which a portion of the fiber/matrix interface has been debonded due to the pullout load. The length of the debonded zone is noted as a.

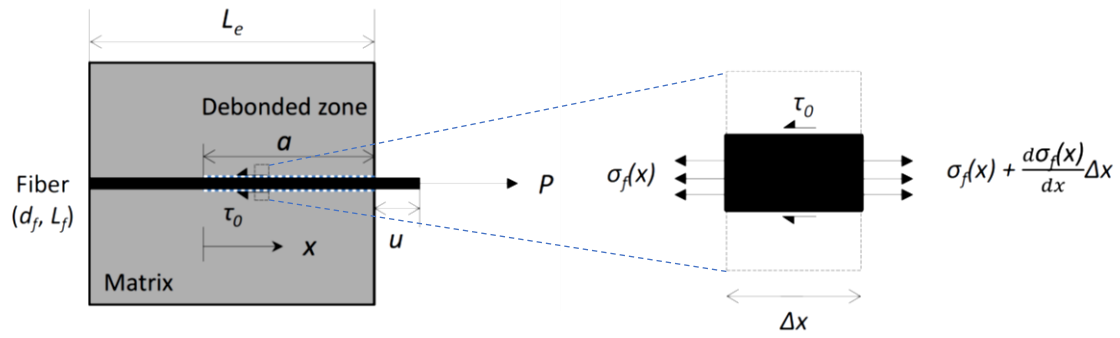

Figure A.1: Schematic model of fiber debonding process with a small segment of the debonded zone adopted from [65].

In the debonded zone, the relative displacement between the fiber and matrix caused by the pullout force is only resisted by the frictional bond. As shown in Figure A.1, we consider a small fiber segment at a distance of x from the tunnel-crack front. Then, if the frictional stress (τ_0) is constant in the debonded zone, the load balance in the small segment is achieved by:

$$\left\{\sigma_f(x) + \frac{d\sigma_f(x)}{dx}\Delta x\right\}A_f = \sigma_f(x)A_f + \tau_0(\pi d_f \Delta x) \tag{A.1}$$

where $\sigma_f(x)$ is the stress in the fiber at a distance of x, Δx is the length of the segment, and A_f is the fiber cross-sectional area, which equals $\pi(d_f/2)^2$. Equation (A.1) therefore becomes:

$$\frac{d\sigma_f(x)}{dx} = \frac{4\tau_0}{d_f} \tag{A.2}$$

Taken into consideration of the boundary condition for Equation (A.2):

$$\sigma_f(a) = \sigma = \frac{P}{A_f} \tag{A.3}$$

The stress in the fiber at the certain distance $\sigma_f(x)$ thereby can be expressed as:

$$\sigma_f(x) = \frac{4\tau_0}{d_f}(x-a) + \sigma \tag{A.4}$$

Next, using the force equilibrium in the debonded segment presented in Figure A.2, the stress in the matrix $\sigma_m(x)$ could be deduced:

$$\sigma_f(x)A_f + \sigma_m(x)A_m = \sigma A_f \tag{A.5}$$

Where A_m is the cross-sectional area of the matrix.

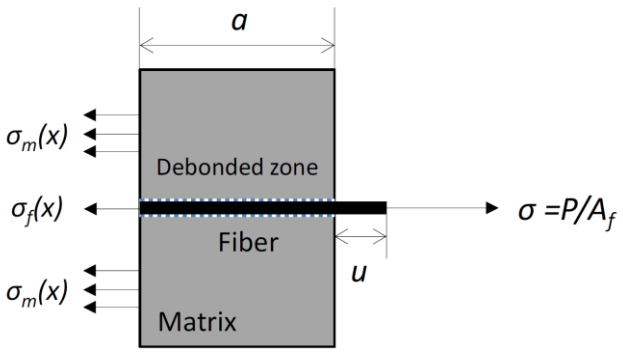

Figure A.2 Force equilibrium in the debonded fiber and surrounding matrix [65].

To reduce the number of the variables, the fiber volume fraction $V_f = A_f/(A_f+A_m)$ is introduced. Equation (A.5) is rewritten as:

$$\sigma_f(x)V_f + \sigma_m(x)(1-V_f) = \sigma V_f \tag{A.6}$$

Solving Equation (A.4) and (A.6) for $\sigma_m(x)$:

$$\sigma_m(x) = \frac{V_f}{1-V_f}\frac{4\tau_0}{d_f}(a-x) \tag{A.7}$$

Then, the displacement of the fiber (u_f) and that of the matrix (u_m) at the distance x caused by the external load is considered. In this case, the relative displacement between the fiber and matrix (γ), or the interface slip, is defined as u_f minus u_m. The strains for the fiber and the matrix are defined as ε_f and ε_m, respectively. From the definition of strain and stress-strain constitutive low, γ at the distance x is calculated as:

$$\gamma(x) = u_f(x) - u_m(x) = \int_0^x \varepsilon_f(x') - \varepsilon_m(x')dx' = \int_0^x \frac{\sigma_f(x')}{E_f} - \frac{\sigma_m(x')}{E_m}dx' \tag{A.8}$$

Where E_f and E_m are the elastic modulus of the fiber and matrix, respectively. Solving Equations (A.4), (A.7), and (A.8):

$$\gamma(x) = \frac{\sigma}{E_f}x + \frac{4\tau_0(1+\eta)}{E_f d_f}\left(\frac{x^2}{2} - ax\right) \tag{A.9}$$

where η is defined as V_fE_f/V_mE_m and V_m is the volume fraction of the matrix. Notably, V_f for the single-fiber pullout process is very small so that η could be assumed to be negligible. Here, when x=0 (i.e., the tunnel-crack front), γ =0 since there is no interface slip in the bonded zone. On the other hand, the interface slip at the fiber exit point (x=a) is given by:

$$\gamma(a) = \frac{\sigma}{E_f}a - \frac{2\tau_0(1+\eta)}{E_f d_f}a^2 \equiv u \tag{A.10}$$

This is equivalent to the fiber pullout displacement *u*. Since *a* is an unknown variable, Equation (A.10) cannot be solved for the fiber pullout load P; the energy balance in the system is considered here to eliminate *a* from the equation.

It is assumed here that both the fiber and the matrix are made up of purely elastic bodies so that the LEFM holds for the calculation. When the tunnel crack is propagated by an infinitesimal step (du_f'), the energy balance in the system requires:

$$Pdu_f' = dU + dW_f + G_d dA \tag{A.11}$$

Where PdU_f' is the work done by the external load P, dU is the change in the stored strain energy of the elastic system, dW_f is the dissipated energy by the friction at the fiber/matrix interface, and G_ddA is the fracture energy consumed to break the interface bonding. It should be noted that u_f' is the displacement of the fiber including not only the elastic stretch of the debonded zone but also that of the bonded zone. The force equilibrium of Equation (A.6) also holds in the bonded zone:

$$\sigma V_f = \sigma_f V_f + \sigma_m V_m = E_f \varepsilon_f V_f + E_m \varepsilon_m V_m = \left(E_f V_f + E_m V_m\right)\varepsilon_f \tag{A.12}$$

where the elastic strains of the fiber ε_f and matrix ε_m are identical.

Therefore, u_f' can be calculated as the elastic displacement of the debonded zone but also that of the bonded zone:

$$u_f' = \int_0^a \frac{\sigma_f(x)}{E_f} dx + \frac{\sigma V_f}{E_f V_f + E_m V_m}(L_e - a) \tag{A.13}$$

In addition, the dissipated energy W_f due to the friction at the fiber/matrix interface can be calculated as:

$$W_f = \int_0^a \tau_0 \left(\pi d_f dx\right)\gamma(x) \tag{A.14}$$

Solving Equation (A.9) and (A.14):

$$W_f = \frac{\pi \tau_0 d_f \sigma}{2E_f} a^2 - \frac{4\pi \tau_0^2 (1+\eta)}{3E_f} a^3 \tag{A.15}$$

For the strain energy term, the change in elastic strain energy of the system is half the work done by the external load in LEFM. Considering the friction as surface traction, the work term minus the friction term can be regarded as the available energy for the strain energy change. That is:

$$dU = \frac{1}{2}\left(P du_f' - dW_f\right) \tag{A.16}$$

Solving Equations (A.11) and (A.16):

$$G_d dA = \frac{1}{2}\left(P du_f' + dW_f\right) \tag{A.17}$$

Where dA is the area of the extended tunnel crack and can be expressed as $\pi d_f da$ where *da* is the length of the crack extension. By solving Equations(A.13), (A.15), and (A.17), the following equation is obtained:

$$G_d = \frac{d_f}{8E_f(1+\eta)}\sigma^2 - \frac{\tau_0 a}{E_f}\sigma + \frac{2\tau_0^2(1+\eta)}{E_f d_f} a^2 \tag{A.18}$$

Solve Equation (A.18) for σ > 0：

$$\sigma = \frac{4\tau_0(1+\eta)}{d_f}a + \sqrt{\frac{8G_d E_f(1+\eta)}{d_f}} \tag{A.19}$$

Combine Equation (A.18) and (A.10), the stress vs displacement relationship can be written as:

$$\sigma(u) = 2\sqrt{\frac{2E_f(1+\eta)}{d_f}(\tau_0 u + G_d)}, \qquad 0 < u \le u_0 \tag{A.20}$$

Equation (A.20) can be rewritten when converting the stress into the pullout force P, thus, the pullout load vs displacement relationship can be written as:

$$P_{debond}(u) = \sqrt{\frac{\pi^2 E_f d_f^3(1+\eta)}{2}\{\tau_0 u + G_d\}}, \qquad 0 < u \le u_0 \tag{A.21}$$

Where u_0 is the critical pullout displacement at the moment when the full debonding process is finished (i.e., a= L_e). Taking u=u_0 into Equation (A.19):

$$\sigma(u_0) = \frac{4\tau_0(1+\eta)}{d_f}L_e + \sqrt{\frac{8G_d E_f(1+\eta)}{d_f}} \tag{A.22}$$

$$u_0 = \gamma(L_e) = \frac{\sigma(u_0)}{E_f}L_e - \frac{2\tau_0(1+\eta)}{E_f d_f}L_e^2 \tag{A.23}$$

Solving Equation (A.22) and (A.23):

$$u_0 = \frac{2\tau_0 L_e^2(1+\eta)}{E_f d_f} + \sqrt{\frac{8G_d L_e^2(1+\eta)}{E_f d_f}} \tag{A.24}$$

A.1.2 Fiber pullout stage

Consider the fiber pullout model shown in Figure A.3 When no slip-dependent behavior is taken into account, the following force equilibrium is obtained:

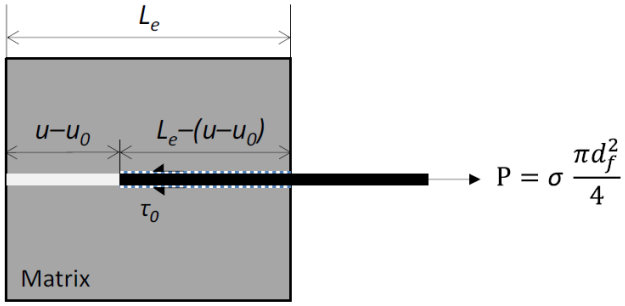

Figure A.3 Model of fiber pullout process adopted from [65].

$$\tau_0 \pi d_f \{L_e - (u - u_0)\} = P \tag{A.25}$$

Then, to include the slip-hardening/softening effect, modify the friction by multiplying a factor that depends on the slip-hardening coefficient (β). The simplest pullout model is given by:

$$P_{pullout}(u) = \pi \tau_0 d_f (L_e - u + u_0)\left(1 + \beta \frac{u - u_0}{d_f}\right), \qquad u_0 \le u \le L_e + u_0 \tag{A.26}$$

A.2 Scale linking model linking P(u) to σ(δ)

Li et al. developed a micromechanics-based constitutive model to relate the abovementioned micromechanical parameters to the macroscopic composite behavior [78]. Later, it has been further modified and extended by other researchers [65, 79, 80]. The idea behind this is that the composite mechanical behavior is governed by fiber pull-out behaviors of individual bridging fibers [66]. The output of the micromechanical model is the σ-δ relationship, which represents the uniaxial tensile stress σ carried by a matrix crack of uniform opening δ. Mathematically, the constitutive law of the σ-δ relation is expressed as follows:

$$\sigma(\delta) = \frac{V_f}{A_f} \int_{\varphi_0}^{\varphi_1} \int_{z=0}^{(L_f/2)\cos\varphi} P(\delta, L_e) g(\varphi) p(\varphi) p(z) dz d\varphi \tag{A.27}$$

where V_f is the fiber volume fraction; A_f is the cross-sectional area of fiber; the term V_f/A_f is equivalent to the number of fibers per unit area of the crack plane with φ=0; φ is the inclination angle of fiber with respect to the normal of the crack plane; L_f is the fiber length; z is the distance between the fiber centroid and the crack plane; L_e is the embedment length of the fiber.

The double integral in Equation (2.4) calculates the total load carried by all bridging fibers in the crack plane with various orientation angles φ and centroid locations z. The bounds of φ integration are limited between φ_0 and φ_1 depending on the casting condition. For 2D random fiber distribution considered in this study, φ varies from 0 to π/2. The upper bound of z integration is calculated as $(L_f/2)\cos(\varphi)$.

The four functions P(δ, L_e), g(φ), p(φ), and p(z) involved in Equation (2.4) are presented as the following:

A.2.1 P(δ, L_e)

P(δ, Le) describes the bridging force of a single aligned fiber for a crack opening δ. The embedment length L_e, could be either the short-embedment side, or the other side has the embedment length of L_f minus L_e. The pullout displacements for both ends of the embedded fiber contribute to the crack opening:

$$\delta = u_L + u_S \tag{A.28}$$

where u_L and u_S are the pullout displacements for the long- and short-embedment sides. The solution of P(δ, L_e) can be obtained by Equation (A.28) together with the equilibrium of pullout loads for the long- and short-embedment segments, which are given by either $P_{debond}(u)$ in Equation (A.21) or $P_{pullout}(u)$ in Equation (A.26). Both equations have been given in the previous section and are given again here.

$$P_{debond}(u) = \sqrt{\frac{\pi^2 E_f d_f^3 (1+\eta)}{2}\{\tau_0 u + G_d\}}, \qquad 0 < u \le u_0 \tag{A.21}$$

$$P_{pullout}(u) = \pi\tau_0 d_f (L_e - u + u_0)\left(1 + \beta\frac{u-u_0}{d_f}\right), \qquad u_0 \le u \le L_e + u_0 \tag{A.26}$$

$$u_0 = \frac{2\tau_0 L_e^2 (1+\eta)}{E_f d_f} + \sqrt{\frac{8G_d L_e^2 (1+\eta)}{E_f d_f}} \tag{A.24}$$

where u_0 is the critical pullout displacement at the moment when the full debonding process is finished.

In determining the pullout load for each side, there are two scenarios, which are illustrated in Figure A.4. In both scenarios, both sides of the fiber first undergo the debonding stage. This is the case when $\delta < 2u_{0S}$, where u_{0S} is the threshold displacement for the short-embedment side. In this case, the pullout displacements at both short- and long-embedded sides are the same (i.e., $u_L = u_S = \delta/2$). Thus, P(δ, L_e) is expressed as:

$$P(\delta, L_e) = P_{\text{debond}}\left(\frac{\delta}{2}\right), \delta < 2u_{0S} \tag{A.29}$$

Once the short-embedded side of fiber enters the pullout stage, the situation will be different between the two scenarios. In the first scenario, the short-embedment side enters the pullout stage, while the other side remains in the debonding stage. This is illustrated in Figure A.4 (a). Mathematically, it is expressed as $\delta = u_L + u_S$ such that $u_S > u_{0S}$ and $u_L < u_{0L}$. Here, u_{0L} is the

threshold displacement for the long-embedment side. For this pullout-debonding case, $P(\delta, L_e)$ is given by:

$$P(\delta, L_e) = P_{\text{pullout}}(u_S; L_e) = P_{\text{debond}}\left(u_L; L_f - L_e\right), u_S > u_{0S} \text{ and } u_L < u_{0L} \tag{A.30}$$

The second scenario also has the pullout-debonding phase. However, as shown in Figure A.4 (b), the pullout load of the short-embedment side can exceed the peak debonding load of the long-embedment side $P_{\text{debond}}(u_{0L})$.

Thus, for $\delta = u_L + u_S$ such that $u_S > u_{0S}$ and $u_L < u_{0L}$, both sides can undergo the pullout stage:

$$P(\delta, L_e) = P_{\text{pullout}}(u_S; L_e) = P_{\text{pullout}}\left(u_L; L_f - L_e\right), u_S > u_{0S} \text{ and } u_L > u_{0L} \tag{A.31}$$

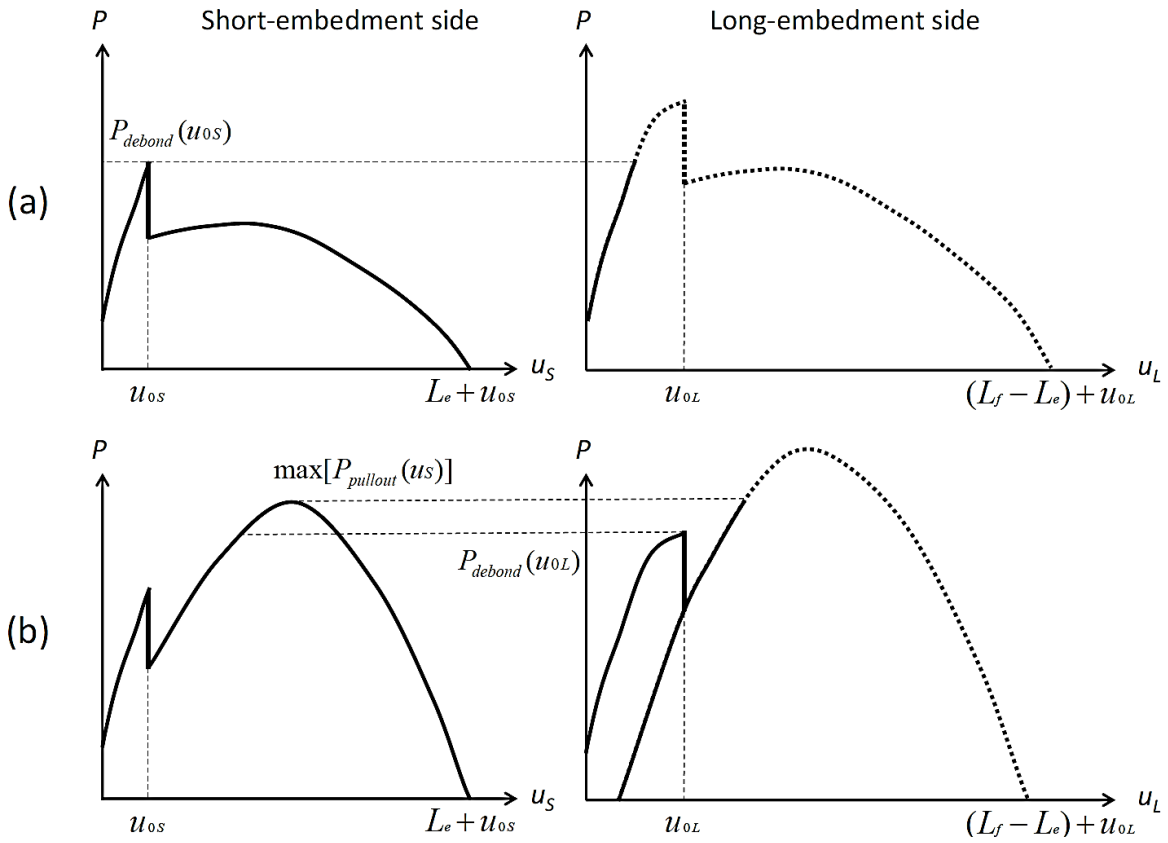

Figure A.4 Schematic model of fiber pullout process adopted from [65]: (a) One-way pullout case; only the short-embedment side enters the pullout stage, while the other side remains in the debonding stage. (b) Two-way pullout case; the long-embedment side also undergo the pullout stage for $\delta = u_L + u_S$ *such that* $u_S > u_{0S}$ *and* $u_L > u_{0L}$.

A.2.2 g(φ)

It is important to note that the equation in the above sections only considers the fiber that is aligned perpendicular to the crack plane, which is not the case in practice. According to Morton and Glove [82] and Li et al. [140], an exponential relationship was found between the normalized maximum pullout force P and the inclination angle φ. This so-called “snubbing” effect is considered by the following empirical equations g(φ):

$$g(\varphi) = e^{f\varphi} \tag{A.32}$$

where *f* is the snubbing coefficient, the value of which is dependent on the particular fiber/matrix combination.

To experimentally determine *f*, the peak pullout load in the single-fiber pullout test is compared between aligned and inclined fibers:

$$f = \frac{1}{\varphi}\ln\left\{\frac{P_{peak}(\varphi)}{P_{peak}(0)}\right\} \tag{A.33}$$

For PVA fiber, the snubbing coefficient *f* ranges from 0.2 to 0.8 [366]. In this study, an f value of 0.3 is used for micromechanical modeling following [21].

A.2.3 p(φ) and p(z)

The randomness of fiber location and orientation/inclination at the crack plane is considered by adopting the probability density function (PDF) that describes the spatial variability of the fibers. p(φ) and p(z) are probability density functions (PDFs) of fiber inclination angle φ and fiber-centroid location z, respectively. In this study, the fiber orientation is constrained by the shape of the thickness of the dogbone specimens. Therefore, a 2-D random fiber distribution was used. Since the PDFs regarding z and φ are independent of each other, p(z, φ) can be expressed as the following Equation (A.34) and (A.35):

$$p(z) = \frac{2}{L_f}, \qquad 0 \le z \le \frac{L_f}{2} \tag{A.34}$$

$$p(\varphi) = \frac{2}{\pi}, \qquad 0 \le \varphi \le \frac{\pi}{2} \tag{A.35}$$

where z is the fiber centroid distance z and orientation angle φ relative to the crack plane, L_f is the fiber length.

A.3 Other considerations

A.3.1 Strength reduction factor f'

Kanda and Li found the decreased in-situ strength for both aligned and inclined fibers [297]. First, when an aligned fiber is embedded in a mortar matrix, its strength is typically smaller than the nominal strength reported by the manufacturer. This reduction is attributed to fiber-surface abrasion that occurs in the debonded zone of the fiber. Further, another significant reduction is observed for inclined fibers. Based on experimental results for PVA fiber, Kanda and Li suggested an exponential function to express the strength-reduction effect of inclined fibers:

$$\sigma_f(\varphi) = \sigma_f(0)e^{-f'\varphi} \tag{A.36}$$

where $\sigma_f(0)$ and $\sigma_f(\varphi)$ are the in-situ strength of aligned and inclined fibers. Then, the strength reduction factor *f'* can be determined by:

$$f' = \frac{1}{\varphi}\ln\left\{\frac{\sigma_f(\varphi)}{\sigma_f(0)}\right\} \tag{A.37}$$

It is suggested that both *f* and *f'* depend mainly on the fiber type. For PVA fiber, the strength-reduction factor *f'* is about 0.3 [366]. In this study, this value is used for micromechanical modeling following [21].

A.3.2 Matrix micro-spalling

When a fiber is pulled at an inclined angle to the crack plane in the matrix, the high stress concentration at the bearing point of the fiber may lead to local micro-spalling of the matrix. This results in a sudden release of the tensioned fiber as shown schematically in Figure A.5. After micro-spalling, the fiber inclination angle decreases while the crack opening width increases [82].

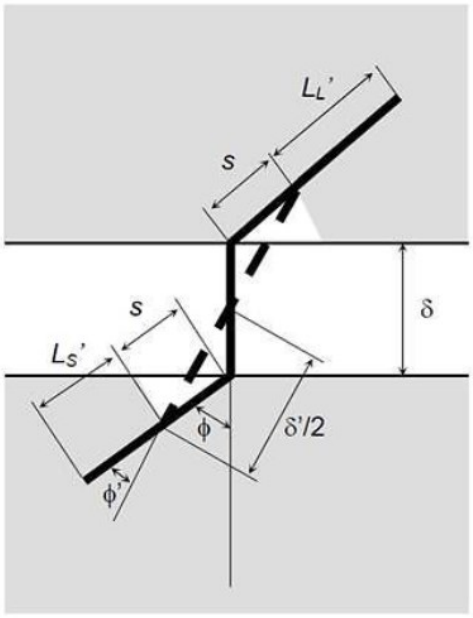

Figure A.5 Schematic illustration of matrix micro-spalling

A semi-empirical equation for estimating the size of the micro-spalling was proposed as Equation (A.38):

$$s = \frac{P\sin\left(\frac{\varphi}{2}\right)}{kd_f\sigma_m\cos^2\left(\frac{\varphi}{2}\right)} \tag{A.38}$$

where P is the external force acting on the fiber; φ is the fiber inclination angle; σ_m is the matrix tensile strength, and k is the spalling coefficient. k is a dimensionless constant related to fiber geometry and matrix stiffness and can be calibrated using the experimental result of the single fiber pullout test.

The modified inclination angle (φ') and the corresponding effective crack opening width (δ_{eff}) can then be calculated by Equation (A.39) to (A.41):

$$\varphi' = \sin^{-1}\left(\frac{\delta\sin\ \varphi}{\delta'}\right) \tag{A.39}$$

$$\delta_{eff} = \delta' - 2s \tag{A.40}$$

where

$$\delta' = \sqrt{4s^2 + 4s\delta\cos\ \phi + \delta^2} \tag{A.41}$$

A.3.3 Cook-Gordon effect

The Cook-Gordon effect, or pre-debonding of the fibers, refers to the debonding of a weak fiber/matrix interface at the location near a blunt crack tip in a fiber-reinforced composite. This means when a fiber intersects a matrix crack, a small segment of the fiber/matrix interface at the crack plane has already been debonded [83], which leads to an additional increase in the crack opening width δ.

The debonded length α a proportional to the diameter of the fiber. This debonded segment due to stretching leads to additional crack opening width δ_{cg} given by:

$$\delta_{cg} = \frac{4\alpha P}{\pi d_f^2 E_f} \tag{A.42}$$

Appendix B

Chemical composition of the reaction product in the PVA fiber/matrix interfacial transition zone (ITZ)

B.1 Reaction product in the ITZ

B.1.1 High-Ca C-(N-)A-S-H phase

The most important finding concerning the reaction product in the ITZ is the formation of a Ca-rich reaction product, namely the high-Ca C-(N-)A-S-H (Table 4.3). In both S30 and S50 mixtures, the location of this phase matches perfectly the location of the Ca-rich rim around PVA fiber in the EDX element mapping (Figure 4.11). As discussed in Section 4.3.1.2, the formation of the high-Ca C-(N-)A-S-H is due to the hydroxyl group on the PVA fiber surface. At an early age, the strong polarity induced by the hydroxyl group will effectively attract the free-moving Ca^{2+} cation in the pore solution to accumulate near the PVA fiber surface.

One possible explanation for the Ca-rich reaction product could be due to the formation of C-(N-)A-S-H gel together with crystalline portlandite (CH). The latter has been previously detected around the PVA fiber in cementitious systems [46, 246, 367] and plays a dominant role in determining the interface bonding properties in PVA-based SHCC [368]. However, the formation of CH in the AASF system is highly unlikely because the solubility product K_{sp} of CH is much higher than of C-(N-)A-S-H gel [218]. Compared to CH as a crystalline phase, the amorphous C-(N-)A-S-H gel is more preferentially formed as predicted by thermodynamics modeling [186, 369]. In fact, the main reaction products of sodium silicate-based AASF are reported to be amorphous [103, 150, 183] and seldom have new crystalline phases except for hydrotalcite has been reported. The above evidence thus precludes the possibility that the Ca-rich reaction product is due to the intermixing of C-(N-)A-S-H gel with CH. It is reasonable, therefore, that the high-Ca C-(N-)A-S-H formed in the ITZ is a kind of C-(N-)A-S-H gel with a high Ca/Si ratio and/or Ca/(Si+Al) ratio.

Furthermore, the high-Ca C-(N-)A-S-H also has a low Al/Si ratio compared to the other two C-(N-)A-S-H phases identified in Chapter 4. This could be due to (1) the high Ca/Si content in high-Ca C-(N-)A-S-H phase and (2) the formation of Al-rich hydrotalcite in C-(N-)A-S-H 1 and 2 phases.

- Firstly, it is known that the incorporation of Al is easier in C-A-S-H gel with a lower Ca/Si ratio [212]. Meanwhile, only a limited amount of Al could be incorporated into the C-A-S-H gel [370]. Since the Al content in the pore solution of AASF is abundant at an early age [178], the Al/Si ratio of C-(N-)A-S-H gel for saturated Al incorporation can be reached very

quickly. As a result, the high-Ca C-(N-)A-S-H with a higher Ca/Si ratio has a lower Al/Si ratio than the other two C-(N-)A-S-H phases [212].

- Secondly, the influence on the Al/Si ratio could come from the formation of the Al-rich hydrotalcite phase. Since hydrotalcite is the only phase containing Mg in the reaction product, its abundance could be indicated by the Mg content. In Table 4.3, the Mg contents (Mg/Ca and Mg/Si ratio) are generally lower in high-Ca C-(N-)A-S-H than those in C-(N-)A-S-H 1 and 2, in particular, C-(N-)A-S-H 1 This indicates the preferential formation of hydrotalcite phase is not around PVA fiber but rather in the reaction products around slag particles (see also [186, 371]). The higher abundance of hydrotalcite in C-(N-)A-S-H 1 and 2 thus also contributes to their higher Al/Si ratio than that in high-Ca C-(N-)A-S-H.

B.1.2 Two types of C-(N-)A-S-H phases

Interestingly, the phase mapping also identified two types of C-(N-)A-S-H phase in both S30 and S50 matrices, viz., C-(N-)A-S-H 1 and C-(N-)A-S-H 2 (see Table 4.3). The presence of the two C-(N-)A-S-H phases could not be shown using the CaO-SiO_2-Al_2O_3 ternary diagram, because their Ca, Si, and Al composition are rather similar. However, they can be distinguished by their different Mg composition (Table 4.3). Hence, the CaO-Al_2O_3-MgO ternary diagram was plotted and the results are shown in Figure B.1. In both ternary diagrams, the C-(N-)A-S-H 1 phase has a higher Mg content than the C-(N-)A-S-H 2 phase.

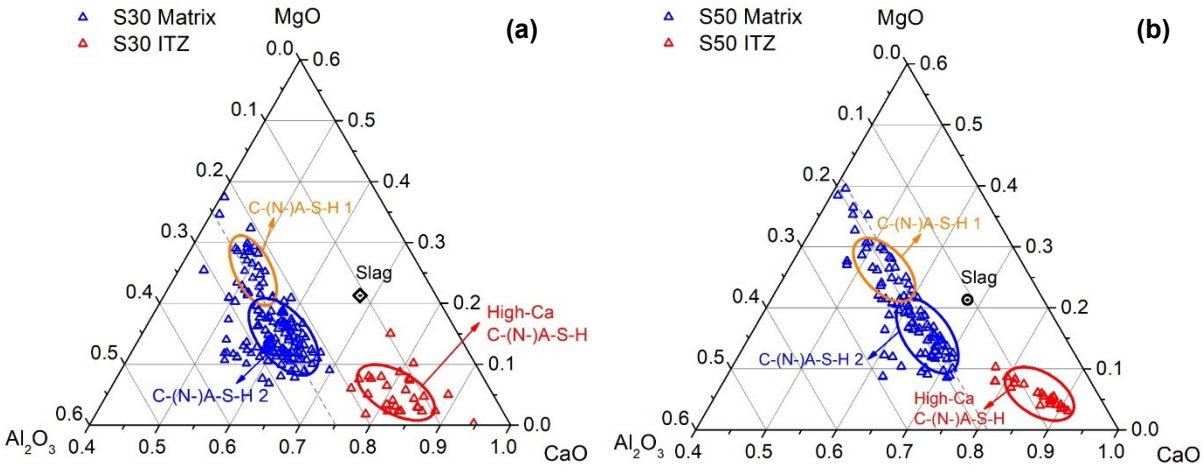

Figure B.1 CaO-Al_2O_3-MgO ternary diagram of EDX spot analysis in the ITZ of (a) S30 and (b) S50

C-(N-)A-S-H 1 phase is majorly distributed around the unreacted slag particles as previously shown in Figure 4.9. This matches the so-called “dark rim” around the remnant slag particles. The element mapping of Mg in Figure 4.9 suggests that the reaction products within the “dark-rim” are most probably a composite phase of C-(N-)A-S-H and hydrotalcite [372]. The “dark rim” has been detected in previous research on AAS and AASF [182, 183, 186, 213, 223] due to the in-situ reaction between the outer layer of GGBFS and alkali [371, 372]. The Mg ions, due to their low mobility, do not significantly migrate from the original slag grain [247]. This also contributes to the formation of the “dark rim”. Unlike the C-(N-)A-S-H 1 phase, the C-(N-)A-S-H 2 phase is distributed quite homogeneously in the matrix. It is also the most

abundant with the largest area coverage in the phase mapping (see Figure 4.12 and Figure 4.13).

Unfortunately, the EDX element/phase mapping cannot distinguish the hydrotalcite and the C-(N-)A-S-H phase. Hydrotalcite is a layered double hydroxide (LDH). Its host brucite-like Mg-Al layers have a strong positive charge [373]. As a result, the hydrotalcite layers are strongly attracted to the negatively charged C-(N-)A-S-H layers during the alkali-activation reaction. This affinity thereby leads to a highly intermixed hydrotalcite and C-(N-)A-S-H gel at the nanoscale [371]. For a clear separation of intermixed phases at this scale, most X-ray based analysis techniques have reached their resolution limits. As a result, the hydrotalcite phase was rarely studied individually in AASF pastes.

B.2 Density plots of phases based on EDX phases mapping

B.2.1 Density plots of reaction products in the ITZ

An alternative way to study the phases formed in the ITZ is to use the density plots. The presence of the phases determined by the automated phase mapping (Section 4.3.2.3) is further examined by the density plots using the channel intensity correlations between (1) Ca+Al+Si versus Mg and (2) Ca+Al+Si+Mg versus Na. The channel intensities used here are the net counts from each pixel of the EDX phase mapping. They were extracted using the spectra imaging (SI) data from the phase mapping results in Figure 4.12 and Figure 4.13. The density plots of the abovementioned two correlations were created following Van Hoek et al. [374] and Nedeljković et al. [183]. The Ca+Al+Si versus Mg density plots help to distinguish the remnant slag and fly ash particles, and the PVA fiber from the reaction products. For both S30 and S50 systems, the density plots are given in Figure B.2 (a) and (b), respectively. The Ca+Al+Si+Mg versus Na density plots help to better illustrate the differences between the reaction products. For both S30 and S50 systems, the density plots are given in Figure B.2 (c) and (d), respectively. In all density plots, the statistically distinct phases could then be distinguished by their different positions in the data cluster, with the abundance of the phases reflected by the different colors.

The PVA fiber occupies most of the areas in the phases mapping in both S30 (Figure 4.12) and S50 systems (Figure 4.13). Accordingly, the clusters of PVA in all density plots show the highest abundance in red color. There are no evident clusters for remnant slag and fly ash particles in both S30 and S50, indicating their limited content in the ITZ. The positions of clusters for slag and fly ash particles have been marked in Figure B.2 (a) and (b) with black dotted circles.

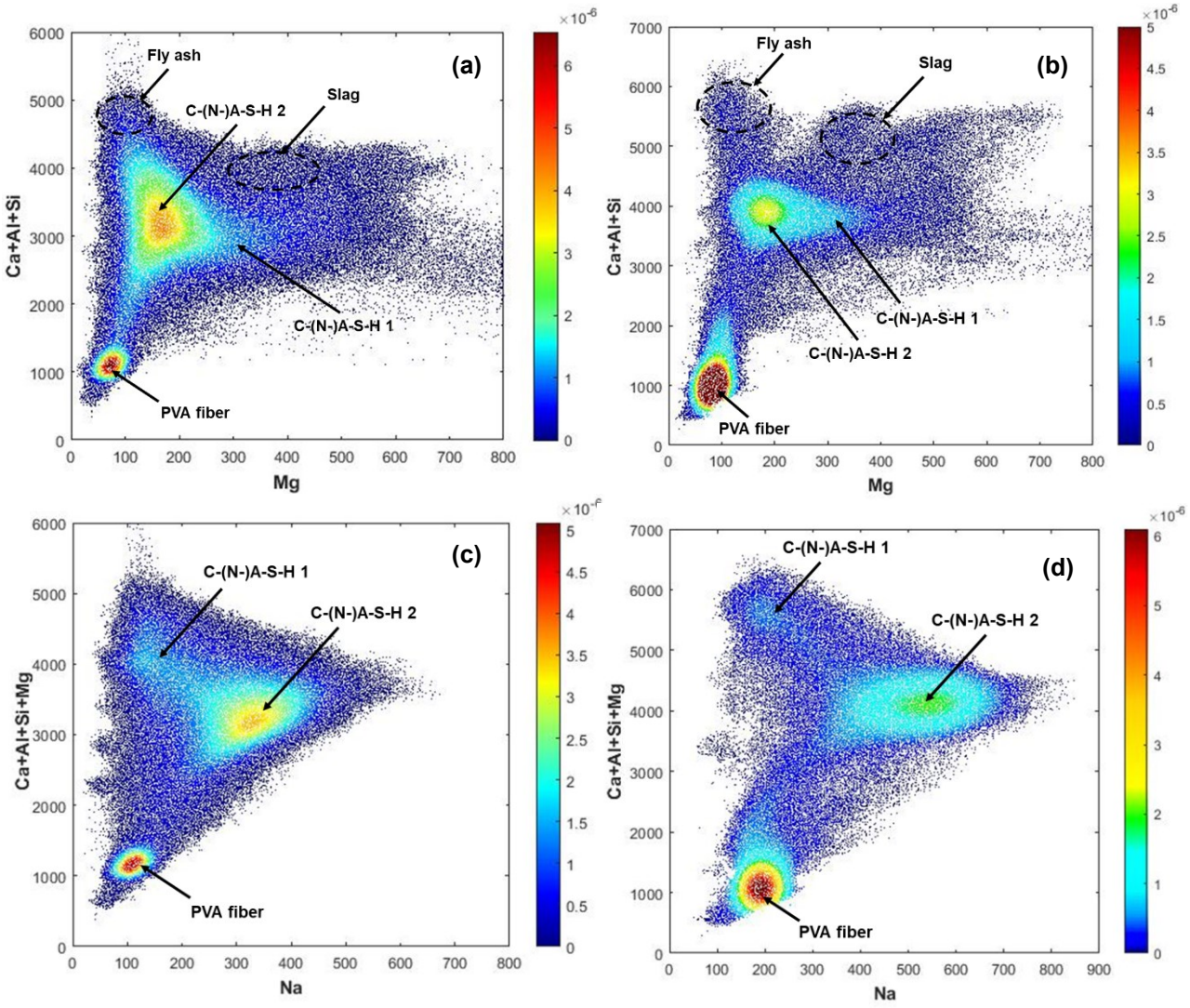

Figure B.2 Density plot of channel intensities Ca+Al+Si versus Mg in (a) S30 and (b) S50, and density plot of channel intensities Ca+Al+Si+Mg versus Na in (c) S30 and (d) S50.

The C-(N-)A-S-H 1 and 2 phases, as the main reaction products, could be distinguished according to their different Mg content. In comparison to C-(N-)A-S-H 1, C-(N-)A-S-H 2 phase is more abundant in all density plots. These results coincide well with the ones from the COMPASS phase mapping (Figure 4.12 and Figure 4.13), in which C-(N-)A-S-H 2 among all reaction products occupies the largest area. No sharp boundaries are observed between these two phases. Similar findings were found by Nedeljković et al. [183] using a Phase Recognition and Characterization (PARC), the reaction products, namely Ca-Mg-Na-Al-Si-H gel and Ca-Na-Al-Si-H gel, correspond to the C-(N-)A-S-H 1 and C-(N-)A-S-H 2 in this study, respectively [183]. The high-Ca C-(N-)A-S-H phase cannot be visually distinguished due to its similar channel intensities with C-(N-)A-S-H 2 phase in the density plots.

Appendix C

Chemical composition determination of C-(N-)A-S-H gel for the construction of C-(N-)A-S-H structures in the molecular dynamics (MD) simulation

C.1 Introduction

As has been confirmed in Chapter 3, the C-(N-)A-S-H type gel is the predominant binding phase in AASF with various slag content and activator silicate modulus M_s. To construct reliable C-(N-)A-S-H structures for the molecular dynamics simulation in Chapter 5, the chemical composition of the "pure" C-(N-)A-S-H gel formed in AASF pastes needs to be determined.

In this Appendix C, the procedures to determine the chemical composition of "pure" C-(N-)A-S-H gel using the results of EDX analysis is explained. The chemical composition of the C-(N-)A-S-H structure is also defined using the CaO-Al_2O_3-SiO_2 ternary diagram.

C.2 Procedures

For the construction of the C-(N-)A-S-H structures in Chapter 5, the chemical composition of C-(N-)A-S-H gel determined by EDX spot analysis in the AASF matrices in Chapter 3 is selected as the starting point. The mixture design of these AASF matrices is shown in Table C.1. Notably, only sodium silicate-based AASF matrices with 50% fly ash incorporation were selected. This selection minimized the influence of the unreacted fly ash particles. Furthermore, the selected matrices also have a more homogenous distribution of the reaction products than the sodium hydroxide-based AASF matrices [186]. Both contribute to a more reliable chemical composition determined by EDX analysis.

Table C.1 Mixture design of AASF matrix

Mixture	Slag (wt.%)	Fly ash (wt.%)	w/b ratio	Na_2O (wt.%)	Silicate Modulus
S50M0.5	50	50	0.32	4	0.5
S50M0.8	50	50	0.32	4	0.8
S50M1.0	50	50	0.32	4	1.0
S50M1.2	50	50	0.32	4	1.2
S50M1.5	50	50	0.32	4	1.5

For a more accurate construction of the C-(N-)A-S-H structure in MD simulation, the chemical composition of the reaction products has to agree with that of the C-(N-)A-S-H gel formed in

AASF matrices. To this end, a statistical approach using Gaussian distribution fitting was applied to extract the essential characteristics of the chemical composition using the Ca/(Si+Al) and the Al/Si ratios of C-(N-)A-S-H gel.

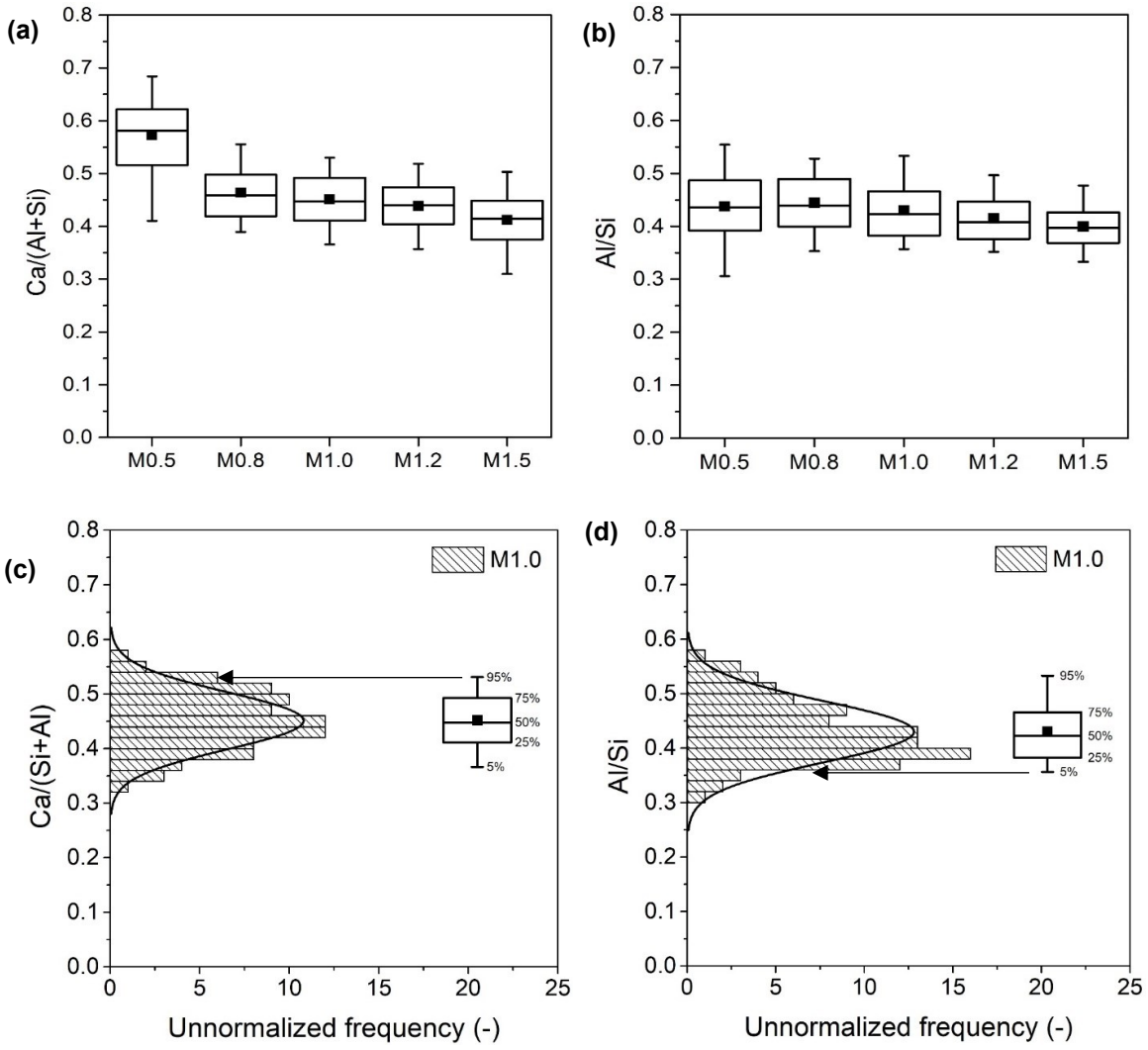

Figure C.1. Box plot of (a) Ca/(Si+Al) ratio and (b) Al/Si ratio of the main reaction products in AASF M0.5-M1.5 matrices; Representative histogram of EDX data points (c) Ca/(Si+Al) ratio and (d) Al/Si ratio of the main reaction products in AASF M1.0 Matrix. The median value (-), the mean value (■), the values at 25%, and 75% (box edges), and the values at 5% and 95% (Whiskers) are illustrated.

Both the Ca/(Si+Al) and Al/Si ratios of the C-(N-)A-S-H gel in S50M0.5-1.5 matrices are shown in Figure C.1 (a) and (b), respectively. The Ca/(Si+Al) ratio declines with increasing activator silicate modulus values (M_s=0.5-1.5), whereas the influence on the Al/Si is insignificant. Furthermore, the histogram of both atomic ratios shown in Figure C.1 (c) and (d) was also fitted with the simple Gaussian distribution curve. The characteristics of the fitted distribution are thus characterized by its mean value (μ) and the standard deviations (STDs, or σ). According to the central limit theorem in statistics, the observation of the well-fitted Ca/(Si+Al) and Al/Si ratios indicate that the results are influenced by a large number of independent random variables. In this case, these variables could be different experimental errors induced

by either the error of the equipment and procedures, or the intermixing of multiple phases within reaction products. Most likely, the influence is due to the "interaction volume" in an EDX spot analysis. Under the acceleration voltage of 15 kV, the interaction volume has a radius of approximately 1.0-2.5 µm into the sample surface when this major reaction product is C-(N-)A-S-H gel [175]. This causes the analysis of intermixed phases.

Although in this case µ could reasonably reflect the Ca/(Si+Al) and Al/Si ratios of the intermixed phases, it cannot properly describe those of the "pure" C-(N-)A-S-H gel. Considering the presence of remnant fly ash particles and unreacted silicate-based activator within the matrix, the intermixing is often influenced by the Si-rich phases. This could lead to underestimation of the true Ca/(Si+Al) ratio. In contrast, the true Al/Si ratio is possibly overestimated considering the higher Al/Si ratio (0.60) in fly ash. Following previous studies on C-(A)-S-H gel [180], the Ca/(Si+Al) values at the higher side of the distribution (µ+2σ) and the Al/Si values at the lower side of the distribution (µ-2σ) are selected to show the effect of phase intermixing on the chemical composition. As marked in Figure C.1 (c) and (d), they correspond to the values at the 95% level and 5% level of the Ca/(Si+Al) ratio and Al/Si ratio in its Gaussian distribution, respectively. In fact, this chemical composition also corresponds to the cloud edge of the C-(N-)A-S-H gel points, i.e., the "least-intermixed" point. These points are shown in the scatter plots in Figure C.2 (a) by a CaO-SiO_2-Al_2O_3 ternary diagram, in which Ca, Al, and Si are normalized to 100% on an oxide basis. A representative ternary diagram is also illustrated in Figure C.2 (b), which shows the chemical composition of "pure" C-(N-)A-S-H gel in S50M1.0 at the cloud edge of the EDX scatter points. The chemical composition of C-(A)-S-H selected this way agrees well with that of the transmission electron microscope (TEM) analyses [375]. Since the intermixing can be avoided in TEM analyses, the proposed chemical compositions of "pure" C-(N-)A-S-H gel served as the basis for the construction of the C-(N-)A-S-H structures for MD simulation.

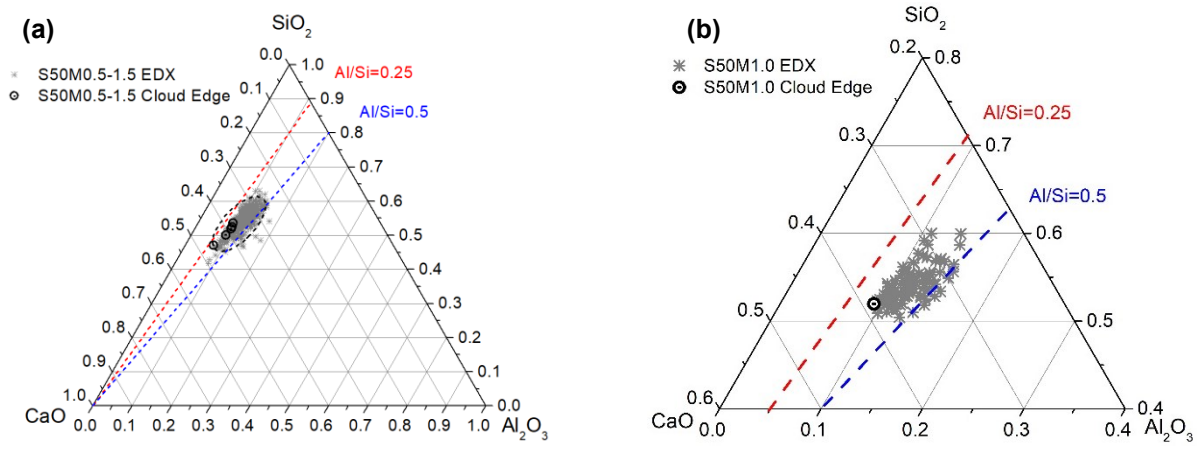

Figure C.2. (a) The scatter plot of EDX spot analyses in the CaO-SiO_2-Al_2O_3 ternary diagram of C-(N-)A-S-H gel in the M0.5-M1.5 AASF matrices and the points for corresponding "pure" C-(N-)A-S-H gel (cloud edge); and (b) representative scatter plot of the chemical composition of "pure" C-(N-)A-S-H gel in S50M1.0 at the cloud edge of the EDX scatter points.

Finally, for the construction of C-(N-)A-S-H structures, two Al/Si ratios of 0.25 and 0.5 were determined using the two tie lines in Figure C.2. (a). They cover the Al/Si ratios of C-(N-)A-S-

H gel formed in S50M0.5-1.5 AASF matrices. The Ca/(Si+Al) ratios of 0.5, 0.75, 1.0, 1.1, and 1.3 were also selected to cover the chemical composition of the C-(N-)A-S-H gel. Particularly, the Ca/(Si+Al) ratio was extended up to 1.3 considering the chemical composition of C-(N-)A-S-H gel formed in AAS [151, 170, 171] and AASF with high slag content [103-105, 150, 172-174]. In this way, the conclusions from MD simulation are also suitable for more Ca-rich binders.

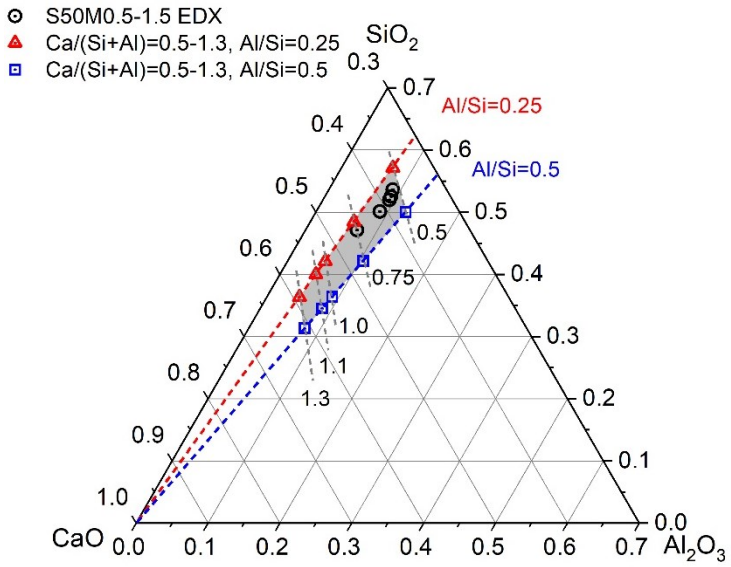

Figure C.3 The CaO-SiO_2-Al_2O_3 ternary diagram of the chemical composition of “pure” C-(N-)A-S-H gel in the M0.5-M1.5 AASF matrices and the defined chemical composition of the C-(N-)A-S-H structures for MD simulation (Ca/(Si+Al)=0.5-1.3 with Al/Si=0.25 and Al/Si=0.5).

References

[1] C.B.v.d. Statistiek, Environmental accounts of the Netherlands, 2011.

[2] Rijksoverheid, A Circular Economy in the Netherlands by 2050, 2016.

[3] B. Lomborg, The skeptical environmentalist: measuring the real state of the world, Cambridge University Press Cambridge2003.

[4] F.P.C.-T. GAL, Introduction to the environmental impact of construction and building materials, Eco-efficient Construction and Building Materials: Life Cycle Assessment (LCA), Eco-Labelling and Case Studies, (2014) 1.

[5] B. Lothenbach, K. Scrivener, R.D. Hooton, Supplementary cementitious materials, Cement and Concrete Research, 41 (2011) 1244-1256.

[6] J. Van Deventer, J. Provis, P. Duxson, G. Lukey, Reaction mechanisms in the geopolymeric conversion of inorganic waste to useful products, Journal of hazardous materials, 139 (2007) 506-513.

[7] P. Duxson, J.L. Provis, G.C. Lukey, J.S.J. van Deventer, The role of inorganic polymer technology in the development of 'green concrete', Cem. Concr. Res., 37 (2007) 1590-1597.

[8] C. Shi, D. Roy, P. Krivenko, Alkali-activated cements and concretes, CRC press2006.

[9] J. Davidovits, Geopolymers, Journal of Thermal Analysis and Calorimetry, 37 (1991) 1633-1656.

[10] P. Duxson, J.L. Provis, G.C. Lukey, J.S. Van Deventer, The role of inorganic polymer technology in the development of 'green concrete', Cement and Concrete Research, 37 (2007) 1590-1597.

[11] D.M. Roy, Alkali-activated cements opportunities and challenges, Cement and Concrete Research, 29 (1999) 249-254.

[12] J. Provis, Green concrete or red herring?–future of alkali-activated materials, Advances in Applied Ceramics, 113 (2014) 472-477.

[13] M. Van Lieshout, S. Nusselder, Update prioritering handelingsperspectieven verduurzaming betonketen 2016, CE Delft, Delft, 2016.

[14] J. Provis, J. van Deventer, Alkali Activated Materials: State-of-the-Art Report, RILEM TC 224-AAM, Springer Netherlands2013.

[15] Z. Pan, J.G. Sanjayan, B.V. Rangan, Fracture properties of geopolymer paste and concrete, Mag Concrete Res, 63 (2011) 763-771.

[16] Y. Ding, C.-J. Shi, N. Li, Fracture properties of slag/fly ash-based geopolymer concrete cured in ambient temperature, Construction and Building Materials, 190 (2018) 787-795.

[17] Z. Yang, W.J. Weiss, J. Olek, Interaction between micro-cracking, cracking, and reduced durability of concrete: developing methods for considering cumulative damage in life-cycle modeling, (2004).

[18] A.E. Naaman, High performance fiber reinforced cement composites: classification and applications, International Workshop "Cement Based Materials and Civil Infrastructure"("CBM-CI"), Karachi, Pakistan, Citeseer, 2007, pp. 10-11.12.

[19] V.C. Li, On engineered cementitious composites (ECC), Journal of advanced concrete technology, 1 (2003) 215-230.

[20] V.C. Li, H.-C. Wu, Conditions for pseudo strain-hardening in fiber reinforced brittle matrix composites, Applied Mechanics Reviews, 45 (1992) 390-398.

[21] M. Ohno, V.C. Li, An integrated design method of Engineered Geopolymer Composite, Cement and Concrete Composites, 88 (2018) 73-85.

[22] B. Nematollahi, J. Sanjayan, F.U.A. Shaikh, Tensile Strain Hardening Behavior of PVA Fiber-Reinforced Engineered Geopolymer Composite, Journal of Materials in Civil Engineering, 27 (2015).

[23] B. Nematollahi, J. Sanjayan, J. Qiu, E.-H. Yang, Micromechanics-based investigation of a

sustainable ambient temperature cured one-part strain hardening geopolymer composite, Construction and Building Materials, 131 (2017) 552-563.

[24] M. Ohno, V.C. Li, A feasibility study of strain hardening fiber reinforced fly ash-based geopolymer composites, Construction and Building Materials, 57 (2014) 163-168.

[25] B. Nematollahi, J. Sanjayan, F.U. Ahmed Shaikh, Tensile strain hardening behavior of PVA fiber-reinforced engineered geopolymer composite, Journal of Materials in Civil Engineering, 27 (2015) 04015001.

[26] A. Naaman, H. Reinhardt, Proposed classification of HPFRC composites based on their tensile response, Materials and structures, 39 (2006) 547-555.

[27] A.E. Naaman, Tensile strain-hardening FRC composites: historical evolution since the 1960, Advances in Construction Materials 2007, Springer2007, pp. 181-202.

[28] A. Naaman, Advances in High Performance Fiber Reinforced Cement Based Composites, Proceedings of the International Symposium on Fiber Reinforced Concrete, VS Parameswaran and TS Krishnamurti, Editors, Oxford IBH Publishing Ltd., New Delhi, India, 1987, pp. 7.87-87.98.

[29] A.E. Naaman, J.R. Homrich, Tensile stress-strain properties of SIFCON, Materials Journal, 86 (1989) 244-251.

[30] V.C. Li, C.K. Leung, Steady-state and multiple cracking of short random fiber composites, Journal of Engineering Mechanics, 118 (1992) 2246-2264.

[31] V.C. Li, Y. Wang, S. Backer, A micromechanical model of tension-softening and bridging toughening of short random fiber reinforced brittle matrix composites, Journal of the Mechanics and Physics of Solids, 39 (1991) 607-625.

[32] W.E. Stone, G.M. El Shafei, J. Sanz, S.A. Selim, Association of soluble aluminum ionic species with a silica-gel surface: a solid-state NMR study, The Journal of Physical Chemistry, 97 (1993) 10127-10132.

[33] T. Kanda, V.C. Li, T. Hamada, Material design and development of high-ductility composite reinforced with short random polyvinyl alcohol fiber, (1998).

[34] S. Wang, V.C. Li, Tailoring of PVA fibre/matrix interface for Engineered Cementitious Composites (ECC), Proceedings of the Fibre Society Symposium on Advanced Flexible Materials and Structures: Engineering with Fibre, Citeseer, 2003, pp. 91-92.

[35] G.P.A.G. Van Zijl, F.H. Wittmann, Durability of strain-hardening fibre-reinforced cement-based composites (SHCC), Springer Science & Business Media2010.

[36] V.C. Li, Engineered Cementitious Composites (ECC): Bendable Concrete for Sustainable and Resilient Infrastructure, Springer2019.

[37] A.E. Naaman, High performance fiber reinforced cement composites: classification and applications, International Workshop Cement Based Materials and Civil Infrastructure (CBM-CI), Karachi, Pakistan, Citeseer, 2007, pp. 10-11.12.

[38] M.B. Weimann, V.C. Li, Hygral Behavior of Engineered Cementitious Composites (ECC)/Vergleich der hygrischen Eigenschaften von ECC mit Beton, Restoration of Buildings and Monuments, 9 (2003) 513-534.

[39] A. Zhao, J. Yang, E.-H. Yang, Self-cleaning engineered cementitious composites, Cement and Concrete Composites, 64 (2015) 74-83.

[40] Y. Yang, M. Lepech, V.C. Li, Self-healing of ECC under cyclic wetting and drying, (2005).

[41] V.C. Li, Engineered Cementitious Composites (ECC) Material, Structural, and Durability Performance, (2008).

[42] H.J. Kong, S.G. Bike, V.C. Li, Electrosteric stabilization of concentrated cement suspensions imparted by a strong anionic polyelectrolyte and a non-ionic polymer, Cement and Concrete Research, 36 (2006) 842-850.

[43] S. Wang, V.C. Li, Engineered cementitious composites with high-volume fly ash, ACI Materials Journal-American Concrete Institute, 104 (2007) 233-241.

[44] S. Qian, V.C. Li, Simplified inverse method for determining the tensile strain capacity of strain

hardening cementitious composites, Journal of Advanced Concrete Technology, 5 (2007) 235-246.

[45] V.C. Li, S. Wang, C. Wu, Tensile strain-hardening behavior of polyvinyl alcohol engineered cementitious composite (PVA-ECC), ACI Materials Journal-American Concrete Institute, 98 (2001) 483-492.

[46] E.-H. Yang, Y. Yang, V.C. Li, Use of high volumes of fly ash to improve ECC mechanical properties and material greenness, ACI materials journal, 104 (2007) 620-628.

[47] J. Zhou, S. Qian, M.G. Sierra Beltran, G. Ye, K. van Breugel, V.C. Li, Development of engineered cementitious composites with limestone powder and blast furnace slag, Materials and Structures, 43 (2010) 803-814.

[48] R. Ranade, V.C. Li, M.D. Stults, W.F. Heard, T.S. Rushing, Composite Properties of High-Strength, High-Ductility Concrete, ACI Materials Journal, 110 (2013).

[49] K. Yu, Y. Wang, J. Yu, S. Xu, A strain-hardening cementitious composites with the tensile capacity up to 8%, Construction and Building Materials, 137 (2017) 410-419.

[50] H. Wu, V.C. Li, Basic interfacial characteristic of polyethylene fiber/cement composites and its modification by plasma, (1997).

[51] M. Chaouche, X.X. Gao, M. Cyr, M. Cotte, L. Frouin, On the origin of the blue/green color of blast‐furnace slag‐based materials: Sulfur K‐edge XANES investigation, Journal of the American Ceramic Society, (2017).

[52] B. Felekoglu, K. Tosun-Felekoglu, R. Ranade, Q. Zhang, V.C. Li, Influence of matrix flowability, fiber mixing procedure, and curing conditions on the mechanical performance of HTPP-ECC, Composites Part B: Engineering, 60 (2014) 359-370.

[53] M. Sierra Beltran, E. Schlangen, Wood fibre reinforced cement matrix: a micromechanical based approach, Key Engineering Materials, Trans Tech Publ, 2008, pp. 445-448.

[54] S.R. Ferreira, M. Pepe, E. Martinelli, F. de Andrade Silva, R.D. Toledo Filho, Influence of natural fibers characteristics on the interface mechanics with cement based matrices, Composites Part B: Engineering, 140 (2018) 183-196.

[55] S.R. Ferreira, R.G.M. de Andrade, E. Koenders, F. de Andrade Silva, E.d.M.R. Fairbairn, R.D. Toledo Filho, Pull-out behavior and tensile response of natural fibers under different relative humidity levels, Construction and Building Materials, 308 (2021) 124823.

[56] V.C. Li, Mechanical Properties of Engineered Cementitious Composites (ECC), Engineered Cementitious Composites (ECC), Springer2019, pp. 101-137.

[57] Q. Zhang, V.C. Li, Development of durable spray-applied fire-resistive Engineered Cementitious Composites (SFR-ECC), Cement and Concrete Composites, 60 (2015) 10-16.

[58] Q. Zhang, V.C. Li, Ductile Fire-Resistive Material for Enhanced Fire Safety Under Multi-Hazards-A Feasibility Study, Structures Congress 2014, 2014, pp. 1148-1158.

[59] S. Wang, V. Li, Lightweight engineered cementitious composites (ECC), PRO 30: 4th International RILEM Workshop on High Performance Fiber Reinforced Cement Composites (HPFRCC 4), RILEM Publications, 2003, pp. 379.

[60] S. Wang, Micromechanics based matrix design for engineered cementitious composites, 2005.

[61] B.-T. Huang, K.-F. Weng, J.-X. Zhu, Y. Xiang, J.-G. Dai, V.C. Li, Engineered/strain-hardening cementitious composites (ECC/SHCC) with an ultra-high compressive strength over 210 MPa, Composites Communications, 26 (2021) 100775.

[62] K.-Q. Yu, J.-T. Yu, J.-G. Dai, Z.-D. Lu, S.P. Shah, Development of ultra-high performance engineered cementitious composites using polyethylene (PE) fibers, Construction and Building Materials, 158 (2018) 217-227.

[63] K. Wille, D.J. Kim, A.E. Naaman, Strain-hardening UHP-FRC with low fiber contents, Materials and structures, 44 (2011) 583-598.

[64] M. Behloul, A. Durukal, J. Batoz, G. Chanvillard, Ductal®: ultra high-performance concrete technology with ductility, 6th International RILEM Symposium on Fibre Reinforced Concretes, RILEM

Publications SARL, 2004, pp. 1281-1290.

[65] M. Ohno, Green and Durable Geopolymer Composites for Sustainable Civil Infrastructure, 2017.

[66] S. Müller, V. Mechtcherine, Use of strain-hardening cement-based composites (SHCC) in real scale applications, International Conference on Strain-Hardening Cement-Based Composites, Springer, 2017, pp. 690-700.

[67] M. Kunieda, K. Rokugo, Recent progress on HPFRCC in Japan required performance and applications, Journal of Advanced Concrete Technology, 4 (2006) 19-33.

[68] K. Rokugo, Tension tests and structural applications of strain-hardening fiber-reinforced cementitious composites, Fracture Mechanics of Concrete and Concrete Structures, (2010) 1533-1540.

[69] H. Mitamura, N. Sakata, K. Shakushiro, K. Suda, T. Hiraishi, Application of overlay reinforcement method on steel deck utilizing engineered cementitious composites–Mihara Bridge, Bridge and Foundation Engineering, 39 (2005) 88-91.

[70] T. Kanda, S. Nagai, M. Maruta, Y. Yamamoto, New high-rise R/C structure using ECC coupling beams, 2nd International RILEM Conference on Strain Hardening Cementitious Composites (SHCC2-Rio), RILEM Publications SARL, 2011, pp. 289-296.

[71] D. Meng, T. Huang, Y.X. Zhang, C.K. Lee, Mechanical behaviour of a polyvinyl alcohol fibre reinforced engineered cementitious composite (PVA-ECC) using local ingredients, Construction and Building Materials, 141 (2017) 259-270.

[72] J. Zhou, S. Quian, K. Van Breugel, Engineered cementitious composites with low volume of cementitious materials, FraMCos-7: Proceedings of the 7th International Conference on Fracture Mechanics of Concrete and Concrete Structures, Jeju Island, Korea, 23-28 May 2010, 2010.

[73] Y. Zhu, Y. Yang, Y. Yao, Use of slag to improve mechanical properties of engineered cementitious composites (ECCs) with high volumes of fly ash, Construction and Building Materials, 36 (2012) 1076-1081.

[74] J.-K. Kim, J.-S. Kim, G.J. Ha, Y.Y. Kim, Tensile and fiber dispersion performance of ECC (engineered cementitious composites) produced with ground granulated blast furnace slag, Cement and Concrete Research, 37 (2007) 1096-1105.

[75] A. Hillerborg, Analysis of fracture by means of the fictitious crack model, particularly for fibre reinforced concrete, International journal of cement composites, 2 (1980) 177-184.

[76] D. Marshall, B. Cox, A J-integral method for calculating steady-state matrix cracking stresses in composites, Mechanics of materials, 7 (1988) 127-133.

[77] V.C. Li, Micromechanics and Engineered Cementitious Composites (ECC) Design Basis, Engineered Cementitious Composites (ECC), Springer2019, pp. 11-71.

[78] Y. Wang, S. Backer, V.C. Li, A statistical tensile model of fibre reinforced cementitious composites, Composites, 20 (1989) 265-274.

[79] T. Kanda, V.C. Li, Practical design criteria for saturated pseudo strain hardening behavior in ECC, Journal of advanced concrete technology, 4 (2006) 59-72.

[80] E.-H. Yang, S. Wang, Y. Yang, V.C. Li, Fiber-bridging constitutive law of engineered cementitious composites, Journal of advanced concrete technology, 6 (2008) 181-193.

[81] V.C. Li, Y. Wang, S. Backer, Effect of inclining angle, bundling and surface treatment on synthetic fibre pull-out from a cement matrix, Composites, 21 (1990) 132-140.

[82] J. Morton, G. Groves, The effect of metal wires on the fracture of a brittle-matrix composite, Journal of Materials Science, 11 (1976) 617-622.

[83] J. Cook, J. Gordon, A mechanism for the control of crack propagation in all-brittle systems, Proc. R. Soc. Lond. A, 282 (1964) 508-520.

[84] E.-H. Yang, V.C. Li, Strain-hardening fiber cement optimization and component tailoring by means of a micromechanical model, Construction and Building Materials, 24 (2010) 130-139.

[85] E.-H. Yang, Designing added functions in engineered cementitious composites, ProQuest2008.

[86] B. Nematollahi, J. Sanjayan, F.U.A. Shaikh, Matrix design of strain hardening fiber reinforced engineered geopolymer composite, Composites Part B: Engineering, 89 (2016) 253-265.

[87] T. Kanda, Design of engineered cementitious composites for ductile seismic resistant elements, University of Michigan1998.

[88] A. Purdon, The action of alkalis on blast-furnace slag, Journal of the Society of Chemical Industry, 59 (1940) 191-202.

[89] V. Glukhovsky, Soil silicates, Gostroiizdat Publish. Kiev, USSR, (1959).

[90] A. Palomo, O. Maltseva, I. Garcia-Lodeiro, A. Fernández-Jiménez, Portland Versus Alkaline Cement: Continuity or Clean Break: “A Key Decision for Global Sustainability”, Frontiers in Chemistry, 9 (2021).

[91] S. Zhang, A. Keulen, K. Arbi, G. Ye, Waste glass as partial mineral precursor in alkali-activated slag/fly ash system, Cement and Concrete Research, 102 (2017) 29-40.

[92] S.A. Bernal, E.D. Rodríguez, A.P. Kirchheim, J.L. Provis, Management and valorisation of wastes through use in producing alkali‐activated cement materials, Journal of Chemical Technology & Biotechnology, 91 (2016) 2365-2388.

[93] J.L. Provis, J.S. van Deventer, Alkali Activated Materials, Springer2014.

[94] F. Pacheco-Torgal, J. Castro-Gomes, S. Jalali, Alkali-activated binders: A review. Part 2. About materials and binders manufacture, Construction and Building Materials, 22 (2008) 1315-1322.

[95] S.A. Bernal, J.L. Provis, V. Rose, R. Mejía de Gutierrez, Evolution of binder structure in sodium silicate-activated slag-metakaolin blends, Cement and Concrete Composites, 33 (2011) 46-54.

[96] P. Duxson, A. Fernández-Jiménez, J. Provis, G. Lukey, A. Palomo, J. Van Deventer, Geopolymer technology: the current state of the art, Journal of Materials Science, 42 (2007) 2917-2933.

[97] J.L. Provis, S.A. Bernal, Geopolymers and related alkali-activated materials, Annual Review of Materials Research, 44 (2014) 299-327.

[98] G. Habert, C. Ouellet-Plamondon, Recent update on the environmental impact of geopolymers, RILEM technical Letters, 1 (2016) 17-23.

[99] K. Arbi, M. Nedeljkovic, Y. Zuo, G. Ye, A Review on the Durability of Alkali-Activated Fly Ash/Slag Systems: Advances, Issues, and Perspectives, Industrial & Engineering Chemistry Research, 55 (2016) 5439-5453.

[100] M. Albitar, M.M. Ali, P. Visintin, M. Drechsler, Durability evaluation of geopolymer and conventional concretes, Construction and Building Materials, 136 (2017) 374-385.

[101] F. Pacheco-Torgal, Z. Abdollahnejad, A. Camões, M. Jamshidi, Y. Ding, Durability of alkali-activated binders: a clear advantage over Portland cement or an unproven issue?, Construction and Building Materials, 30 (2012) 400-405.

[102] J. Zhang, C. Shi, Z. Zhang, Z. Ou, Durability of alkali-activated materials in aggressive environments: A review on recent studies, Construction and Building Materials, 152 (2017) 598-613.

[103] I. Ismail, S.A. Bernal, J.L. Provis, R. San Nicolas, S. Hamdan, J.S. van Deventer, Modification of phase evolution in alkali-activated blast furnace slag by the incorporation of fly ash, Cement and Concrete Composites, 45 (2014) 125-135.

[104] F. Puertas, A. Fernández-Jiménez, Mineralogical and microstructural characterisation of alkali-activated fly ash/slag pastes, Cement and Concrete composites, 25 (2003) 287-292.

[105] N.K. Lee, H.K. Lee, Reactivity and reaction products of alkali-activated, fly ash/slag paste, Construction and Building Materials, 81 (2015) 303-312.

[106] S. Puligilla, P. Mondal, Role of slag in microstructural development and hardening of fly ash-slag geopolymer, Cement and Concrete Research, 43 (2013) 70-80.

[107] J. Gourley, Geopolymers in Australia, J. Aus. Ceram. Soc, 50 (2014) 102-110.

[108] M. Farooq, A. Bhutta, N. Banthia, Tensile performance of eco-friendly ductile geopolymer composites (EDGC) incorporating different micro-fibers, Cement and Concrete Composites, 103 (2019)

183-192.

[109] L.-l. Kan, W.-s. Wang, W.-d. Liu, M. Wu, Development and characterization of fly ash based PVA fiber reinforced Engineered Geopolymer Composites incorporating metakaolin, Cement and Concrete Composites, 108 (2020) 103521.

[110] L. Kan, F. Wang, Mechanical properties of high ductile alkali-activated fiber reinforced composites incorporating red mud under different curing conditions, Ceramics International, 48 (2022) 1999-2011.

[111] L. Kan, R. Shi, Y. Zhao, X. Duan, M. Wu, Feasibility study on using incineration fly ash from municipal solid waste to develop high ductile alkali-activated composites, Journal of Cleaner Production, 254 (2020) 120168.

[112] B.Y. Lee, C.-G. Cho, H.-J. Lim, J.-K. Song, K.-H. Yang, V.C. Li, Strain hardening fiber reinforced alkali-activated mortar – A feasibility study, Construction and Building Materials, 37 (2012) 15-20.

[113] J.-I. Choi, B.Y. Lee, R. Ranade, V.C. Li, Y. Lee, Ultra-high-ductile behavior of a polyethylene fiber-reinforced alkali-activated slag-based composite, Cement and Concrete Composites, 70 (2016) 153-158.

[114] B. Nematollahi, J. Sanjayan, J. Qiu, E.-H. Yang, High ductile behavior of a polyethylene fiber-reinforced one-part geopolymer composite: A micromechanics-based investigation, Arch Civ Mech Eng, 17 (2017) 555-563.

[115] Y. Alrefaei, J.-G. Dai, Tensile behavior and microstructure of hybrid fiber ambient cured one-part engineered geopolymer composites, Construction and Building Materials, 184 (2018) 419-431.

[116] H. Zhong, M. Zhang, Effect of recycled tyre polymer fibre on engineering properties of sustainable strain hardening geopolymer composites, Cement and Concrete Composites, 122 (2021) 104167.

[117] B. Nematollahi, J. Qiu, E.-H. Yang, J. Sanjayan, Micromechanics constitutive modelling and optimization of strain hardening geopolymer composite, Ceramics International, 43 (2017) 5999-6007.

[118] B. Nematollahi, J. Sanjayan, F.U.A. Shaikh, Influence of Matrix Related Parameters on Strain Hardening Behavior of Engineered Geopolymer Composite (EGC).

[119] B. Nematollahi, J. Sanjayan, F.U.A. Shaikh, Strain hardening behavior of engineered geopolymer composites: effects of the activator combination, Journal of The Australian Ceramic Society Volume, 51 (2015) 54-60.

[120] N. Ranjbar, M. Zhang, Fiber reinforced geopolymer composites: A review, Cement and Concrete Composites, (2019) 103498.

[121] B.-C. Lyu, C. Ding, L.-P. Guo, B. Chen, A.-g. Wang, Basic performances and potential research problems of strain hardening geopolymer composites: A critical review, Construction and Building Materials, 287 (2021) 123030.

[122] F.U.A. Shaikh, A. Fairchild, R. Zammar, Comparative strain and deflection hardening behaviour of polyethylene fibre reinforced ambient air and heat cured geopolymer composites, Construction and Building Materials, 163 (2018) 890-900.

[123] F.U.A. Shaikh, Tensile and flexural behaviour of recycled polyethylene terephthalate (PET) fibre reinforced geopolymer composites, Construction and Building Materials, 245 (2020) 118438.

[124] M. Alshaaer, S.A. Mallouh, J.a. Al-Kafawein, Y. Al-Faiyz, T. Fahmy, A. Kallel, F. Rocha, Fabrication, microstructural and mechanical characterization of Luffa Cylindrical Fibre - Reinforced geopolymer composite, Applied Clay Science, 143 (2017) 125-133.

[125] A.C.C. Trindade, P.H.R. Borges, F. de Andrade Silva, Mechanical behavior of strain-hardening geopolymer composites reinforced with natural and PVA fibers, Materials Today: Proceedings, 8 (2019) 753-759.

[126] J. Wei, C. Meyer, Degradation mechanisms of natural fiber in the matrix of cement composites, Cement and Concrete Research, 73 (2015) 1-16.

[127] J. Zhang, C. Shi, Z. Zhang, Effect of Na2O concentration and water/binder ratio on carbonation of alkali-activated slag/fly ash cements, Construction and Building Materials, (2020) 121258.

[128] M. Xu, Y. Bao, K. Wu, H. Shi, X. Guo, V.C. Li, Multiscale investigation of tensile properties of a

TiO2-doped Engineered Cementitious Composite, Construction and Building Materials, 209 (2019) 485-491.

[129] S. Zhang, V.C. Li, G. Ye, Micromechanics-guided development of a slag/fly ash-based strain-hardening geopolymer composite, Cement and Concrete Composites, 109 (2020) 103510.

[130] B. Nematollahi, J. Qiu, E.-H. Yang, J. Sanjayan, Microscale investigation of fiber-matrix interface properties of strain-hardening geopolymer composite, Ceramics International, 43 (2017) 15616-15625.

[131] S.-J. Choi, J.-I. Choi, J.-K. Song, B.Y. Lee, Rheological and mechanical properties of fiber-reinforced alkali-activated composite, Construction and Building Materials, 96 (2015) 112-118.

[132] L. Kan, L. Zhang, Y. Zhao, M. Wu, Properties of polyvinyl alcohol fiber reinforced fly ash based Engineered Geopolymer Composites with zeolite replacement, Construction and Building Materials, 231 (2020) 117161.

[133] Y. Wang, Y. Wang, M. Zhang, Effect of sand content on engineering properties of fly ash-slag based strain hardening geopolymer composites, Journal of Building Engineering, 34 (2021) 101951.

[134] M. Şahmaran, M. Lachemi, K.M. Hossain, R. Ranade, V.C. Li, Influence of aggregate type and size on ductility and mechanical properties of engineered cementitious composites, ACI Materials Journal, 106 (2009) 308-316.

[135] P. Nath, P.K. Sarker, Fracture properties of GGBFS-blended fly ash geopolymer concrete cured in ambient temperature, Materials and Structures, 50 (2016) 32.

[136] A. Katz, V.C. Li, A special technique for determining the bond strength of micro-fibres in cement matrix by pullout test, Journal of Materials Science Letters, 15 (1996) 1821-1823.

[137] M. Li, V.C. Li, Cracking and Healing of Engineered Cementitious Composites under Chloride Environment, ACI Materials Journal, 108 (2011).

[138] C. Redon, V.C. Li, C. Wu, H. Hoshiro, T. Saito, A. Ogawa, Measuring and modifying interface properties of PVA fibers in ECC matrix, Journal of Materials in Civil Engineering, 13 (2001) 399-406.

[139] V.C. Li, C. Wu, S. Wang, A. Ogawa, T. Saito, Interface tailoring for strain-hardening polyvinyl alcohol-engineered cementitious composite (PVA-ECC), ACI Materials Journal, 99 (2002) 463-472.

[140] C.K. Leung, V.C. Li, Effect of fiber inclination on crack bridging stress in brittle fiber reinforced brittle matrix composites, Journal of the Mechanics and Physics of Solids, 40 (1992) 1333-1362.

[141] V.C. Li, H. Stang, Interface property characterization and strengthening mechanisms in fiber reinforced cement based composites, Advanced Cement Based Materials, 6 (1997) 1-20.

[142] Z. Lin, V.C. Li, Crack bridging in fiber reinforced cementitious composites with slip-hardening interfaces, Journal of the Mechanics and Physics of Solids, 45 (1997) 763-787.

[143] Z. Lin, T. Kanda, V. Li, On interface property characterization and performance of fiber reinforced cementitious composites, Concrete Science and Engineering, 1 (1999) 173-174.

[144] B. Nematollahi, R. Ranade, J. Sanjayan, S. Ramakrishnan, Thermal and mechanical properties of sustainable lightweight strain hardening geopolymer composites, Arch Civ Mech Eng, 17 (2017) 55-64.

[145] J. Guinée, M. Gorrée, R. Heijungs, G. Huppes, R. Kleijn, A. De Koning, L. Van Oers, A.W. Sleeswijk, S. Suh, H. Udo de Haes, Life cycle assessment–an operational guide to the ISO standards–Part 3: Scientific background, Centre for Environmental Studies (CML), Leiden University, Leiden, the Netherlands, (2001).

[146] B.P. Weidema, M. Thrane, P. Christensen, J. Schmidt, S. Løkke, Carbon footprint: a catalyst for life cycle assessment?, Journal of industrial Ecology, 12 (2008) 3-6.

[147] M.E. Launey, R.O. Ritchie, On the fracture toughness of advanced materials, Advanced Materials, 21 (2009) 2103-2110.

[148] ASTM, C618, Standard specification for fly ash and raw or calcined natural pozzolan for use as a mineral Admixture in Portland Cement Concrete, C618 (2003).

[149] S. Zhang, M. Nedeljković, B. Ghiassi, G. Ye, A Comparative Study on Deflection-Hardening Behavior of Ductile Alkali-Activated Composite, International Conference on Strain-Hardening Cement-Based Composites, Springer, 2017, pp. 123-130.

[150] X. Gao, Q.L. Yu, H.J.H. Brouwers, Reaction kinetics, gel character and strength of ambient temperature cured alkali activated slag–fly ash blends, Construction and Building Materials, 80 (2015) 105-115.

[151] D. Ravikumar, N. Neithalath, Effects of activator characteristics on the reaction product formation in slag binders activated using alkali silicate powder and NaOH, Cement and Concrete Composites, 34 (2012) 809-818.

[152] NEN, 196-1. Methods of testing cement–Part 1: Determination of strength, European Committee for standardization, 2005.

[153] ASTM, C 469 Standard Test Method for Static Modulus of Elasticity and Poisson's Ratio of Concrete in Compression, 2010.

[154] TU1404, Cost Action: Towards the next generation of standards for service life of cement-based materials and structures, main phase of the extended round robin testing programme testing protocols, 2016.

[155] Y. Zhu, S. Xu, Fracture properties of cement paste and mortar: an experimental investigation, Proceedings IA-FraMCoS-6, International Assoc. of Fracture Mech. for Concrete and Concrete Structures, Catania, Italy, 1-3 (2007) 17-22.

[156] A. Hillerborg, Concrete fracture energy tests performed by 9 laboratories according to a draft RILEM recommendation, Report to RILEM TC50-FMC, Report TVBM-3015, Lund, Sweden, (1983).

[157] J. Standard, Method of test for fracture energy of concrete by use of notched beam, JCI-S-001e2003, Japan Concrete Institute, (2003).

[158] J. Lee, M.M. Lopez, An Experimental Study on Fracture Energy of Plain Concrete, International Journal of Concrete Structures and Materials, 8 (2014) 129-139.

[159] F. Aslani, M. Bastami, Relationship between deflection and crack mouth opening displacement of self-compacting concrete beams with and without fibers, Mechanics of Advanced Materials and Structures, 22 (2015) 956-967.

[160] S. Zhao, W. Sun, D. Lange, Deflection–crack mouth opening displacement relationship for concrete beams with and without fibres, Mag Concrete Res, 67 (2015) 532-540.

[161] G. Ye, Experimental study and numerical simulation of the development of the microstructure and permeability of cementitious materials, TU Delft, Delft University of Technology2003.

[162] X. Ouyang, Y. Ma, Z. Liu, J. Liang, G. Ye, Effect of the Sodium Silicate Modulus and Slag Content on Fresh and Hardened Properties of Alkali-Activated Fly Ash/Slag, Minerals, 10 (2020) 15.

[163] D. Ravikumar, N. Neithalath, Reaction kinetics in sodium silicate powder and liquid activated slag binders evaluated using isothermal calorimetry, Thermochimica Acta, 546 (2012) 32-43.

[164] K. Kendall, A. Howard, J.D. Birchall, The relation between porosity, microstructure and strength, and the approach to advanced cement-based materials, Philosophical Transactions of the Royal Society of London. Series A, Mathematical and Physical Sciences, 310 (1983) 139-153.

[165] R.A. Helmuth, D.H. Turk, Elastic moduli of hardened Portland cement and tricalcium silicate pastes: effect of porosity, 1966.

[166] B. Hillemeier, H.K. Hilsdorf, Fracture mechanics studies on concrete compounds, Cement and Concrete Research, 7 (1977) 523-535.

[167] T. Nishikawa, M. Takatsu, M. Daimon, Fracture behavior of hardened cement paste incorporating mineral additions, Cement and Concrete Research, 25 (1995) 1218-1224.

[168] D.A. Lange, H.M. Jennings, S.P. Shah, Relationship between fracture surface roughness and fracture behavior of cement paste and mortar, Journal of the American Ceramic Society, 76 (1993) 589-597.

[169] T. Ficker, D. Martišek, H.M. Jennings, Roughness of fracture surfaces and compressive strength of hydrated cement pastes, Cement and Concrete Research, 40 (2010) 947-955.

[170] S.-D. Wang, K.L. Scrivener, Hydration products of alkali activated slag cement, Cement and Concrete Research, 25 (1995) 561-571.

[171] I. Richardson, A. Brough, G. Groves, C. Dobson, The characterization of hardened alkali-activated blast-furnace slag pastes and the nature of the calcium silicate hydrate (CSH) phase, Cement and Concrete Research, 24 (1994) 813-829.

[172] F. Puertas, S. Martínez-Ramírez, S. Alonso, T. Vazquez, Alkali-activated fly ash/slag cements: strength behaviour and hydration products, Cement and Concrete Research, 30 (2000) 1625-1632.

[173] E. Deir, B.S. Gebregziabiher, S. Peethamparan, Influence of starting material on the early age hydration kinetics, microstructure and composition of binding gel in alkali activated binder systems, Cement and Concrete Composites, 48 (2014) 108-117.

[174] F. Puertas, M. Palacios, H. Manzano, J.S. Dolado, A. Rico, J. Rodríguez, A model for the C-A-S-H gel formed in alkali-activated slag cements, Journal of the European Ceramic Society, 31 (2011) 2043-2056.

[175] M. Nedeljković, B. Šavija, Y. Zuo, M. Luković, G. Ye, Effect of natural carbonation on the pore structure and elastic modulus of the alkali-activated fly ash and slag pastes, Construction and Building Materials, 161 (2018) 687-704.

[176] Y. Zuo, M. Nedeljković, G. Ye, Coupled thermodynamic modelling and experimental study of sodium hydroxide activated slag, Construction and Building Materials, 188 (2018) 262-279.

[177] J.E. Oh, P.J.M. Monteiro, S.S. Jun, S. Choi, S.M. Clark, The evolution of strength and crystalline phases for alkali-activated ground blast furnace slag and fly ash-based geopolymers, Cement and Concrete Research, 40 (2010) 189-196.

[178] Y. Zuo, M. Nedeljković, G. Ye, Pore solution composition of alkali-activated slag/fly ash pastes, Cement and Concrete Research, 115 (2019) 230-250.

[179] H.F. Taylor, Cement chemistry, Thomas Telford London1997.

[180] J. Rossen, K. Scrivener, Optimization of SEM-EDS to determine the C–A–S–H composition in matured cement paste samples, Materials Characterization, 123 (2017) 294-306.

[181] K. Kjellsen, A. Monsøy, K. Isachsen, R. Detwiler, Preparation of flat-polished specimens for SEM-backscattered electron imaging and X-ray microanalysis—importance of epoxy impregnation, Cement and concrete research, 33 (2003) 611-616.

[182] H. Ye, A. Radlińska, Fly ash-slag interaction during alkaline activation: Influence of activators on phase assemblage and microstructure formation, Construction and building materials, 122 (2016) 594-606.

[183] M. Nedeljković, Carbonation mechanism of alkali-activated fly ash and slag materials: In view of long-term performance predictions, Delft University of Technology, 2019.

[184] A.R. Brough, A. Atkinson, Sodium silicate-based, alkali-activated slag mortars: Part I. Strength, hydration and microstructure, Cement and Concrete Research, 32 (2002) 865-879.

[185] S. Song, H.M. Jennings, Pore solution chemistry of alkali-activated ground granulated blast-furnace slag, Cement and Concrete Research, 29 (1999) 159-170.

[186] Y. Zuo, Experimental Study and Numerical Simulation of the Reaction Process and Microstructure Formation of Alkali-Activated Materials, Delft University of Technology, 2019.

[187] D.P. Tuchman, Research toward direct analysis of quartz dust on filters using FTIR spectroscopy, US Department of the Interior, Bureau of Mines1992.

[188] Z. Zhang, H. Wang, J.L. Provis, Quantitative study of the reactivity of fly ash in geopolymerization by FTIR, Journal of Sustainable Cement-Based Materials, 1 (2012) 154-166.

[189] I. García Lodeiro, D.E. Macphee, A. Palomo, A. Fernández-Jiménez, Effect of alkalis on fresh C–S–H gels. FTIR analysis, Cement and Concrete Research, 39 (2009) 147-153.

[190] S. Zhang, Waste Glass as Partial Binder Precursor and Fine Aggregate Replacement in Alkali Activated Slag/Fly ash System, (2015).

[191] F.B. Reig, J.G. Adelantado, M.M. Moreno, FTIR quantitative analysis of calcium carbonate (calcite) and silica (quartz) mixtures using the constant ratio method. Application to geological samples, Talanta, 58 (2002) 811-821.

[192] M. Criado, A. Fernández-Jiménez, A. Palomo, Alkali activation of fly ash: Effect of SiO_2/Na_2O ratio: Part I: FTIR study, Microporous and mesoporous materials, 106 (2007) 180-191.

[193] I. García-Lodeiro, A. Fernández-Jiménez, M.T. Blanco, A. Palomo, FTIR study of the sol–gel synthesis of cementitious gels: C–S–H and N–A–S–H, Journal of Sol-Gel Science and Technology, 45 (2008) 63-72.

[194] I. Garcia-Lodeiro, A. Palomo, A. Fernández-Jiménez, D.E. Macphee, Compatibility studies between N-A-S-H and C-A-S-H gels. Study in the ternary diagram Na2O–CaO–Al2O3–SiO2–H2O, Cement and Concrete Research, 41 (2011) 923-931.

[195] W. Lee, J. Van Deventer, Use of infrared spectroscopy to study geopolymerization of heterogeneous amorphous aluminosilicates, Langmuir, 19 (2003) 8726-8734.

[196] N. Clayden, S. Esposito, A. Aronne, P. Pernice, Solid state 27 Al NMR and FTIR study of lanthanum aluminosilicate glasses, Journal of non-crystalline solids, 258 (1999) 11-19.

[197] Z. Li, S. Zhang, Y. Zuo, W. Chen, G. Ye, Chemical deformation of metakaolin based geopolymer, Cement and Concrete Research, 120 (2019) 108-118.

[198] A. Fernández-Jiménez, A. Palomo, Mid-infrared spectroscopic studies of alkali-activated fly ash structure, Microporous and Mesoporous Materials, 86 (2005) 207-214.

[199] F.P. Glasser, K. Luke, M. Angus, Modification of cement pore fluid compositions by pozzolanic additives, Cement and Concrete Research, 18 (1988) 165-178.

[200] I. Garcia-Lodeiro, A. Fernández-Jiménez, D. Macphee, I. Sobrados, J. Sanz, A. Palomo, Stability of synthetic calcium silicate hydrate gels in presence of alkalis, aluminum, and soluble silica, Transportation Research Record: Journal of the Transportation Research Board, (2010) 52-57.

[201] I. Lecomte, C. Henrist, M. Liegeois, F. Maseri, A. Rulmont, R. Cloots, (Micro)-structural comparison between geopolymers, alkali-activated slag cement and Portland cement, Journal of the European Ceramic Society, 26 (2006) 3789-3797.

[202] X. Yang, P. Roonasi, A. Holmgren, A study of sodium silicate in aqueous solution and sorbed by synthetic magnetite using in situ ATR-FTIR spectroscopy, Journal of Colloid and Interface Science, 328 (2008) 41-47.

[203] J.L. Provis, P. Duxson, G.C. Lukey, F. Separovic, W.M. Kriven, J.S. van Deventer, Modeling speciation in highly concentrated alkaline silicate solutions, Industrial & engineering chemistry research, 44 (2005) 8899-8908.

[204] J.S. Dolado, M. Griebel, J. Hamaekers, A molecular dynamic study of cementitious calcium silicate hydrate (C–S–H) gels, Journal of the American Ceramic Society, 90 (2007) 3938-3942.

[205] F. Pelisser, P.J.P. Gleize, A. Mikowski, Effect of the Ca/Si molar ratio on the micro/nanomechanical properties of synthetic CSH measured by nanoindentation, The Journal of Physical Chemistry C, 116 (2012) 17219-17227.

[206] J.J. Beaudoin, L. Raki, R. Alizadeh, A 29Si MAS NMR study of modified C–S–H nanostructures, Cement and Concrete Composites, 31 (2009) 585-590.

[207] D. Hou, Y. Zhu, Y. Lu, Z. Li, Mechanical properties of calcium silicate hydrate (C–S–H) at nano-scale: a molecular dynamics study, Materials Chemistry and Physics, 146 (2014) 503-511.

[208] A. Katz, A. Thompson, Quantitative prediction of permeability in porous rock, Physical review B, 34 (1986) 8179.

[209] J.F. Young, S. Mindess, D. Darwin, Concrete, Prentice Hall2002.

[210] L. Alarcon-Ruiz, G. Platret, E. Massieu, A. Ehrlacher, The use of thermal analysis in assessing the effect of temperature on a cement paste, Cement and Concrete research, 35 (2005) 609-613.

[211] M.J. DeJong, F.-J. Ulm, The nanogranular behavior of CSH at elevated temperatures (up to 700 C), Cement and Concrete Research, 37 (2007) 1-12.

[212] E. Kapeluszna, Ł. Kotwica, A. Różycka, Ł. Gołek, Incorporation of Al in C-A-S-H gels with various Ca/Si and Al/Si ratio: Microstructural and structural characteristics with DTA/TG, XRD, FTIR and TEM analysis, Construction and Building Materials, 155 (2017) 643-653.

[213] M. Ben Haha, G. Le Saout, F. Winnefeld, B. Lothenbach, Influence of activator type on hydration kinetics, hydrate assemblage and microstructural development of alkali activated blast-furnace slags, Cement and Concrete Research, 41 (2011) 301-310.

[214] M.B. Haha, B. Lothenbach, G. Le Saout, F. Winnefeld, Influence of slag chemistry on the hydration of alkali-activated blast-furnace slag — Part I: Effect of MgO, Cement and Concrete Research, 41 (2011) 955-963.

[215] B. Lothenbach, P. Durdzinski, K. De Weerdt, Thermogravimetric analysis, A practical guide to microstructural analysis of cementitious materials, CRC Press Oxford, UK2016, pp. 177-212.

[216] P. Rovnaník, P. Bayer, P. Rovnaníková, Characterization of alkali activated slag paste after exposure to high temperatures, Construction and Building Materials, 47 (2013) 1479-1487.

[217] J.J. Chen, J.J. Thomas, H.F. Taylor, H.M. Jennings, Solubility and structure of calcium silicate hydrate, Cement and concrete research, 34 (2004) 1499-1519.

[218] R.J. Myers, S.A. Bernal, J.L. Provis, A thermodynamic model for C-(N-) ASH gel: CNASH_ss. Derivation and validation, Cement and Concrete Research, 66 (2014) 27-47.

[219] I.G. Richardson, Model structures for c-(a)-sh (i), Acta Crystallographica Section B: Structural Science, Crystal Engineering and Materials, 70 (2014) 903-923.

[220] E. Ryshkewitch, Compression strength of porous sintered alumina and zirconia: 9th communication to ceramography, Journal of the American Ceramic Society, 36 (1953) 65-68.

[221] Z. Sun, G. Ye, S.P. Shah, Microstructure and early-age properties of Portland cement paste–effects of connectivity of solid phases, ACI Materials Journal, 102 (2005) 122-129.

[222] B. Pichler, C. Hellmich, J. Eberhardsteiner, J. Wasserbauer, P. Termkhajornkit, R. Barbarulo, G. Chanvillard, Effect of gel–space ratio and microstructure on strength of hydrating cementitious materials: An engineering micromechanics approach, Cement and Concrete Research, 45 (2013) 55-68.

[223] A. Keulen, Q.L. Yu, S. Zhang, S. Grünewald, Effect of admixture on the pore structure refinement and enhanced performance of alkali-activated fly ash-slag concrete, Construction and Building Materials, 162 (2018) 27-36.

[224] X. Gao, Q. Yu, H. Brouwers, Assessing the porosity and shrinkage of alkali activated slag-fly ash composites designed applying a packing model, Construction and building materials, 119 (2016) 175-184.

[225] W. Kunther, S. Ferreiro, J. Skibsted, Influence of the Ca/Si ratio on the compressive strength of cementitious calcium–silicate–hydrate binders, Journal of Materials Chemistry A, 5 (2017) 17401-17412.

[226] M. Zajac, J. Skocek, S. Adu-Amankwah, L. Black, M.B. Haha, Impact of microstructure on the performance of composite cements: Why higher total porosity can result in higher strength, Cement and Concrete Composites, 90 (2018) 178-192.

[227] P. Termkhajornkit, Q.H. Vu, R. Barbarulo, S. Daronnat, G. Chanvillard, Dependence of compressive strength on phase assemblage in cement pastes: Beyond gel–space ratio — Experimental evidence and micromechanical modeling, Cement and Concrete Research, 56 (2014) 1-11.

[228] E. L'Hôpital, B. Lothenbach, K. Scrivener, D.A. Kulik, Alkali uptake in calcium alumina silicate hydrate (C-A-S-H), Cement and Concrete Research, 85 (2016) 122-136.

[229] C. Plassard, E. Lesniewska, I. Pochard, A. Nonat, Nanoscale experimental investigation of particle interactions at the origin of the cohesion of cement, Langmuir, 21 (2005) 7263-7270.

[230] H.M. Jennings, Refinements to colloid model of C-S-H in cement: CM-II, Cement and Concrete Research, 38 (2008) 275-289.

[231] R.J.-M. Pellenq, H. Van Damme, Why does concrete set?: The nature of cohesion forces in hardened cement-based materials, Mrs Bulletin, 29 (2004) 319-323.

[232] S. Lesko, E. Lesniewska, A. Nonat, J.-C. Mutin, J.-P. Goudonnet, Investigation by atomic force microscopy of forces at the origin of cement cohesion, Ultramicroscopy, 86 (2001) 11-21.

[233] X. Ouyang, D. Koleva, G. Ye, K. Van Breugel, Understanding the adhesion mechanisms between CSH and fillers, Cement and Concrete Research, 100 (2017) 275-283.

[234] C. Labbez, I. Pochard, B. Jönsson, A. Nonat, C-S-H/solution interface: Experimental and Monte Carlo studies, Cement and Concrete Research, 41 (2011) 161-168.

[235] R.J.M. Pellenq, N. Lequeux, H. van Damme, Engineering the bonding scheme in C–S–H: The iono-covalent framework, Cement and Concrete Research, 38 (2008) 159-174.

[236] C. Gunasekara, D.W. Law, S. Setunge, J.G. Sanjayan, Zeta potential, gel formation and compressive strength of low calcium fly ash geopolymers, Construction and building materials, 95 (2015) 592-599.

[237] H.M. Jennings, Colloid model of C-S-H and implications to the problem of creep and shrinkage, Materials and structures, 37 (2004) 59-70.

[238] A.R. Sakulich, V.C. Li, Nanoscale characterization of engineered cementitious composites (ECC), Cement and Concrete Research, 41 (2011) 169-175.

[239] D. West, Principal component analysis in EDS: the COMPASS algorithm, Thermo Fisher Scientific white paper WP52773, 2015.

[240] P.G. Kotula, M.R. Keenan, Application of multivariate statistical analysis to STEM X-ray spectral images: Interfacial analysis in microelectronics, Microscopy and Microanalysis, 12 (2006) 538-544.

[241] K. Thompson, Large-Area Quantitative Phase Mapping in the Scanning Electron Microscope, Microscopy Today, 25 (2017) 36-45.

[242] I. Curosu, V. Mechtcherine, O. Millon, Effect of fiber properties and matrix composition on the tensile behavior of strain-hardening cement-based composites (SHCCs) subject to impact loading, Cement and Concrete Research, 82 (2016) 23-35.

[243] S.-D. Wang, K.L. Scrivener, P.L. Pratt, Factors affecting the strength of alkali-activated slag, Cement and Concrete Research, 24 (1994) 1033-1043.

[244] C. Shi, P. Xie, Interface between cement paste and quartz sand in alkali-activated slag mortars, Cement and Concrete Research, 28 (1998) 887-896.

[245] R. San Nicolas, J.L. Provis, The interfacial transition zone in alkali-activated slag mortars, Frontiers in Materials, 2 (2015) 70.

[246] T. Horikoshi, A. Ogawa, T. Saito, H. Hoshiro, G. Fischer, V. Li, Properties of Polyvinylalcohol fiber as reinforcing materials for cementitious composites, International RILEM workshop on HPFRCC in structural applications, 2006, pp. 147.

[247] M. Yio, J. Phelan, H. Wong, N. Buenfeld, Determining the slag fraction, water/binder ratio and degree of hydration in hardened cement pastes, Cement and concrete research, 56 (2014) 171-181.

[248] M.B. Haha, B. Lothenbach, G. Le Saout, F. Winnefeld, Influence of slag chemistry on the hydration of alkali-activated blast-furnace slag — Part II: Effect of Al2O3, Cement and Concrete Research, 42 (2012) 74-83.

[249] S.-Y. Hong, F.P. Glasser, Alkali sorption by C-S-H and C-A-S-H gels: Part II. Role of alumina, Cement and Concrete Research, 32 (2002) 1101-1111.

[250] S. Zhang, Z. Li, B. Ghiassi, S. Yin, G. Ye, Effect of alkali activator modulus on fracture properties of alkali-activated slag/fly ash pastes, 15th Congress on the Chemistry of CementsPrague, Czech Republic, 2019.

[251] S. Zhang, Y. Zuo, Z. Li, G. Ye, Isothermal calorimetric study on heat evolution and of apparent activation energy of alkali-activated slag/fly ash pastes, 2th International Conference on Sustainable Building MaterialsEindhoven, the Netherlands, 2019.

[252] D. Hou, J. Yu, P. Wang, Molecular dynamics modeling of the structure, dynamics, energetics and mechanical properties of cement-polymer nanocomposite, Composites Part B: Engineering, 162 (2019) 433-444.

[253] Y. Zhou, L. Tang, J. Liu, C. Miao, Interaction mechanisms between organic and inorganic phases in calcium silicate hydrates/poly(vinyl alcohol) composites, Cement and Concrete Research, 125 (2019) 105891.

[254] Y.-W. Chan, V.C. Li, Effects of transition zone densification on fiber/cement paste bond strength

improvement, Advanced Cement Based Materials, 5 (1997) 8-17.

[255] S. He, Z. Li, E.-H. Yang, Quantitative characterization of anisotropic properties of the interfacial transition zone (ITZ) between microfiber and cement paste, Cement and Concrete Research, 122 (2019) 136-146.

[256] Z. Lu, R. Yin, J. Yao, C.K.Y. Leung, Surface modification of polyethylene fiber by ozonation and its influence on the mechanical properties of Strain-Hardening Cementitious Composites, Composites Part B: Engineering, 177 (2019) 107446.

[257] Z. Lu, J. Yao, C.K.Y. Leung, Using graphene oxide to strengthen the bond between PE fiber and matrix to improve the strain hardening behavior of SHCC, Cement and Concrete Research, 126 (2019) 105899.

[258] A. Drechsler, R. Frenzel, A. Caspari, S. Michel, M. Holzschuh, A. Synytska, I. Curosu, M. Liebscher, V. Mechtcherine, Surface modification of poly(vinyl alcohol) fibers to control the fiber-matrix interaction in composites, Colloid and Polymer Science, 297 (2019) 1079-1093.

[259] S. Zhang, B. Ghiassi, G. Ye, Experimental study on the interface properties of PVA fibers in slag/fly ash based geopolymer pastes, 4th International Conference on Service Life Design for Infrastructures, Rilem2018, pp. 739-745.

[260] W. Zhang, X. Zou, F. Wei, H. Wang, G. Zhang, Y. Huang, Y. Zhang, Grafting SiO2 nanoparticles on polyvinyl alcohol fibers to enhance the interfacial bonding strength with cement, Composites Part B: Engineering, 162 (2019) 500-507.

[261] A. Naaman, G. Namur, H. Najm, J. Alwan, Bond mechanisms in fiber reinforced cement-based composites, MICHIGAN UNIV ANN ARBOR DEPT OF CIVIL ENGINEERING, 1989.

[262] N. Hadjis, M. Piggott, The effect of matrix stresses on fibre pull-out forces, Journal of Materials Science, 12 (1977) 358-364.

[263] H. Ye, A. Radlińska, Shrinkage mechanisms of alkali-activated slag, Cement and Concrete Research, 88 (2016) 126-135.

[264] Z. Li, T. Lu, X. Liang, H. Dong, G. Ye, Mechanisms of autogenous shrinkage of alkali-activated slag and fly ash pastes, Cement and Concrete Research, 135 (2020) 106107.

[265] M. Ranjbarian, V. Mechtcherine, Z. Zhang, I. Curosu, J. Storm, M. Kaliske, Locking Front Model for pull-out behaviour of PVA microfibre embedded in cementitious matrix, Cement and Concrete Composites, (2019).

[266] Y. Zhou, D. Hou, G. Geng, P. Feng, J. Yu, J. Jiang, Insights into the interfacial strengthening mechanisms of calcium-silicate-hydrate/polymer nanocomposites, Physical Chemistry Chemical Physics, 20 (2018) 8247-8266.

[267] R.K. Mishra, R.J. Flatt, H. Heinz, Force field for tricalcium silicate and insight into nanoscale properties: Cleavage, initial hydration, and adsorption of organic molecules, The Journal of Physical Chemistry C, 117 (2013) 10417-10432.

[268] H. Heinz, T.-J. Lin, R. Kishore Mishra, F.S. Emami, Thermodynamically consistent force fields for the assembly of inorganic, organic, and biological nanostructures: the INTERFACE force field, Langmuir, 29 (2013) 1754-1765.

[269] F. Shalchy, N. Rahbar, Nanostructural Characteristics and Interfacial Properties of Polymer Fibers in Cement Matrix, ACS Applied Materials & Interfaces, 7 (2015) 17278-17286.

[270] Y. Zhou, D. Hou, H. Manzano, C.A. Orozco, G. Geng, P.J. Monteiro, J. Liu, Interfacial connection mechanisms in calcium–silicate–hydrates/polymer nanocomposites: a molecular dynamics study, ACS applied materials & interfaces, 9 (2017) 41014-41025.

[271] J. Du, Y. Bu, Z. Shen, Interfacial properties and nanostructural characteristics of epoxy resin in cement matrix, Construction and Building Materials, 164 (2018) 103-112.

[272] D. Lau, O. Büyüköztürk, M.J. Buehler, Characterization of the intrinsic strength between epoxy and silica using a multiscale approach, Journal of Materials Research, 27 (2012) 1787-1796.

[273] M.D. Hanwell, D.E. Curtis, D.C. Lonie, T. Vandermeersch, E. Zurek, G.R. Hutchison, Avogadro: an advanced semantic chemical editor, visualization, and analysis platform, Journal of cheminformatics,

4 (2012) 17.

[274] S. Plimpton, Fast parallel algorithms for short-range molecular dynamics, Journal of computational physics, 117 (1995) 1-19.

[275] B.R. Brooks, R.E. Bruccoleri, B.D. Olafson, D.J. States, S.a. Swaminathan, M. Karplus, CHARMM: a program for macromolecular energy, minimization, and dynamics calculations, Journal of computational chemistry, 4 (1983) 187-217.

[276] C.M. Breneman, K.B. Wiberg, Determining atom‐centered monopoles from molecular electrostatic potentials. The need for high sampling density in formamide conformational analysis, Journal of Computational Chemistry, 11 (1990) 361-373.

[277] E. Bonaccorsi, S. Merlino, A.R. Kampf, The crystal structure of tobermorite 14 Å (plombierite), a C–S–H phase, Journal of the American Ceramic Society, 88 (2005) 505-512.

[278] R.J.-M. Pellenq, A. Kushima, R. Shahsavari, K.J. Van Vliet, M.J. Buehler, S. Yip, F.-J. Ulm, A realistic molecular model of cement hydrates, Proceedings of the National Academy of Sciences, 106 (2009) 16102-16107.

[279] M.A. Qomi, K. Krakowiak, M. Bauchy, K. Stewart, R. Shahsavari, D. Jagannathan, D.B. Brommer, A. Baronnet, M.J. Buehler, S. Yip, Combinatorial molecular optimization of cement hydrates, Nature communications, 5 (2014) 4960.

[280] G. Kovačević, B. Persson, L. Nicoleau, A. Nonat, V. Veryazov, Atomistic modeling of crystal structure of Ca1. 67SiHx, Cement and concrete research, 67 (2015) 197-203.

[281] A. Kumar, B.J. Walder, A. Kunhi Mohamed, A. Hofstetter, B. Srinivasan, A.J. Rossini, K. Scrivener, L. Emsley, P. Bowen, The atomic-level structure of cementitious calcium silicate hydrate, The Journal of Physical Chemistry C, 121 (2017) 17188-17196.

[282] J.M. Martínez, L. Martínez, Packing optimization for automated generation of complex system's initial configurations for molecular dynamics and docking, Journal of computational chemistry, 24 (2003) 819-825.

[283] K. Chenoweth, A.C. Van Duin, W.A. Goddard, ReaxFF reactive force field for molecular dynamics simulations of hydrocarbon oxidation, The Journal of Physical Chemistry A, 112 (2008) 1040-1053.

[284] H. Manzano, S. Moeini, F. Marinelli, A.C. Van Duin, F.-J. Ulm, R.J.-M. Pellenq, Confined water dissociation in microporous defective silicates: mechanism, dipole distribution, and impact on substrate properties, Journal of the American Chemical Society, 134 (2012) 2208-2215.

[285] R. Shahsavari, R.J.-M. Pellenq, F.-J. Ulm, Empirical force fields for complex hydrated calcio-silicate layered materials, Physical Chemistry Chemical Physics, 13 (2011) 1002-1011.

[286] M. Brehm, B. Kirchner, TRAVIS-a free analyzer and visualizer for Monte Carlo and molecular dynamics trajectories, ACS Publications, 2011.

[287] T. Steiner, The hydrogen bond in the solid state, Angewandte Chemie International Edition, 41 (2002) 48-76.

[288] J.D. Gale, GULP: A computer program for the symmetry-adapted simulation of solids, Journal of the Chemical Society, Faraday Transactions, 93 (1997) 629-637.

[289] B. Feuston, S. Garofalini, Empirical three‐body potential for vitreous silica, The Journal of chemical physics, 89 (1988) 5818-5824.

[290] C. Chen, W. Li, Y. Song, L. Weng, N. Zhang, The effect of geometrical criteria on hydrogen bonds analysis in aqueous glycerol solutions, J Mol Imag Dyn, 1 (2011) 101.

[291] C. Tang, X. Li, Z. Li, J. Hao, Interfacial hydrogen bonds and their influence mechanism on increasing the thermal stability of nano-SiO2-modified meta-aramid fibres, Polymers, 9 (2017) 504.

[292] G.A. Jeffrey, G.A. Jeffrey, An introduction to hydrogen bonding, Oxford university press New York1997.

[293] L. Schaeffer, The role of functional groups in drug–receptor interactions, The Practice of Medicinal Chemistry, Elsevier2008, pp. 464-480.

[294] V.C. Li, D.K. Mishra, H.-C. Wu, Matrix design for pseudo-strain-hardening fibre reinforced

cementitious composites, Materials and Structures, 28 (1995) 586-595.

[295] V.C. LI, From Micromechanics to Structural Engineering, Doboku Gakkai Ronbunshu, 1993 (1993) 1-12.

[296] C.C.M. ASTM, Standard test method for splitting tensile strength of cylindrical concrete, 2011.

[297] T. Kanda, V.C. Li, Interface property and apparent strength of high-strength hydrophilic fiber in cement matrix, Journal of materials in civil engineering, 10 (1998) 5-13.

[298] V. C. Li, Postcrack scaling relations for fiber reinforced cementitious composites, Journal of Materials in Civil Engineering, 4 (1992) 41-57.

[299] G.P. van Zijl, V. Slowik, R.D. Toledo Filho, F.H. Wittmann, H. Mihashi, Comparative testing of crack formation in strain-hardening cement-based composites (SHCC), Materials and Structures, 49 (2016) 1175-1189.

[300] E.-H. Yang, M. Sahmaran, Y. Yang, V.C. Li, Rheological Control in Production of Engineered Cementitious Composites, ACI Materials Journal, 106 (2009) 357.

[301] Z. Lin, L. Wood, Concrete uniaxial tensile strength and cylinder splitting test, Journal of Structural Engineering, 129 (2003) 692-698.

[302] C. Rocco, G.V. Guinea, J. Planas, M. Elices, Review of the splitting-test standards from a fracture mechanics point of view, Cement and Concrete Research, 31 (2001) 73-82.

[303] Y. Li, Y. Li, T. Shi, J. Li, Experimental study on mechanical properties and fracture toughness of magnesium phosphate cement, Construction and Building Materials, 96 (2015) 346-352.

[304] P. Kabele, M. Stemberk, Stochastic model of multiple cracking process in fiber reinforced cementitious composites, Engineered Composites, (2005).

[305] S. Wang, V.C. Li, Tailoring of pre-existing flaws in ECC matrix for saturated strain hardening, (2004).

[306] C. Lu, V.C. Li, C.K. Leung, Flaw characterization and correlation with cracking strength in Engineered Cementitious Composites (ECC), Cement and Concrete Research, 107 (2018) 64-74.

[307] V.C. Li, Processing of Engineered Cementitious Composites (ECC), Engineered Cementitious Composites (ECC), Springer2019, pp. 73-99.

[308] J. Zhou, S. Qian, G. Ye, O. Copuroglu, K. van Breugel, V.C. Li, Improved fiber distribution and mechanical properties of engineered cementitious composites by adjusting the mixing sequence, Cement and Concrete Composites, 34 (2012) 342-348.

[309] X. Gao, Q.L. Yu, A. Lazaro, H.J.H. Brouwers, Investigation on a green olivine nano-silica source based activator in alkali activated slag-fly ash blends: Reaction kinetics, gel structure and carbon footprint, Cement and Concrete Research, 100 (2017) 129-139.

[310] M. Izquierdo, X. Querol, C. Phillipart, D. Antenucci, M. Towler, The role of open and closed curing conditions on the leaching properties of fly ash-slag-based geopolymers, Journal of Hazardous Materials, 176 (2010) 623-628.

[311] M. Nedeljković, B. Ghiassi, S. van der Laan, Z. Li, G. Ye, Effect of curing conditions on the pore solution and carbonation resistance of alkali-activated fly ash and slag pastes, Cement and Concrete Research, 116 (2019) 146-158.

[312] D.L. Kong, J.G. Sanjayan, Effect of elevated temperatures on geopolymer paste, mortar and concrete, Cement and concrete research, 40 (2010) 334-339.

[313] The International Standards Organisation, ISO 14040:2006 Environmental management - Life cycle assessment - Principles and framework, 2006.

[314] C. EN, Sustainability of Construction Works-Environmental Product Declarations-Core Rules for the Product Category of Construction Products, EN, (2012) 15804.

[315] S. Bouwkwaliteit, Bepalingsmethode Milieuprestatie Gebouwen en GWW-werken, Berekeningswijze voor het bepalen van de milieuprestatie van gebouwen en GWW-werken gedurende hun gehele levensduur, gebaseerd op de EN, 15804 (2014).

[316] H.-L. Wu, D. Zhang, B.R. Ellis, V.C. Li, Development of reactive MgO-based Engineered Cementitious Composite (ECC) through accelerated carbonation curing, Construction and Building Materials, 191 (2018) 23-31.

[317] D.A. Salas, A.D. Ramirez, N. Ulloa, H. Baykara, A.J. Boero, Life cycle assessment of geopolymer concrete, Construction and Building Materials, 190 (2018) 170-177.

[318] H. Hafez, R. Kurda, W.M. Cheung, B. Nagaratnam, A Systematic Review of the Discrepancies in Life Cycle Assessments of Green Concrete, Applied Sciences, 9 (2019) 4803.

[319] J.L. Provis, Alkali-activated materials, Cement and Concrete Research, 114 (2018) 40-48.

[320] J.L. Provis, A. Kilcullen, P. Duxson, D.G. Brice, J.S. van Deventer, Stabilization of low-modulus sodium silicate solutions by alkali substitution, Industrial & engineering chemistry research, 51 (2012) 2483-2486.

[321] ORCEM B.V., Environmentally relevant Product information eco2cem hoogovenslak, 2014.

[322] Vliegasunie B.V., Environmentally Relevant Product Information vliegasunie coal fly ash., 2018.

[323] Intertek GmbH, Environmental product declaration: in accordance with ISO 14025:2016 and PCR 2010:16 version 3.01 for: 1 kg of average hydropol polymer pellets, 2020.

[324] R. Frazão, R. Fernandes, D.C. Peneda, Comparative Analysis of the Life Cycle of AT Fibre-cement and NT Fibre-cement, International Chrysotile Association, 2004.

[325] Nibe B.V., Evironmental Product Declaration (EPD) Database for the Netherlands Market, 2019.

[326] G. Wernet, C. Bauer, B. Steubing, J. Reinhard, E. Moreno-Ruiz, B. Weidema, The ecoinvent database version 3 (part I): overview and methodology, The International Journal of Life Cycle Assessment, 21 (2016) 1218-1230.

[327] M. Fawer, M. Concannon, W. Rieber, Life cycle inventories for the production of sodium silicates, The International Journal of Life Cycle Assessment, 4 (1999) 207.

[328] M.Z. Hauschild, M. Goedkoop, J. Guinée, R. Heijungs, M. Huijbregts, O. Jolliet, M. Margni, A. De Schryver, S. Humbert, A. Laurent, Identifying best existing practice for characterization modeling in life cycle impact assessment, The International Journal of Life Cycle Assessment, 18 (2013) 683-697.

[329] J.B. Guinée, E. Lindeijer, Handbook on life cycle assessment: operational guide to the ISO standards, Springer Science & Business Media2002.

[330] G.P. Hammond, C.I. Jones, Embodied energy and carbon in construction materials, Proceedings of the Institution of Civil Engineers-Energy, 161 (2008) 87-98.

[331] J. Bare, T. Gloria, G. Norris, Development of the method and US normalization database for life cycle impact assessment and sustainability metrics, Environmental science & technology, 40 (2006) 5108-5115.

[332] J. Kim, Y. Yang, J. Bae, S. Suh, The importance of normalization references in interpreting life cycle assessment results, Journal of Industrial Ecology, 17 (2013) 385-395.

[333] A.W. Sleeswijk, L.F. van Oers, J.B. Guinée, J. Struijs, M.A. Huijbregts, Normalisation in product life cycle assessment: An LCA of the global and European economic systems in the year 2000, Science of the total environment, 390 (2008) 227-240.

[334] H.K. Stranddorf, L. Hoffmann, A. Schmidt, LCA guideline. Update on impact categories, normalisation and weighting in LCA—selected EDIP97 data, (2005).

[335] L. van Oers, CML-IA database, characterization and normalization factors for midpoint impact category indicators. Version 4.8, August 2016, 2016.

[336] V. Aymard, V. Botta-Genoulaz, Normalisation in life-cycle assessment: consequences of new European factors on decision-making, Supply Chain Forum: An International Journal, Taylor & Francis, 2017, pp. 76-83.

[337] E. commission, About the energy label and ecodesign, 2019.

[338] X. Wu, Z. Zhang, Y. Chen, Study of the environmental impacts based on the “green tax”—applied to several types of building materials, Building and Environment, 40 (2005) 227-237.

[339] P. Van der Lugt, A. Van den Dobbelsteen, J. Janssen, An environmental, economic and practical assessment of bamboo as a building material for supporting structures, Construction and building materials, 20 (2006) 648-656.

[340] G. Verbeeck, H. Hens, Life cycle inventory of buildings: A contribution analysis, Building and Environment, 45 (2010) 964-967.

[341] A. Passuello, E.D. Rodríguez, E. Hirt, M. Longhi, S.A. Bernal, J.L. Provis, A.P. Kirchheim, Evaluation of the potential improvement in the environmental footprint of geopolymers using waste-derived activators, Journal of cleaner production, 166 (2017) 680-689.

[342] G. Habert, J.B. d'Espinose de Lacaillerie, N. Roussel, An environmental evaluation of geopolymer based concrete production: reviewing current research trends, Journal of Cleaner Production, 19 (2011) 1229-1238.

[343] M. Scholand, H.E. Dillon, Life-cycle assessment of energy and environmental impacts of LED lighting products part 2: LED manufacturing and performance, Pacific Northwest National Lab.(PNNL), Richland, WA (United States), 2012.

[344] P.J. Monteiro, S.A. Miller, A. Horvath, Towards sustainable concrete, Nature materials, 16 (2017) 698-699.

[345] C. Chen, G. Habert, Y. Bouzidi, A. Jullien, Environmental impact of cement production: detail of the different processes and cement plant variability evaluation, Journal of Cleaner Production, 18 (2010) 478-485.

[346] J.S. Damtoft, J. Lukasik, D. Herfort, D. Sorrentino, E.M. Gartner, Sustainable development and climate change initiatives, Cement and concrete research, 38 (2008) 115-127.

[347] M. Weil, K. Dombrowski, A. Buchwald, Life-cycle analysis of geopolymers, Geopolymers, Elsevier2009, pp. 194-210.

[348] B.C. McLellan, R.P. Williams, J. Lay, A. van Riessen, G.D. Corder, Costs and carbon emissions for geopolymer pastes in comparison to ordinary portland cement, Journal of Cleaner Production, 19 (2011) 1080-1090.

[349] P. Van den Heede, A. Mignon, G. Habert, N. De Belie, Cradle-to-gate life cycle assessment of self-healing engineered cementitious composite with in-house developed (semi-)synthetic superabsorbent polymers, Cement and Concrete Composites, 94 (2018) 166-180.

[350] M. Guo, R. Murphy, Is There a Generic Environmental Advantage for Starch–PVOH Biopolymers Over Petrochemical Polymers?, Journal of Polymers and the Environment, 20 (2012) 976-990.

[351] B. Tempest, O. Sanusi, J. Gergely, V. Ogunro, D. Weggel, Compressive strength and embodied energy optimization of fly ash based geopolymer concrete, world of coal ash (WOCA) conference, 2009.

[352] M. Abdulkareem, J. Havukainen, M. Horttanainen, How environmentally sustainable are fibre reinforced alkali-activated concretes?, Journal of Cleaner Production, 236 (2019) 117601.

[353] A. Heath, K. Paine, M. McManus, Minimising the global warming potential of clay based geopolymers, Journal of Cleaner Production, 78 (2014) 75-83.

[354] E. Irena, Renewable energy prospects for the European Union, International Renewable Energy Agency (IRENA), European Commission (EC), Abu Dhabi, (2018).

[355] C. Ouellet-Plamondon, G. Habert, Life cycle assessment (LCA) of alkali-activated cements and concretes, Handbook of alkali-activated cements, mortars and concretes, Elsevier2015, pp. 663-686.

[356] E. Scherpbier, H. Eerens, Decarbonisation options for the dutch chlor-alkali industry, Den Haag: PBL, 2021.

[357] M. Torres-Carrasco, J. Palomo, F. Puertas, Sodium silicate solutions from dissolution of glasswastes. Statistical analysis, Materiales de Construcción, 64 (2014) e014.

[358] E. Kamseu, L.B. à Moungam, M. Cannio, N. Billong, D. Chaysuwan, U.C. Melo, C. Leonelli, Substitution of sodium silicate with rice husk ash-NaOH solution in metakaolin based geopolymer cement concerning reduction in global warming, Journal of cleaner production, 142 (2017) 3050-3060.

[359] F. Puertas, M. Torres-Carrasco, Use of glass waste as an activator in the preparation of alkali-activated slag. Mechanical strength and paste characterisation, Cement and Concrete Research, 57 (2014) 95-104.

[360] D. Vaičiukyniene, V. Vaitkevičius, A. Kantautas, V. Sasnauskas, Utilization of by-product waste silica in concrete-based materials, Materials Research, 15 (2012) 561-567.

[361] E. Jamieson, B. McLellan, A. van Riessen, H. Nikraz, Comparison of embodied energies of Ordinary Portland Cement with Bayer-derived geopolymer products, Journal of Cleaner Production, 99 (2015) 112-118.

[362] M. Guo, Life cycle assessment (LCA) of light-weight eco-composites, Springer Science & Business Media2013.

[363] X. Lin, J. Yu, H. Li, J.Y.K. Lam, K. Shih, I.M.L. Sham, C.K.Y. Leung, Recycling polyethylene terephthalate wastes as short fibers in Strain-Hardening Cementitious Composites (SHCC), Journal of Hazardous Materials, 357 (2018) 40-52.

[364] D. Gastaldi, F. Canonico, L. Capelli, L. Buzzi, E. Boccaleri, S. Irico, An investigation on the recycling of hydrated cement from concrete demolition waste, Cement and Concrete Composites, 61 (2015) 29-35.

[365] M. Behera, S. Bhattacharyya, A. Minocha, R. Deoliya, S. Maiti, Recycled aggregate from C&D waste & its use in concrete–A breakthrough towards sustainability in construction sector: A review, Construction and building materials, 68 (2014) 501-516.

[366] Z. Lin, T. Kanda, V.C. Li, On interface property characterization and performance of fiber reinforced cementitious composites, (1999).

[367] T. Chu, R. Robertson, H. Najm, A. Naaman, Effects of poly (vinyl alcohol) on fiber cement interfaces. Part II: Microstructures, Advanced Cement Based Materials, 1 (1994) 122-130.

[368] P. Xu, Q. Zhao, W. Qiu, Y. Xue, N. Li, Microstructure and Strength of Alkali-Activated Bricks Containing Municipal Solid Waste Incineration (MSWI) Fly Ash Developed as Construction Materials, Sustainability, 11 (2019) 1283.

[369] R.J. Myers, B. Lothenbach, S.A. Bernal, J.L. Provis, Thermodynamic modelling of alkali-activated slag cements, Applied Geochemistry, 61 (2015) 233-247.

[370] X. Pardal, I. Pochard, A. Nonat, Experimental study of Si–Al substitution in calcium-silicate-hydrate (CSH) prepared under equilibrium conditions, Cement and Concrete Research, 39 (2009) 637-643.

[371] H. Ye, Nanoscale attraction between calcium-aluminosilicate-hydrate and Mg-Al layered double hydroxides in alkali-activated slag, Materials Characterization, 140 (2018) 95-102.

[372] Z. Jia, C. Chen, H. Zhou, Y. Zhang, The characteristics and formation mechanism of the dark rim in alkali-activated slag, Cement and Concrete Composites, 112 (2020) 103682.

[373] Q. Wang, D. O'Hare, Recent advances in the synthesis and application of layered double hydroxide (LDH) nanosheets, Chemical reviews, 112 (2012) 4124-4155.

[374] C. van Hoek, J. Small, S. van der Laan, Large-Area Phase Mapping Using PhAse Recognition and Characterization (PARC) Software, Microscopy Today, 24 (2016) 12-21.

[375] K. Scrivener, R. Snellings, B. Lothenbach, A practical guide to microstructural analysis of cementitious materials, CRC Press2018.

Summary

Alkali-activated Materials (AAMs), including those classified as geopolymer, are obtained through the reaction between a solid precursor and an alkaline solution. Compared with ordinary Portland cement (OPC) binders, these materials maintain comparable mechanical properties but have the advantage of reducing greenhouse gas emissions and utilization of industrial by-products and residuals which helps to meet sustainability goals. AAMs are thus considered an environment-friendly construction material with great potential for next-generation concrete.

AAMs are inherently brittle. The low ductility of AAMs makes them prone to cracking and corresponding performance degradation, which is detrimental to their durability. Based on the concept of strain-hardening cementitious composite (SHCC), one solution relates to a family of fiber-reinforced composites that have high tensile ductility and multiple-cracking characteristics, i.e., strain-hardening geopolymer composite (SHGC). While much effort has been taken to develop conventional SHCC, scientific and technical knowledge of SHGC is still in the very early stage of development. This PhD project deals with the development of a cement-free strain-hardening geopolymer composite (SHGC) as a high-performance construction material using industrial wastes and by-products through alkaline activation technology:

The fracture properties and other mechanical properties of the alkali-activated slag/fly ash (AASF) paste as the matrix for SHGC were experimentally tested. The microstructure and chemistry of the reaction products were investigated to understand the fracture mechanism. It was found that the fracture properties of pastes are strongly related to the chemical composition (Ca/Si ratio) of the main reaction product, i.e., C-(N-)A-S-H gel. The fracture properties were also found to be dominated by a cohesion/adhesion-based mechanism. Furthermore, the compressive strength of AASF paste is primarily determined by its capillary porosity.

The fiber/matrix properties, including chemical bonding energy, initial frictional bond, and slip-hardening behavior of fiber during the pullout process were also experimentally studied. The chemistry and microstructure of the reaction product in the fiber/matrix interfacial transition zone (ITZ) were characterized. Their influence on the interface bonding properties was also investigated. It is found that the chemical bonding between PVA fiber and AASF matrix increases with increasing Ca/Si and Ca/(Si+Al) ratio of C-(N-)A-S-H gel. Hence, changing the slag content and the alkali activator M_s appears to be an effective way to modify chemical bonding. Unlike the formation of portlandite near the PVA fiber surface in conventional SHCC, a high-Ca C-(N-)A-S-H phase was formed in the fiber-matrix ITZ of SHGC. This explains the higher chemical bonding energy found in SHGC compared to that in conventional SHCCs. Furthermore, the adhesion mechanism of the PVA molecule in reaction products was studied using MD simulation. The study suggests that the adhesion between PVA fiber and C-(N-)A-S-H gel is primarily due to electrostatic interactions rather than van der Waals interactions.

Based on the result of fracture properties of the matrix and fiber/matrix interface properties, the SHGC is then systematically developed following a micromechanics-based design approach. The experimentally-attained matrix and interface properties served as input for the numerical micromechanics model to simulate the crack bridging behavior. Through the micromechanical modeling, the optimal fiber length and volume were selected and the behavior of mixtures with different fiber/matrix combinations was predicted. With this approach, researchers and materials engineers can design and tailor future SHGC more efficiently than by using the commonly used trial-and-error method.

Finally, the environmental impact of the SHGC with the most promising performance was also evaluated. This evaluation was conducted using a cradle-to-gate life-cycle assessment (LCA) of SHGC compared to that of conventional SHCC materials. The developed SHGC demonstrates a very promising environmental profile. It has a significant reduction of the global warming potential (GWP) and a lower or similar total environmental impact compared to conventional SHCC materials. In addition, the results also provide recommendations for further improvements in mixture design for the future development of SHGC.

This study successfully developed a sustainable slag/fly ash-based SHGC with a lower carbon footprint than conventional SHCC. It is considered a good example to utilize industrial by-products as secondary resources and at the same time contribute to a circular economy. Furthermore, this study helps to understand the fracture properties of AAMs. It also clarifies the adhesion mechanism of PVA fiber in AAMs. All of these give promising guidance for researchers and engineers to design fiber-reinforced AAMs with required fracture properties and interface bonding properties. In particular, it contributes to the design and tailoring strategies for high-performance composite, for instance, SHGC, through proper mixture design.

Samenvatting

Alkali-geactiveerde materialen (AAMs), waaronder degene die als geopolymeer worden geclassificeerd, worden verkregen door de reactie tussen een vaste precursor en een alkalische oplossing. In vergelijking met bindmiddelen op basis van portlandcement (PC) behalen deze materialen vergelijkbare mechanische eigenschappen, maar hebben ze het voordeel dat ze de uitstoot van broeikasgassen verminderen en dat ze industriële bijproducten en reststoffen gebruiken, wat bijdraagt tot het bereiken van duurzaamheidsdoelstellingen. AAMs worden daarom beschouwd als een milieuvriendelijk bouwmateriaal met een groot potentieel voor de volgende generatie beton.

AAMs zijn van nature bros. De lage vervormbaarheid van AAMs maakt ze vatbaar voor scheuren en de daarmee gepaard gaande prestatievermindering, wat nadelig is voor hun levensduur. Gebaseerd op het concept van rek-verhardende cementgebonden composiet (SHCC), is er een oplossing die betrekking heeft op een familie van vezel versterkte composieten welke beschikken over een hoge trek taaiheid en meervoudige scheurvorming, en wel de rek-verhardende geopolymeer composiet (SHGC). Hoewel er bij de ontwikkeling van de conventionele SHCC al veel werk is verricht, bevindt de wetenschappelijke en technische kennis van SHGC zich nog in een zeer vroeg ontwikkelingsstadium. Dit doctoraatsproject behandelt de ontwikkeling van een cementvrij rek-verhardend geopolymeer composiet (SHGC) als hoogwaardig bouwmateriaal door gebruik te maken van industriële rest- en bijproducten door middel van alkalische activeringstechnologie:

De breukeigenschappen en andere mechanische eigenschappen van de alkali-geactiveerde slak/vliegas (AASF) pasta als matrix voor SHGC werden experimenteel getest. De microstructuur en de chemie van de reactieproducten werden onderzocht om het breukmechanisme te begrijpen. Hieruit is gebleken dat de breukeigenschappen van de pasta's sterk gerelateerd zijn aan de chemische samenstelling (Ca/Si verhouding) van het belangrijkste reactieproduct, zijnde C-(N-)A-S-H gel. De breukeigenschappen van AASF-pasta's bleken te worden gedomineerd door een cohesie/adhesie-gebaseerd mechanisme. Tenslotte werd aangetoont dat de druksterkte van AASF-pasta's voornamelijk wordt bepaald door de capillaire porositeit.

De vezel/matrix eigenschappen, inclusief chemische bindingsenergie, initiële wrijvingsbinding, en slip-verharding gedrag van de vezel tijdens het pull-out proces, werden ook experimenteel bestudeerd. Hierbij werd de chemie en de microstructuur van het reactieproduct in het vezel/matrix grensvlakzone (ITZ) gekarakteriseerd. Tevens is de invloed hiervan op de hechtingseigenschappen van de ITZ ook onderzocht. Gebleken is dat de chemische verbinding tussen PVA-vezel en AASF-matrix toeneemt met toenemende Ca/Si en Ca/(Si+Al) verhouding van de C-(N-)A-S-H gel. Het veranderen van het slakgehalte en de alkali-activator Ms lijkt dan ook een effectieve manier om de chemische binding te modificeren. In tegenstelling tot conventionele SHCC, waar voornamelijk portlandiet wordt gevormd nabij het PVA-vezeloppervlak, werd in de vezel/matrix ITZ van SHGC een hoog calcium houdende C-(N-)A-S-H fase gevormd. Dit verklaart de hogere chemische bindingsenergie in SHGC vergeleken met die in conventionele SHCCs. Bovendien werd het adhesiemechanisme van de PVA-

molecule in reactieproducten bestudeerd met behulp moleculaire dynamica. De studie toont aan dat de adhesie tussen PVA-vezel en C-(N-)A-S-H gel vooral het gevolg is van elektrostatische interacties en niet zozeer van der Waals interacties.

De SHGC is vervolgens, op basis van het resultaat van de breukeigenschappen van de matrix en de eigenschappen van de vezel/matrix ITZ en doormiddel van een op micromechanica gebaseerde ontwerpmethode, systematisch doorontwikkeld. De experimenteel verkregen matrix- en ITZ-eigenschappen werden gebruikt voor het numerieke micro-mechanische model om het scheur overbruggingsgedrag te simuleren. Met het micro-mechanische model werden de optimale vezellengte en vezelvolume geselecteerd en werd het gedrag van mengsels met verschillende vezel/matrix-combinaties voorspeld. Met deze aanpak kunnen onderzoekers en materiaalingenieurs toekomstig SHGC efficiënter ontwerpen en optimaliseren dan met de gangbare trial-and-error-methode.

Ten slotte werd ook het milieueffect van de SHGC met de meest veelbelovende prestaties geëvalueerd. Deze evaluatie werd uitgevoerd aan de hand van een "cradle-to-gate"-levenscyclusanalyse (LCA), waarbij SHGC is vergeleken met conventionele SHCC-materialen. De ontwikkelde SHGC vertoont een veelbelovend milieuprofiel. Het “global warming potential” (GWP) wordt aanzienlijk verminderd en de totale milieu-impact is lager of vergelijkbaar met die van conventionele SHCC-materialen. Bovendien geven de resultaten ook aanbevelingen voor verdere verbeteringen in het mengselontwerp voor de toekomstige ontwikkeling van SHGC.

Deze studie heeft met succes een duurzame op slakken/vliegas gebaseerde SHGC ontwikkeld met een lagere koolstofvoetafdruk dan conventionele SHCC. Het wordt beschouwd als een goed voorbeeld om industriële bijproducten te gebruiken als secundaire grondstoffen en tegelijkertijd bij te dragen aan een circulaire economie. Bovendien helpt deze studie om de breukeigenschappen van AAM te begrijpen. Het verduidelijkt ook het adhesiemechanisme van PVA-vezels in AAMs. Dit alles geeft veelbelovende richtlijnen voor onderzoekers en ingenieurs om vezel versterkte AAMs te ontwerpen met de vereiste breukeigenschappen en ITZ hechtingseigenschappen. In het bijzonder, draagt het bij aan de ontwerp en optimalisatie strategieën voor een hoogwaardig composiet, zoals SHGC, door middel van een goed mengselontwerp.

Acknowledgments

This PhD research was carried out in Microlab, Delft University of Technology and financially supported by the Netherlands Organization for Scientific Research (NWO), Grant No.729.001.013, and the National Natural Science Foundation of China (NSFC), Grant No. 5151101050. It has been such a fascinating and rewarding adventure for me and I cannot imagine I could have gotten this far without the support of many people.

I would like to first express my most sincere acknowledgment to my promotor Prof. Klaas van Breugel for his continuous guidance, inspiration, and support during my study. It is hard to describe how tremendously you have influenced me on the way for me to become a responsible researcher with the capability for critical thinking. With an “eagle eye”, you always have keen observation together with powerful logic, which benefits me a great deal in my scientific writing. I also enjoyed very much all our scientific discussions and casual conversations.

My deepest gratitude also goes to my copromotor and daily advisor Dr. Guang Ye for his guidance, caring, patience, and encouragement all these years. For me, what you have done in the past years is much more than just mentoring a PhD student on a specific project. I am truly grateful to you for putting your trust in me, giving me the freedom to explore in research activities, and helping me improve to become a better scientific researcher. Because of your support, I was able to connect with so many brilliant researchers worldwide and step on an upward trajectory for my career. I feel extremely lucky to have a mentor like you.

Furthermore, I want to give my sincere acknowledgment to Prof. Victor C. Li at University of Michigan, Ann Arbor, for hosting me for my research visit. You have been so supportive and your valuable suggestions on micromechanics turn out to be an important basis for my PhD research. My big appreciation also goes to Dr. Jorge Dolado and Dr. Eduardo Duque-Redondo for their tremendous help and nice collaboration in molecular dynamics simulation. What a pleasant research visit to San Sebastián in a beautiful summer. I also owe my gratitude to Prof. Erik Schlangen, who has given me generous and long-term support. Thank you for all the valuable insights and discussions on fracture mechanics-related questions and experiments. Moreover, I would also like to extend my gratitude to Prof. Wei Chen from Wuhan University of Technology. You have been supportive ever since I was an undergraduate student. Your inspirations and encouragements mean a lot to me.

Meanwhile, I would also like to express my thanks to other committee members, Prof. Pavel Krivenko, Prof. Viktor Mechtcherine, and Prof. Max Hendriks for their availability and the efforts spent on my thesis. It is also my great honor that you can serve on my defense committee and be involved in one of my most important milestones.

I would like to thank all my other collaborators during my PhD. Great appreciation goes to Dr. Zhenming Li, Dr. Marija Nedeljković, Dr. Yibing Zuo, Dr. Bahman Ghiassi, and Dr. Kamel Arbi for their great assistance and inspiring discussions. Special thanks go to Dr. Hua Dong for all the experiments, casting, and discussions we had together. Your down-to-earth attitude and optimistic mindset to embrace everything in life truly touched me. Many thanks to Shan He, Yu

Zhang, Albina Kostiuchenko, Luiz Miranda de Lima, Chen Liu, Xuhui Liang, Boyu Chen for all the interesting discussions and idea exchange. There has been so much fun in all our collaborations and without saying it would be impossible to validate all the nice research ideas without you! I would also like to thank Dr. Oguzhan Copuroglu for all the helpful advice on the microscopy and EDX analysis, Prof. Henk Jonkers for helping with the life-cycle assessment, Dr. Fred Veer for helping with the surface roughness test, Dr. Branko Šavija for introducing me the DIC technique and much other advice, Dr. Lupita Sierra-Beltran for generously sharing all her knowledge about fiber pullout, Dr. Hongzhi Zhang for helping with lattice modeling and nanoindentation, and Prof. Jian Zhou for all his help and guidance on SHCC at the beginning of my PhD. In the last phase of finishing my PhD, I feel very lucky to work together with Hao Cheng, Dr. Yuguang Yang, Zhenxu Qian, and Dr. Mladena Luković on geopolymer concrete for infrastructural applications. Thanks also goes to Dr. Sonja Fennis for all the interesting discussions in the meetings. Without your great efforts and dedication, it is impossible for us to finally deliver this very challenging project.

My gratitude also extends to researchers from external institutions. Many thanks go to Dr. Duo Zhang, Dr. Haoliang Wu, and Dr. He Zhu for teaching me experimental techniques such as uniaxial tensile tests but also for their care and help during my stay in Ann Arbor, Dr. Motohiro Ohno and Dr. Ravi Ranade for their help in micromechanical modeling, Dr. Bo Li for the very interesting discussion on the formation of hydrotalcite and molecular dynamics simulation, Prof. Qingliang Yu for his valuable feedbacks and also the input on particle packing models, Prof. Suhong Yin, Prof. Jie Hu, and Prof. Xuemin Cui for taking good care of me during the project workshops in China, Yubo Sun and Dr. Xiujiao Qiu for your kind assistance during our stay in Ghent. I would also like to thank all the TC committee members in RILEM-TC TRM and MPA, it is such a nice experience to collaborate with field-renowned experts on a similar topic.

Or course, I also appreciate the support of the kind technicians on my experimental work: Arjan for helping with XRD analysis and teaching me the operation of ESEM and EDX, John for helping on TGA, ICP, and calorimetry, Paul for single fiber pullout tests, Ron for XRF tests, Ton for concrete casting, and Jakub and Albert for structural test arrangements. Many thanks also go to Fred and Kees for the assistance in the creep and rebar pullout test. My special thanks go to Maiko for what seems to be never-ending instron tests we have done together (here we go again!). You also happened to be an amazing friend and your optimism and encouragement mean a great deal to me! I also appreciate the kind assistance from other employees at the university, especially the previous and current secretaries in 3MD, Nynke, Claire, Jacqueline, and Jaap.

I would like to extend my warm acknowledgments to my colleagues in Microlab. It has been such a pleasant experience for me working together with so many nice and talented people: Ameya, Balqis, Bart, Bei, Emanuele, Fernando, Guilherme, Hao, Hu Shi, Irving, Jiayi, Minfei, Renee, Xuliang, Yading, Yask, Yidong, Yu Zeng, Yun, Ze, Zhi Wan, and Zhiyuan. I am grateful for all the enjoyable lunches, drinks, parties, and conferences that we had together. Many thanks, Claudia, Marija, Patrick, and Stefan for all the nice talks and your kind suggestions on my career. Special thanks go to Yu Chen for helping to design the thesis cover and Anne-Linde for helping with the Dutch translation of the summary. I would also like to acknowledge the former colleagues of Microlab: Dr. Fuhai Li, Dr. Haoliang Huang, Jiahua Liu, Dr. Leyang Lyu, Dr. Lourdes Souza, Dr. Xiaowei Ouyang, Dr. Peng Gao, Dr. Shi Xu, Dr. Tianshi Lu, Dr. Xu Ma, Dr. Yong Zhang, Dr. Yun Huang, Dr. Yuwei Ma, Dr. Zhipei Chen, Dr. Zhuqing Yu, Prof.

Jiangxiong Wei, Prof. Yingzi Yang, and many more for the care and support they have given me ever since I was a master student in Microlab. Thank you, I really had a wonderful time with you all.

My appreciation also goes to many colleagues in the industry: Hendrik Herder and Arend Scharringa for their continuous support and collaboration on the pilot project, Anya Niehaus, Dr. Arno Keulen, Dr. Ding Luo, Dr. Jeanette Visser, Jos Kronemeijer, Juan Felipe Garzon, Dr. Liesbeth Horckmans, Marc Brito van Zijl, Dr. Natalie Carr, Dr. Qadeer Alam, Dr. Ruben Snellings, Rob Bleijerveld, Ron Leppers, Dr. Siska Valcke, Dr. Wenjuan Lyu, and Dr. Yury Villagran-Zaccardi for the kind help and advice on my career, Dr. Xuerun Li for helping with the admixtures supply, Tomohiro Terasawa and Dr. Naho Takeda for helping with the supply of PVA fibers. I would also like to thank many people for their valuable input during my proposal writing and idea valorization for the potential start-up: Dr. Bin Hu, Boudewijn Piscaer, Dr. Evgeny Uslamin, Ivor Rhodes, Jaap Meijer, Jian Yuan, Justin Kok, Keji Pan, Mark de Kruijff, Martin Megalla, Merlijn Bazuine, Dr. Paul Dennisen, Dr. Pingping Wen, Dr. Robbert van Putten, and Dr. Zhiwei Qian. So much have I learned and I am very grateful for all your support.

I thank all my dear friends here in the Netherlands and China, for sharing all the sorrow and happiness with me throughout the entire time. Thank you, Claudia and Fernando, Chengbo and Alex, Chenjie and Quanxin, Chen Xu, Donggang Wang, Fei Xie, Guandong and Yiji, Grace Zhang, Haoyu and Xiaoman, Ivor and Cynthia, Jiani and Bo, Jiawei and Lin, Kai and Naiyi, Luiz and Barbara, Marija and Patrick, Qian and Anton, Qiao Han, Stefan and Bianca, Xiaoyu Qin, Xuan Li, Vincent Gong, Yan Xie, Yuning Chen, Yunzhou and Weixiao, Yue and Jingjing, and many more for all the fun and good memories together. Agita and Boudewijn have always been supportive and your warmth made me feel less homesick abroad. Thank You, Ms. Lei Zhang, for your hospitality and being a wonderful host for all the new year parties. Special gratitude goes to Yongchang and Sarah, and Yuyao Zhang for being amazing friends ever since my master's study. Thanks also go to my skiing buddies Hua, Hu, and Zhiyuan for all the fun we had in snowworld, and Keji, Shan, and Ze for the good tennis games together. The time we spent sporting together is one of my happiest memories during my PhD.

Last but absolutely not least, I owe the most to my family, especially to my mother and father, who always believe in me. This PhD thesis would not even be possible for me without your endless love, encouragement, and sacrifice. My gratitude also extends to my parents-in-law for their support and kindness. I wish all the four of you good health and lots of fun in your retirement. My deepest acknowledgment also goes to my beloved Kelly, for her everlasting love, patience, encouragement, and understanding. Together we have come far but I still cannot imagine how big the courage you had and the sacrifice you made to give up an already-built career and start over in a new country. I love you so much and I am so blessed to have you by my side in this vast adventure called life.

Shizhe Zhang

Delft, Nov 2022

Curriculum vitae

Personal information

Shizhe Zhang 张世哲

Born on Feb 1991

Dongying, Shandong Province, P.R. China

Education and professional experience

Sep 2009 - Jun 2013	B.E. in Materials Science and Engineering
	Wuhan University of Technology, PR China
Sep 2013 - Sep 2015	M.Sc./Ingenieur (ir.) in Materials Science and Engineering
	Faculty of Mechanical, Maritime and Materials Engineering
	Delft University of Technology, the Netherlands
Mar 2014 - May 2016	R&D Intern/Project researcher waste mineral characterization and valorization
	Van Gansewinkel Minerals, the Netherlands
June 2016 - Sep 2022	PhD researcher
	Faculty of Civil Engineering and Geosciences
	Delft University of Technology, the Netherlands
Sep 2018 – Dec 2018	Visiting researcher
	Faculty of Civil and Environmental Engineering
	University of Michigan, Ann Arbor, the United States
July 2019	Visiting researcher
	Materials Physics Center, San Sebastián, Spain
Sep 2020 - Dec 2022	Postdoctoral researcher
	Faculty of Civil Engineering and Geosciences
	Delft University of Technology, the Netherlands

List of publications

Journal publications

1. **Zhang, S.**, Duque-Redondo, E., Kostiuchenko, A., Dolado, J. S., & Ye, G. (2021). Molecular dynamics and experimental study on the adhesion mechanism of polyvinyl alcohol (PVA) fiber in alkali-activated slag/fly ash. *Cement and Concrete Research*, 145, 106452.
2. **Zhang, S.**, Li, Z., Ghiassi, B., Yin, S., & Ye, G. (2021). Fracture properties and microstructure formation of hardened alkali-activated slag/fly ash pastes. *Cement and Concrete Research*, 144, 106447.
3. **Zhang, S.**, Li, V. C., & Ye, G. (2019). Micromechanics-guided development of a slag/fly ash-based strain-hardening geopolymer composite. *Cement and Concrete Composites*, 102, 29-40.
4. **Zhang, S.**, Keulen, A., Arbi, K., & Ye, G. (2017). Waste glass as partial mineral precursor in alkali-activated slag/fly ash system. *Cement and Concrete Research*, 102, 29-40.
5. Sun, Y., **Zhang, S.**, Rahul, A. V., Tao, Y., Van Bockstaele, F., Dewettinck, K., ... & De Schutter, G. (2022). Rheology of alkali-activated slag pastes: New insight from microstructural investigations by cryo-SEM. *Cement and Concrete Research*, 157, 106806.
6. Zhang, Y., **Zhang, S.**, Chen, Y., & Çopuroğlu, O. (2022). The effect of slag chemistry on the reactivity of synthetic and commercial slags. *Construction and Building Materials*, 335, 127493.
7. He, S., **Zhang, S.**, Luković, M., & Schlangen, E. (2022). Effects of bacteria-embedded polylactic acid (PLA) capsules on fracture properties of strain-hardening cementitious composite (SHCC). *Engineering Fracture Mechanics*, 108480.
8. Li, B., **Zhang, S.**, Li, Q., Li, N., Yuan, B., Chen, W., Brouwers, H. J. H., & Yu, Q.L. (2019). Uptake of heavy metal ions in layered double hydroxides and applications in cementitious materials: Experimental evidence and first-principle study. *Construction and Building Materials*, 222,96-107.
9. Li, Z., **Zhang, S.**, Liang, X., Granja, J., Azenha, M., & Ye, G. (2020). Internal curing of alkali-activated slag-fly ash paste with superabsorbent polymers. *Construction and Building Materials*, 263,120985.
10. Li, Z., **Zhang, S.**, Liang, X., & Ye, G. (2020). Cracking potential of alkali-activated slag and fly ash concrete subjected to restrained autogenous shrinkage. *Cement and Concrete Composites*, 114,103767.
11. Li, Z., **Zhang, S.**, Zuo, Y., Chen, W., & Ye, G. (2019). Chemical deformation of metakaolin-based geopolymer. *Cement and Concrete Research*, 120, 108-118.
12. Keulen, A., Yu, Q. L., **Zhang, S.**, & Grunewald, S. (2018). Effect of admixture on the pore structure refinement and enhanced performance of alkali-activated fly ash-slag concrete. *Construction and Building Materials*, 162, 27-36.

13. Zhang, H., Gan, Y., Xu, Y., **Zhang, S.**, Schlangen, E. & Savija, B., (2019). Experimentally informed fracture modeling of interfacial transition zone at micro-scale. *Cement and Concrete Composites*, 104,383.

14. Li, X., Snellings, R., [et al. Including **Zhang, S.**] (2018). Reactivity tests for supplementary cementitious materials: RILEM TC 267-TRM phase 1." *Materials and Structures* 51.6: 151

15. Avet, F., Li, X., [et al. Including **Zhang, S.**] (2022). Report of RILEM TC 267-TRM phase 2: optimization and testing of the robustness of the R3 reactivity tests for supplementary cementitious materials. Materials and Structures, 55(3), 1-14.

16. Londono-Zuluaga, D., Gholizadeh-Vayghan, A., [et al. Including **Zhang, S.**] (2022). Report of RILEM TC 267-TRM phase 3: Validation of the R3 reactivity test across a wide range of materials. Submitted to Materials and Structures.

Conference contributions

1. **Zhang, S.**, Duque-Redondo, E., Kostiuchenko, A., Dolado, J. S., & Ye, G. (2022). Adhesion mechanism of polyvinyl alcohol (PVA) fiber in alkali-activated slag/fly ash. 5th Bond in Concrete International Conference, Stuttgart, Germany

2. **Zhang, S.**, Feng, Q., Wang, D., & Ye, G. (2021). Environmental impact of a sustainable slag-fly ash-based strain hardening geopolymer composite SHGC. 11th ACI/RILEM International Conference on Cementitious Materials and Alternative Binders for Sustainable Concrete. Toulouse, France.

3. **Zhang, S.**, Li, V. C., & Ye, G. (2020). Development of Strain-hardening Geopolymer Composite through Micromechanics Modelling. RILEM WEEK 2020, Sheffield, UK

4. **Zhang, S.**, Li, Z., Ghiassi, B., Yin, S., & Ye, G. (2019). Effect of alkali activator modulus on fracture properties of alkali-activated slag/fly ash pastes. 15th International Congress on the Chemistry of Cement, Prague, Czech.

5. **Zhang, S.**, Li, Z., Zuo, Y., & Ye, G. (2019). Isothermal calorimetric study on heat evolution and apparent activation energy of alkali-activate slag fly ash pastes. 2nd International Conference on Sustainable Building Materials, Eindhoven, the Netherlands.

6. **Zhang, S.**, & Ye, G. (2019). Influence of reaction products chemistry on the interface bonding properties of PVA fiber in geopolymer matrix. Science of cement and Related Complex Materials (SCRCM) Workshop, San Sebastian, Spain.

7. **Zhang, S.**, Ghiassi, B., & Ye, G. (2018). Experimental study on the interfacial properties of PVA fibers in slag/fly ash-based geopolymer pastes. 4th International Conference on Service Life Design for Infrastructures, Delft, the Netherlands.

8. **Zhang, S.**, Ghiassi, B., & Ye, G. (2018). PVA fiber/matrix interface characterization in alkali-activated slag/fly ash system: Effect of SiO2/Na2O ratio. 2nd International Conference on Alkali Activated Materials and Geopolymers. Tomar, Portugal.

9. **Zhang, S.**, Nedeljkovi´c, M., Ghiassi, B., & Ye, G. (2017). A Comparative Study on Deflection-Hardening Behavior of Ductile Alkali-Activated Composite. 4th International Conference on Strain-Hardening Cement-Based Composites (pp. 123-130). Dresden, Germany.

10. **Zhang, S.**, Keulen, A., Arbi, K. & Ye, G., (2016). Characterization and Preliminary Processing of Biomass Ash for Possible Utilization in Alkali-activated Materials. The 3rd International Conference on Microstructure Related Durability of Cementitious Composites, Nanjing, China.
11. **Zhang, S.**, Keulen, A., Arbi, K. and Ye, G., (2015). Waste Glass Powder as Partial Binder Precursor in FA/BFS Geopolymer Paste. Geopolymers: The route to eliminate waste and emissions in ceramic and cement manufacturing, p.48. (Best Oral Presentation Award)
12. Li, Z., **Zhang, S.**, Liang, X., Kostiuchenko, A., & Ye, G. (2020). Cracking Potential of Alkali-activated Concrete Induced by Autogenous Shrinkage. 3rd RILEM Spring Convention 2020, Guimarães, Portugal
13. Li, Z., **Zhang, S.**, Zuo, Y., Chen, W., & Ye, G. (2019). Chemical deformation of metakaolin-based geopolymer. 73rd RILEM Annual Week & International Conference on Innovative materials for sustainable Civil Engineering. Nanjing, China.
14. Li, B., **Zhang, S.**, et al. (2018). Uptake of heavy metal ions in layered double hydroxides and applications in cementitious materials. 4th International Conference on Service Life Design for Infrastructures, Delft, the Netherlands.
15. Wang, W., **Zhang, S.**, Ye, G., & Noguchi, T. (2021). Effect of reactive aggregate on the early age reaction of water-glass activated slag/fly ash mortars. The 4th International Conference on Microdurability of Cementitious Composites, Delft, the Netherlands
16. Sun, Y., Chen, B., **Zhang, S.**, & Ye, G. (2019) Investigation on the potential application of MSWI bottom ash as cement substitutes, 6th Slag valorization symposium. Leuven, Belgium.
17. Sun, Y., Chen, B., **Zhang, S.**, Blom, K., Lukovic, M., & Ye, G. (2021) Potential application of mswi bottom ash as substitute material in portland cement concrete: Filler or binder. The 4th International Conference on Microdurability of Cementitious Composites, Delft, the Netherlands
18. Chen, B., Sun, Y., Jacquemin, L., **Zhang, S.**, Blom, K., Lukovic, M., & Ye, G. (2019) Pre-treatment of MSWI bottom ash for the application of supplementary cementitious materials in blended cement paste. RILEM Spring convention, Croatia.
19. Li, Z., Li, Z., Wyrzykowski, M., Dong, H., **Zhang, S.**, Lura, P., & Ye, G. (2021). Mitigating the autogenous shrinkage of alkali-activated slag by internal curing. The 4th International Conference on Microdurability of Cementitious Composites, Delft, the Netherlands